CRANFIELD UNIVERSITY

A BUONANNO

AERODYNAMIC CIRCULATION CONTROL FOR FLAPLESS FLIGHT CONTROL OF AN UNMANNED AIR VEHICLE

SCHOOL OF ENGINEERING

PhD THESIS

CRANFIELD UNIVERSITY

SCHOOL OF ENGINEERING

PhD THESIS

Academic Year 2008-2009

A BUONANNO

AERODYNAMIC CIRCULATION CONTROL FOR FLAPLESS FLIGHT CONTROL OF AN UNMANNED AIR VEHICLE

Supervisor: M.V. Cook

January 2009

ABSTRACT

The supporting Flight Dynamics research contribution to the design of *Demon*, a *flapless* UAV demonstrator which is the subject of the national research programme FLAVIIR, is described in this thesis. In particular, an integrated flight control and fluidic control system which employs aerodynamic circulation control (CC) to enhance, or replace a conventional aileron is presented.

The elimination, or reduction in size, of hinged flight control surfaces on an aircraft offers the possibility of reducing aircraft signature and reducing maintenance requirements; fluidic maneuver effectors provide the opportunity to produce the forces and moments required for flight vehicle maneuvering without using conventional control surfaces. A novel alternative to a conventional single slot trailing edge CC actuator that enables proportional bi-directional control was developed. The CC actuator was manufactured and tested, and experimental evaluation confirmed that bi-directional incremental lift generation comparable to that produced by a mechanical flap of similar trailing edge span is entirely feasible.

Wind tunnel tests of a 50% full-span scale *Demon* model were carried out to establish a representative aerodynamic model of the vehicle. A high fidelity 6DoF simulation of the air vehicle was developed, based on the wind tunnel data and was used to assess vehicle trim, stability and control properties. A mathematical model of the flow control actuator, for interfacing the CC system with the flight control system, was developed and incorporated in the dynamic model of the vehicle. The model determined flapless performance and controllability of the aircraft and, in particular, specific saturation limits and their impact on different phases of flight. Also, the requirements for a secondary air supply system for the CC system and practical values of the volumetric air flow requirement have been assessed.

A semi-autonomous primary Flight Control System to enable command and control by a remote pilot throughout the flight was developed. A novel re-configurable control architecture that shares control moment demand between conventional flaps and fluidic

motivators was designed and demonstrated to provide a sufficient degree of safety and a flexibility to facilitate future experimental flight research.

The results of the research study showed the CC actuator to be a practical solution to the problem of direct flow control at subsonic velocities and, hence, to have significant potential to act as a direct replacement for a flap type control surface. Roll control power equivalent to that of conventional ailerons can be achieved at practical trailing edge slot blowing conditions. Thus, it is concluded that the CC actuator, in combination with conventional elevator and rudder, can effectively control the *Demon* over its proposed flight envelope.

ACKNOWLEDGEMENTS

I would like to express my sincere gratitude to my supervisor, Mike Cook, for his help and guidance. Throughout the duration of the project I received valuable advice, support and motivation. I am eternally indebt.

I also would like to thank Dr Sasha Erbsloeh for his advice and especially his guidance through the wind tunnel tests. Sasha always had time to discuss issues and always provided me with valuable insights.

I gratefully acknowledge the support of EPSRC/BAE Systems who have jointly funded the FLAVIIR research programme. I am also indebted to Dr Clyde Warsop, the current industrial programme manager, for his enthusiastic support and contribution to the project.

I would also like to thank the aerodynamics research group under the leadership of Dr Bill Crowther at Manchester University who has willingly provided information from their many and varied flow control experiments. Thanks also to the aircraft design research group at Cranfield University under the leadership of Prof. John Fielding for its contribution.

At last, a lot of thanks to all the people I do not name, but whose help has been invaluable to me.

TABLE OF CONTENTS

TABLE OF FIGURES

NOTATION

Roman alphabet

a	Speed of sound, Wing lift curve slope
a_0	Wing section lift curve slope
ac	Aerodynamic centre
$\mathrm{a_x}$	Axial acceleration
$\mathrm{a_y}$	Lateral acceleration
$\mathrm{a_z}$	Normal acceleration
A_j	Slot area
AR	Aspect ratio
$\mathbf{A}$	State matrix
b	Wing span, bleed
$\mathbf{B}$	Input matrix
c	Chord
$\bar{c}$	Mean aerodynamic chord
cg	Centre of gravity
cp	Centre of pressure
$\mathbf{C}$	Output matrix
C_D	Drag coefficient
C_{D_0}	Zero lift drag coefficient
C_L	Lift coefficient
C_{L_α}	Lift curve slope
C_{L_q}	Lift coefficient due to pitch rate
C_{L_η}	Rate of change of lift coefficient with elevator deflection
$C_{L_{\max}}$	Maximum lift coefficient
C_{LL}	Rolling moment coefficient
C_{LL_p}	Rolling moment coefficient due to roll rate
C_{LL_r}	Rolling moment coefficient due to yaw rate
C_{LL_β}	Rolling moment coefficient due to sideslip
C_{LL_ξ}	Rolling moment coefficient due to aileron deflection
C_{LL_ζ}	Rolling moment coefficient due to rudder deflection
C_M	Pitching moment coefficient
C_{M_0}	Pitching moment coefficient about aerodynamic centre of wing
C_{M_q}	Pitch damping moment coefficient
C_{M_α}	Slope of C_M-α plot
C_{M_η}	Pitching moment coefficient due to elevator deflection
C_N	Yawing moment coefficient
C_{N_p}	Yawing moment coefficient due to roll rate
C_{N_r}	Yawing moment coefficient due to yaw rate
C_{N_β}	Yawing moment coefficient due to sideslip
C_{N_ξ}	Yawing moment coefficient due to aileron deflection

$C_{N_{\varsigma}}$	Yawing moment coefficient due to rudder deflection
C_Y	Side-force coefficient
C_{Y_r}	Side-force coefficient due to roll rate
C_{Y_r}	Side-force coefficient due to yaw rate
C_{Y_β}	Side-force coefficient due to sideslip
C_{Y_ξ}	Sideforce coefficient due to aileron deflection
C_{Y_ς}	Sideforce coefficient due to rudder deflection
C_μ	Blowing momentum coefficient
D	Drag
DCM	Direction cosine matrix
e	Oswald coefficient factor
F	Aerodynamic force
g	Acceleration due to gravity
h	Altitude, Slot height
h_n	Control fixed neutral point position on reference chord
h_{ac}	Aerodynamic centre position on reference chord
h_{cg}	Gravity centre position on reference chord
I_x	Moment of inertia in roll
I_y	Moment of inertia in pitch
I_z	Moment of inertia in yaw
I_{xy}	Product of inertia about *ox* and *oy*
I_{xz}	Product of inertia about *ox* and *oz*
I_{yz}	Product of inertia about *oy* and *oz*
K	Induced drag factor
K_n	Control fixed static stability margin
K_p	Roll rate SAS gain
K_q	Pitch rate SAS gain
K_r	Yaw rate SAS gain
K_v	Auto-Throttle gain
K_Φ	Roll attitude SAS gain
K_{Φ_q}	Turn coordination gain
K_{Φ_r}	Turn coordination gain
K_θ	Pitch attitude SAS gain
K_μ	Lift augmentation
L	Lift, Rolling moment
m	Mass
$\dot{m}$	Mass flow rate
M	Pitching moment
M	Mach number
n	Total normal load factor
N	Yawing moment
o	Origin of axes
p	Roll rate
p_{ss}	Steady state roll rate
P	Atmospheric pressure
P_c	Plenum pressure
P_{intake}	Engine intake pressure
P_E	East position in earth axis
P_N	North position in earth axis
P_0	Sea level pressure
q	Pitch rate
Q_{dyn}	Dynamic pressure

r	Yaw rate, Coanda surface radius
r_W	Washout yaw rate
R	Universal gas constant
RPM	Engine speed
Re	Reynolds number
s	Wing semi-span
s	Laplace operator
S	Wing reference area
t	Time
t/c	Airfoil thickness to chord ratio
T	Temperature, Uninstalled thrust @STP
T_c	Plenum temperature
T_G	Gross thrust
T_{intake}	Engine intake temperature
T_r	Roll mode time constant
T_s	Spiral mode time constant
T_W	Wash out filter time constant
X	Axial force component
y	Lateral coordinate in axis system
$\mathbf{y}$	Output vector
Y	Side force component
z	Normal coordinate in axis system
Z	Normal force component
w	Normal velocity perturbation
W	Normal velocity
T_τ	Thrust
T_0	Sea level temperature
u	Axial velocity perturbation
$\mathbf{u}$	Input vector
U	Axial velocity
v	Lateral velocity perturbation
V	Perturbed total velocity, Lateral velocity
V_D	Normal velocity in earth axes
V_E	East velocity in earth axes
V_j	Jet velocity
V_N	North velocity in earth axes
V_T	True airspeed
V_W	Wind velocity
V_∞	Free stream velocity
x	Longitudinal coordinate in axis system
$\mathbf{x}$	State vector

Greek alphabet

α	Angle of attack
α_0	Zero lift angle of attack
β	Sideslip
γ	Flight path angle, Specific heat ratio of air
δ	Control angle
Δ	Increment
η	Elevator angle
ζ	Rudder angle, Damping
ζ_d	Dutch roll damping ratio
ζ_p	Phugoid damping ratio
ζ_s	Short period pitching oscillation damping ratio
θ	Pitch angle
λ	Coanda surface axis offset
Λ	Wing sweep angle
ξ	Aileron angle
ξ_{cc}	CC aileron actuator deflection
ρ	Air density
ρ_0	Sea level air density
τ	Throttle
ϕ	Roll angle
ψ	Yaw angle
ω	Undamped natural frequency
ω_p	Phugoid undamped natural frequency
ω_s	Short period undamped natural frequency

Subscripts

0	Nominal slot height, Free stream flow conditions
∞	Free stream conditions
¼	Quarter chord point
ac	Aerodynamic centre
b	Bleed
B	Aeroplane body axes
c	Plenum chamber
cp	Centre of pressure
d	Demanded
e	Equilibrium
E	Aeroplane Earth axes
G	Gravitational
I	Initial
j	Jet slot
l	Lower slot
p	Roll rate
q	Pitch rate
r	Yaw rate
s	Slot position, Stagnation point location
S	Aeroplane stability axes
trim	Trim condition
u	Upper slot, axial velocity
v	Lateral velocity
w	Normal velocity
wt	Wind tunnel
α	Angle of attack
ζ	Rudder
ξ	Aileron

1 INTRODUCTION

1.1 The FLAVIIR project

The research reported in this thesis describes the supporting Flight Dynamics contribution to the Flapless Aerial Vehicle Integrated Interdisciplinary Research programme (FLAVIIR).

The FLAVIIR project is a five year research programme looking at new technologies for future Unmanned Air Vehicles (UAVs), funded jointly by BAE Systems and the Engineering and Physical Sciences Research Council (EPSRC) in the UK. Managed jointly by BAE Systems and Cranfield University, the project includes nine additional collaborating university partners. The research programme covers all essential aspects of aeronautical technologies integration for the next generation of advanced UAV concepts. The focus for the research is the “Grand Challenge” proposed by BAE Systems:

> ***“****To develop technologies for maintenance free, low cost UAV without conventional control surfaces and without performance penalty over conventional craft****”***

The principal goal of this ambitious programme of research is to design, build and fly a small, but representative, UAV embodying the integrated technologies developed in the various research studies comprising the project. In particular, it is intended to demonstrate the feasibility of total flight control utilizing flapless technologies. In the context of the project, flapless flight control is interpreted to mean circulation control on the wing by means of trailing edge blowing, and thrust vectoring the exhaust from a small propulsive gas turbine engine. The project will culminate with the flight of a demonstrator vehicle equipped with novel technologies related to flapless flight, currently being developed at by the participating British Universities.

Further information about the FLAVIIR programme can be found on the project website: www.flaviir.com.

From the beginning of the FLAVIIR programme it was recognized that the flying demonstrator should use as much as possible of an existing vehicle to recycle design effort; this will reduce development, manufacturing and operating costs.

The demonstrator air vehicle selected for the project (*Demon*) is a modified version of the *Eclipse* air vehicle, a pre-existing UAV design developed at Cranfield University jointly with BAE Systems. The *Eclipse* air vehicle is shown in Fig. 1-1, together with the modified version of the *Demon*.

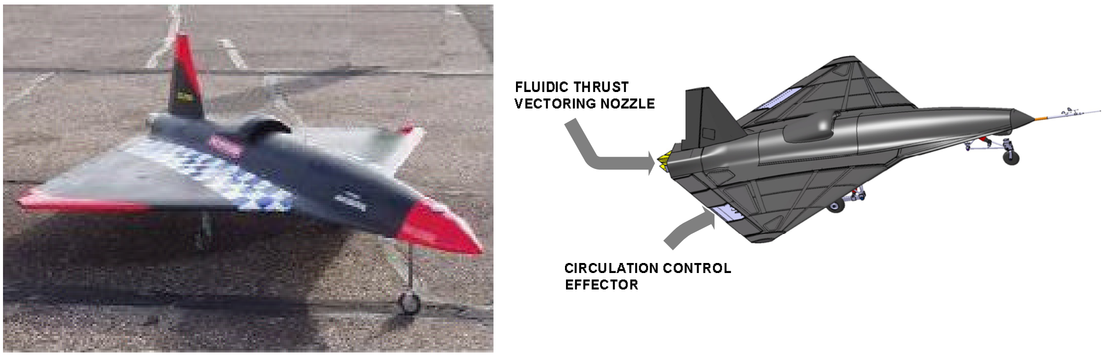

Fig. 1-1. The Eclipse UAV and the Demon modified version

Two flow control mechanisms for flapless flight control are being developed by Manchester University for *Demon*. The first utilises engine thrust vectoring for pitch control by means of secondary blowing over fixed upper and lower Coanda surfaces installed in the rectangular exhaust nozzle (Fig. 1-2). The second utilises wing circulation control in place of conventional ailerons for roll control. The CC "aileron" control also utilises blowing over a Coanda surface embedded in the trailing edge of the wing (Fig. 1-3).

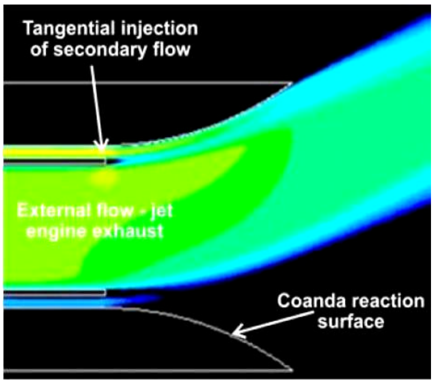

Fig. 1-2. FTV flow schematic (Wilde, Gill, Michie & Crowther, 2007)

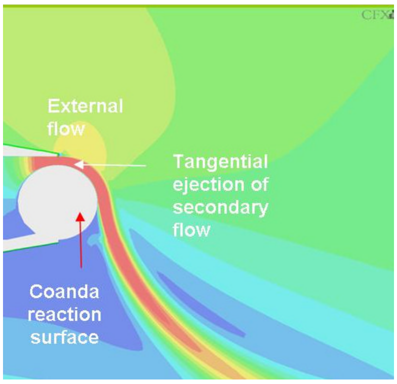

Fig. 1-3. CC flow schematic

1.2 Background and Motivation

In recent years there has been an increasing interest in developing means by which conventional flight controls can be replaced by controls that operate without altering the external geometry of the aircraft. The elimination or reduction in size of hinged flight control surfaces on an aircraft offers the possibility of reducing aircraft signature and reducing maintenance requirements.

The conventional high lift generation by means of mechanical flaps not only results in high noise levels, but is also structurally inefficient for the following reasons:

- The need to retract flaps in cruise imposes the use of a complex variable geometry wing.
- Heavy mechanical loads and hinge moments due to flap deflection are transferred to the thin trailing edge of the wing.
- Storage of flaps and slats within the wing structure reduces the effective volume available for fuel storage and thus impacts effective aircraft range.
- Wing structural weight is increased and torsional loading on the wing box is increased.

One of the most promising techniques to provide direct control of lift, involving virtual aerodynamic shape change as opposed to a real mechanical shape change, is flow control based on the Coanda effect, termed Circulation Control (CC). The concept of a fluidic control refers to an actuator that provides control forces through modification of the fluidic boundary conditions of a flow, as opposed to a conventional moving surface actuator that functions by modifying the geometric boundary of the flow. A CC system consists of a fixed geometry lifting surface with a circular trailing edge cross section. Air is blown tangentially over the curved trailing edge to vary the location of trailing edge separation. In a similar manner to conventional control surfaces, this changes the section circulation, and hence varies the lift coefficient at a fixed angle of attack (Fig. 1-3).

Fluidic flight controls are considered as a type of flow control device and thus are based on the extension of well established flow control principles developed as aerodynamics research over the last 100 years.

Circulation Control technologies have been around since the early 1930s and have been successfully demonstrated (Englar, 2000). Exploratory investigations have demonstrated a threefold gain in lift over the conventional flapped airfoil section (Englar, 1975) and at least a doubling of maximum lift coefficient for a three-dimensional aircraft configuration (Englar & Hammerly, 1981). The main purpose of the Circulation Control Wing (CCW) applications has been to increase the lifting force of an aircraft at times when large lifting forces at slow speeds are required, such as take off and landing. Wing flaps and slats are currently used during landing on almost all aircraft and on take-off by larger jets. While flaps and slats are effective in increasing lift, they do so at a high cost of drag. The benefit of the Circulation Control Wing is that no extra drag is created and the lift coefficient is greatly increased. Such advances in wing design could allow for dramatic wing size reduction in large, wide body jets.

The use of a CCW system eliminates the need for large complex components in the free stream such as flaps and slats greatly reducing the noise pollution of modern aircraft. Additionally, a much shorter ground roll coupled with steeper climb outs and approaches reduces the ground noise footprint.

For performance enhancement applications, the gross changes to the flow are typically smaller and it is convenient to use ‘low authority’ types of actuation, e.g. boundary layer control. At low speeds, an aircraft has reduced airflow over the wing and vertical stabilizer. This causes the control surfaces (ailerons, elevator and rudder) to be less effective. The CCW system increases the airflow over these surfaces and consequently can allow higher maneuverability at low speeds.

A distinguishing factor in more recent work is the drive to use flow control to provide the forces and moments necessary for vehicle flight control as opposed to aerodynamic tailoring for performance enhancement. Flight control applications by their nature tend to require significant changes to the flow to be effective, and this leads to the concept of ‘high authority’ flow control actuators.

An experimental investigation has been performed by Frith and Wood (2004) at Manchester University in which the interest was focused on potential manoeuvre performance with a CCW. Work by Manchester University has established the physical principles for flight dynamic flapless control of air vehicles replacing conventional ailerons with span-wise pairs of slots which permit differential operation sufficient for lateral control and without the adverse yaw effect of a flap surface.

This work at Manchester University has led directly to the flapless flight control vehicle concept which is central to the UK EPSRC/BAE Systems funded FLAVIIR research programme.

The general challenges associated with the application of such flow control devices compared to conventional flapped controls include:

- Effectiveness: devices must effect maneuver moments of sufficient magnitude to meet the requirement of the aircraft's flight envelope.
- Robustness to operating conditions: it is relatively easy to design conventional hinged control surfaces that maintain effectiveness over a range of Mach numbers, aerodynamic attitudes and rates. Flow control maneuver effectors, on the other hand, are typically much more sensitive to the local flow conditions and thus there may be additional cost in order achieve acceptable levels of robustness.
- Linearity: the nature of the fluid mechanic coupling at the heart of flow control devices means that the control response obtained tends to be considerably more nonlinear than that obtained from conventional hinged controls. In order to achieve adequate stability margins for the overall flight control system it will typically be necessary to linearize the actuator characteristics by appropriate use of inner control laws. Of particular concern is the presence of non monotonic control response, bi-stability and hysteresis.

Designing with Circulation Control is complex for the following reasons: the relation between lift increase and blowing momentum is non-linear; for good cruise performance one must change the wing geometry in flight from a round to a sharp trailing edge. The bleed air from the propulsion engines or an auxiliary compressor must be used efficiently. In designing with CC, the propulsion and control aspects are just as important as aerodynamics.

Modulation of the resultant control force and moment generated by a fixed trailing edge geometry utilising internal air flow throttling poses an interesting challenge. Potential engineering difficulties include increased mechanical complexity for bi-directional control, control bandwidth limitation associated with airflow throttling and, probably most significantly, the back pressure impact of on-off bleed air demand on a small gas turbine engine compressor.

In view of the limitation associated with the standard CC control arrangement an obvious question might be raised: "How to control the flow in a manner compatible with conventional aircraft flight control?". An attempt to answer this question provided the basis for the design and development of an alternative CC actuator solution.

1.3 Overview of the research

In support of the project, a programme of flight dynamics research is underway in which the main objective is to provide modelling and simulation as well as stability and control analysis to the collaborating partners. The main aim of this research is the application and modelling of circulation control technology for the purpose of representative flight simulation. The main contributions to the project include flight modelling, simulation and control, fluidic circulation control actuator development and flight control system design.

The first objective of this research was to develop a six degree of freedom simulation model (6DoF), based on the *Eclipse* airframe and to evaluate the control and stability characteristics of the conventional flap control configuration. In order to obtain a representative aerodynamic model of the vehicle an extensive Wind Tunnel (WT) test campaign has been carried out. The contribution to aerodynamic modelling also included a review of previous *Eclipse* aerodynamic tests and predictions from semi-empirical sources to provide confirmation and accuracy, and to indicate areas of testing. As new design data has become available through the life of the project, so the simulation model has been continuously improved to be as representative as possible of the *Demon* configuration. This process continues as the air vehicle design is refined further. The flying demonstrator presents an unusual aircraft configuration and, due to the small aspect ratio and large leading edge sweep performs not unlike a conventional delta wing. Therefore the simulation model of the *Demon* air vehicle has been used to assess the peculiar stability and control properties of the vehicle in the flight envelope.

Additionally, the configuration which utilizes only conventional flaps provided a useful reference for the subsequent analysis of flapless control.

An objective of this research was to develop a flow control mechanism which could be integrated with conventional flight controls, relying on minimal changes. An alternative flow control mechanisation was proposed, comprising an actuator device fully capable of proportional bi-directional control; the arrangement is envisaged as a direct wedge shaped trailing edge replacement for a conventional surface flap and aims to avoid the problems of the more typical arrangement described in section 1.2. What was not so obvious was how practical the actuator might be and how much control power could be achieved compared with a conventional flap of similar size.

The circulation control actuator prototype was manufactured and tested in a low speed open section wind tunnel. The purpose of the experimental programme was to establish the viability of the actuator mechanical design and to compare its performance with a conventional equivalent flap surface.

The design method in sizing CC controls should be integrated with the overall aircraft design, in the sense that the pneumatic power supply system requirements should be included in the overall design cost function. The ability to achieve higher performance is counteracted by the overall systems and performance cost associated with the implementation. A study that aims to identify a design cost function, that weights performance efficiency and systems cost, falls outside the scope of this research. This study aims at looking at the flying demonstrator as a case study, to assess, with a first order approximation, the impact of geometric saturation and power limits of CC on performance at different flight phases and how that limit can change the boundaries of the flight envelope with respect to the flap configuration. The effort/power saturation limits for fluidic actuation arise due to the finite performance of the pneumatic power supply for the actuator. Different options considered within the *Demon* system design to supply compressed air are discussed.

This study was carried out by creating a model of the flow actuator that includes the trends established from experiments, complemented by a first principles model. First, a reference point has been established for a configuration which utilizes only conventional flaps. Second, the model of the flow control actuator was incorporated into the computational model representing the dynamics of the vehicle full scale.

Having established a comprehensive understanding of the flight dynamics of the *Demon*, further studies were undertaken to develop a primary flight control system architecture. The full six degree of freedom (6DoF) simulation model including flap and flapless motivators provided an essential tool for the subsequent development of the Flight Control System (FCS). The FCS is a semi-autonomous system to assist control by a remote pilot throughout the flight.

The *Demon* Flight Control System design challenges were as follows:

- To provide a safe stable platform with dynamics compatible with expected manoeuvre envelope of *Demon*.
- Control characteristics consistent with "carefree" remote handling of a fast highly loaded unconventional air vehicle.
- Configurable control architecture to enable conventional flap control, circulation control and thrust vectoring separately and in combination.
- Provision for switching to alternative advanced primary control laws.
- System flexibility to facilitate future experimental flight research

Fluidic controls differ mainly from the conventional controls in their strong dependency on the free stream velocity and variable air supply. It is important that the flight control system should correctly compensate for flight condition dependent effects. The primary flight control system retains the same functionality as a conventional auto-stabilisation system, but with modifications to allocate commands to the various flap and flapless motivators, and to provide a degree of safety in the event of failure of the flapless controls.

1.4 Aim and objectives

The aim of this research is to evaluate the effect of installing fluidic maneuver effectors on the flight control of a low observable (LO) air vehicle. In particular it is intended to introduce a methodology for integrated flight control system design using flow control devices as primary flight control motivators.

The objectives of this work are:

- To introduce the air-vehicle used in this research and analyse the stability and control properties of the modified airframe configuration.
- To develop a flight dynamics model of the air-vehicle with particular emphasis on producing a representative aerodynamic model for the air-vehicle.
- To research and develop a novel flow control actuator mechanical design, which provides bi-directional flow control in a manner compatible with conventional aircraft flight control.
- To identify the design factors, which determine the control effectiveness of CC effectors in a similar manner to conventional trailing edge devices. In particular, specific saturation limits and their impact on different flight operation phases will be assessed.
- To develop a hybrid flight control system using flap and flapless flight control features. Configurable control architectures using multiple systems (flap and flapless motivators), while providing a flexible flight test bench, is envisaged to provide reliability to guarantee that no element is critical to a safe recovery of the aircraft.

This thesis will focus mainly on the implementation of the wing circulation control device developed as a replacement for conventional ailerons. The Fluidic Thrust Vectoring controller will not be discussed, because at the time of writing sufficient technical design details were not available. Nevertheless, general conclusions about interfacing fluidic controls with a flight control system will be drawn.

2 LITERATURE REVIEW

The literature review focuses on two objectives. The first is to introduce the air vehicle used in this research and gather all the sources of information and data required to develop a simulation model of the air-vehicle. The second is to gain an understanding of circulation control wing and its technology and provide a context for this current study in relation to the state of the art.

2.1 The Eclipse UAV

The *Eclipse* UAV was designed and built in Cranfield University as the subject of the BAE SYSTEMS/Cranfield Part-Time MSc in Aircraft Engineering. The aim was to build and fly an Unmanned Air Vehicle of a novel aerodynamic configuration.
The air vehicle is a low aspect ratio diamond wing configuration and it weighs 35kg with a 2.2 m wingspan. The *Eclipse* UAV is powered by an AMT Olympus jet propulsion system, capable of producing a maximum thrust of 190N. The Aircraft Systems are based around an Avionics crate known as XRAE, developed by Cranfield under contract with DERA and flown successfully in the XRAE1.

The final design was notably different from the one chosen out of the conceptual design stage (Bradbrook, 1999). The configuration evolved from an initial double-diamond canard concept to a flying wing configuration. The wing was designed with an un-cambered section and zero setting angle. The leading edge radius was sufficient to delay separation at the tip and it was not necessary to twist the wing.

As part of the design process of the *Eclipse,* a series of wind tunnel tests were performed in October 1998 at BAe Warton. The wind tunnel model was a 1/10th-scale aluminium flat plate model with the *Eclipse* plan-form and a solid fuselage, machined from model board. This process resulted in squared off leading edges.
According to Harrison (1999), the ‘flat plate’ technique has been used successfully to characterize the aerodynamics of aircraft conceptual designs on a number of occasions

at Warton. The approach was, therefore, justified, and, prior to the 1/10th-scale tests, model ‘scalability’ was demonstrated through a series of separate wind tunnel tests on flat plate and full scale models of another aircraft of similar plan-form to that of the *Eclipse*. Wind tunnel test results for a 1/5th-scale flat plate model were found to be sufficiently comparable to those for an Eclipse-scale model of a diamond wing aircraft. (This 1/5th-scale diamond wing model had the same mean aerodynamic chord as the 1/10th-scale Eclipse model). Model performance at different Reynold’s numbers was also investigated. Wind tunnel tests on the 1/10th-scale flat plate model were performed with a flow velocity of 20m/s which produced a low Reynolds number of $1.8x10^5$.

However, tests on a similar, larger reference model (the 1/5th-scale model mentioned above) with a diamond wing plan-form at a *Re* number of $3x10^6$ had also previously been performed. Data from the low and high *Re* numbers were therefore compared, and the differences in aircraft longitudinal behavior due to change in *Re* number were deemed sufficiently small to justify the continued testing of the small 1/10th scale model. The remaining tests were therefore performed at the lower *Re* number (Bradbrook, 1999). The effects of the sharp leading edge of the 1/10th-scale model are unknown, and may reflect an increased normal force with incidence. This observation was discussed by Bradbrook (1999).

A more extensive series of tests was performed on the 1/10th-scale flat plate Eclipse model to include the effects of control surfaces (Harrison, 1999). Control surface deflections were achieved by bending the metal plate, and forces and moments were measured using an internal strain gauge 5-component balance, which did not record axial force. Therefore, the conversion of the body axes data to wind axes for assessing performance was not possible, except by estimating the drag of the vehicle (Bradbrook, 1999).

This wind tunnel test data, produced early in the design phase of *Eclipse*, was used to evaluate normal force and pitching moment control power. The pitching moment control power was found to be significantly less than the one predicted during the early design. This resulted in an insufficient control power to trim at high incidence, leaving very little for control. Therefore, the vehicle was balanced to be neutrally stable at low incidence and a leading edge strake was proposed to reduce the control deflection to trim at high incidence. The strake was sized during wind tunnel test and a strake with a leading edge sweep angle of 80^o was chosen; this was effectively a chined edge to the fore-body (Bradbrook, 1999). An investigation was carried out in order to remove the vertical tail using alternative yaw effectors. However, no suitable alternative to the rudder was found; the need for a vertical tail to stabilize the vehicle, and the provision of sufficient rudder authority were demonstrated (Bradbrook, 1999).

The wind tunnel test results delivered an aerodynamic database that was used by Gledhill (1999) to develop a six degree of freedom simulation model of the *Eclipse*, using an Advanced Continuos Simulation Language (ACSL). The aerodynamic derivatives for the simulation model were calculated from a combination of the wind tunnel test (Harrison, 1999) and predictions from semi-empirical sources (ESDU data sheets).

A longitudinal and lateral flight control system was also designed. However, the design was affected by some limitations. The simulation incorporates a simple model engine which was not based on real engine test data. Discontinuous elements such as actuator rate limiting, control surface ends-stop and backlash were not modelled. Difficulties in acquiring the correct trim from the 6DoF simulation affected the control law design.

The FLAVIIR flying demonstrator (*Demon*) proposed configuration at the start of the conceptual design was as an Eclipse-Class Vehicle. However, the original *Eclipse* configuration, first designed and build in 1999, has been subjected to many modifications to accommodate the new integrated technologies. Design changes to the back rear of the fuselage were made to permit installation of thrust vectoring. The *Eclipse* is marginally unstable but internal layout changes have resulted in a more forward *cg* to ensure a statically stable vehicle. A positive longitudinal stability was envisaged as a risk reduction. The pitch control power was increased by revised design of the elevator surfaces. Update aircraft configuration can be found in Yarf-Abbasi and Allegri (2004).

These configuration changes undermine the aerodynamic model obtained from the *Eclipse* wind tunnel tests. Moreover the wind tunnel test conducted on the 1/10th scale model can not be considered sufficient to confirm the adequacy of the aerodynamic model used for the 6DoF simulation model for the following reasons:

- Aerodynamic data should be obtained at a flight scale Reynolds number.
- The estimated zero-lift drag and lift dependant drag should be confirmed.
- The effects of the sharp leading edge of the 1/10th-scale model are unknown.
- A more thorough set of test cases needs to be run for completeness, especially for the lateral dynamics.

These conclusions directly influence the proposal of further wind tunnel tests to address the following:

- Evaluate basic aircraft aerodynamics at a flight scale Reynolds numbers. At the low *Re* used for the tests to date it is possible that the flow has remained laminar. Therefore, it could be also be required to fix transition on the aircraft wing. Implementation of flow visualisation should, also, be considered.
- The *Demon* wind tunnel model should be modified to reflect the change in aft-fuselage. It is, also, necessary to add fixed landing gear to the wind tunnel model and evaluate its contribution to aircraft stability and drag.
- Additional lateral-directional stability information is required; particularly, sideslip data are especially required. It would be useful to assess the inboard aileron roll control power separately from the outboard aileron.

2.2 Coanda effect and circulation control wing concept

The basic Circulation Control concept involves the Coanda principle, where a thin jet air of high momentum air is ejected over a rounded trailing edge, as shown in Fig. 2-1. The jet remains attached due to a balance between the pressure gradient normal to the surface and the centrifugal force caused by the streamline curvature. Initially, at very low blowing values, the jet entrains the boundary layer to prevent aft flow separation, and is, thus, a very effective boundary layer control. Eventually, as the jet continues to turn, a rise in the static pressure, plus viscous shear stress and centrifugal force, combine to separate the sheet, and a new stagnation point and streamline are formed on the lower surface. The large deflection of the stagnation streamline produces a pneumatic camber, thereby increasing the airfoil circulation, and hence, the lift.

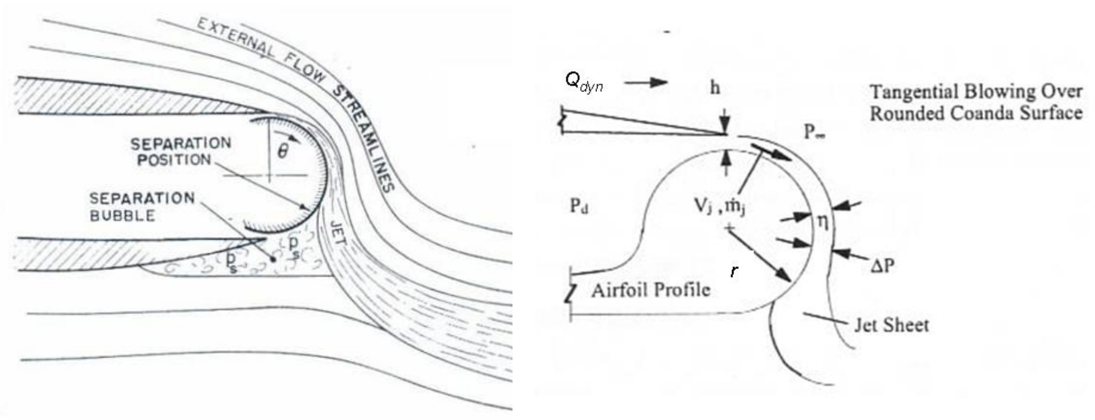

Fig. 2-1. Basic circulation control aerodynamic. (Kind,1968),(Englar,1975)

Conventional airfoils feature a sharp trailing edge, which not only streamlines the flow, but, also, determines the location of rear stagnation point. In other words, it can be stated that lift generated by an airfoil with sharp trailing edge is only dependant on its incidence, as the rear stagnation point is located at the trailing edge. If, however, the aerofoil has a blunt trailing edge, the usual Kutta condition cannot be enforced and the rear stagnation point is free to move dependent upon the circulation, incidence angle, and free-stream velocity. Since the freedom of the rear stagnation point to move around the trailing edge characterizes an inviscid fluid, a potential flow solution can be shown to model approximately the flow around the airfoil.

Consider the irrotational flow in the ς -plane past the circle $|\varsigma| = a$. On the circle itself let $\varsigma = ae^{i\phi}$. Consider the transformation:

$$z = \varsigma + b^2\varsigma^{-1} \tag{2-1}$$

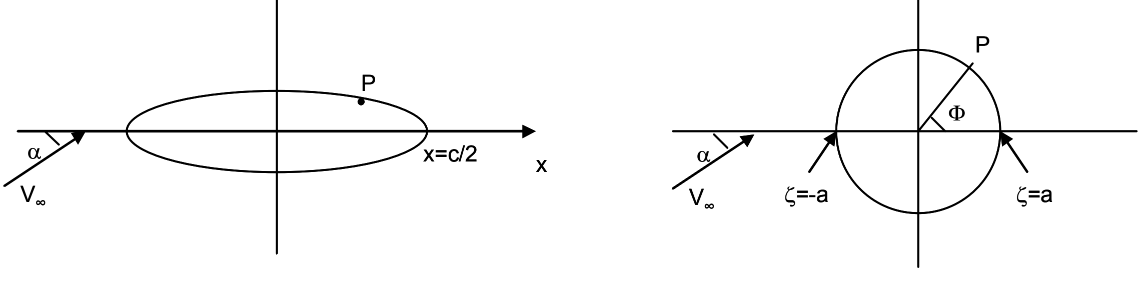

ξ - plane

ζ - plane

Fig. 2-2. Notation used in the transformation between an aerofoil and a circle

The circle becomes the ellipse given by

$$x = (a + b^2 a^{-1})\cos\phi, \quad y = (a - b^2 a^{-1})\sin\phi, \tag{2-2}$$

whose thickness /chord ratio is $t/c = (a^2 - b^2)/(a^2 + b^2)$.

The Kutta condition asserts that in the ζ-plane the speed on the surface must be zero at the point Φ =-β which corresponds to the trailing edge of the airfoil. This condition gives,

$$C_L = 2\pi(4a/c)\sin(\alpha + \beta) \tag{2-3}$$

Eqs. (2-2) and (2-3) give,

$$C_L = 2\pi(1 + \frac{t}{c})\sin(\alpha + \beta) \tag{2-4}$$

Where the separation point is given by

$$\frac{x_s}{y_s} = \tan\gamma = \frac{t}{c}\tan\beta \tag{2-5}$$

Hence, for small values of β,

$$C_L = 2\pi(1 + \frac{t}{c})\sin(\alpha + \frac{c}{t}\gamma) \tag{2-6}$$

Fig. 2-3 shows the variation of lift coefficient with position of rear stagnation point based on Eq. (2-6), for a 20 percent thick ellipse.

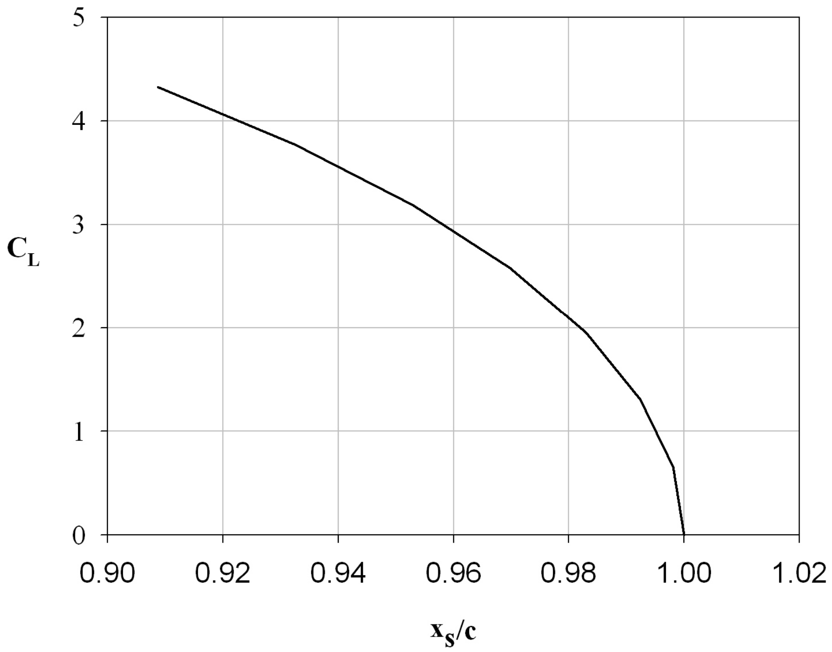

Fig. 2-3. Variation of lift coefficient with rear stagnation point, for a 20% thick ellipse, α=0°

The dependence of Circulation Control technology on boundary layer control, through tangential wall jet blowing, distinguishes it from other forms of powered lift system like Jet Flap. The Jet Flap relies on ejection of a considerable air mass flow in the form of a jet sheet to generate lift and thrust simultaneously, (Fig. 2-4). The ejected jet sheet contributes to the airfoil forces directly due to the horizontal and vertical components of jet momentum and indirectly due to its influence on the flow field external to airfoil. As the jet sheet penetrates the free stream, it causes a deflection and hence changes the airfoil flow field in a manner very much similar to a mechanical flap. This interaction between jet sheet and free stream produces extra lift and thrust.

The lift due to jet flaps can be attributed to three different sources:

a) Direct lift component of the jet reaction.

b) Circulation generated around the airfoil.

c) Boundary layer control.

The boundary layer effect is most significant when the jet momentum turn is small while the super-circulation effect predominates when the momentum is moderate or large.

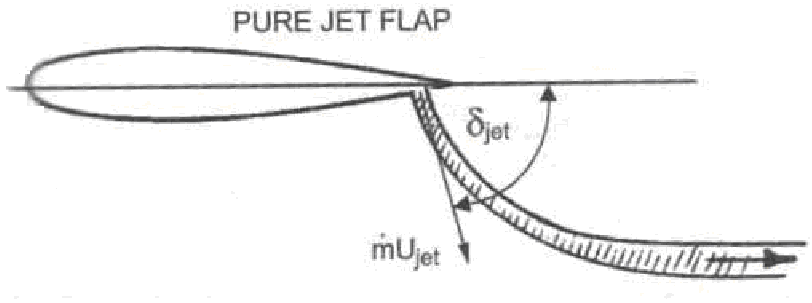

Fig. 2-4. Pure jet flap concept

The efficiency of a pure jet flap (typically vectored normal to surface) compared to typical CC airfoils (vectored tangentially to the upper surface), is realized in the differences in the induced effects that accompany the pressure field. It is recognized that both of these airfoil techniques benefit from induced forces and reaction forces that can be correlated to jet position and orientation. Nominally, Jet Flap airfoils depend largely on the reaction force of the jet momentum. Coanda-type systems capture the induced forces more efficiently and typically deliver larger lift gains than a pure Jet Flap.

In contrast to Jet Flap's direct interaction with flow field, Circulation Control features direct control of circulation and, hence, lift by suppression of separation by boundary layer control. Consequently, lift generated by CC is very sensitive to changes in tangential jet momentum.

Aerodynamic performance of a CC device is characterized as a function of slot flow momentum coefficient, C_μ, which is the momentum flux exiting from the slot normalized by the free stream dynamic pressure and a reference area – usually the area of the wing with full span trailing edge slot:

$$C_\mu = \frac{\dot{m}_j V_j}{Q_{dyn} S} \tag{2-7}$$

A measure of the effectiveness of the blowing in generating lift is the lift augmentation ($\Delta C_l / C_\mu$,) which is defined as the ratio of the lift due to blowing to the jet blowing momentum coefficient.

Comparison of lift generated by Jet Flap and Circulation Control shows that CC can produce as much as 4 times more lift than Jet Flap for the same value of Jet Momentum (Fig. 2-5). Typical initial values of Lift augmentation ratio are 10.0 for a Jet Flap system; however, for Circulation Control this will be from 30 to 40.

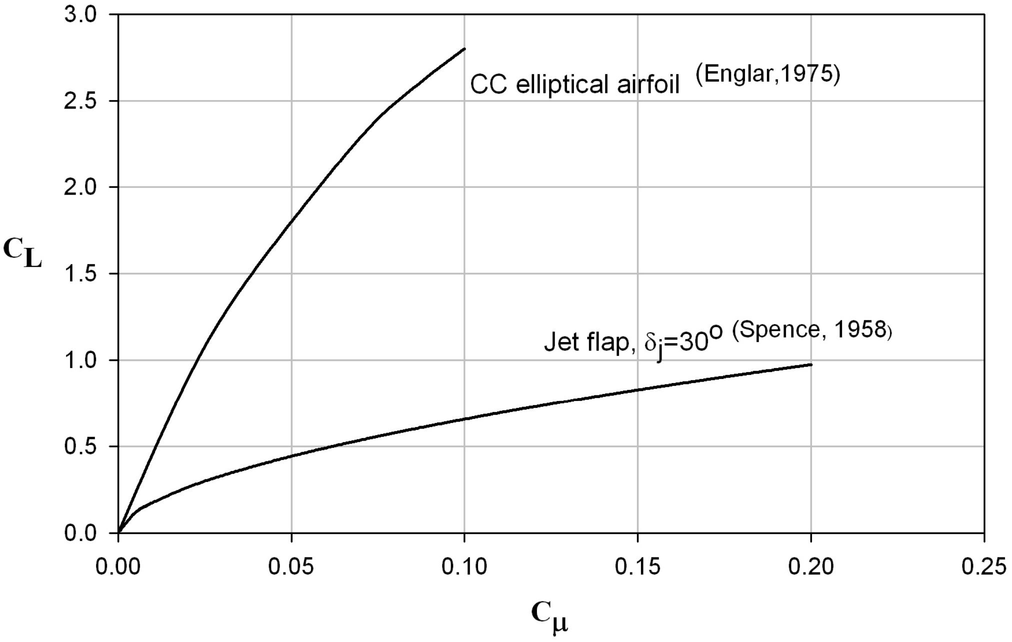

Fig. 2-5. Blown lift capabilities of a CC elliptical airfoil, 20% thick at $\alpha=0^o$

Generally, the following relationship is true,

C_L is proportional to $\sqrt{C_\mu}$ for Jet Flap

C_L is proportional to C_μ for Circulation Control with low C_μ

However, for Circulation Control, the relationship is linear at low values of C_μ and, as C_μ increases, the relationship approaches that of Jet Flap. The reduction in lift generation performance at high C_μ occurs due to increased losses in wall jet turning around the trailing edge. These losses result in the jet leaving the airfoil surface as it approaches the stagnation point and being exhausted, still having excess momentum into the free stream like a jet sheet.

The characteristic of a wall jet remaining attached to a curved surface dates back to 1800 when Young first described the phenomena and later to Henri Coanda in 1910.

The circulation control concept was not seriously investigated until the early 1960's by Dunham and later on by Kind. Dunham (1968) focused on application of CC to a circular cylinder and his method represents the earliest method for representing lift of circulation control airfoils with external flow. In 1966 R.J. Kind finished his PhD at Cambridge University and provided the world with a proof of high C_L =6 capability of an elliptical wing section with circulation control by blowing at very low C_μ (Kind, 1968).

After 1970 The David Taylor Naval Ship Research and Development Center (DTNSRDC) became a major center for circulation control research. Most of CC research was focused on the application to rotorcraft and short take-off and landing (STOL) vehicles, where an elliptical or rounded trailing edge airfoil was used. Experiments by Englar, Abramson and others examined the effect of a wide range of parameters on circulation control airfoils. For a summary of this work the reader is referred to Englar and Applegate (1984).

It is useful to highlight some parametric dependencies of Circulation Control airfoils, in order to identify the driving design parameters of interest which are thickness distribution, camber distribution, location of the blowing slots, slot height to the mean aerodynamic chord, shape of the Coanda surface and curvature. A review of the available literature justified the engineering judgment that drove the design of the CC actuator and provide an insight of potential area for testing.

Sizing the Coanda surfaces can be related to optimizing the lift and drag. Nominally a larger trailing edge Coanda radius would lead to a higher CC lift coefficient as well as a higher cruise drag. Jones (2005) tested different shape trailing edges with a fixed slot height to chord ratio of h/c=0.0022. The shapes include circular, elliptic, and biconvex profiles having effective trailing edge radius of r/c=2%, 1%, and 0% respectively. The lift and the drag performance are compared in Fig. 2-6. The lift performance of the larger radius configuration is higher than the other configurations. A comparison of the drag performance highlights the improvement of the drag as a function of the smaller *r/c*. The elliptic trailing edge (*r/c*=1%) has less drag than the circular trailing edge (*r/c*=2%) throughout the boundary layer and super-circulation region.

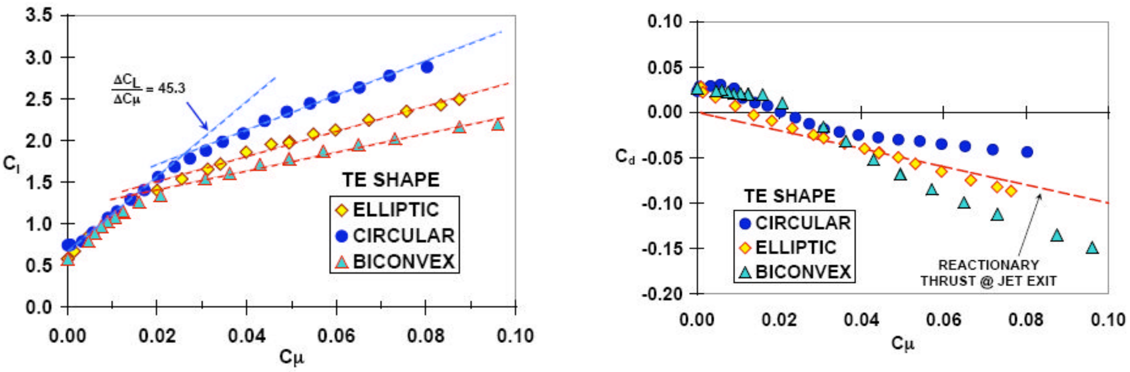

Fig. 2-6. Effect of trailing edge geometry, (Jones, 2005)

Aft-slot location can significantly improve the CC section performance. Englar test data on a 15% thick CC airfoil, reported in Wood and Nielsen (1985), show comparison between a rounded trailing edge with actual slot location at 96% of the chord and a pure ellipse trailing edge with actual slot location at 92.4% of the chord, for different Mach number. The rounded configurations are preferred for low speed operation. At low speed the rounded trailing edge produces more lift than the elliptic geometry, although the drag rises significantly as the Mach number increases compared to the pure ellipse. Therefore, it appears that forward slot location and mild curvature at the slot exit are more efficient at high speed compared to the rounded configuration favored at low speed. This result seems to be further validated by an experimental study conducted by Alexander, Anders and Johnson, (2004). A wind tunnel test was carried out on a six percent thick slightly cambered elliptical circulation control airfoil with both upper and lower surface blowing Parametric evaluations of jet slot heights and Coanda surface shapes were conducted, using Coanda shapes with different elliptical ratio, (Fig. 2-7).

a) End view of the Coanda surface

b) Coanda surface − aft. slot location: x_s/c =0.9

Fig. 2-7. End view of Coanda surfaces with different elliptical ratio, (Alexander et al., 2004)

At the transonic cruise condition, Mach =0.8, it was found that the effectiveness increased with increasing Coanda surface elliptical ratio. At the low speed condition, Mach =0.3, it was found that the effectiveness increased with decreasing Coanda surface elliptical ratio, (Fig. 2-8).

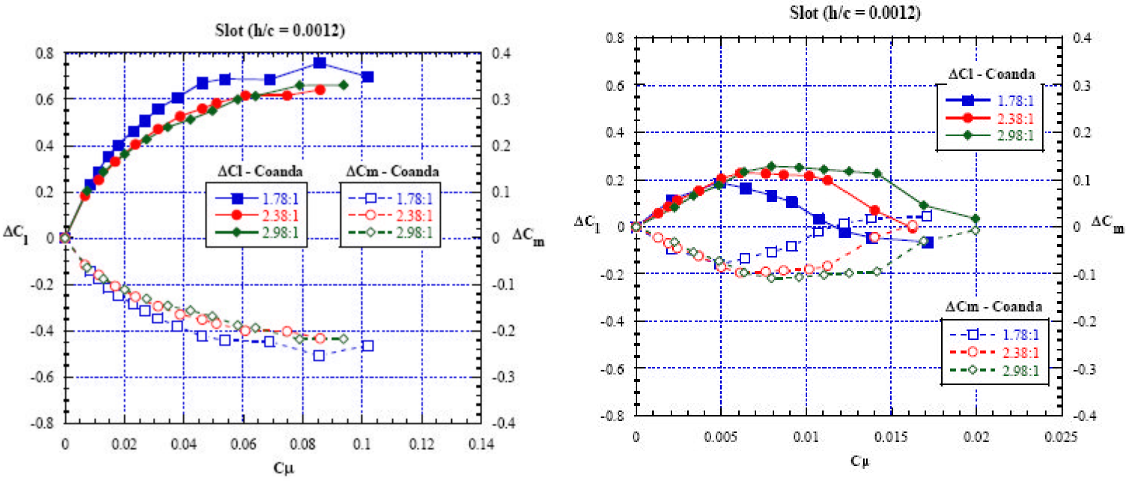

a) upper slot blowing-Mach=0.3, α=3°

b) upper slot blowing-Mach=0.8, α=3°

Fig. 2-8. Effect of coanda surface, (Alexander et al., 2004)

The efficiency of the Coanda blowing can be related to the slot height and the radius of the coanda surface. For a fixed Coanda surface radius, experiments have proved that a higher lift coefficient can be achieved with a smaller slot height for the same momentum coefficient (Englar, 1975, Wood & Nielsen, 1985 and Jones, 2005). This result is valid only for subsonic free-stream velocity. Since it is always preferable to obtain higher lift with as low a mass flow rate as possible, a thin jet is more beneficial than a thick jet. However, the pressure required to generate a jet issuing through a smaller slot is higher than the one for a larger slot at the same momentum coefficient. The circulation around the airfoil poses an optimization problem dependant upon whether the blowing air supply is mass flow or pressure ratio limited.

The level of performance of circulation control airfoils is directly related also to specific aspects regarding airfoil design. Increases in camber and thickness ratio can double the CC section performance, as shown in Fig. 2-9.

However, excessive camber or thickness have been shown to significantly increase the growth of the upper surface boundary layer as it approaches the slot, which may result in reduced lift augmentation (Wood & Nielsen, 1985).

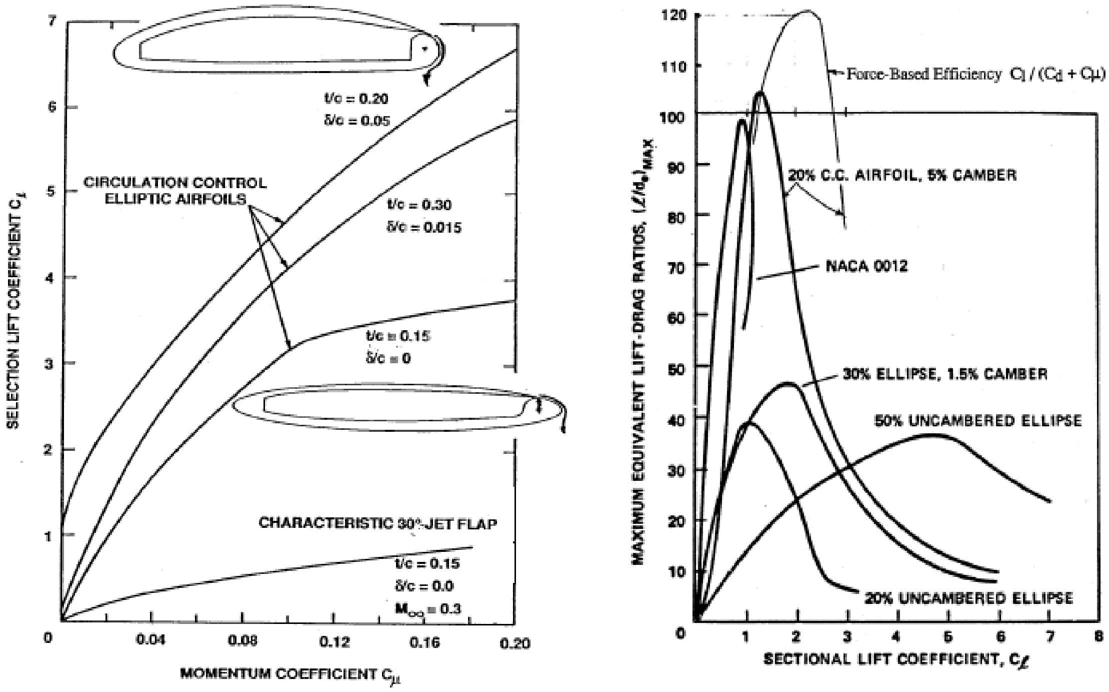

a) Typical Blown-Lift Capabilities of 2-D CC Elliptic Airfoils at $\alpha = 0°$

b) Equivalent Efficiencies for CC and Conventional 2-D Airfoils

Fig. 2-9. Effect of thickness and camber on CC airfoil performances, (Englar, 2000)

The lift increment is proportional, for high value of blowing, to the square root of the blowing momentum. Therefore the blowing momentum that can be used to produce lift augmentation is clearly limited to a maximum usable blowing coefficient that if exceed will not produce any higher lift. It could be inferred from the definition of C_μ , Eq. (2-7), that the lift augmentation is directly proportional to the velocity ratio, V_j/V_∞, and the last has a significant role in the performance of CC system. Loth and Boasson (1984) replotted data from Englar (1975) and showed that, at constant slot height, the lift augmentation increases rather linearly with V_j/V_∞. Loth and Boasson (1984), also, determined that for single-slot blowing at constant slot height, the maximum value of lift increment will be obtained at a value V_j/V_∞ of approximately 4.6. However, at a given C_μ, there is only about 10% variation in ΔC_L over a range of V_j/V_∞ values between 2.5 and 12. At a constant blowing power $[C_\mu\ V_j/(2V_\infty)]$ the optimum ΔC_L is reached at a velocity ratio of 2.

Although circulation control can be achieved with a supersonic wall jet, Englar (1975) showed that such a jet loses a significant portion of its momentum to wall shear, and only the remaining jet momentum will be available to energize the Coanda surface boundary layer.

The effect of free-stream velocity on the lift generated by blowing seems to be negligible. Liu (2003) applied an unsteady three-dimensional Navier-Stokes analysis procedure to CCW and showed that the performance of CC airfoils is independent of the free-stream velocity under a fixed C_μ and fixed jet slot height conditions, except at very low free stream velocity where the jet velocity will be too low to generate a sufficiently strong Coanda effect that eliminates separation.

2.3 Circulation Control aerospace applications

Historically, only two CC aircraft have ever been build and flight-tested in the past 30 years. The main reason for lack of success would appear to be not lack of effectiveness; rather, the benefits of application have not exceeded the cost of implementation.

For fixed wing vehicles, the high lift generated by CC wings makes them ideal candidates for short take off and landing (STOL) aircraft. In 1968, West Virginia University started the theoretical and experimental investigation of an elliptical Circulation Control Rotor section for Navy Heavy Lift Rotor Helicopter development under the contract with Office of Naval Research. A BD-4 airframe was modified by rotating its flap by 166 degrees that would convert wing flap's sharp trailing edge into the round CC Wing and leading edge was dropped down to prevent leading edge stall (Loth, 2005). Details of the modification are shown in Fig. 2-10 .
The BD-4 airplane was further modified and flight testing was performed in April, 1974 (Loth, 1976). The blowing air was supplied by an onboard 200HP compressor APU.

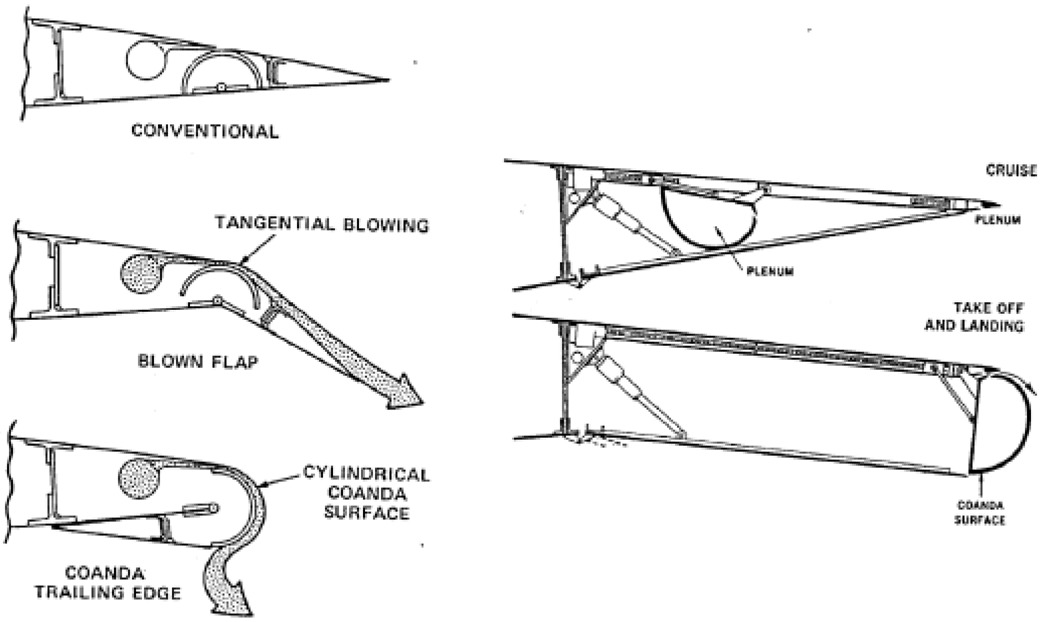

Fig. 2-10. Retractable/Storable CCW trailing edge, (Loth, 2005)

Numerous wind tunnel tests evaluation (Englar & Hammerly, 1981) led up to flight test of a fixed CCW device on an A-6/CCW STOL demonstrator in 1979. Fig. 2-11 shows the CCW installation on the fixed flap of the A-6 aircraft. The Grumman A-6 was modified and flight tested to demonstrate the high lift and STOL capability of the circulation control wing concept which employs a circular trailing edge blown by the standard J-52 turbojet engine high pressure bleed air. A fully comprehensive description of the flight test can be found in Pugliese (1979).

Fig. 2-11. A-6/CCW STOL Flight Demonstrator Aircraft, (Englar, 2000)

The results of BD-4 Flight test demonstrator and A-6A Flight test demonstrator have been compared and results showed full agreement. Lift curve slope was 4.74 for A-6A and 5.0 for BD-4, while $dC_L \Big/ \sqrt{C_\mu}$ was 6.6 for both the airplanes.

Both these programs identified the following aspects:

- Circulation control airfoils, when producing high values of C_L, are subject to high drag loads which unlike Jet Flap are not nullified by jet thrust. This high value of drag along with high lift is beneficial for STOL and Super STOL airplane applications as it enables a stable, steep gradient landing approach at very low forward speeds.
- During cruise, which constitutes a very big portion of any airplane mission, the profile drag associated with blunt trailing edge produces very low values of Lift to Drag ratio(*L/D*). Any significant reduction in cruise (*L/D*) can seriously reduce the utility of an airplane. Therefore, the need to reduce the CCW drag in cruise was a necessity for operational flight.
- The airflow acquired from high-pressure compressor bleed ports could be increased up to 3 to 4 times than that of the standard engine spec bleed limit without overheating, but obviously at the cost of takeoff thrust lost. High induced drag may also preclude adequate acceleration at take off.
- To go very slow, at minimum level speed, all available 180 HP where required. This is a clear indication of flying on the backside of the power curve. Flying

> slow, on the backside of the power curve, is not recommended because no power is then left over to assist in stall recovery.

The high drag associated with the blunt, large radius trailing edge can be prohibitive under cruise conditions when Circulation Control is no longer necessary. One way to reduce the drag is to reduce the trailing edge radius. This, however, causes a loss of lift compared to a large radius configuration. It was also found that the small radius CC airfoil with larger slot height could cause jet detachment and sudden lift loss at higher momentum coefficients (Englar & Huson, 1983). Thus a compromise was needed. The advanced CC airfoil, i.e., a circulation hinged flap (Englar et al., 1983, Englar, 1994), was developed to replace the original rounded trailing edge CC airfoil. The advanced CC airfoil developed by Englar is shown in Fig. 2-12.

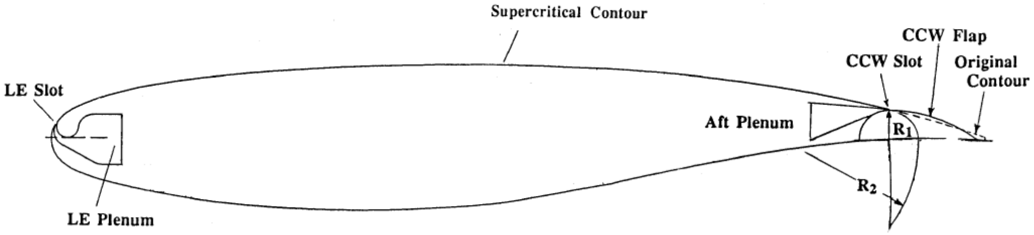

Fig. 2-12. Dual radius CCW configuration, applied to a 16% Thick Supercritical Airfoil, (Englar, 1994)

The upper surface of the CCW flap is a large-radius arc surface, but the low surface of the flap is flat. The flap could be deflected from 0 degrees to 90 degrees. When an aircraft takes-off or lands, the flap is deflected. Then, this large radius on the upper surface produces a large jet turning angle, leading to a high lift. When the aircraft is in cruise, the flap is retracted and a conventional sharp trailing edge shape results, greatly reducing the drag. Overall, the hinged flap design still maintains most of the Circulation Control high lift advantages, while greatly reducing the drag in cruise, associated with the rounded trailing edge CCW designs. However, this kind of flap does have some moving elements, which increase the weight and complexity over an earlier CCW design.

It is interesting to note that the majority of applications reviewed focuses on the application of CC as a high lift device to pneumatically augment the lift. Englar (2000) has experimentally observed that CC can produce usable control moments; for example, high rolling moment increments can be produced by differential wing blowing. However, an integrated flight control and CC system, which could be used to effectively control the aircraft attitude, appears to be missing.

2.3.1 The use of circulation control for flight control

A distinguishing factor in more recent work is the drive to use flow control to provide the forces and moments necessary for vehicle flight control as opposed to aerodynamic tailoring for performance enhancement.

Research into flow physics and the application of flow control to aircraft flight control has been made over a period of years, see for example, Frith and Wood (2002) and Sellar, Wood and Kennaugh (2002). Recently concluded flow control research with direct relevance to the FLAVIIR programme was completed by Frith and Wood (2003). An experimental investigation into the application of circulation control on a 50° swept delta wing was performed. This was then extended to a sting-mounted circulation control demonstrator with two control surfaces, (Fig. 2-13), in order to determine whether the technique could be used for roll control, whilst maintaining high lift coefficients within the limits of pitch trim (Frith & Wood, 2004). A lift augmentation of approximately 20 was achieved when symmetrical blowing was applied on both ports and starboard slots. The control of rolling moment by circulation control was also demonstrated (Fig. 2-14). A particular rolling moment could be achieved with a particular value of C_μ independent of the angle of attack. A gradient of rolling moment curves with C_μ of approximately 7 was found and a blowing momentum coefficient of 0.0021, equivalent to an aileron deflection of 10 deg was obtained.

This finding is significant to this current study, as it has demonstrated the potential for CC to produce roll control and pitch trim.

However, a significant rearward movement of centre of pressure was observed that result in a pitching down moment that will need to be trimmed out. This finding suggests that differential blowing on each side of the aircraft is necessary to cancel out the pitch down moment. Hence, the development of a bidirectional CC actuator is required.

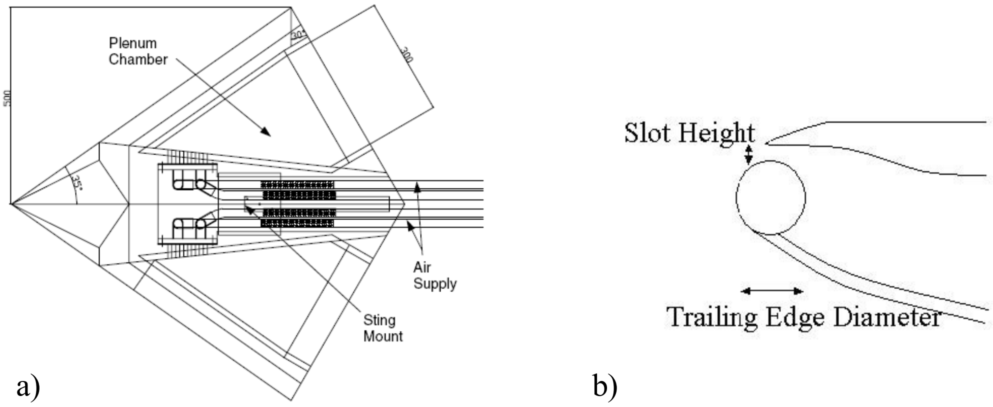

Fig. 2-13. a) Schematic of the full span model; b) 6mm diameter TE and 0.15-0.3 mm slot height, (Frith et al., 2004)

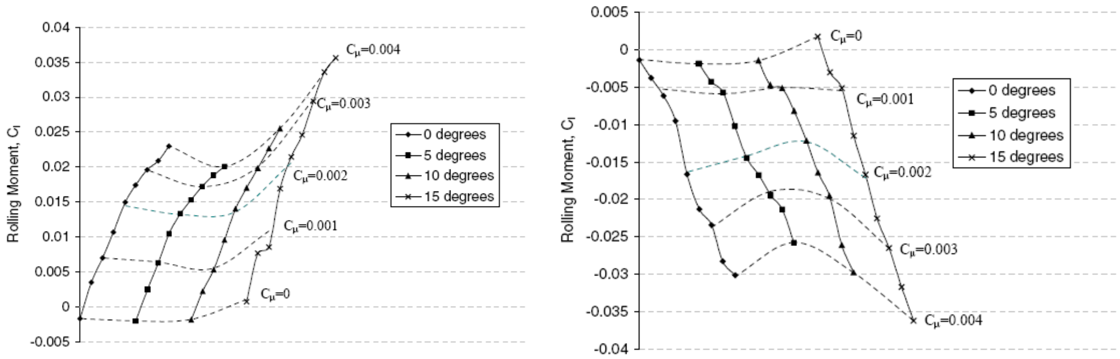

a) Left CC rolling only

b) Right CC blowing only

Fig. 2-14. Variation of rolling moment with asymmetric blowing, (Frith et al., 2004)

2.3.2 Dual slotted circulation control

Dual slotted devices correspond to system incorporating two slots at the trailing edges. The literature published on this topic is quite narrow but a review of published materials aims to introduce the concept exploited in this research.

The first dual slotted airfoil was designed and tested in 1987 by Jane Abramson and the test documentation can be found in Imber (2005).

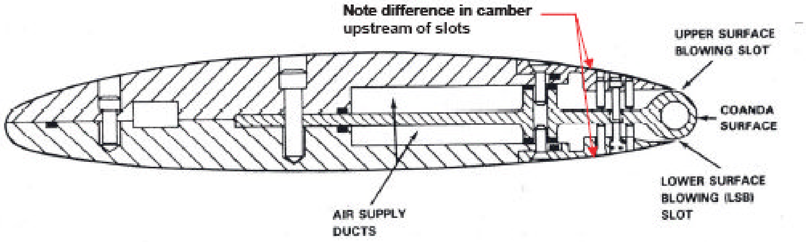

Fig. 2-15. LSB17 dual slot model cross section-slot location (x_s/c): upper: 0.968, lower: 0.97, (Imber, 2005)

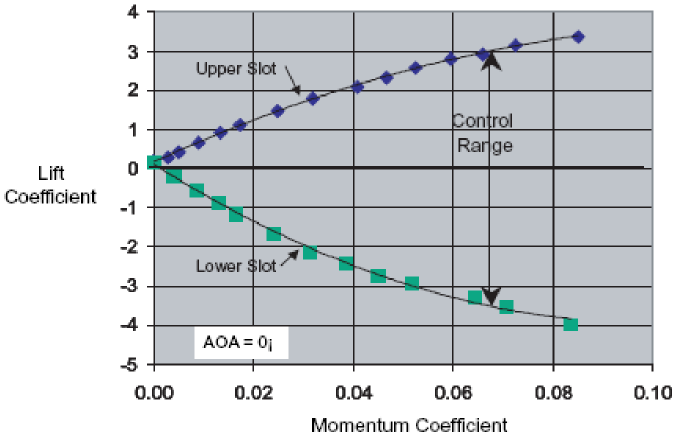

Fig. 2-16. Control range increase with upper and lower slot, (Imber, 2005)

The airfoil was the first CC model designed at Carderock to incorporate both upper and lower trailing edge blowing slots (h/c: 0.0013 and 0.0020). The dual slots provide the ability to produce lift in either direction. The cross section sketch in Fig. 2-15 shows the LSB17 model. Testing included three blowing modes: upper surface only, lower surface only and dual blowing. One of the main design goals was to have the dual slotted model perform as well as the single slotted 'parent' model.

The keys findings were:

- There was no detrimental effect of adding the 2nd slot.
- The control range was double so that the force control in both directions was available, (Fig. 2-16).

An extremely comprehensive investigation was conducted by Rogers and Donelly (2004) of a low aspect ratio CC wing in the Navy's 10-foot large cavitation channel in

Tennessee, shown in Fig. 2-17. Although the intended application is to naval hydrodynamics, some interesting conclusions can be drawn.

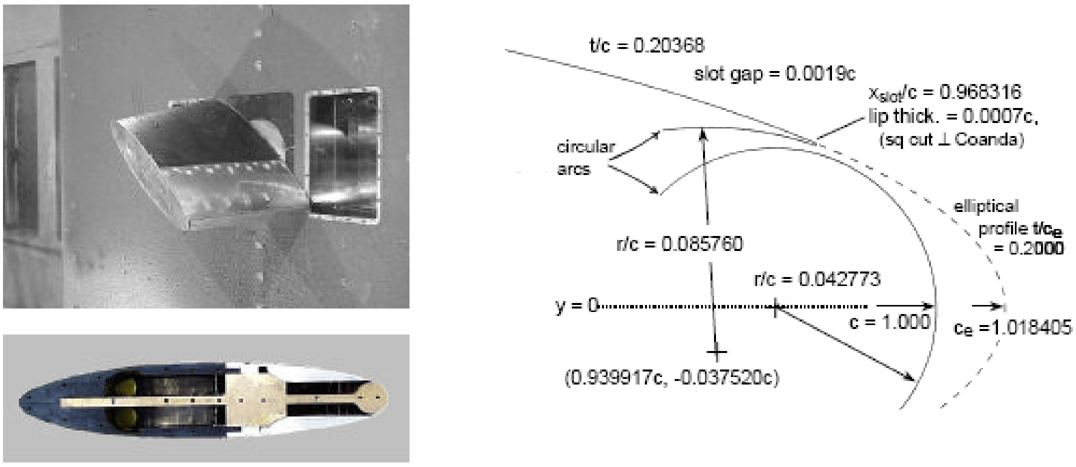

a) model cross section and CC wing AR=2 b) detailed of the trailing edge design

Fig. 2-17. Dual slot low aspect ratio wing design, (Rogers & Donelly, 2004)

The key findings of this investigation were:

- For the wing, which has an aspect ratio of two, the response of C_L to C_μ is about 50% of that on the corresponding 2-D airfoil. This is the same percentage as the C_L versus angle of attack change for a conventional wing. Hence, there is no indication of any basic effects of low aspect ratio that are unique to lift developed by means of the Coanda form of circulation control, (Fig. 2-18a). This study confirms the decision of testing the CC actuator on a low aspect ratio rectangular wing.
- A clear advantage of dual slots is the ability to vector the jet thrust. In fact, in static conditions, as representative of very low speed operation, when dual slot blowing was examined, the yarn tufts showed that the two wall jets merged to form a single free planar jet that could be adjusted to any angle, (Fig. 2-20).
- Wake filling is viable with dual slots, (Fig. 2-18b).
- It was concluded that excessive turning of the jet was causing the loss in lift. The lower slot produces a very small counter flow to prevent the excessive turning of the jet and lift roll-off, (Fig. 2-19).

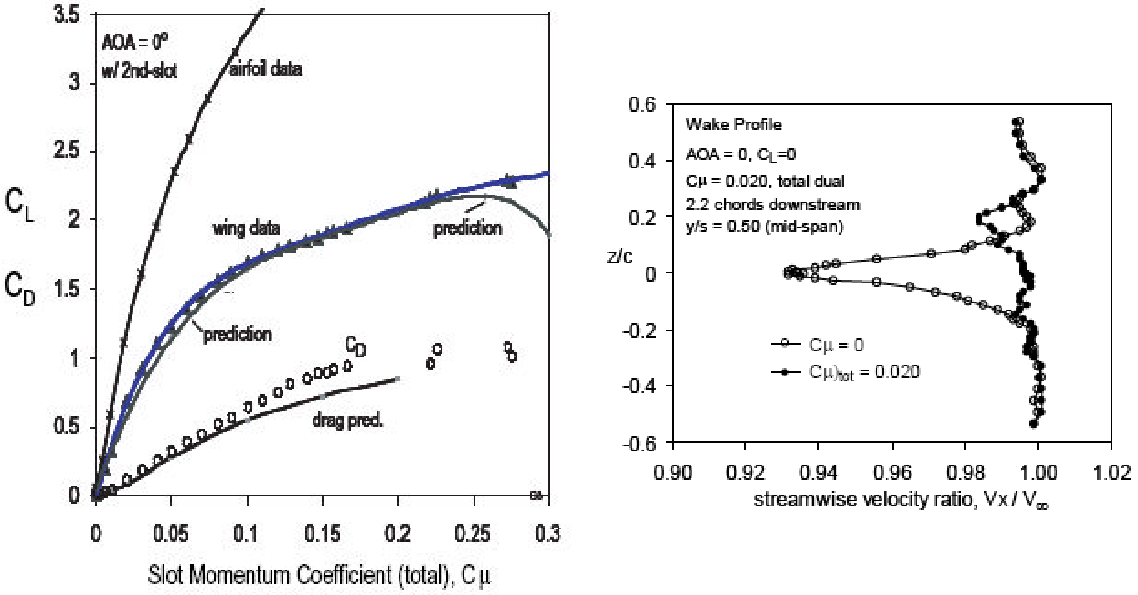

a) Comparison of actual performances to lift line theory prediction

b) Wake filling

Fig. 2-18. Dual slot low aspect ratio wing performance, (Rogers, 2004)

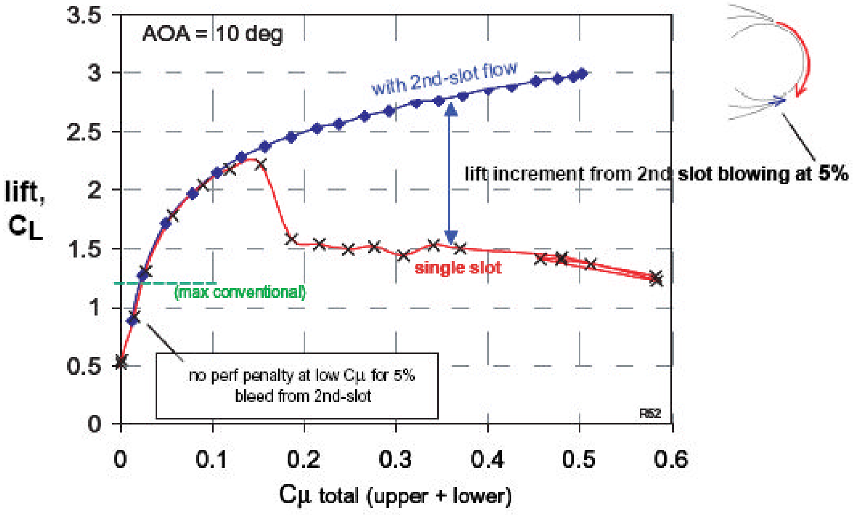

Fig. 2-19. Small counter-flow (5%) from the second slot used to influence the excessively turned jet, (Rogers, 2004)

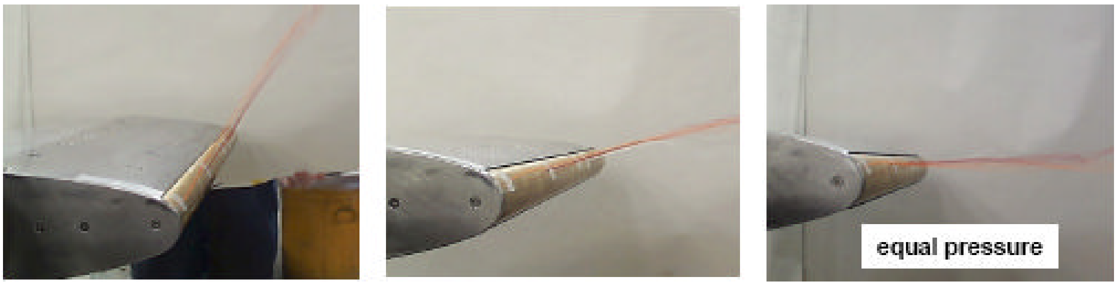

Fig. 2-20. Static flow visualization of the jet using tufts, (Rogers, 2004)

Several roadblocks to real aircraft application of CC guided the development of a 2-D General Aviation Circulation Control (GAAC) wing concept (Fig. 2-21). A comprehensive description of this work can be found in Jones (2005). Primary objectives of this effort were to reduce the drag penalty associated with a large circulation control trailing edge, to evaluate the dual blown pneumatic concept as a control device and to determine benefit of returned thrust. A 17% thick supercritical airfoil was chosen as baseline for the GAAC. The A-6/CCW airfoil was a 6% thick supercritical wing section that incorporated a circular trailing edge radius of 3.67 percent chord. In order to minimize the drag, a baseline circular *r/c* of 2 % was chosen for the GAAC.

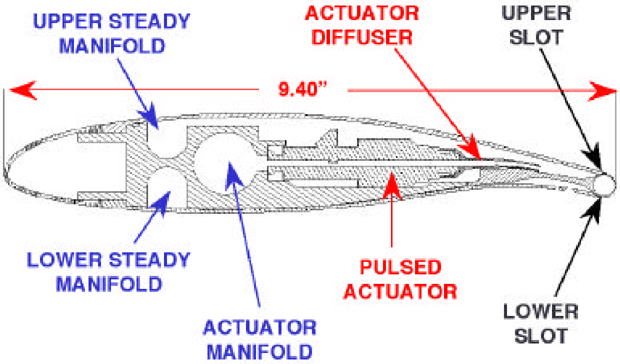

Fig. 2-21. 2-Dimensional 17% Supercritical General Aviation Circulation Control Airfoil with a circular trailing edge *r/c*: 2%, (Jones, 2005)

This blown configuration shows the possibility of reducing the cruise drag by blowing both the upper and lower slot simultaneously. The equivalent cruise drag is showed in Fig. 2-22. A 40% drag reduction compared to the un-blown case was realized. The drag polar indicated that thrust can be adjusted for a given lift to reach an optimum cruise configuration. This frame work was a useful reference for the wind tunnel test model to explore CC actuator.

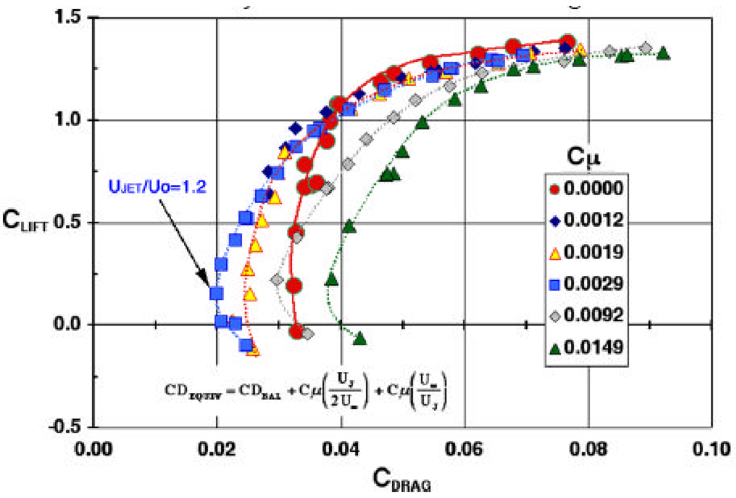

Fig. 2-22. 2-Dimensional 17% Supercritical General Aviation Circulation Control Airfoil with a circular trailing edge *r/c*: 2% , (Jones, 2005)

McGowan, Gopalarathnam and Jones (2004) explored the use of adaptive circulation control airfoil to achieve low drag at cruise and climb conditions while retaining the well-known very-high-lift capability of traditional circulation-control airfoils. Circulation control was achieved by blowing a jet of high-velocity air through slots on the upper and lower surfaces over a small adjustable mechanical flap, so that extensive laminar flow is achieved over a significant portion of the chord and turbulent separation in the recovery region of the airfoil is avoided by use of the jet blowing. This study suggests the use of a concept that integrate traditional high lift devices with blowing to explore the capability of circulation control to adapt an airfoil to suit different flight conditions.

3 DESCRIPTION OF THE AIRCRAFT

3.1 Introduction

The *Demon* air vehicle selected for the project is derived from the *Eclipse* air vehicle, which is a pre-existing UAV design developed at Cranfield University jointly with BAE Systems. *Eclipse* is a tailless configuration, with a cropped diamond wing plan-form and powered by a single AMT Olympus HP ES gas turbine engine. Table 3-1 shows the main geometry and mass properties of the *Demon* variant of the vehicle. All data presented is from Yarf-Abbassi and Allegri, (2004), unless otherwise stated. The flight envelope is presented in Fig. 3-1. The *Eclipse* air vehicle has four trailing edge flaps either side of the centre line. Outboard and inboard flap are used symmetrically for longitudinal control and outboard aileron flaps are used differentially for lateral control. The addition of a rudder allows the aircraft to be controlled about the three axes independently.

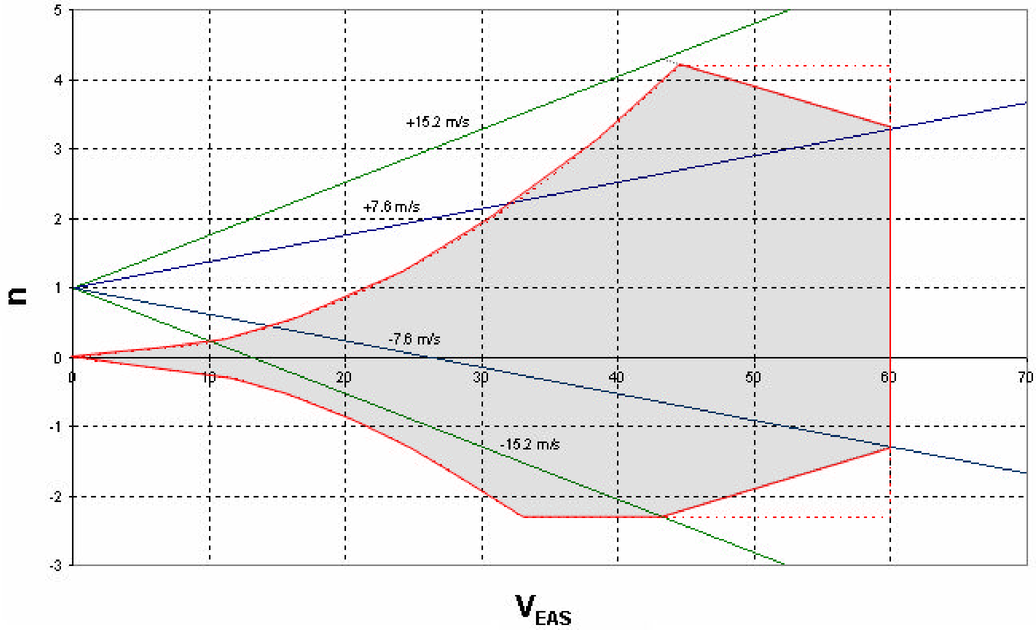

Fig. 3-1. Demon Flight Envelope

Fig. 3-2 illustrates the numbering system employed to identify control surface deflections. The trailing edge control surfaces are referenced by number frequently throughout the results and analysis sections of the report according to the following scheme:

- Surfaces No.1: Outboard ailerons
- Surfaces No.2: Inboard ailerons (at the location of the flow control devices)
- Surfaces No.3: Outboard flap
- Surfaces No.4: Inboard elevator

The intended convention for the *Demon* is that surfaces No.1 should be ailerons, and surfaces No.3 and No.4 should operate together as a large elevator.

The maximum symmetric and differential deflection of the wing trailing edge flaps is +/- 15°.The maximum rudder deflection is +/- 20°.

MTOW	m	44.2 kg
Wing area	S	2.635 m^2
Wing span	b	2.2 m
Mean chord	$\bar{c}$	1.34 m
Roll moment of inertia	I_{xx}	1.207 kgm^2
Pitch moment of inertia	I_{yy}	1.38 kgm^2
Yaw moment of inertia	I_{zz}	12.28 kgm^2
Inertia product	I_{xz}	-0.25 kgm^2

Table 3-1. Demon geometry and mass properties

A principal feature of the *Demon* aircraft variant is that the aerodynamic flap control surfaces No.2 shall be replaced with flow control mechanisms sufficient to demonstrate total flapless flight control of the vehicle. In the context of the experimental programme, the vehicle will be fitted with both flapless and conventional flap controls such that it will be controllable by either means, or by a combination of both.

Two flow control mechanisms for flapless flight control are being developed for *Demon*. The first utilises engine thrust vectoring for pitch control by means of secondary blowing over fixed upper and lower Coanda surfaces installed in the rectangular exhaust nozzle. The second utilises wing Circulation Control in place of conventional ailerons for roll control. The CC "aileron" control also utilises blowing over a Coanda surface embedded in the trailing edge of the wing.

The *Eclipse* is marginally unstable but internal layout changes in the *Demon* configuration have resulted in a more forward *cg* to ensure a statically stable vehicle. During the flight envelope change of *cg* due to fuel consumption are marginal and negligible, being the fuel tank placed at the *cg*. The *cg* position as measured with respect to the nose point of the aircraft and its flat base is reported in Table 3-2.

***cg* position** (measured with respect to the nose point of the a/c and its flat base)		
x_{cg} [m]	y_{cg} [m]	z_{cg} [m]
1.203	0	0

Table 3-2. Demon centre of gravity

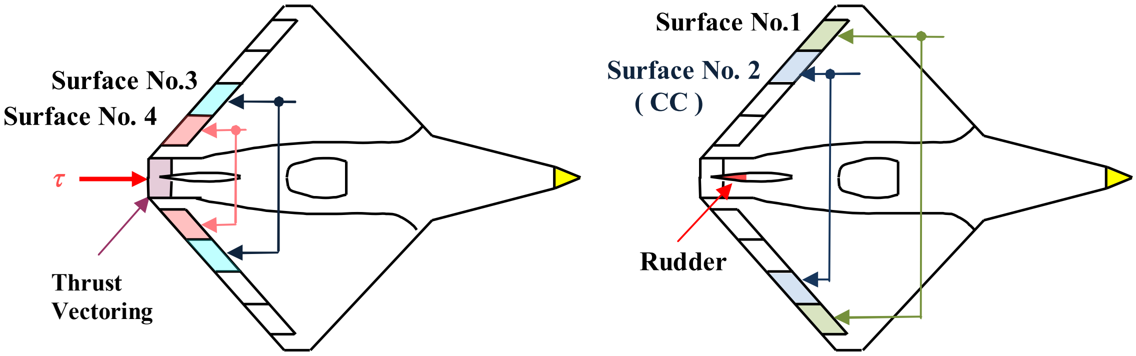

Fig. 3-2. The Demon control configuration

3.2 Aerodynamic performance

3.2.1 Wind tunnel testing of the demon ½ scale model

As part of the design process of the *Demon* at Cranfield University a wind tunnel test campaign was performed with the full-span 50% scale *Demon* in the 8x6 ft facility at Cranfield University.

The model was suspended from the wind tunnel ceiling with a rigid faired strut which was mounted to a 6 component strain gauge balance placed inside the model. This positioned the model just off-centre within the working section of the 8x6 ft closed return wind tunnel at Cranfield University. The model also incorporated a tail-arm supported by a set of high tension bracing wires that were used to set the angle of attack of the model (Fig. 3-3). Representative conventional control surfaces and undercarriage were incorporated. The engine system and jet exit system was not simulated and a simple fairing was added to the front of the intake.

A summary of the test conditions is given in Table 3-3. Tested Reynolds number compares to a Reynolds number flight range of between 1.8×10^6 and 4.5×10^6.

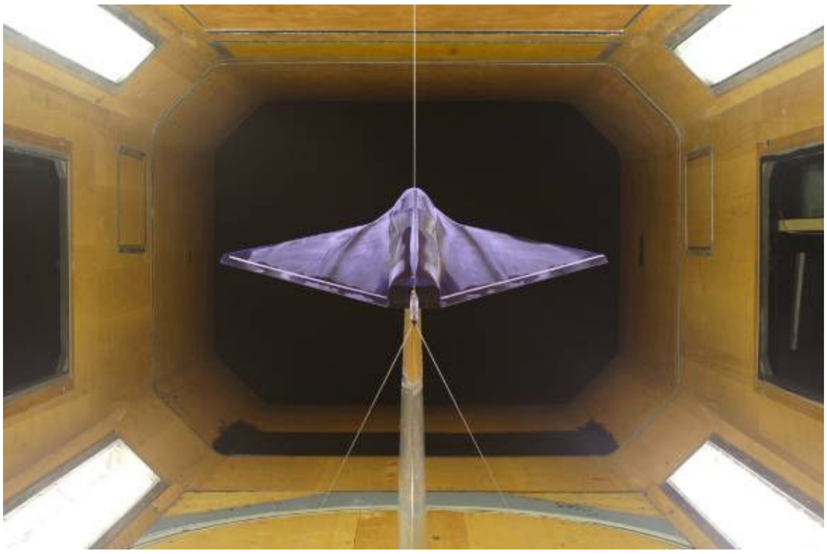

Fig. 3-3. 50% scale full-span DEMON model mounted in the 8x6 foot wind tunnel at Cranfield University. (Downstream/back view, image was rotated through 180°)

Scale	Re	α	β	ξ	ζ	η
50%	1.5×10^6	-5°, + 20°	-12° , +12°	±15°	± 20°	± 15°

Table 3-3. Summary of test conditions

Results were corrected for flow blockage and induced angle of attack and implementation of the wind tunnel test corrections is given in appendix A.

3.2.2 Sign and conventions

The non-dimensionalising of forces and moments was performed using the following factors:

- Forces: $\frac{1}{2}\rho V^2 S_{ref}$
- Lateral moments: $\frac{1}{2}\rho V^2 S_{ref} \frac{b}{2}$
- Longitudinal moment: $\frac{1}{2}\rho V^2 S_{ref} \bar{c}$

where V is the wind tunnel velocity and the remaining model scale factors are summarized in Table 3-4.

Reference area	Mean aerodynamic chord	Wing Gross semi-span
S_{ref} (m^2)	$\bar{c}$ (m)	$b/2$ (m)
0.5913	0.67	0.55

Table 3-4. Scale factors used for the preparation of coefficients

Sign convention, which accords with Cook (2007), is that positive control displacements give rise to a negative aeroplane response:

- Elevator (η): positive trailing edge down
- Aileron (ξ): positive if starboard aileron is deflected trailing edge down and port trailing edge up
- Rudder (ζ): positive if trailing edge of rudder is to port
- Incidence (α): positive aircraft nose upwards
- Sideslip (β): positive aircraft nose to the right of the wind vector

3.2.3 Wind tunnel results

3.2.3.1 Surface flow visualization

Due to the small aspect ratio and large leading edge sweep the *Demon* configuration performs not unlike a conventional delta wing.

A leading edge separation bubble forms at small angles of attack (α~5°), most likely due to laminar to turbulent transition. Increasing α further gives rise to a pair of vortices that emanate from the fore-body with its leading edge extensions. These vortices travel downstream parallel on either side of the fuselage causing the distinct streak line pattern observed in Fig. 3-4. The flow over the remaining wing is initially unaffected and is essentially parallel to the free stream. Typically, also, up to three smaller vortices form along the leading edge extension.

Test conducted at 50% scale were subject to an extremely tight schedule considering the large volume of test points that needed to be included to support the simulation work adequately. Hence, only a very rudimentary consideration could be given to force boundary layer transition in a sensible manner. Serrated tape was used to suppress localized flow separation on the fore-body and intake as well as on the rudder (at around 10% chord). Forced transition could not be obtained in a sensible fashion on the main wing and the decision was made to continue with free transition along the main wing leading edge and fore-body strakes.

Wing leading edge separation occurs at around $\alpha=7°$ with free transition. Once wing stall has occurred the flow separates from the leading edge to form a secondary vortex system that includes a tornado like focal point separation at the leading edge. This feature travels inboard along the leading edge as α increases. The wing leading edge vortex displays an especially obvious attachment line diagonally across the wing, (Fig. 3-4).

3.2.3.2 Longitudinal aerodynamics

Fig. 3-5 shows the static longitudinal aerodynamic characteristics results. Lift increases linearly until wing stall occurs after which a complex three dimensional vortex structure is formed evident by an increase in the lift curve slope and drag coefficient. The lift curve is markedly linear up to the point where the fore-body vortex forms after which a non-linear trend develops. It is troublesome trying to infer wing stall from the lift curve, but a noticeable step change in the drag coefficient occurs. Pitching moment decreases gradually with increasing α without any abrupt step changes (Fig. 3-5).

An indication of *Demon* efficiency can be inferred from Fig. 3-6. Maximum lift to drag ratio of this configuration is around *L/D*=8. Wing stall causes an abrupt change in the induced drag factor, listed in Fig. 3-6 as K1, before wing stall, and K2, post-stall.

3.2.3.3 Longitudinal static stability

The classical theory for static stability of aeroplanes, as discussed by Duncan (1959), states that the condition for stability is:

$$\frac{dC_M}{dC_R} < 0 \tag{3-1}$$

where C_R is the total resultant aerodynamic force coefficient. Now, for the flying demonstrator, as for the majority of aeroplanes, the lift to drag ratio is in order of 10 so the condition for stability may be approximated by,

$$\frac{dC_M}{dC_L} < 0 \quad \text{provided that} \quad \frac{\partial C_L}{\partial \alpha} \equiv a > 0$$

Applying the condition for longitudinal static stability, the controls fixed neutral point, is given (for α small) by:

$$h_n = C_{L_\alpha} - \frac{C_{M_\alpha}}{C_{L_\alpha}} \tag{3-2}$$

The controls fixed static margin is given by,

$$K_n = h_n - h_{cg} \tag{3-3}$$

which is the slope of the C_M-C_L curve, (Fig. 3-7).

As it can be inferred from Fig. 3-7, *Demon* is characterized by a relatively low stability due to a low static margin at lower incidence, associated with higher speed. As the angle of attack increases there is a significant rearward shift of the aerodynamic centre (*ac*) which results in a higher static margin.

3.2.3.4 Lateral directional and static stability

Fig. 3-8 illustrates the lateral/directional stability of *Demon*. Fig. 3-8 clearly shows that a positive lateral stability is maintained over an increased angle of attack range. The large sweepback is the main contributor to the lateral static stability, resulting in a quite large roll due to sideslip, at low speeds (high C_L) and a smaller one at high speed.
When held in sideslip the aircraft will generate yawing moment due to sideslip, which will tend to restore the aircraft to symmetric flight, known as 'weathercock' stability. Fig. 3-8 shows a healthy level of $C_{N\beta}$ against angle of attack. The directional stability is derived almost entirely from the fin and it is nominally constant for increasing incidence at all the angle of attacks tested.

3.2.3.5 Lateral control

Fig. 3-9 illustrates the roll control power of the outboard aileron (5°, 10° and 15°). Up to approximately 15° angle of attack the outboard flap control is linear with alpha. The effectiveness between 0° and 15° is about 40% higher than between 15° and 30°. Above 15° the control power reduces probably as a result of tip separation moving inboard. More detailed data of inboard aileron effectiveness is given in Fig. 3-10 and this dataset will also serves as the reference for the circulation control devices.

Outboard aileron effectiveness is about 1.5 as effective as inboard aileron below 10° alpha. However above 10° alpha the roll power on the inboard aileron increases.
A small and acceptable pro-verse yaw effect from both the inboard and outboard aileron is evident, (Fig. 3-9 and Fig. 3-10).

Rudder control power is linear and constant against alpha. (Fig. 3-11)

3.2.3.6 Summary of mid-range derivative data

Table 3-5 contains a summary of the main derivatives obtained from the ½ scale model wind tunnel test data. The table presents a comparison with limited data available from two sources:

- Predictions from semi-empirical Datcom, obtained by the Cranfield Design Integration group (Allegri, 2006).

- Mid-range values of the derivatives obtained from the 1/10th scale flat plate model wind tunnel test data.(Bradbrook, 1999)

The following observations can be made:

- The flat plate 1/10th model produced a higher $C_{L\alpha}$ and this is due, probably, to the effect of the sharp leading edge of the 1/10th-scale model, as it was discussed in the literature review.
- Elevator control effectiveness compares well with Datcom estimates.
- Similar lateral directional and control derivatives were obtained to those achieved from the flat -plate tests. Comparisons of aileron effectiveness with the 1/10th – scale flat plate model could not be made, as only the effect of double aileron (surface No.2 and No.1 deflected together) was tested on the flat plate model.

		½ model	**$1/10^{th}$ model**	**Datcom**
$C_{L\alpha}$		2.37	2.51	--
$C_{M\alpha}$	0°<α<2.8° 2.8°<α<11.8° 11°<α<20°	-0.022 -0.112 -0.220	--	--
$C_{L\eta}\left(\eta \leq 10^{\circ}\right)$	α = -5° 0° 5° 10° 15°	0.2739 0.262 0.256 0.289 0.325	--	0.294
$C_{M\eta}\left(\eta \leq 10^{\circ}\right)$	α = -5° 0° 5° 10° 15°	-0.1318 -0.1307 -0.1295 -0.1467 -0.1673	--	-0.1399
$C_{N\beta}\left(\beta \leq 10^{\circ}\right)$	α = -5° 0° 5° 10° 25°	0.1105 0.1193 0.1282 0.1227 0.1319	0.16	--
$C_{LL\xi}\left(outboard, \xi \leq 10^{\circ}\right)$	α = 0° 5° 10° 15°	-0.0807 -0.0823 -0.0937 -0.0736	--	-0.04
$C_{LL\xi}\left(inboard, \xi \leq 10^{\circ}\right)$	α = 0° 5° 10° 15°	-0.0631 -0.0619 -0.0782 -0.1009	--	--
$C_{N\xi}\left(inboard, \xi \leq 10^{\circ}\right)$	α = 0° 5° 10° 15°	-0.009 -0.009 -0.0153 -0.01269	--	--
$C_{N\xi}\left(outboard, \xi \leq 10^{\circ}\right)$	α = 0° 5° 10° 15°	-0.006 -0.008 -0.0114 -0.005	--	-0.0035
$C_{N\zeta}\left(\zeta \leq 10^{\circ}\right)$	0°<α <15°	-0.09	-0.112	--

Table 3-5. Summary of selected aerodynamic derivatives of the 50% scale full-span model. All derivates are defined in (rad^{-1}).

3.2.4 Damping derivatives for the *Demon* flying demonstrator

The damping derivatives have been obtained by the Cranfield Design Integration group using digital –Datcom and a doublet lattice method (Allegri, 2006). Table 3-6 contains a summary of the damping derivatives

The Digital-Datcom (empirical methodology, where historical data are reported and properly interpolated) package has been employed to calculate the *Demon* damping derivatives; these include the lift due to pitch rate, the pitching moment due to pitch rate, the rolling and yawing moments due to roll rate and the rolling and yawing moments due to yaw rate. All the damping terms involving moments are normalised with respect to *half* of the aircraft wingspan for the lateral terms and the mean aerodynamic chord for the longitudinal terms; the same convention holds for the pitch and yaw rates.

No Digital-Datcom method is available for the estimation of the lift and pitching moment due to the angle of attack rate for an aircraft without horizontal tail; therefore these have been computed developing a doublet lattice method of the aircraft configuration using MSC/NASTRAN (this simulation tool is based on potential aerodynamics with a lifting surface assumption).

C_{Lq}	--	1.37
C_{Mq}	--	-0.473
C_{Yp}	α = -5° 0° 5° 10° 15°	-0.1040 -0.1040 0.1050 0.2170 0.3720
C_{LLp}	α = -5° 0° 5° 10° 15°	-0.6820 -0.6830 0.6920 -0.6240 -0.4480
C_{LLr}	α = -5° 0° 5° 10° 15°	0.0826 0.0916 0.0979 0.1020 0.1020
C_{Np}	α = -5° 0° 5° 10° 15°	0.0135 0.0135 -0.0149 -0.0364 -0.1040
C_{Nr}	α = -5° 0° 5° 10° 15°	-0.2720 -0.2800 -0.3040 -0.3440 -0.3930

Table 3-6. Damping aerodynamic derivatives evaluated for a centre of gravity position of 1203mm measured from the aircraft nose. All derivatives defined in (rad^{-1}).

3.2.5 Control requirements

The longitudinal condition for wings-level, equilibrium flight is for the lift to balance the weight and the pitching moment to vanish, which can be written in algebraic matrix form (Etkin, 1972):

$$\begin{pmatrix} C_{L\alpha} & C_{L_\eta} \\ C_{M\alpha} & C_{M_\eta} \end{pmatrix}\begin{pmatrix} \alpha_{trim} \\ \eta_{trim} \end{pmatrix} = \begin{pmatrix} C_{Ltrim} \\ -C_{M_0} \end{pmatrix}$$

$$C_{Ltrim}\left(\frac{1}{2}\rho V^2 S\right) = W \tag{3-4}$$

The *Demon* trim condition derivation was firstly calculated using a Mathcad Programme with the aerodynamic model described in Table 3-5. The curve of control angle (η) to trim plotted against lift coefficient, known as the trim curve, is given in Fig. 3-12. The stability is indicated by the negative trend of the trim curve. This result indicates a sufficient control power to trim over the design operating range, leaving sufficient margin for maneuvering.

3.3 Dynamic stability mode approximation

To gain an insight into the important aerodynamic derivatives influencing the longitudinal dynamics, approximations for the modes can be formulated, as presented by Cook (2007).

The short period and phugoid modes can be calculated from the dominant concise derivatives taken directly from the state matrix of the longitudinal Eq. (3-5).

$$\dot{\mathbf{x}} = \mathbf{A}\mathbf{x} + \mathbf{B}\mathbf{u} \qquad (3\text{-}5)$$

where:

$$\mathbf{A} = \begin{bmatrix} \mathrm{x_u} & \mathrm{x_w} & \mathrm{x_q} & \mathrm{x}_\theta \\ \mathrm{z_u} & \mathrm{z_w} & \mathrm{z_q} & \mathrm{z}_\theta \\ \mathrm{m_u} & \mathrm{m_w} & \mathrm{m_q} & \mathrm{m}_\theta \\ 0 & 0 & 1 & 0 \end{bmatrix} \qquad \mathbf{B} = \begin{bmatrix} x_\eta \\ z_\eta \\ m_\eta \\ 0 \end{bmatrix}$$

$$\mathbf{x}^T = [u \quad w \quad \theta \quad q] \quad \text{and} \quad \mathbf{u}^T = [\eta]$$

The coefficients of the state matrix **A** are the aerodynamic stability derivatives, referred to aeroplane body axes, in concise form, and the coefficients of the input matrix **B** are the control derivatives also in concise form. The definitions of the concise derivatives are given in full in Cook (2007). The derivatives can be referred to wind axes, θ_e=0, by making the following simplifications: $U_e = V_e$, $sin\theta_e$=0, and $cos\,\theta_e$=1, where the subscript ‘e’ indicate equilibrium condition.

A complete list of longitudinal dimensionless aerodynamic stability and control derivatives referred to aircraft wind axis is provided in Table 3-7 and Table 3-8. The notation is consistent with Cook (2007).

Derivative	**Description**	**Expression**	**Multiplier**
X_u	Axial force due to velocity	$-2C_{De}+\left.\frac{\partial T}{\partial V}\right\|_e \frac{1}{\frac{1}{2}\rho V_e S}$	$\frac{1}{2}\rho V_e S$
X_w	Axial force due to incidence	$C_{Le}-\left.\frac{\partial C_D}{\partial \alpha}\right\|_e$	$\frac{1}{2}\rho V_e S$
X_q	Axial force due to pitch rate	0	$\frac{1}{2}\rho V_e S\bar{c}$
$X_{\dot{w}}$	Axial force due to downwash	0	$\frac{1}{2}\rho S\bar{c}$
Z_u	Normal force due to velocity	$-2C_{Le}$	$\frac{1}{2}\rho V_e S$
Z_w	Normal force due to incidence	$-C_{De}-C_{L\alpha}$	$\frac{1}{2}\rho V_e S$
Z_q	Axial force due to pitch rate	0	$\frac{1}{2}\rho V_e S\bar{c}$
$Z_{\dot{w}}$	Axial force due to downwash	$-C_{L_{\dot{\alpha}}}$	$\frac{1}{2}\rho S\bar{c}$
M_u	Pitching moment due to velocity	0	$\frac{1}{2}\rho V_e S\bar{c}$
M_w	Pitching moment due to incidence	$-C_{L_\alpha}K_n$	$\frac{1}{2}\rho V_e S\bar{c}$
M_q	Pitching moment due to pitch rate	C_{M_q}	$\frac{1}{2}\rho V_e S\bar{c}^2$
$M_{\dot{w}}$	Pitching moment due to downwash	$C_{M_{\dot{\alpha}}}$	$\frac{1}{2}\rho S\bar{c}^2$

Table 3-7. Longitudinal aerodynamic stability derivatives referred to wind axis

Derivative	**Description**	**Expression**	**Multiplier**
X_η	Axial force due to elevator	$-2KC_{L_\eta}\left(C_{L\eta}\right)_e$	$\frac{1}{2}\rho V_e^2 S$
Z_η	Normal force due to elevator	$-C_{L_\eta}$	$\frac{1}{2}\rho V_e^2 S$
M_η	Pitching moment due to elevator	$-C_{L_\eta}(h_{cpe}-h_{cg})$	$\frac{1}{2}\rho V_e^2 S\bar{c}$

Table 3-8 Longitudinal aerodynamic control derivatives referred to wind axis

The short period mode is a damped oscillation in pitch. The principle variables are incidence, pitch rate and pitch attitude with speed remaining largely constant.

In terms of dimensional derivatives, taking into account their relative magnitudes, the damping and natural frequency of the short period mode are given to a good approximation by,

$$\omega_s \approx \sqrt{\frac{-M_w U_e}{I_y}} \tag{3-6}$$

$$2\zeta_s \omega_s \approx -\frac{M_q}{I_y} + \frac{Z_w}{m} \tag{3-7}$$

For a slender delta wing M_q is assumed to arise predominantly from the moment of the wing trailing edge lift about the *cg*. M_q is negative for positive static stability.

The pitching moment due to normal velocity M_w is negative for a statically stable aircraft and is a measure of the control fixed static margin, as it can be seen in Eq. (3-8):

$$M_w = 0.5\rho V_e S \frac{dC_L}{d\alpha} K_n \tag{3-8}$$

Z_w is principally dependant on the lift/curve slope, as it can be seen in Eq. (3.9):

$$Z_w = -0.5\rho V_e S\left(\frac{dC_L}{d\alpha} + C_D\right) \tag{3-9}$$

The phugoid mode is a low frequency oscillation in speed, which couples into pitch attitude and height. The undamped natural frequency is inversely proportional to speed. A simplified approximate expression for the damping ratio and the frequency is:

$$\omega_p = \sqrt{\frac{\rho g S C_L}{m}} = \frac{g\sqrt{2}}{V_0} \tag{3-10}$$

$$\zeta_p \approx \frac{1}{\sqrt{2}}\left(\frac{C_D}{C_L}\right) \tag{3-11}$$

The algebraic expressions in Table 3-7 for different trim conditions were derived with the aid of Mathcad which includes a facility for symbolic calculation. The longitudinal modes can be calculated using the reduced order model approximation described above. Results of this computation are shown in Table 3-9.

The short period natural frequency increase with airspeed is due to the forward velocity term in the numerator of Eq. (3-6), being the control fixed static margin constant in the range of velocities considered. The short period damping slightly increases as the airspeed reduces, but it can be considered almost constant over the velocity range. It is to be expected that the viscous ‘paddle’ generated pitch damping will reduce with airspeed as the dynamic pressure decreases. However, this effect is compensated by the decrease in the short period frequency with speed, in Eq. (3-7).

The frequency of the phugoid mode increases as the airspeed decreases due to velocity term in Eq. (3-10).

Table 3-9. Longitudinal dynamic stability modes approximations

Airspeed (m/s)	Short period mode		Phugoid mode		Concise derivatives		
	ζ_s	ω_s (rad/s)	ζ_p	ω_p (rad/s)	m_w	m_q	z_w
30	0.479	4.1950	0.1040	0.4620	-0.587	-1.655	-2.367
35	0.477	4.8940	0.0920	0.3960	-0.684	-1.931	-2.742
40	0.477	5.5930	0.1000	0.3470	-0.782	-2.207	-3.127
45	0.476	6.2930	0.1120	0.3080	-0.88	-2.483	-3.513
50	0.476	6.9920	0.1290	0.2770	-0.978	-2.759	-3.901
55	0.476	7.6910	0.1500	0.2520	-1.075	-3.035	-4.289
60	0.476	8.3900	0.1730	0.2310	-1.173	-3.311	-4.678

The roll mode, the spiral mode and the dutch roll mode can be calculated from the dominant concise derivatives taken directly from the state matrix of the Eq. (3-12):

$$\dot{\mathbf{x}} = \mathbf{A}\mathbf{x} + \mathbf{B}\mathbf{u} \tag{3-12}$$

where:

$$\mathbf{A} = \begin{bmatrix} y_v & y_p & y_r & y_\phi \\ l_v & l_p & l_r & l_\phi \\ n_v & n_p & n_r & n_\phi \\ 0 & 1 & 0 & 0 \end{bmatrix} \qquad \mathbf{B} = \begin{bmatrix} y_\xi & y_\zeta \\ l_\xi & l_\zeta \\ n_\xi & n_\zeta \\ 0 & 0 \end{bmatrix}$$

$$\mathbf{x}^T = [v \quad p \quad r \quad \phi] \text{ and } \mathbf{u}^T = [\xi \quad \zeta]$$

The coefficients of the state matrix **A** are the aerodynamic stability derivatives, referred to aeroplane body axes, in concise form, and the coefficients of the input matrix **B** are the control derivatives also in concise form. The definitions of the concise derivatives are given in full in Cook (2007).

A complete list of lateral dimensionless aerodynamic stability and control derivatives referred to aircraft wind axis is provided in Table 3-10. The notation is consistent with Cook (2007).

Derivative	**Description**	**Expression**	**Multiplier**
Y_v	Side force due to sideslip	$\frac{C_{Y_{\beta W}}}{C_L^2} C_{Le}^2 + C_{Y_{\beta B}} + C_{Y_{\beta V}}$	$\frac{1}{2}\rho V_e S$
Y_p	Side force due to roll rate	$\frac{C_{Y_{pW}}}{C_L} C_{Le} + C_{Y_{p_V}}$	$\frac{1}{2}\rho V_e S \frac{b}{2}$
Y_r	Side force due to yaw rate	$C_{Y_{r_V}}$	$\frac{1}{2}\rho V_e S \frac{b}{2}$
L_v	Rolling moment due to sideslip	$\frac{C_{LL_{\beta W}}}{C_L} C_{Le} + C_{LL_{\beta_B}} + C_{LL_{\beta_V}}$	$\frac{1}{2}\rho V_e S \frac{b}{2}$
L_p	Rolling moment due to roll rate	$C_{LL_{pW}} + C_{LL_{pV}}$	$\frac{1}{2}\rho V_e S \frac{b^2}{2}$
L_r	Rolling moment due to yaw rate	$\frac{C_{LL_{rW}}}{C_L} C_{Le} + C_{LL_{r_V}}$	$\frac{1}{2}\rho V_e S \frac{b^2}{2}$
N_v	Yawing moment due to sideslip	$\frac{C_{N_{\beta W}}}{C_L^2} C_{Le}^2 + C_{N_{\beta B}} + C_{N_{\beta V}}$	$\frac{1}{2}\rho V_e S \frac{b}{2}$
N_p	Yawing moment due to roll rate	$\frac{C_{N_{pW}}}{C_L} C_{Le} + C_{N_{p_V}}$	$\frac{1}{2}\rho V_e S \frac{b^2}{2}$
N_r	Yawing moment due to yaw rate	$\frac{C_{N_{pW}}}{C_L^2} C_{Le}^2 + C_{N_{r_V}}$	$\frac{1}{2}\rho V_e S \frac{b^2}{2}$

Table 3-10. Lateral aerodynamic stability derivatives referred to wind axis

For small perturbations the transfer function of a simple first order lag with time constant T_r describes the first second or two of roll response to aileron. The classical approximate expression for the roll mode time constant being,

$$T_r \approx -\frac{I_x}{L_p} \tag{3-13}$$

where L_p is the dimensional derivative describing the aerodynamic damping in roll.

The spiral mode time constant may be expressed conveniently in terms of the dimensional aerodynamic stability derivatives. An approximate expression for the time constant of the spiral mode is defined as,

$$T_s \approx \frac{V_0}{g} \frac{\left(L_v N_p - L_p N_v\right)}{\left(L_r N_v - L_v N_r\right)} \tag{3-14}$$

The condition for the mode to be stable simplifies in,

$$L_r N_v < L_v N_r \tag{3-15}$$

The damping and frequency properties of the dutch roll mode are given approximately by,

$$\omega_d{}^2 \approx -V_0 \frac{N_v}{I_z} \tag{3-16}$$

$$2\zeta_d \omega_d \approx -\left(\frac{N_r}{I_z} + \frac{Y_v}{m}\right) \tag{3-17}$$

The algebraic expressions in Table 3-10 were derived with the aid of *Matchcad*. The lateral modes can be calculated using reduced order model approximation described above. Results of this computation are shown in Table 3-11.

The lateral motion of the *Demon* is characterized by low roll inertia, I_{xx}, due to the concentration of mass along the aircraft centreline and high roll damping L_p due to the large wing area. This results in a very short roll mode time constant that increases with velocity as it is to be expected that the roll damping will reduce with airspeed as the dynamic pressure decreases.

The spiral mode is stable which means that Eq. (3-15) is satisfied. The values on the left and right of inequality condition of Eq. (3-15) become close at high speed, suggesting the mode to be close to neutrally stable. Indeed this could be inferred by the fact that the dihedral effect becomes smaller at high velocity (Fig. 3-8). It is important to note that the spiral mode time constant becomes very high as velocity increases and the mode manifests itself as a very slow exponential convergence.

Table 3-11. Lateral dynamic stability modes approximations

Airspeed (m/s)	Spiral mode	Roll mode	Dutch roll mode	
	T_s (s)	T_r (s)	ω_d (rad/s)	ζ_d
30	11.2360	0.0250	3.8510	0.4200
35	22.7273	0.0190	4.5090	0.3920
40	45.4545	0.0160	5.1690	0.3770
45	100.0000	0.0140	5.8120	0.3680
50	228.6237	0.0120	6.4180	0.3650
55	1391.9822	0.0110	7.0280	0.3620
60	613.4969	0.0100	7.6410	0.3610

3.4 Concluding remarks

Since the *Demon* presents an unconventional configuration, some observations, based on the stability analysis carried out in the previous sections, can be made.

Eclipse-based platforms have a relatively large wing area, thus, the damping terms attain significant values with respect to more conventional configurations. This is particularly reflected in the very high roll damping; this results in a very fast roll mode time constant. Tailless aircraft are expected to have a lower value of pitch damping with respect to tail aircraft, where the tail is a very effective damper. The *Demon* short period mode is, however, quite well damped; this can be explained by the high pitch damping caused by the large wing area, and, also, by the low moment inertia in pitch which makes the pitch damping more effective than a similar value would be in conventional types.

Since the aircraft has a relatively low aerodynamic efficiency (*L/D* ratio), the phugoid oscillations are likely to be under-damped with respect to more conventional configurations.

The sweepback wing has inherent lateral static stability that increases with increasing lift coefficient. This treat is reflected in the spiral mode characteristic. At low speed, where the lateral stability is high and greater than the directional stability, the spiral mode is stable; at high speed, when the lateral static stability is low and nearly equal the directional stability, the spiral mode is close to be neutrally stable and the time constant is very large.

Given that the moments of inertia in pitch and yaw are of similar magnitude, the frequency of the dutch roll mode and longitudinal short period are of the same order.

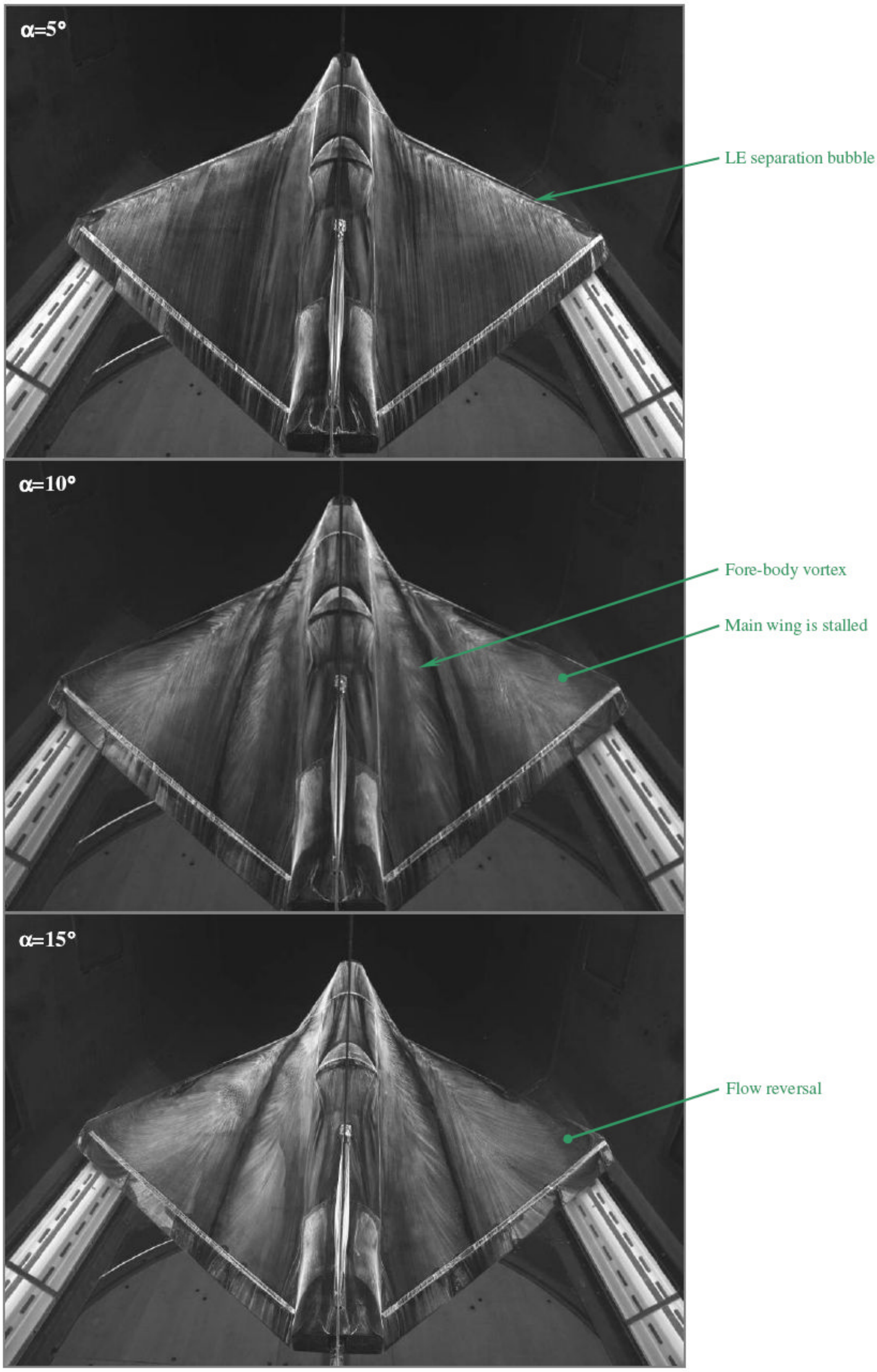

Fig. 3-4. Surface flow visualization of the half-scale Demon vehicle; free transition on main wing. (β=0°)

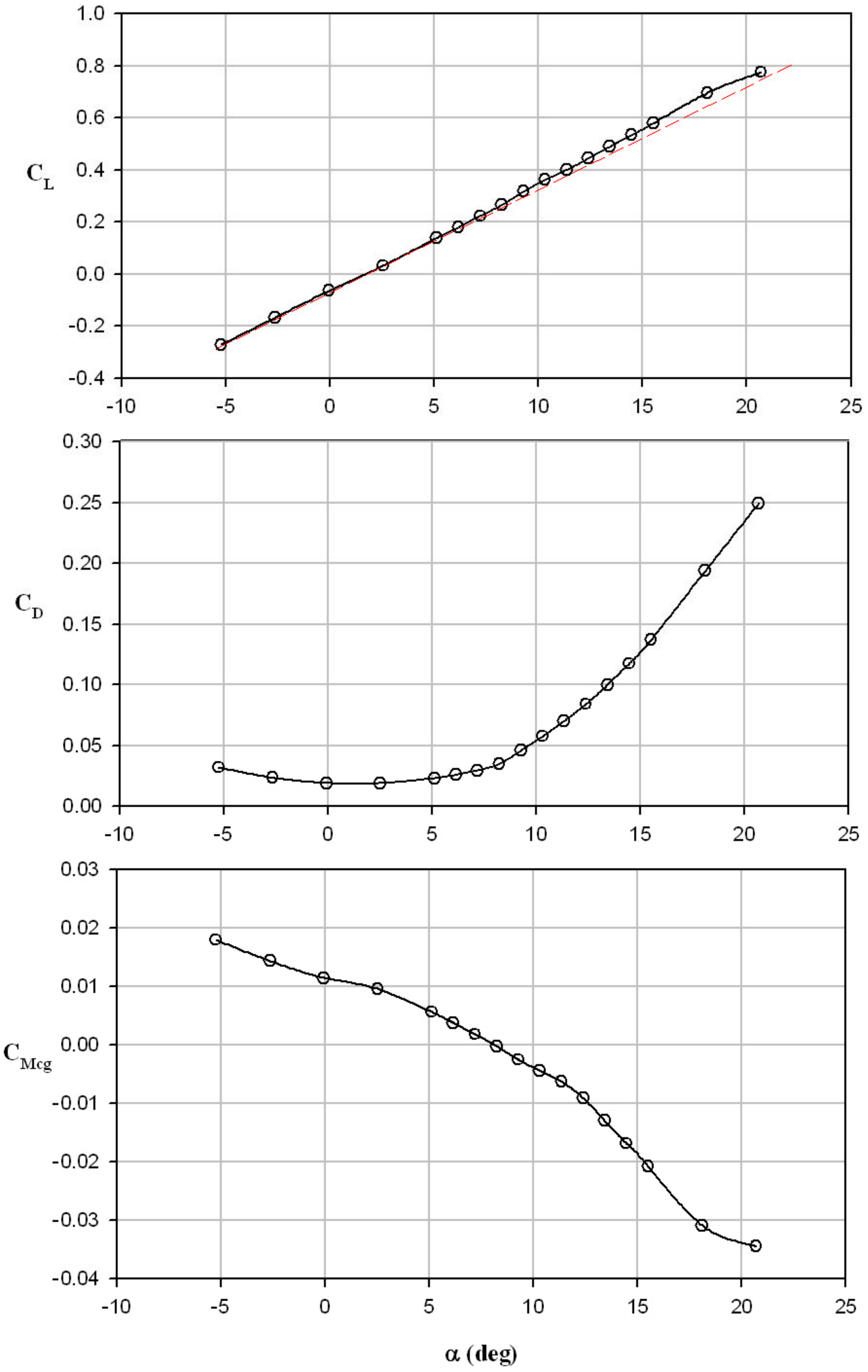

Fig. 3-5. Static longitudinal aerodynamic characteristics of the *Demon*

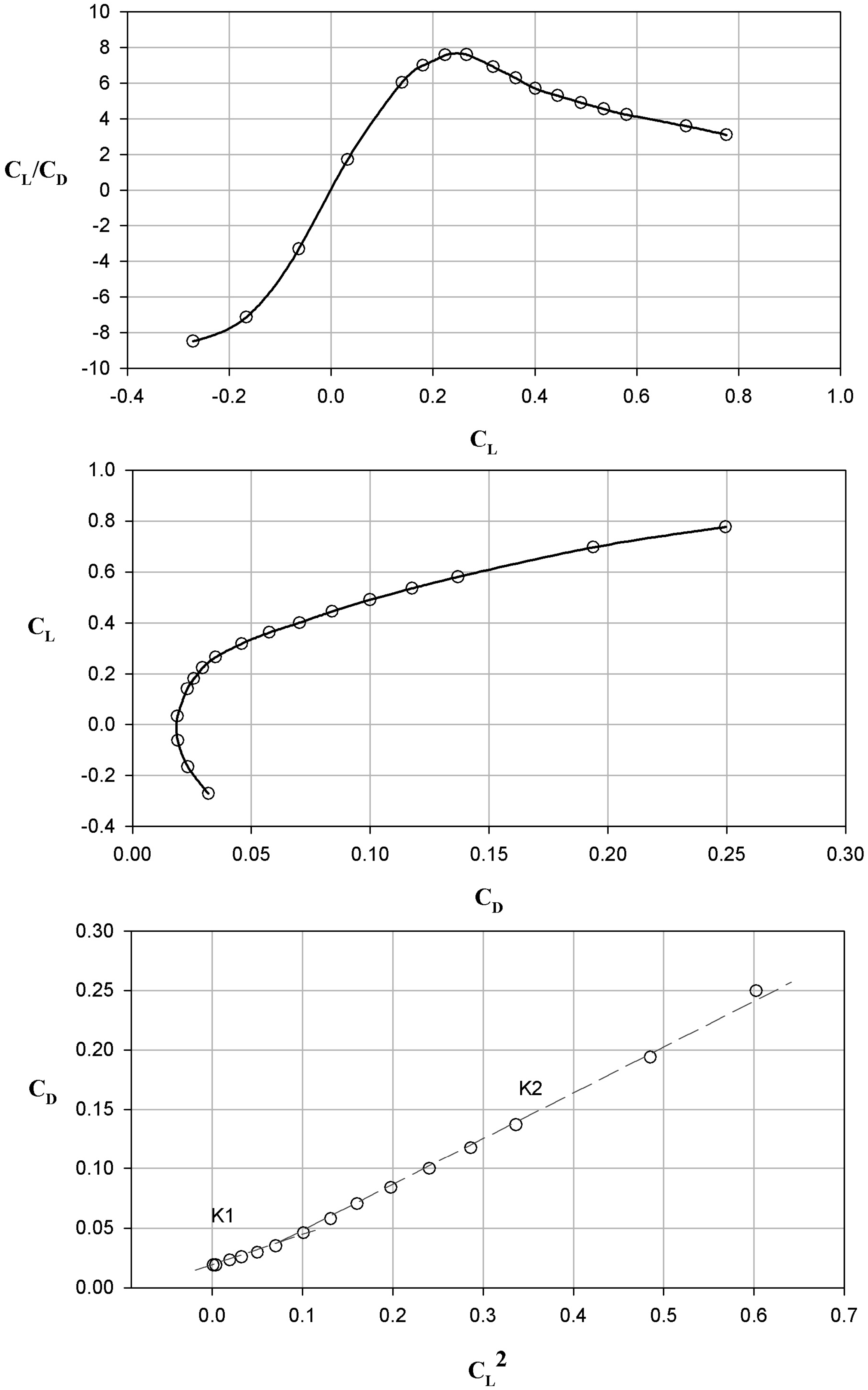

Fig. 3-6. Indication of the Demon aerodynamic efficiency. 50% scale: K1=0.21, K2= 0.4

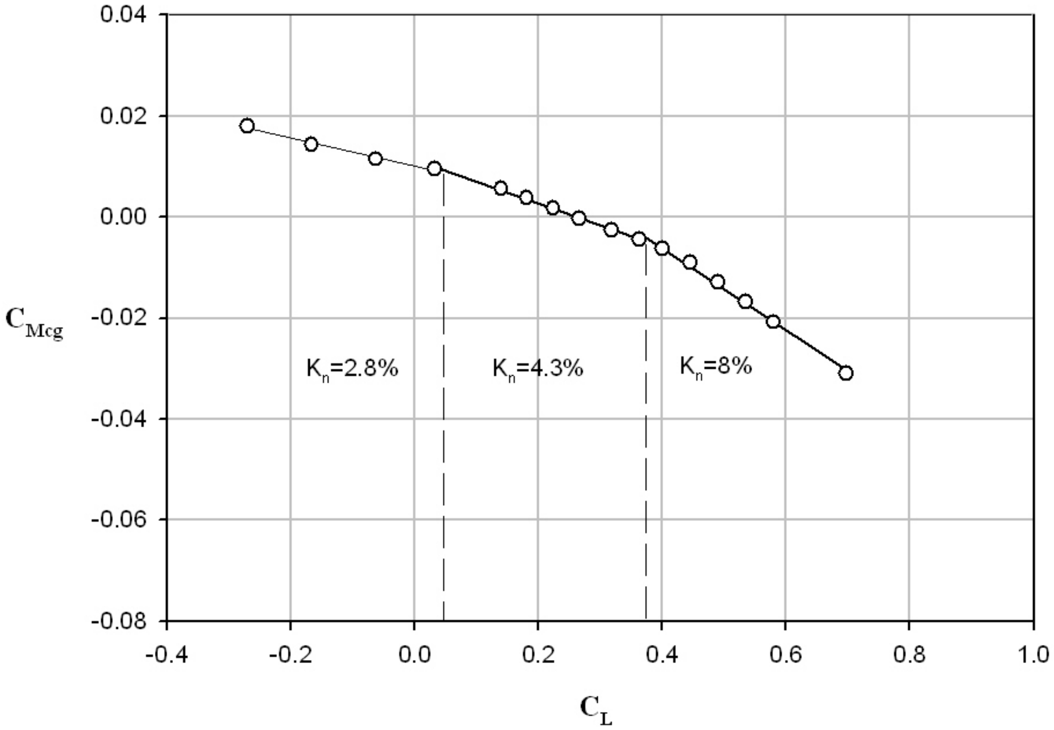

Fig. 3-7. Demon static margin characteristic

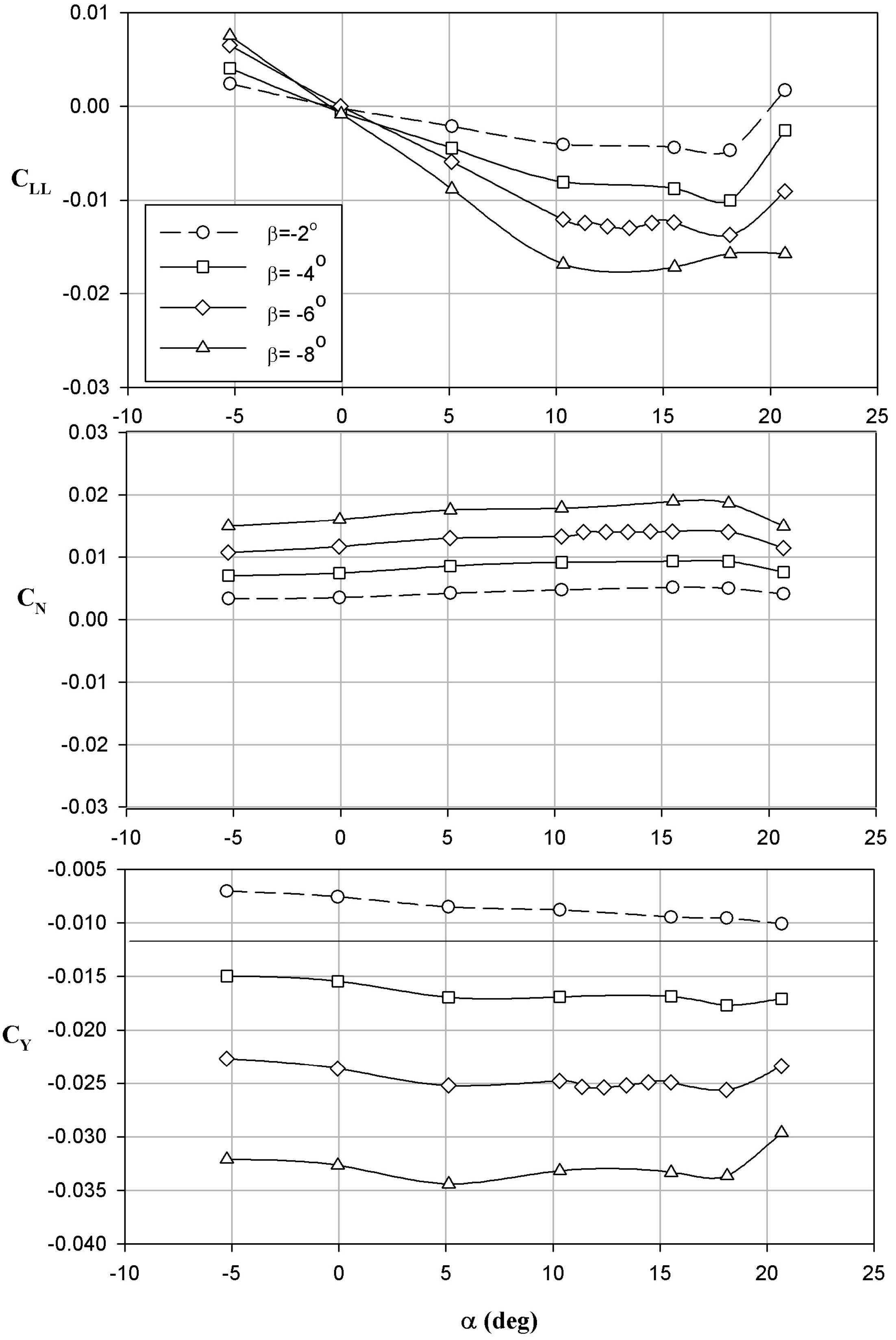

Fig. 3-8. Indication of the lateral and directional static stability. 50% scale full span model

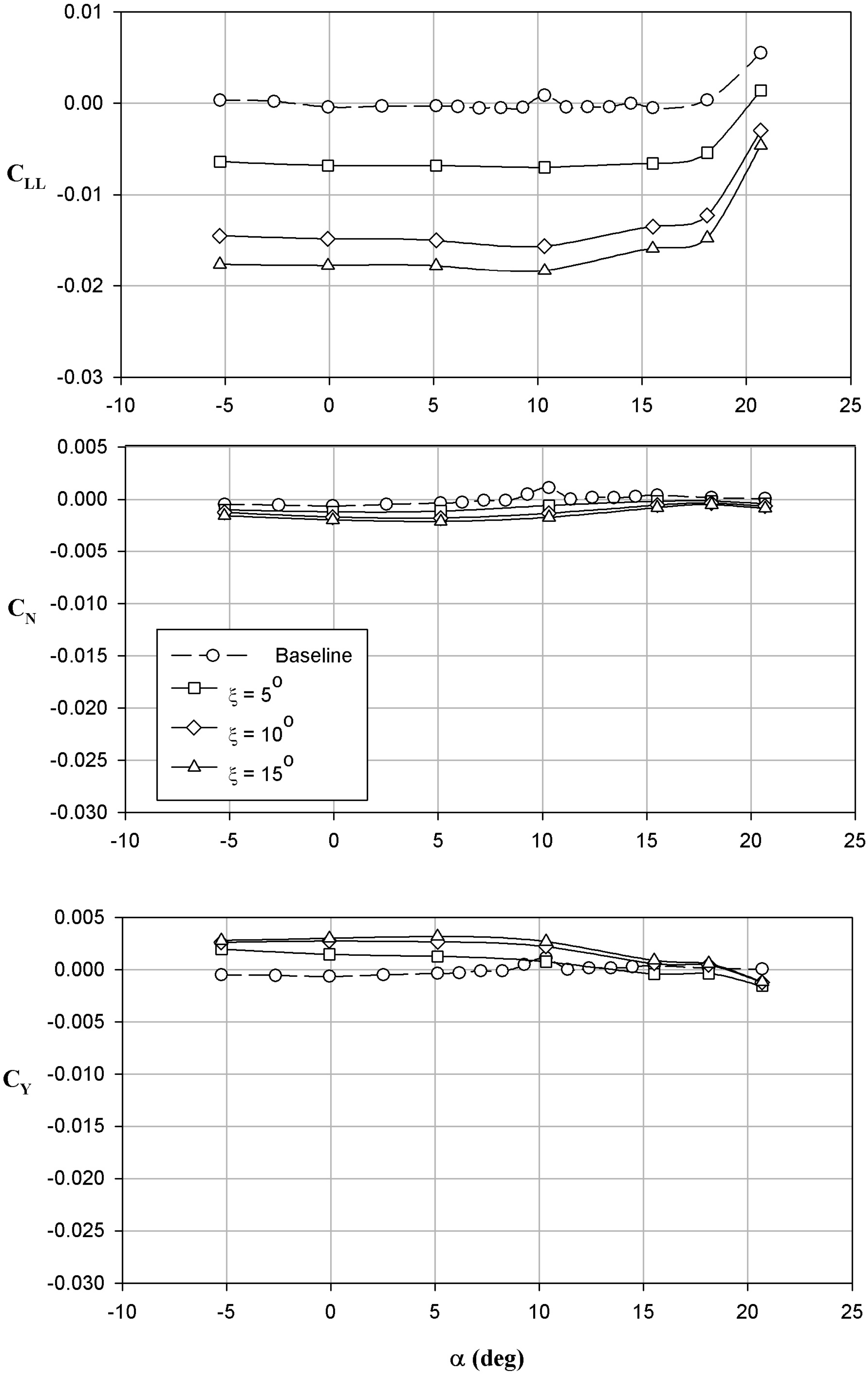

Fig. 3-9. Outboard aileron control characteristics of the 50% scale full span model

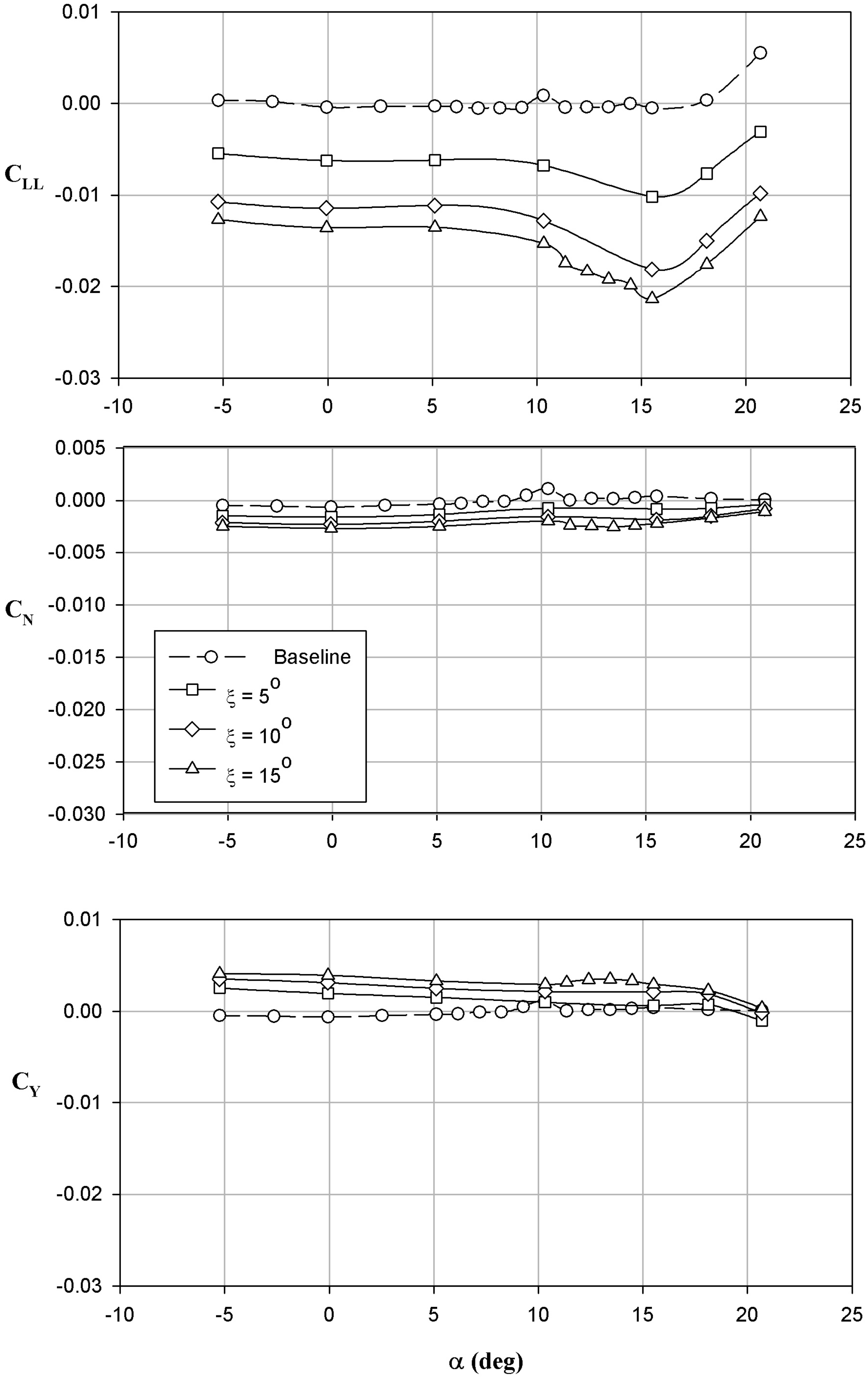

Fig. 3-10. Inboard aileron control characteristics of the 50% scale full span model

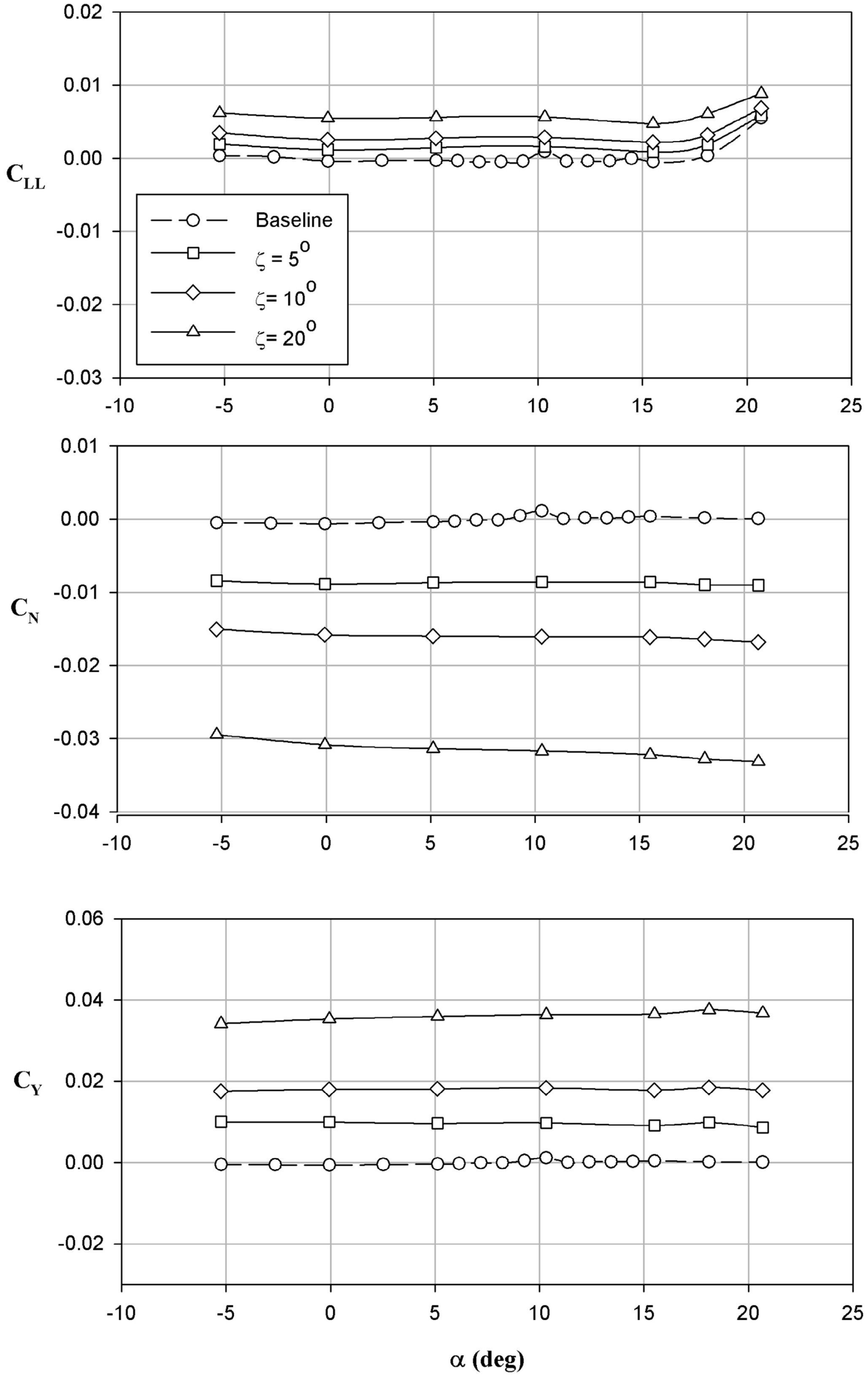

Fig. 3-11. Rudder control characteristics of the 50% scale full span model.

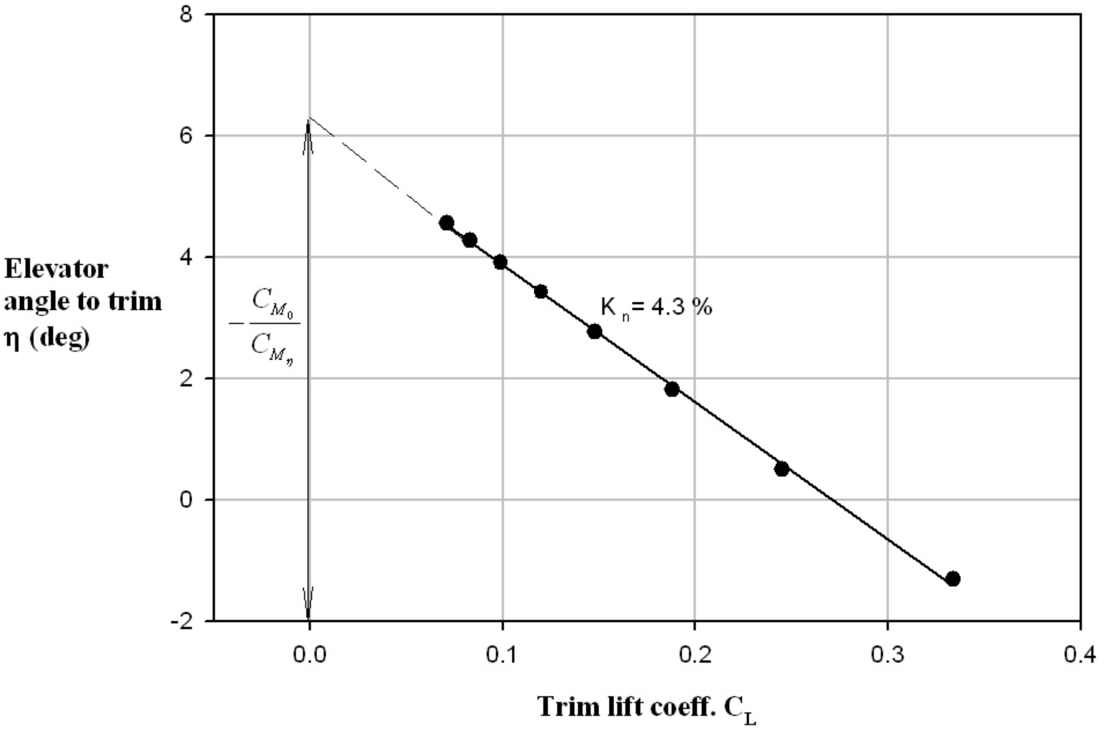

Fig. 3-12. Elevator angle to trim

4 DEVELOPMENT OF THE SIMULATION MODEL

4.1 Introduction

The vital step between developing novel control mechanisms and actually utilizing such devices in an aircraft is the flight modelling and simulation. In fact, although several investigations have already experimentally demonstrated fluidic technologies to be able to augment lift, a detail simulation model is required. A quantitative estimate of their impact from a system point of view has to be made to assess the feasibility of fluidic control technology.

Moreover the use of flight simulation tools to reduce the risk and required amount of flight testing for complex aerospace systems is a well recognized benefit of these tools. However, some special challenges arise when one attempts to extrapolate these benefits to low-cost Unmanned Aerial Vehicle (UAV). This type of vehicle is characterized by a lack of payload capacity (and therefore limited capacity for additional flight test instrumentation or telemetry), limited baseline capabilities (processing, instrumentation), and by a lower marginal cost of additional flight tests.

Hence great attention was applied in developing a flight dynamic simulation model of *Demon*, managing the consolidation of constantly evolving design data into the overall simulation model.

A six degree of freedom (6DoF) simulation model has been developed, based on the *Eclipse* airframe, to evaluate the control and stability characteristics of the conventional flap control configuration. For this study Matlab and its associated graphical interface, Simulink, was chosen as the simulation platform. This choice was based on the extensive use of this program in industry and the functionality which the program provides. The aircraft model was constructed in a modular manner to allow easy reconfiguration and to allow for the flow control actuator model to be developed separately and to be integrated into the complete model.

The equations of motion were implemented in a modular format and include the 1976 standard atmosphere model. The equations represent the conventional six degree-of-freedom motion of a rigid aircraft relative to a flat, non-rotating earth. Two major subsystems represent the vehicle dynamics in the longitudinal and lateral-directional axes respectively. The coupling between these two subsystems is due to inertial and gravitational effects. The usefulness of the simulation model was enhanced by incorporating several additional output equations, in particular, air data parameters, acceleration variables and flight path variables. Representative aerodynamic/inertia properties have been modelled based on an extensive wind tunnel tests on a half scale *Demon* model, which has been presented in Chapter 3.

In order to improve the fidelity of the simulation model and to enhance representative interpretation of the flight dynamic properties of the air vehicle, a model of the AMT Olympus engine is included in the *Demon* simulation. A surface actuator model has also been developed and included in the model, which consists of a second order transfer function including the essential discontinuities (end stops and rate limiting), as these were shown to be critical to satisfactory UAV control (Thomasson, 1993).

The structure of the simulation model follows standard practice and it is depicted in Fig. 4-1. The simulation model is defined in the following sections and this definition is supplemented by appendix B.

This model has been used to carry out a flight dynamic analysis of the basic airframe in order to validate the design choices and to test the control power of the conventional controls configuration. As no previous flight dynamic investigation was conducted on the aircraft, there are no alternative static or dynamic data available for comparison at the present time. Therefore coupled with the simulation development an off-line linear stability analysis has been carried on with the aid of *Mathcad* in order to validate the simulation model results.

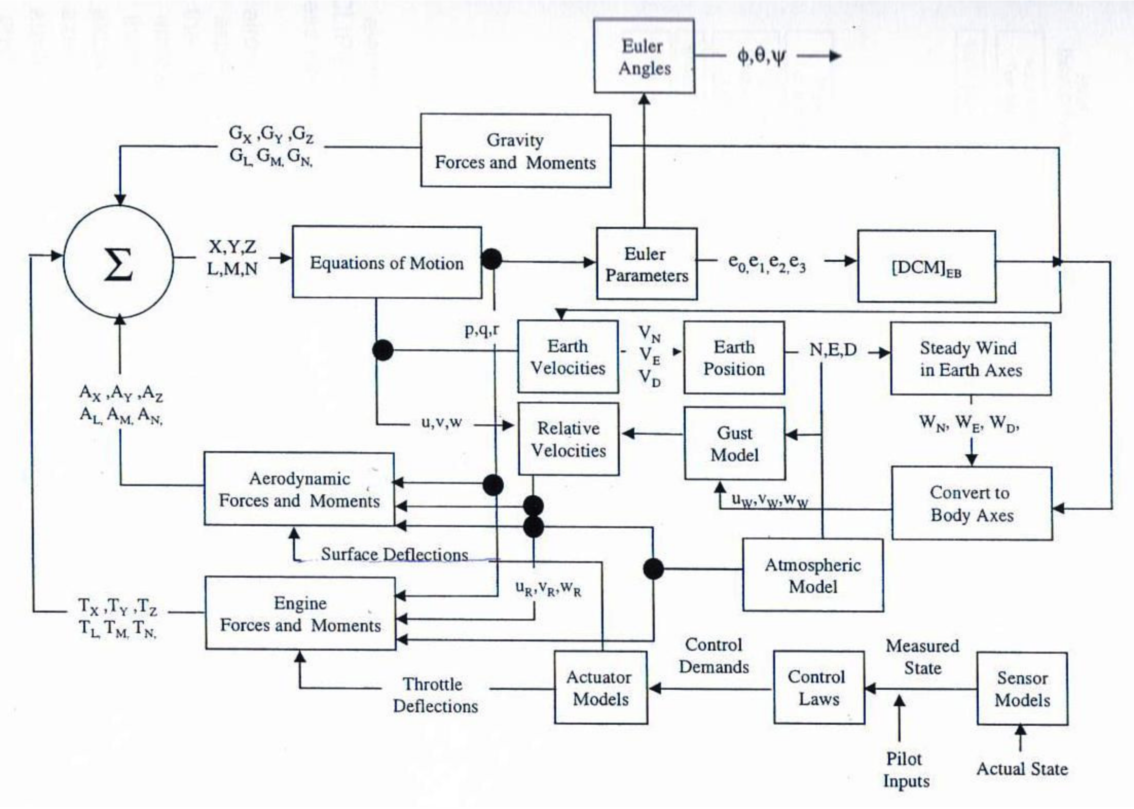

Fig. 4-1. Non-linear simulation model data flow diagram

4.2 Axes system and notation

Three axes systems are used in the development of the simulation model. A fixed axis system relative to a point on the surface of the earth, referred to as the 'Earth Axes', a fixed axes system relative to the aircraft's centre of gravity, referred to as the 'Body Axes' and a fixed axes referred to as 'Stability Axes'.

The axes systems follow the convention and notation defined by Cook (2007).

4.2.1 Earth Axes

For the purposes of normal atmospheric flight, air-vehicle motion can be measured with reference to an earth fixed framework. The accepted convention for defining earth axes determines that a reference point O_0 on the surface of the earth is the origin of a right-handed orthogonal system of axes (O_o, x_o, y_o, z_o) where O_ox_o points to the north, O_oy_0

points to the east and O_oz_0 points vertically down along the gravity vector, as illustrated in Fig. 4-2.

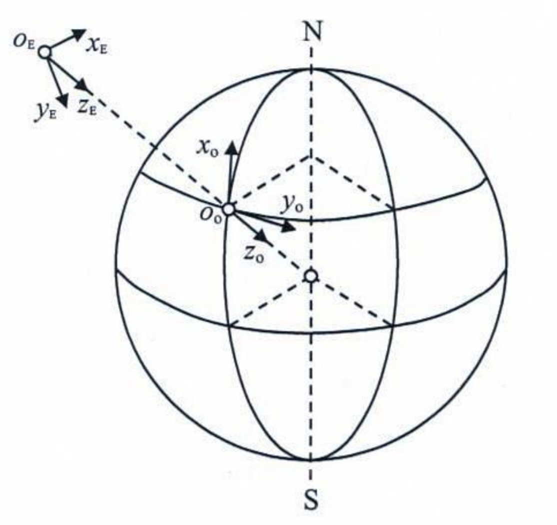

Fig. 4-2. Earth Axes (Cook, 2007)

4.2.2 Aircraft body axes

It is usual practice to define a right-handed orthogonal body-fixed axis system, (o, x_B, y_B, z_B) fixed in a rigid air-vehicle with the origin at o, which is fixed coincident with the Centre of Gravity of the aircraft. The fore-aft, x_B, and vertical, z_B axes define the plane of symmetry, with the x_B axis directed towards the nose, the y_B-axis pointing to starboard and the z_B-axis directed downwards. The aircraft body axes system is presented in Fig. 4-3.

4.2.3 Stability Axes

The stability axis system is obtained by a rotation of the body axes system about oy_B axis trough an angle of attack, α until ox_B is aligns with the velocity vector. A positive angle α corresponds to a negative rotation about oy_B. The resultant axis system is denoted by (o, x_S, y_S, z_S) and it is illustrated in Fig. 4-3.

4.3 Aircraft notation

The motion of the aircraft is described in terms of force, moment, linear and angular velocities and attitude resolved into components with respect to the aircraft body axes system. These variables are presented in Fig. 4-3.

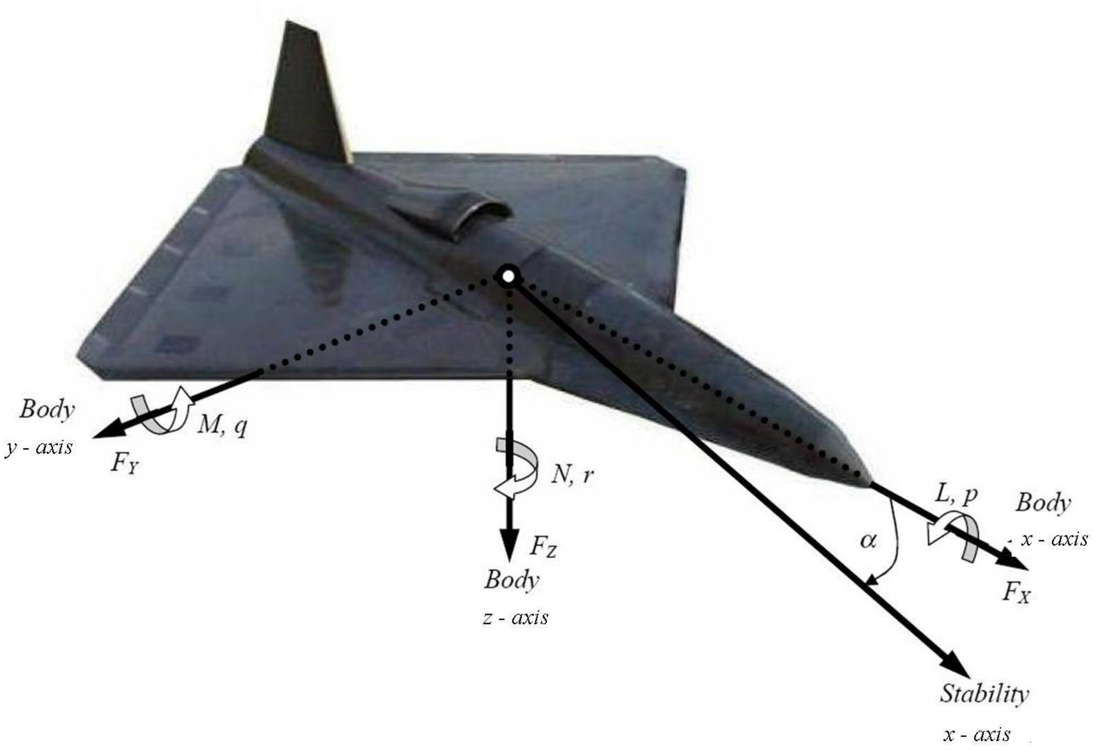

Fig. 4-3. Aircraft motion variables notation

4.3.1 Control angle definition

The elevator, aileron and rudder control angle deflections are defined so that a positive control surface displacement gives rise to a negative aircraft response.

4.4 Equation of motions

The development of the non linear state-space model started from the standard rigid body six degree of freedom equations of motion, derived under the following assumptions:

- The airframe is a rigid body.

- An Earth Centred Inertial (ECI) reference frame is utilised.
- The airframe, and hence the axes, are in motion with respect to an external reference frame such as the earth (or inertial) axes. Note: The curvature of the earth can be neglected for relatively short time simulations.
- The origin of the body axes is coincident with the vehicle's *cg*.
- The mass of the air-vehicle is assumed constant for the duration of any particular dynamic analysis

The model was extended with the equations of the Euler angles and altitude, needed to determine the gravitational, aerodynamic and propulsive forces and moments.

The resulting equations can be combined in a single vector equation:

$$\dot{\mathbf{x}} = f(\mathbf{x}, \mathbf{F}_{tot}(t), \mathbf{M}_{tot}(t)) \tag{4-1}$$

where **x** represent the state variables (the linear and angular velocities of the aircraft, the attitude and the coordinates relative to the surface of the Earth).

Expressing the external forces and moment as non linear functions of the input and state variables yields the non linear state-space system:

$$\dot{\mathbf{x}} = f(\mathbf{x}(t), \mathbf{u}(t), t) \tag{4-2}$$

The input variables to this model are the control surface deflections which affect the aerodynamic forces and moments and the engine inputs which affect the propulsive forces and moments.

By calculating the disturbing forces and moments and knowing the initial values of the body axes velocities, U_i, V_i, W_i, and body axes rotational rates, p_i, q_i, r_i, the equations of motion can be solved for the body axes velocities, U, V, W, and the body axes rotational rates, p, q, r.

Having determined the basic equations of motion, a simulation model of the complete aircraft was built by developing models for the aerodynamic, propulsive and gravitational forces and moments, and by determining some atmosphere and air-data variables that are required to compute these forces and moments. All elements combined result in the mathematical model from Fig. 4-4. This model was enhanced with several useful output equations including additional air-data parameters, accelerations quantities and flight path variables.

The generalized equations of motion derived from first principles (Cook, 2007 and Stevens & Lewis, 1992) and the subsequent derivation of the aircraft attitude, relative velocity, earth velocity and earth position are presented in the appendix B, and the formulation of the aerodynamic, gravitational and thrust moments and forces are presented in the following section.

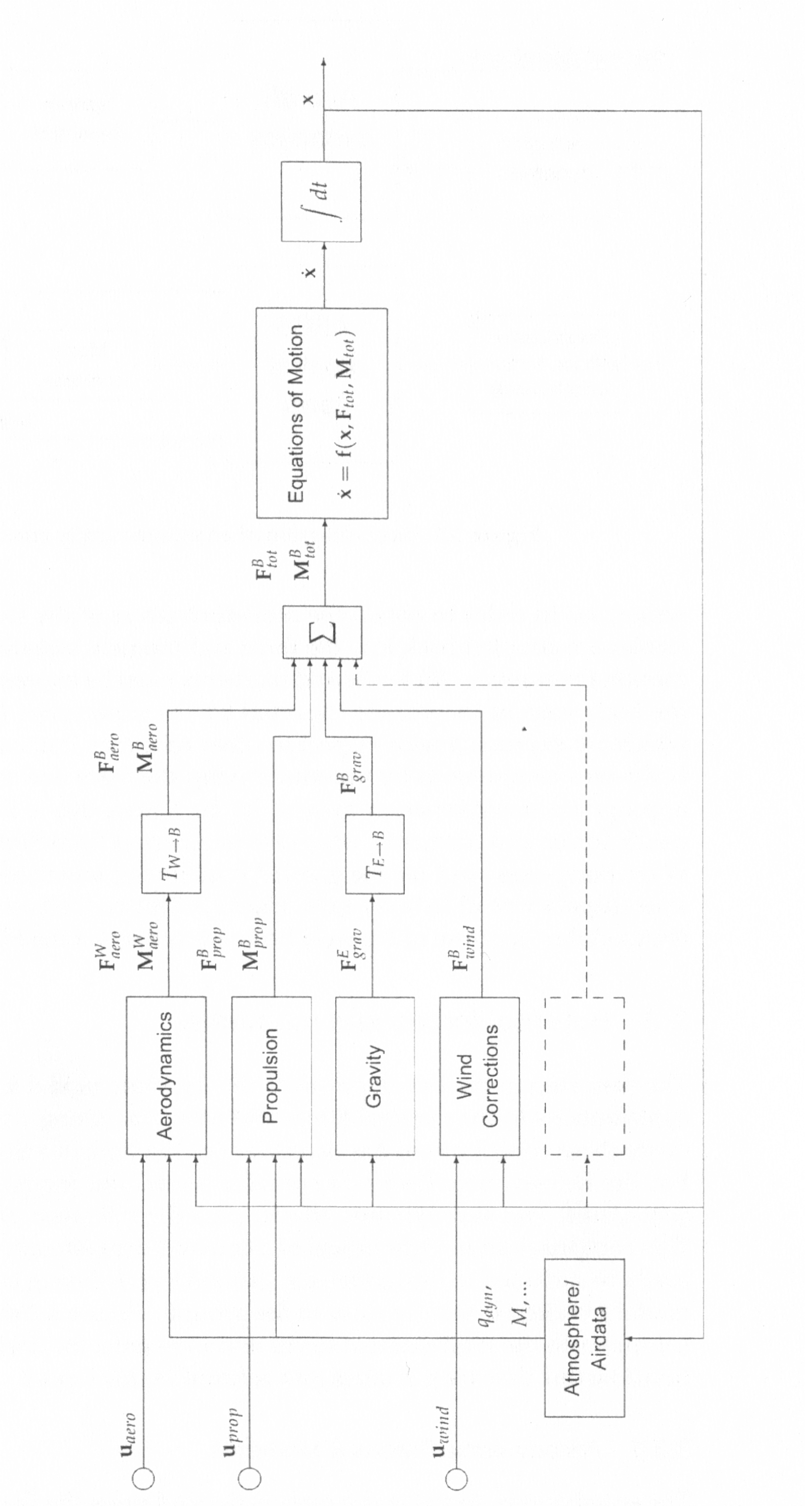

Fig. 4-4. General rigid body dynamics

4.5 Aerodynamic forces and moments

The aerodynamic model of the *Demon* was derived from the wind tunnel tests results, which are summarised in Chapter 3.

The total aerodynamic coefficients in each axis are expressed as a baseline component, plus incremental or correction terms. The wind tunnel data comprised aerodynamic force and moment coefficients at various combinations of angle of attack, sideslip angle and control surface deflection. The range of variation for these parameters corresponds to angle of attack limited to values below 20 degrees. The baseline component is primarily a function of alpha, beta. Coupling terms between angle of attack and control deflection are used to account for the dependence of control effectiveness on angle of attack. Additional terms were added to the Taylor series expressions in an *ad hoc* manner to account for dependence on angular rates (i.e., dynamic derivatives). Terms associated with the pitch rates were added to lift (C_{Lq},) and pitching moment (C_{Mq},). C_{Dq} was considered negligible and it was omitted. Terms associated with rate of change of normal velocity were considered negligible and omitted. Terms associated with roll and yaw rates were added to side force (C_{Yp},), rolling moment (C_{Np}, C_{LLr}) and yawing moment (C_{Np}, C_{Nr}). C_{Yr} was negligible. Derivatives were considered not dependant of velocity (subsonic regime). The equations used to calculate the total aerodynamic coefficients in the *Demon* Simulink model are given in Eq. (4-3).

$$
\begin{aligned}
C_L &= C_L(\alpha) + \Delta C_L(\alpha,\eta) + C_{L_q} q\left(\frac{\bar{c}}{2V}\right)\\
C_D &= C_D(\alpha) + \Delta C_D(\alpha,\eta)\\
C_M &= C_M(\alpha) + \Delta C_M(\alpha,\eta) + C_{M_q} q\left(\frac{\bar{c}}{2V}\right)\\
C_Y &= C_Y(\alpha,\beta) + \Delta C_Y(\alpha,\xi) + \Delta C_Y(\alpha,\zeta) + C_{Y_p} p\left(\frac{b}{2V}\right)\\
C_{LL} &= C_{LL}(\alpha,\beta) + \Delta C_{LL}(\alpha,\xi) + \Delta C_{LL}(\alpha,\zeta) + C_{LL_p} p\left(\frac{b}{2V}\right) + C_{LL_p} r\left(\frac{b}{2V}\right)\\
C_N &= C_N(\alpha,\beta) + \Delta C_N(\alpha,\xi) + \Delta C_N(\alpha,\zeta) + C_{N_p} p\left(\frac{b}{2V}\right) + C_{N_p} r\left(\frac{b}{2V}\right)
\end{aligned}
\tag{4-3}
$$

The six degree of freedom aerodynamic model is built-up using look-up tables to interpolate the coefficient data provided in the aerodynamic database. The coefficient data is interpolated based on a number of independent variables including incidence, sideslip and control surface deflection. Linear interpolation is applied over the range of each independent variable with the end values of the coefficient data used for values outside the range.

4.5.1 Force and moment equations

The total forces and moments acting on the aircraft are defined in terms of the total dimensionless aerodynamic coefficients multiplied by a dimensional factor based on the dynamic pressure, reference area and for the moment equations an appropriate scaling length (wing semi-span, *b/2*, for the lateral moments and mean aerodynamic chord, $\bar{c}$ for the longitudinal moment). The longitudinal force acts in a direction opposite to the drag force and the vertical force acts in a direction opposite to the lift force. The moments are computed around the moment reference centre, which is the centre of gravity of the vehicle.

$$\begin{aligned}
&\text{Longitudinal Force} && F_{xS} = -Q_{dyn} S C_D \\
&\text{Lateral Force} && F_y = Q_{dyn} S C_Y \\
&\text{Vertical force} && F_{zS} = -Q_{dyn} S C_L \\
&\text{Lateral moment} && L_{cgB} = Q_{dyn} S \frac{b}{2} C_{LL} \\
&\text{Pitching moment} && M_{cg.} = Q_{dyn} S \bar{c} C_M \\
&\text{Yawing moment} && N_{cg.B} = Q_{dyn} S \frac{b}{2} C_N
\end{aligned} \tag{4-4}$$

where,

$$\text{Dynamic pressure} \quad Q_{dyn} = \frac{1}{2} \rho V^2 S$$

Since the lift and drag forces are defined in stability axes, the transformation from stability to body axes described by Eq. (4-5) must be applied.

$$\begin{bmatrix} F_x \\ F_y \\ F_z \end{bmatrix}_B = \begin{bmatrix} Cos\alpha & 0 & -Sin\alpha \\ 0 & 1 & 0 \\ Sin\alpha & 0 & Cos\alpha \end{bmatrix} \begin{bmatrix} F_{xS} \\ F_y \\ F_{zS} \end{bmatrix} \tag{4-5}$$

4.6 Propulsive forces and moments

The *Demon* UAV propulsion system is provided by an AMT Netherlands 190N Olympus HP engine. The simulation model of the engine has been developed based on a combination of limited engine data, and first principles. Key Engine characteristics are listed in Table 4-1. Data presented are mainly from two sources:

- The manufacturer website (www.amjets.com)
- Preliminary engine static test conducted at Manchester University (Wilde, Gilde, Michie & Crowther, 2007)

The engine model is based on the following assumptions:

- The engine thrust acts through the aircraft centre of gravity.
- The thrust line is aligned with the axial body axis system x_B.

As the thrust is assumed to act through the *cg* along the body axes system *x*-axis, then, in component form, there is only one component of thrust which is in the axial direction. This component is determined as illustrated in the following section.

4.6.1 Thrust model

The engine uninstalled thrust at different throttle setting can be extracted from Fig. 4-5 and Fig. 4-6. The value of thrust corrected for flight speed is obtained through the following procedure.

The engine intake pressure P_{intake} and intake temperature T_{intake} are defined by equations (4-6) and (4-7) respectively.

$$P_{intake} = P\left(1 + 0.2M^2\right)^{3.5} \tag{4-6}$$

$$T_{intake} = T\left(1 + 0.2M^2\right) \tag{4-7}$$

where *P* and *T* are the atmospheric pressure and temperature, respectively.

Engine mass flow rate can be approximated as a linear function of the engine speed by Eq. (4.8),

$$\dot{m} = k_m \frac{\delta}{\sqrt{\vartheta}} \tag{4-8}$$

where k_m is defined as,

$$k_m = 0.4 \frac{RPM}{110000} \tag{4-9}$$

δ and θ are corrections factors defined by equations (4-10) and (4-11) respectively.

$$\delta = \frac{P_{intake}}{101.325 \cdot 10^3} \tag{4-10}$$

$$\theta = \frac{T_{intake}}{288.2} \tag{4-11}$$

Engine intake drag is defined as,

$$D_{ram} = \dot{m} V_T \tag{4-12}$$

The engine gross thrust is defined as

$$T_G = T \cdot \delta \tag{4-13}$$

where the static thrust at standard pressure and temperature (STP) condition T is given as a function of the *RPM* in Fig. 4-5.

When the inlet momentum is added to the thrust the net thrust is defined,

$$T_\tau = T_G - D_{ram} \tag{4-14}$$

Thrust @max RPM @ S.T.P.	190 N
Maximum RPM	110000
Idle RPM	36000
Thrust at idle RPM	8 N
Mass flow @ max RPM	400 g/s

Table 4-1. Engine specification (www.amjets.com)

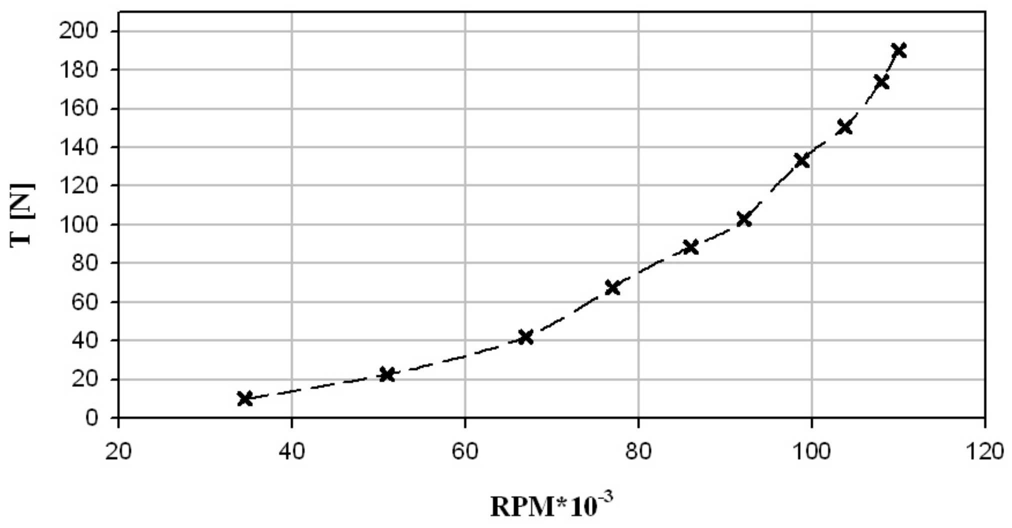

Fig. 4-5. Static thrust of the uninstalled engine @ STP (www.amjets.com)

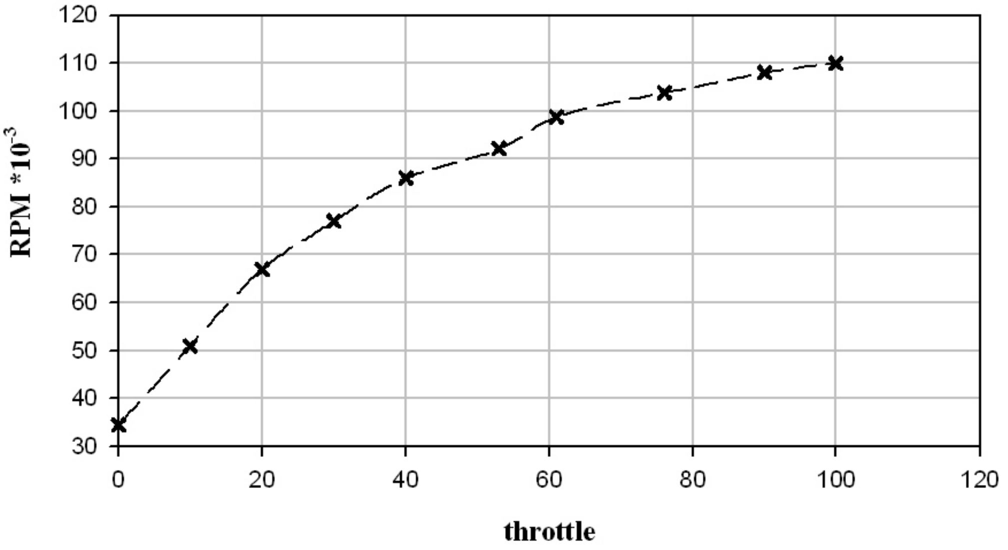

Fig. 4-6. RPM commanded as a function of throttle (0-100 %) (Wilde et al., 2007)

4.7 Gravitational forces and moments

As the body axes origin is coincident with the centre of gravity the gravitational forces and moments, referred to the body axes, can be defined by Eq. (4-15).

$$\begin{bmatrix} X_G \\ Y_G \\ Z_G \end{bmatrix} = [DCM] \begin{bmatrix} 0 \\ 0 \\ mg \end{bmatrix} \tag{4-15}$$

Where the direction cosine matrix DCM is defined in appendix B.

4.8 Atmosphere model

The aerodynamic and thrust model presented are for an aircraft in atmospheric flight; hence a model of the International Standard Atmosphere (ISA) has been implemented.

4.8.1 International Standard Atmosphere model

The ISA implementation in the simulation model defines the atmospheric properties with respect to pressure, P, temperature, T, and density, ρ, from sea level to 20000 m, i.e. the Troposphere and the lower Stratosphere.

The ISA is based on the assumption that the air consists of perfect gas which obeys the equation of state,

$$P = \rho RT \tag{4-16}$$

where R is the universal gas constant (287 J/kg/K).
Sea level temperature T_0, pressure P_0, and density ρ_0 are defined as,

$$\begin{aligned} T_0 &= 288.15\ K \\ P_0 &= 101325\ N/m^2 \\ \rho_0 &= 1.225\ kg/m \end{aligned}$$

The temperature is defined to vary linearly from sea level with altitude,

$$T = T_0 + T(h) \tag{4-17}$$

Where the temperature lapse rate *T(h)* is defined as,

$$\begin{aligned} T(h) &= -6.5K/km \quad && 0 < h < 11\,km \\ T(h) &= 0K/km && 11 < h < 20km \end{aligned} \tag{4-18}$$

The other parameters of interest such as density, ρ, and pressure P, can be calculated as follows,

$$\begin{aligned} P &= P_0\left(\frac{T}{T_0}\right)^{4.25588} \\ \rho &= \rho_0\left(\frac{T}{T_0}\right)^{5.25588} \end{aligned} \tag{4-19}$$

The local speed of sound in air, a, is defined as,

$$a = \sqrt{\gamma RT} \tag{4-20}$$

where the specific heat ratio of air is γ=1.4.

4.9 Actuator model

The actuators installed on the aircraft are pulse width modulated servos FUTABA-S9204. The actuator is modelled as a second order system by Eq. (4-21), with positive and negative slew rate limits, as well as end stops as per Table 4-2. The second order response parameters, ω, ζ, were extracted from Gledhill (1999), and are equal respectively to 25rad/s and 0.6.

$$\frac{\delta}{\delta_d} = \frac{\omega^2}{s^2 + 2\zeta\omega s + \omega^2} \tag{4-21}$$

Where:

δ = actual deflection

δ_d = demanded deflection

ω = natural frequency

ζ = actuator damping

$\delta_{\max}$ (rad)	$\delta_{\min}$ (rad)	$\dot{\delta}_{\max}$ (rad/s)	$\dot{\delta}_{\min}$ (rad/s)
0.313	-0.313	1.55	-1.55

Table 4-2. Actuator saturation limits

The essential discontinuities have been modelled following the method determined by Thomasson, (1993). The mathematical model is presented.

Unconstrained motion is governed by the differential equation:

$$\ddot{\delta} + 2\zeta\omega\dot{\delta} + \omega^2\delta = \omega^2\delta_d \qquad (4\text{-}22)$$

The two ends stops are governed by equation:

$$\dot{\delta} = 0 \qquad (4\text{-}23)$$

The two rate limiting cases are governed by equation:

$$\ddot{\delta} = 0 \qquad (4\text{-}24)$$

There are five continuous regimes and the system makes transition between these regimes when it encounters the end stop discontinuity.
For this problem a set of equations can be written**:**

$$a = \omega^2(\delta_d - \delta) - 2\zeta\omega\dot{\delta} \qquad (4\text{-}25)$$

$$\ddot{\delta} = K_r a \qquad (4\text{-}26)$$

$$\dot{v} = \ddot{\delta} \qquad (4\text{-}27)$$

$$\dot{\delta} = K_a v \qquad (4\text{-}28)$$

The K_r and K_s constant values within each path (as per Table 4-3) are given in Table 4-4.

Path	Transition	Criterion
a	From Free to +Rate limit	$\dot{\delta} >= \dot{\delta}_{\max}$ *and* $a >= 0$
b	From +Rate limit to Free	$\dot{\delta} >= \dot{\delta}_{\max}$ *and* $a < 0$
c	From Free to -Rate limit	$\dot{\delta} <= -\dot{\delta}_{\max}$ *and* $a <= 0$
d	From –Rate limit to Free	$\dot{\delta} <= -\dot{\delta}_{\max}$ *and* $a > 0$
e	From Free to +Amplitude limit	$\delta >= \delta_{\max}$ *and* $a >= 0$
f	From +Amplitude limit to Free	$\delta >= \delta_{\max}$ *and* $a < 0$
g	From Free to – Amplitude limit	$\delta <= -\delta_{\max}$ *and* $a <= 0$
h	From –Amplitude limit to Free	$\delta <= -\delta_{\max}$ *and* $a > 0$

Table 4-3. Transition criteria

Path	K_r	K_a
a	0	1
b	1	1
c	0	1
d	1	1
e	0	0 (ν=0)
f	1	1
g	0	0 (ν=0)
h	1	1

Table 4-4. Actions for each transition

Simulations results for the rate and amplitude limited actuator are given in Fig. 4-7. The amplitude and rate limiting are clearly visible and the jump of the velocity to zero on reaching the end stops can also be seen. On the same graph the results of the simulation implementing location of discontinuities without transition criteria and actions that are required following the crossing of a boundary are plotted.

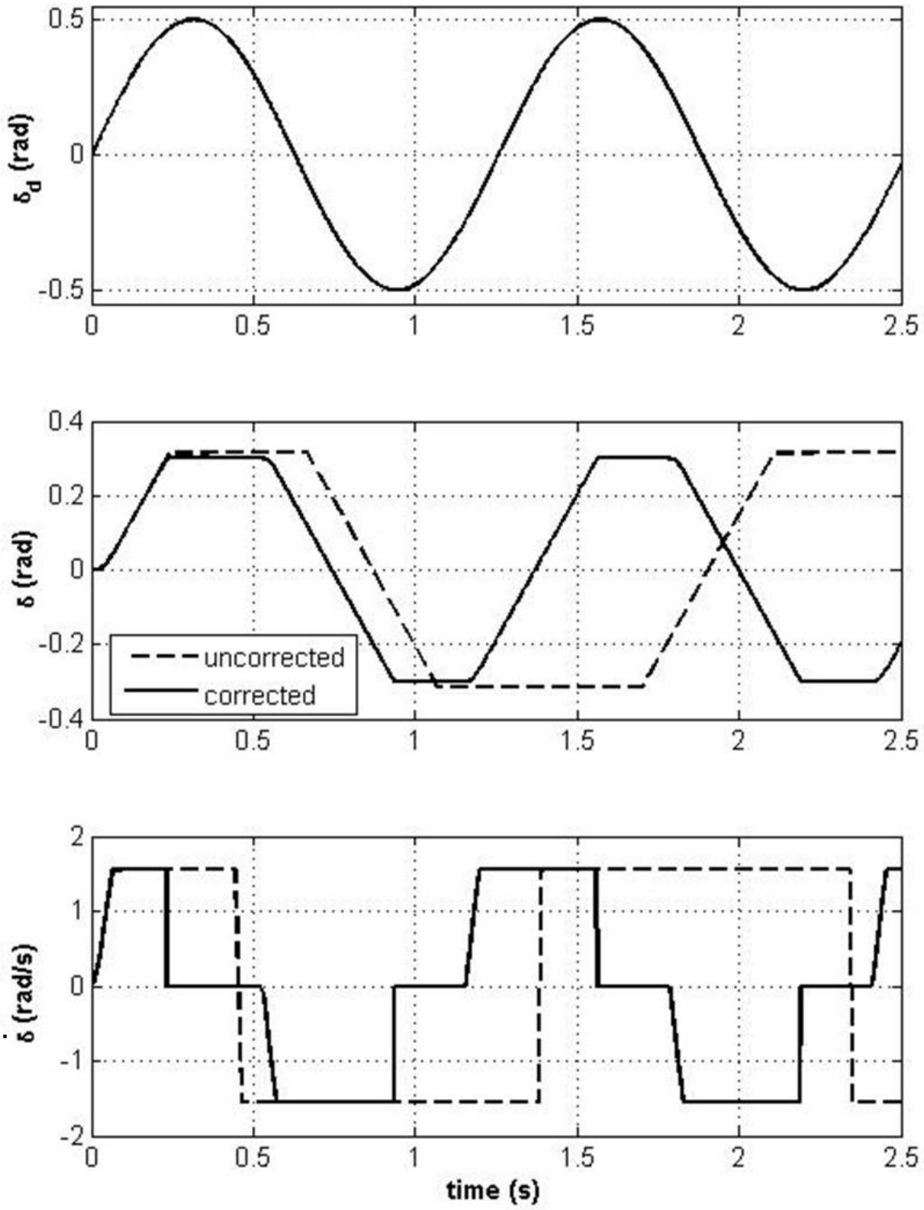

Fig. 4-7. Actuator response to sin wave signal

4.10 Trim

The simulation model of the *Demon* air vehicle was used to assess the stability and control properties of the air vehicle. These analyses do not, however, constitute a validation or verification of the simulation model since there are no alternative static or dynamic data available for comparison at the present time. However, results were assumed for plausibility.

A trim map was made for the vehicle in straight level flight at different flight speed. In terms of assessing the trim parameters for a given flight conditions, two methods were used. First, the computed trim was obtained from the *Demon* non linear simulation model using the Matlab ‘trim’ routine. The ‘trim’ routine uses a sequential quadratic programming algorithm to find values for the input (controls) and the states that determine steady state points of the aircraft dynamic system, and satisfy user specified output (speed and flight path angle). Second, an alternative simplified analytical trim was determined using the method described by Eqs (4.29) Equations 4-29 were solved to determine trim, angle of attack, symmetric elevon angle (η) and thrust throttle (τ) setting, for a demanded airspeed and flight path angle. The method has been implemented in Mathcad and the Mathcad routine is documented in appendix C.

$$\begin{pmatrix} C_{L\alpha} & C_{L_\eta} \\ C_{M\alpha} & C_{M_\eta} \end{pmatrix}\begin{pmatrix} \alpha_{trim} \\ \eta_{trim} \end{pmatrix} = \begin{pmatrix} C_{Ltrim} \\ -C_{M_0} \end{pmatrix}$$

$$C_{Ltrim}\left(\frac{1}{2}\rho V^2 S\right) = W \tag{4-29}$$

$$T(\tau) = \left(C_{D0} + KC^2{}_{Ltrim}\right)1/2\rho V^2 S$$

$$with \quad \alpha << 0 \Rightarrow \quad Sin\alpha \approx 0 \quad and \quad \cos\alpha \approx 1$$

The results of the two longitudinal trim studies are shown in Table 4-5. The velocity (30, 40 and 45 m/s) is representative of typical flight speeds of the *Demon*.

Comparison of the alternative trim analyses shows very good agreement for angle of attack, elevator deflection, and throttle setting.

Velocity (m/s)	Throttle	Angle of attack (deg)	Elevator (deg)
Computed trim			
35	29.6	7.60	0.4872
40	32.5	6.1	1.7168
45	37.12	5	2.6623
Analytical trim			
30	28.3	7.4	0.5
40	30.2	5.9	1.8
45	33.139	4.86	2.7

Table 4-5. Analytical and simulation based longitudinal trim

4.11 Longitudinal and lateral mathematical model

This section presents the analysis of the longitudinal and lateral motion of the un-augmented basic airframe. The study is based on the assumption of small perturbations and linear aerodynamic forces. The effects of actuator dynamic delays are neglected.

The 6DoF model was initialised as per Table 4-6 and the linear state space description, referred to body axes, generated, in order to enable a comprehensive analysis of the flight dynamics of the aircraft.

A linear model has been generated directly from the Simulink model, using the Matlab routine ‘linmod’. Since the equilibrium flight (straight flight) is symmetric the longitudinal and lateral directional dynamics can be decoupled.

Angle of attack (deg)	Flight path angle (deg)	Speed (m/s)	Height (m)	Throttle	Elevator (deg)
5.03	0	45	121	37.12	2.66

Table 4-6. Trim condition

4.11.1 Longitudinal mathematical model

The state and output equation describing the longitudinal motion is shown below.

$$\begin{aligned}\dot{\mathbf{x}} &= \mathbf{Ax}+\mathbf{Bu}\\ \dot{\mathbf{y}} &= \mathbf{Cx}+\mathbf{Du}\end{aligned} \tag{4-30}$$

Where:

$$\mathbf{A}=\begin{bmatrix} -0.0708 & 0.3757 & -3.8286 & -9.7722\\ -0.1324 & -3.4476 & 43.4938 & -0.8602\\ 0.0606 & -0.6882 & -2.4628 & 0\\ 0 & 0 & 1.0000 & 0 \end{bmatrix} \qquad \mathbf{B}=\begin{bmatrix} 0.0037 & 0.0612\\ -0.3238 & 0\\ -0.8112 & 0\\ 0 & 0 \end{bmatrix}$$

$\mathbf{x}^T=[u \quad w \quad \theta \quad q]$ and $\mathbf{u}^T=[\eta,\tau]$

$$\mathbf{C}=\begin{bmatrix} 1 & 0 & 0 & 0\\ 0 & 1 & 0 & 0\\ 0 & 0 & 57.3 & 0\\ 0 & 0 & 0 & 57.3 \end{bmatrix} \qquad \mathbf{D}=[0]$$

The validity of the longitudinal model was checked by comparing the response of longitudinal response parameters to a step control input with those generated by the non-linear model at the same flight conditions, see Fig. 4-8. The response shows a good match over the first 5 seconds of simulation, hence confirming the validity for small perturbation analysis.

Solution of the equations of motion determines the following response transfer functions:

$$\frac{u(s)}{\eta(s)}=\frac{0.0037\,(\mathrm{s}+811)\,(\mathrm{s}^2+1.445\mathrm{s}+8.469)}{(\mathrm{s}^2+0.06613\mathrm{s}+0.07527)\,(\mathrm{s}^2+5.915\mathrm{s}+38.66)}\ \text{m/s/deg}$$

$$\frac{w(s)}{\eta(s)}=\frac{-0.3238\,(\mathrm{s}+111.4)\,(\mathrm{s}^2+0.0644\mathrm{s}+0.03304)}{(\mathrm{s}^2+0.06613\mathrm{s}+0.07527)\,(\mathrm{s}^2+5.915\mathrm{s}+38.66)}\ \text{m/s/deg}$$

$$\frac{q(s)}{\eta(s)}=\frac{-46.4784\,\mathrm{s}\,(\mathrm{s}+3.154)\,(\mathrm{s}+0.08944)}{(\mathrm{s}^2+0.06613\mathrm{s}+0.07527)\,(\mathrm{s}^2+5.915\mathrm{s}+38.66)}\ \text{deg/s/deg}$$

$$\frac{\theta(s)}{\eta(s)} = \frac{-46.4784\,(s+0.08944)\,(s+3.154)}{(s^2+0.06613s+0.07527)\,(s^2+5.915s+38.66)}\ \text{deg/deg}$$

The longitudinal characteristic equation is given by,

$$\Delta(s) = (s^2+0.06613s+0.07527)\,(s^2+5.915s+38.66) = 0 \qquad (4\text{-}31)$$

Therefore the stability modes at the given flight condition are given by the roots of Eq. (4-31). The first pair of complex roots describes the *phugoid* stability mode with characteristics,

$$\begin{aligned} \text{Damping ratio} \quad & \zeta_p = 0.121 \\ \text{Undamped natural frequency} \quad & \omega_p = 0.275\ \text{rad/s} \\ \text{Period} \quad & T_p = 22.85s \end{aligned}$$

The second pair of complex roots describes the *short period pitching* mode (SPPO),

$$\begin{aligned} \text{Damping ratio} \quad & \zeta_s = 0.476 \\ \text{Undamped natural frequency} \quad & \omega_s = 6.22\ \text{rad/s} \\ \text{Period} \quad & T_s = 1.01\text{s} \end{aligned}$$

These mode characteristics indicate that the airframe is longitudinally aerodynamically stable.

In order to excite the airframes longitudinal dynamic modes a 1 deg step has been input to the elevator. The long term response of the aircraft to a unit step (1 deg) elevator input is shown in Fig 4-9. The responses show both the dynamic stability mode, the short period pitching oscillation and the phugoid. However, the magnitude of each stability mode differs in each variable. The pitching mode is more visible in the initial transient in the variable w and q, whereas the phugoid mode is visible in all variables although the relative magnitude varies considerably. From the longitudinal airspeed component u response a time period for the phugoid, T_p, of approximately 20s can be measured; this compares favourably with the time period calculated from the linear state model.

The mode content in each of the motion variables is given most precisely by the eigenvectors. With the aid of MATLAB the eigenvector matrix **V** is determined as follows,

$$
\begin{array}{c}
\qquad\qquad \textbf{Short period mode} \qquad\qquad\qquad\qquad\qquad\qquad \textbf{Phugoid mode} \\
\mathbf{V}=\left[\begin{array}{cccc}
-0.0650+0.0041i & -0.0650-0.0041i & -0.9977 & -0.9977 \\
0.9898 & 0.9898 & -0.0605+0.0019i & -0.0605-0.0019i \\
0.0113+0.1243i & 0.0113-0.1243i & -0.0077+0.0003i & -0.0077-0.0003i \\
0.0167-0.0111i & 0.0167+0.0111i & 0.0045+0.0278i & 0.0045-0.0278i
\end{array}\right]
\begin{array}{c} u \\ w \\ q \\ \theta \end{array}
\end{array}
$$

The magnitude of each component eigenvector is calculated as follows:

$$
|\mathbf{V}|=\left[\begin{array}{cccc}
0.0651 & 0.0651 & 0.9977 & 0.9977 \\
0.9898 & 0.9898 & 0.0605 & 0.0605 \\
0.1248 & 0.1248 & 0.0077 & 0.0077 \\
0.0201 & 0.0201 & 0.0281 & 0.0281
\end{array}\right]
\begin{array}{c} u \\ w \\ q \\ \theta \end{array}
$$

Clearly, the phugoid mode is dominant in u since 0.9977 >0.0651, the short period mode is dominant in q since 0.1248>0.0077 and the short period and phugoid modes content in h are of similar order. These observations accord very well with the responses show in Fig 4-9.

4.11.2 Lateral-directional mathematical model

The state and output equation describing the lateral- directional motion is shown below.

$$
\begin{bmatrix} \dot{v} \\ \dot{p} \\ \dot{r} \\ \dot{\phi} \end{bmatrix}
=
\begin{bmatrix}
-0.3543 & 4.2835 & -44.7969 & 9.772 \\
-3.0273 & -79.0645 & 4.8937 & 0 \\
0.7543 & 1.7585 & -3.9643 & 0 \\
0 & 1.0000 & 0.0880 & 0
\end{bmatrix}
\begin{bmatrix} v \\ p \\ r \\ \phi \end{bmatrix}
+
\begin{bmatrix}
0.0157 & 0.1246 \\
-3.0072 & 0.8730 \\
0.0199 & -0.4857 \\
0 & 0
\end{bmatrix}
\begin{bmatrix} \xi \\ \zeta \end{bmatrix}
$$

The validity of the lateral-directional model was checked by comparing the response parameters to a step control input with those generated by the non-linear model at the same flight conditions, see Fig 4-10. The response shows a good match over the first 5 seconds of simulation, hence confirming the validity for small perturbation analysis. The transfer functions describing the response to ailerons are,

$$\frac{v(s)}{\xi(s)} = \frac{0.0157\,(s-786.9)\,(s-5.675)\,(s-1.694)}{(s+78.98)\,(s+0.01326)\,(s^2+4.393s+32.93)}\ \text{m/s/deg}$$

$$\frac{p(s)}{\xi(s)} = \frac{-172.3126\,(s-0.01835)\,(s^2+4.32s+34.41)}{(s+78.98)\,(s+0.01326)\,(s^2+4.393s+32.93)}\ \text{deg/s/deg}$$

$$\frac{r(s)}{\xi(s)} = \frac{1.1403\,(s-188.4)\,(s^2+2.677s+5.755)}{(s+78.98)\,(s+0.01326)\,(s^2+4.393s+32.93)}\ \text{deg/s/deg}$$

$$\frac{\phi(s)}{\xi(s)} = \frac{-172.2122\,(s^2+4.413s+34.64)}{(s+78.98)\,(s+0.01326)\,(s^2+4.393s+32.93)}\ \text{deg/deg}$$

The transfer functions describing the response to rudder are,

$$\frac{v(s)}{\zeta(s)} = \frac{0.1246\,(s+227.6)\,(s+60.03)\,(s-0.0124)}{(s+78.98)\,(s+0.01326)\,(s^2+4.393s+32.93)}\ \text{m/s/deg}$$

$$\frac{p(s)}{\zeta(s)} = \frac{50.0229\,(s+7.128)\,(s-5.946)\,(s-0.01887)}{(s+78.98)\,(s+0.01326)\,(s^2+4.393s+32.93)}\ \text{deg/s/deg}$$

$$\frac{r(s)}{\zeta(s)} = \frac{-27.8306\,(s+75.8)\,(s^2+0.2626s+0.2155)}{(s+78.98)\,(s+0.01326)\,(s^2+4.393s+32.93)}\ \text{deg/s/deg}$$

$$\frac{\phi(s)}{\zeta(s)} = \frac{47.5738\,(s+5.541)\,(s-8.233)}{(s+78.98)\,(s+0.01326)\,(s^2+4.393s+32.93)}\ \text{deg/deg}$$

The dutch roll poles are almost cancelled out of the p/ξ transfer function by the complex zeros. Therefore weak coupling exists between the rolling and yawing motions. The rudder to roll rate transfer function has a non minimum phase (NMP) zero farther away from the origin. A positive deflection of the rudder directly produces a positive rolling moment and a negative yawing moment. The negative yawing moment rapidly leads to a positive sideslip, which will in turn produce a negative rolling moment.

The characteristic equation is given by,

$$\Delta(s) = (s + 78.98)(s + 0.01326)(s^2 + 4.393s + 32.93) = 0 \qquad (4\text{-}32)$$

and its roots give the stability mode characteristics.

The first real root describes the stable spiral mode with time constant,

$$T_s = \frac{1}{0.01326} = 75\text{s}$$

The second real root describes the roll subsidence mode with time constant,

$$T_r = \frac{1}{78.98} = 0.0127\text{ s}$$

The pair of complex roots describes the oscillatory dutch roll mode with characteristics,

Damping ratio $\zeta_d = 0.38$
Undamped natural frequency $\omega_d = 5.73$ rad/s

Since both real roots are negative and the pair of complex roots have negative real parts then the mode characteristics indicate the airframe to be aerodynamically stable.

Fig. 4-11 shows the lateral directional response to a unit (1°) rudder step input. A positive rudder step input is chosen and this will cause the aircraft to turn left. Once the turn is established this results in a negative yaw rate and a negative roll and roll rate induced by yaw-roll coupling. The roll response to rudder exhibits a sign reversal for the first second or so of its response and it is the manifestation of the non minimum phase effect, referred as adverse roll to rudder. This is a clear effect of the non minimum phase numerator terms highlighted before. The cancellation of the roll subsidence mode by the respective numerator zero in the yaw rate response to rudder means that the spiral mode and dutch roll will dominate the shape of the yaw response. However, the oscillatory dutch roll mode is almost not discernible being that this mode quite well damped.

The response of the airplane to a unit (1°) aileron pulse, held for 1 second and then returned to zero, is shown in Fig. 4-12. At first glance the dutch roll mode is not so distinctive since it is damped out after the first few seconds due to the relatively high damping. Both the roll and spiral mode appears as exponentially convergent characteristics since they are both stable. The roll converges quite quickly with a time constant of 0.013 sec, whereas the spiral mode converges very slowly with a time constant of 80 sec. The spiral mode characteristic is seen in the roll attitude response where it determines the longer term convergence to zero and it is fully established at 30 sec.

As it was observed from the linear analysis conducted in Chapter 3 the spiral mode results in a much more longer time constant at low incidence (high speed) with respect to low incidence (low speed), as a result of the lower directional stability. Fig. 4-13 compares the roll attitude response to aileron pulse correspondent to each of these conditions. It is clear that at high velocity the spiral mode results in an almost neutral stable behaviour.

The roll subsidence mode is observed to involve almost pure rolling motion. Thus a reduced order model of the lateral directional dynamics, removing the side-force and yawing moment equations and assuming wind axes, can be obtained. The roll response to aileron transfer function is shown in Eq. (4-33) and is derived from the complete lateral model assuming the previous hypothesis and that the rudder is held fixed:

$$\frac{p(s)}{\xi(s)} = \frac{l_\xi}{(s - l_p)} \tag{4-33}$$

First order roll mode approximation:

$$\frac{p(s)}{\xi(s)} = \frac{-172.3}{\mathrm{s} + 79.06}\ \mathrm{deg/s/deg}$$

Comparison between the first order and the complete state space model step aileron response is shown in Fig. 4-14. It can be seen that the two models compare vary favourably.

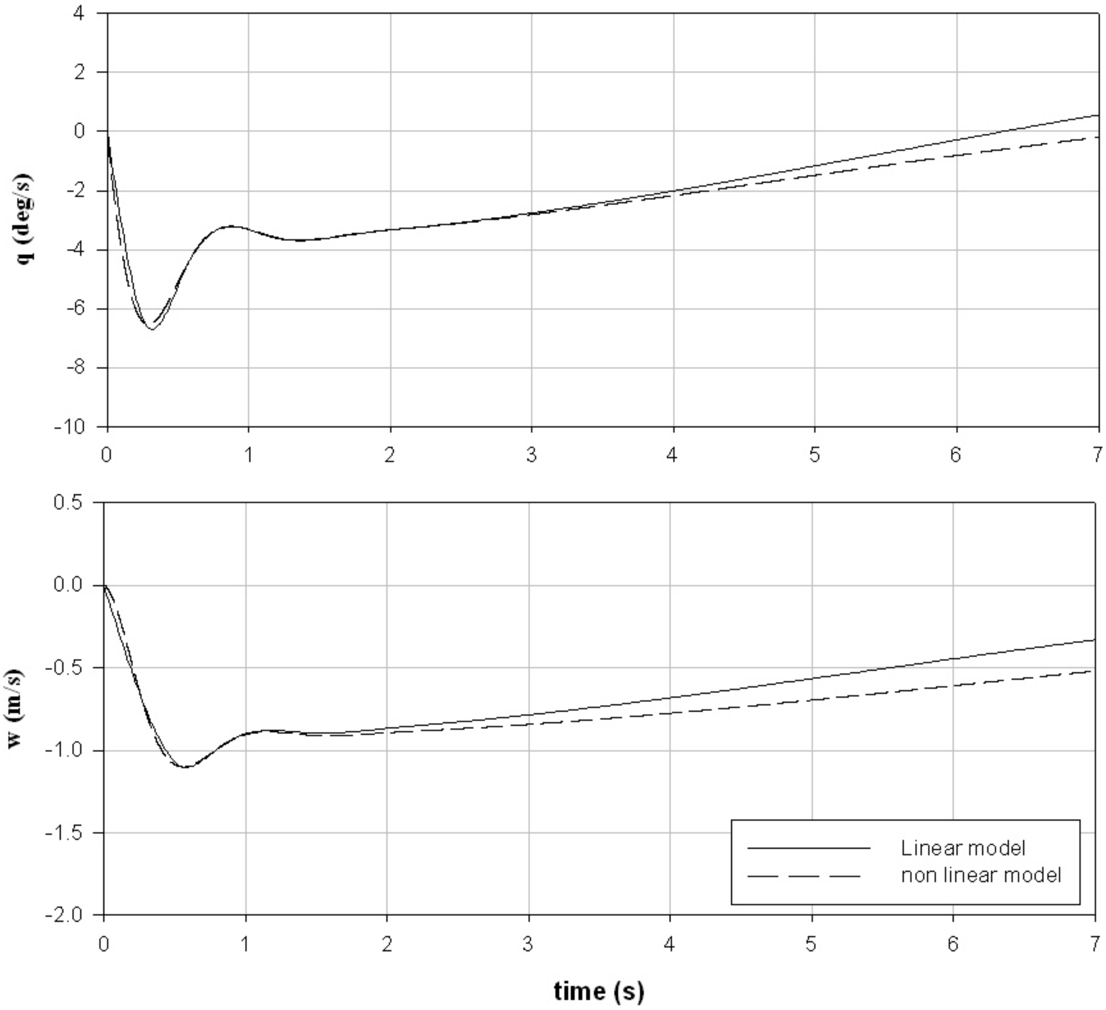

Fig. 4-8. Longitudinal linear model non linear model comparison

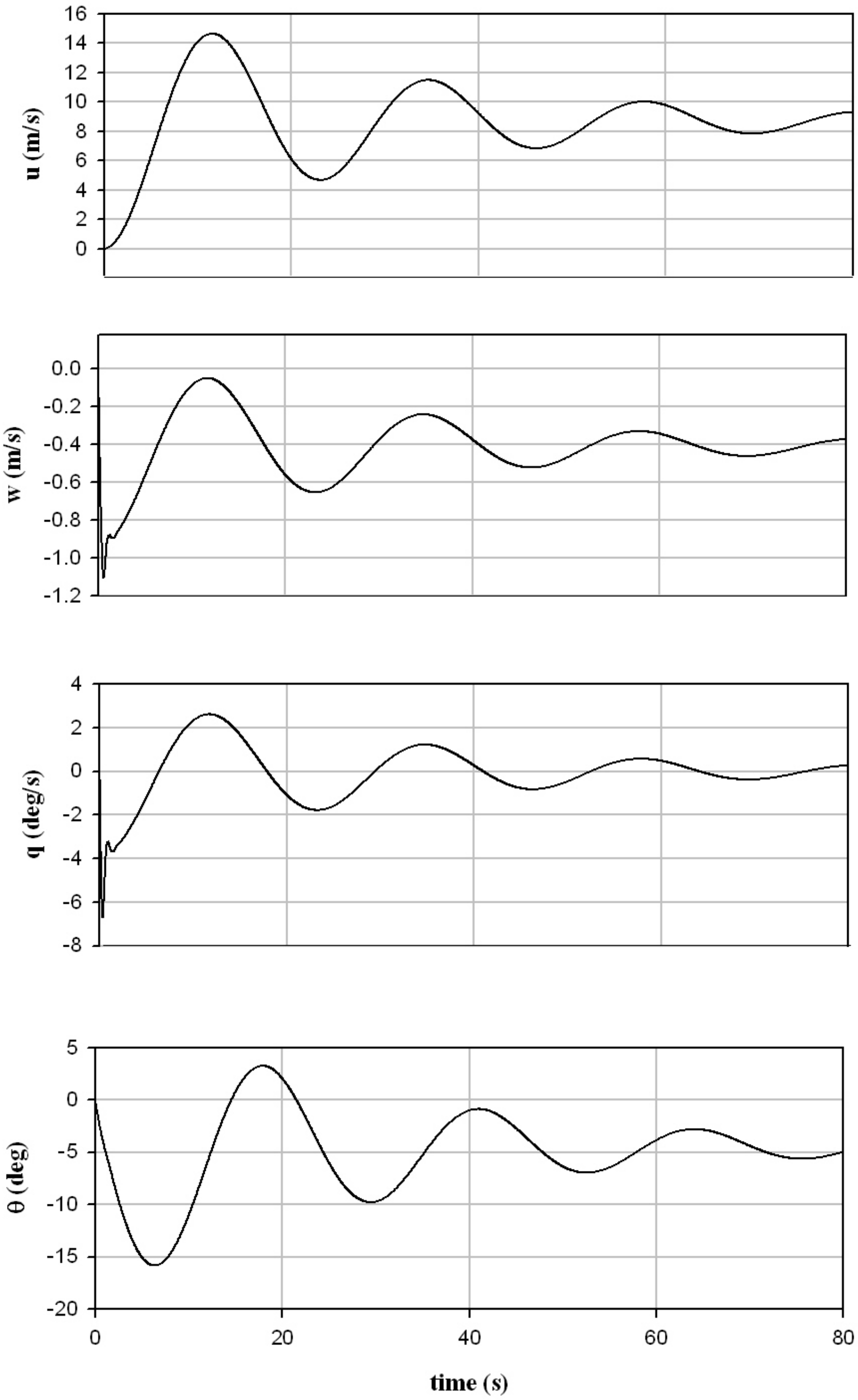

Fig 4-9 Aircraft response to 1 deg elevator step input

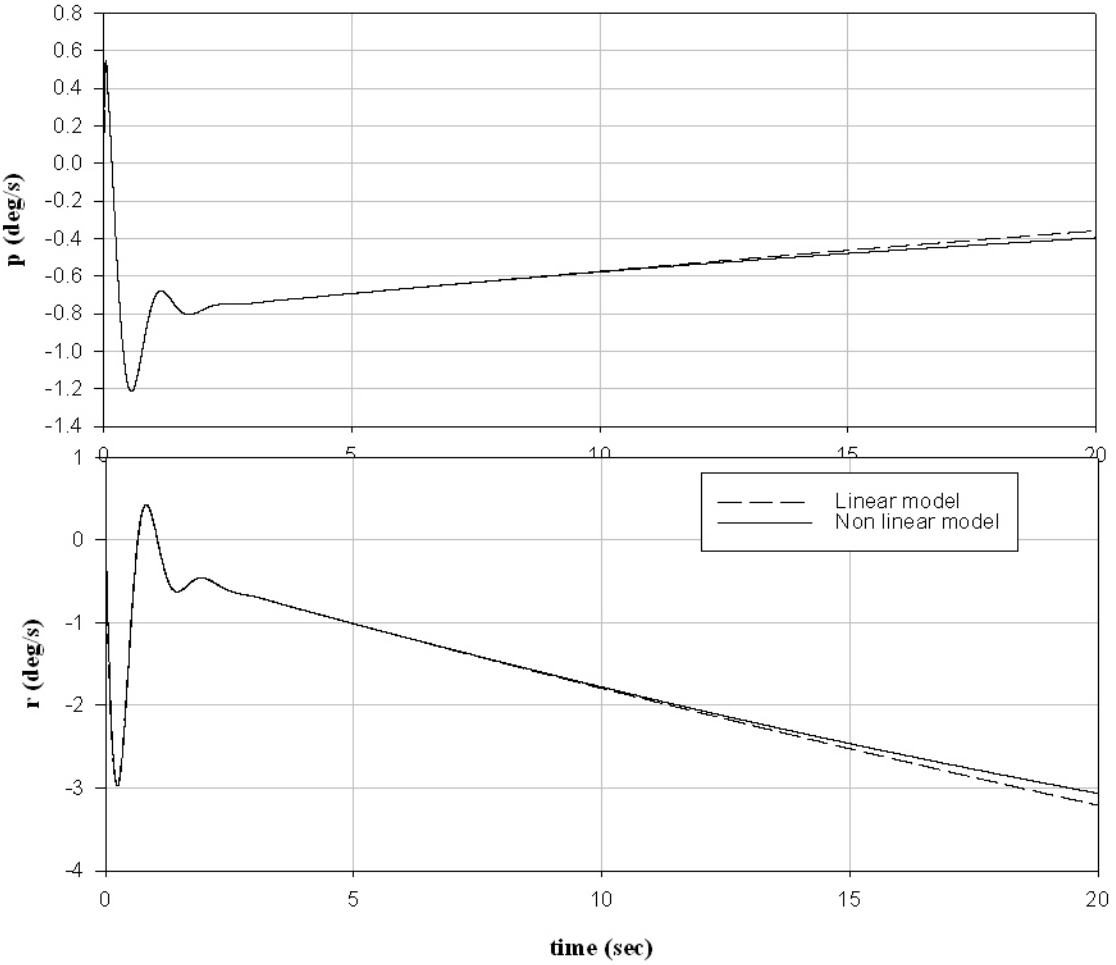

Fig 4-10. Lateral linear model non linear model comparison

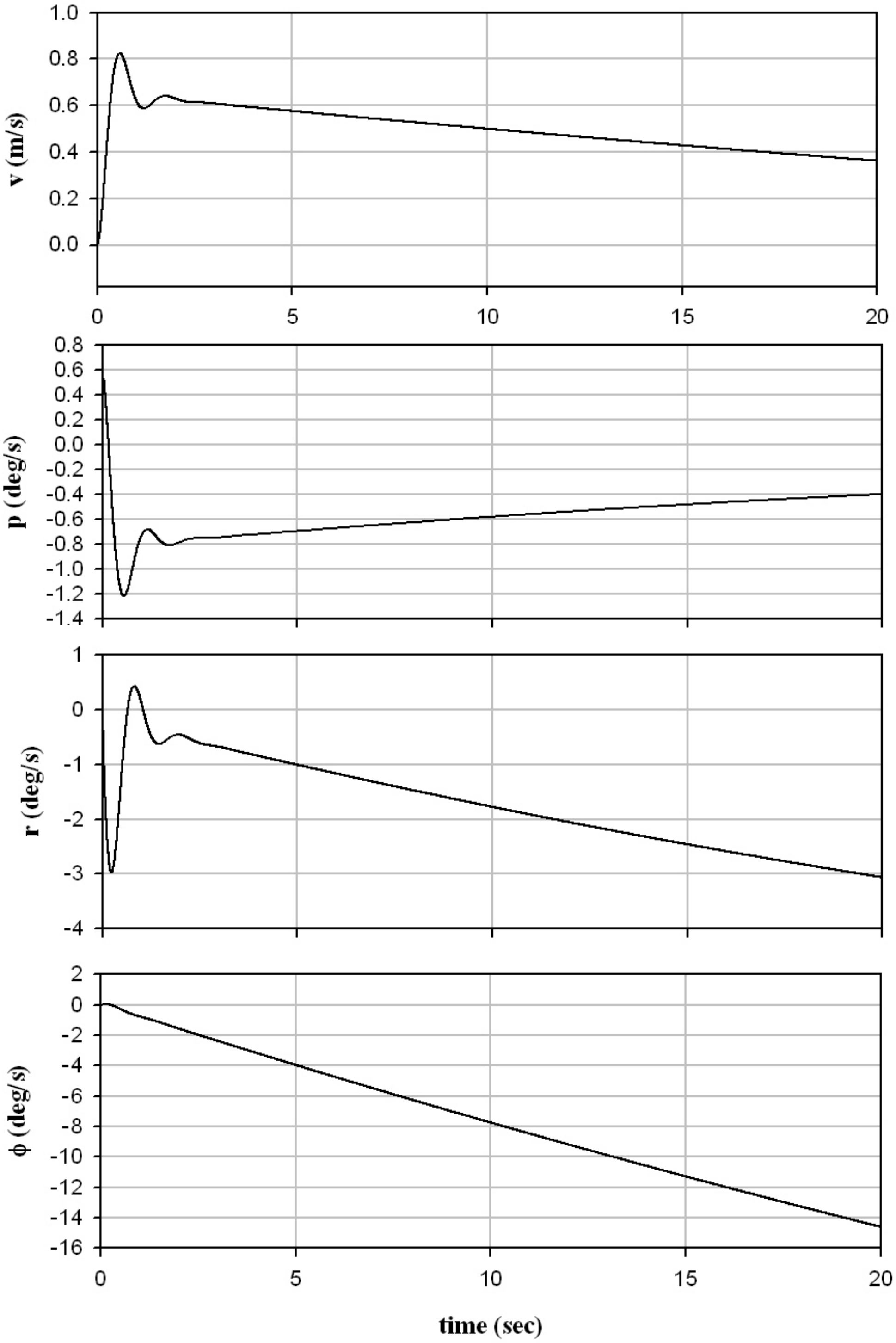

Fig. 4-11. Aircraft response to 1 deg rudder step input

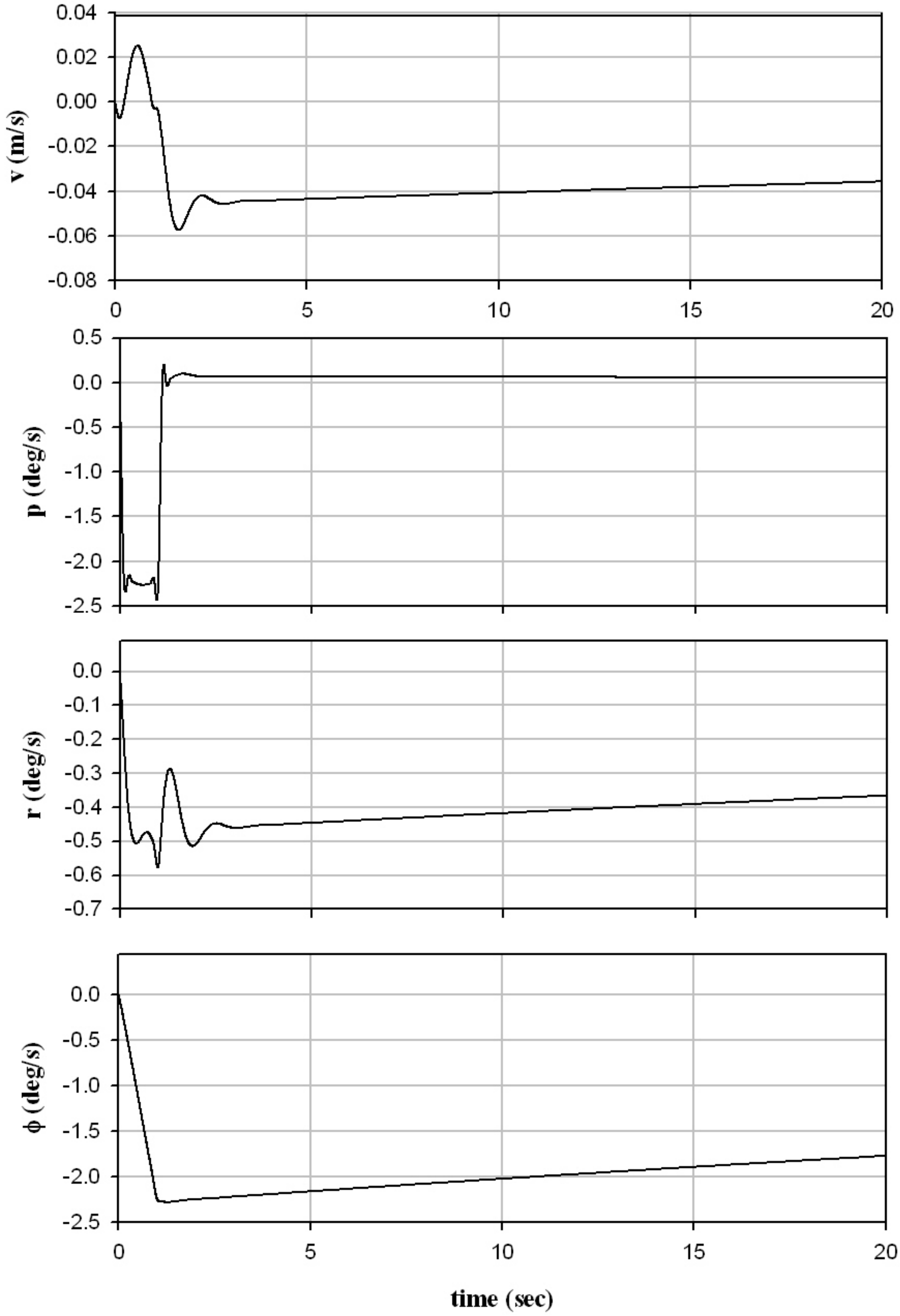

Fig. 4-12. Aircraft response to 1 deg -2s aileron pulse input

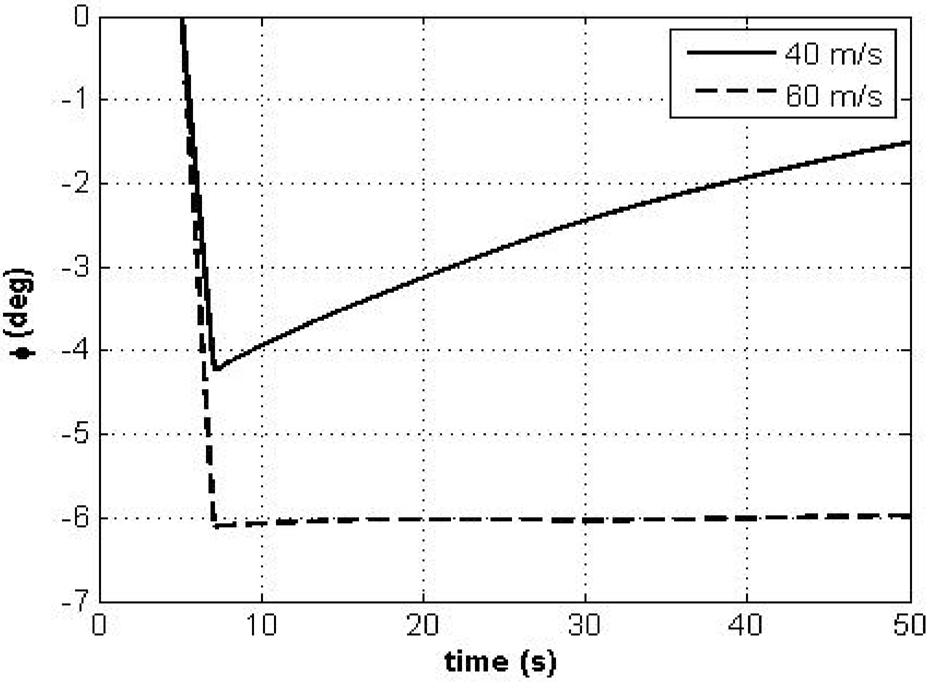

Fig. 4-13. Roll attitude response to 1°- 2s aileron pulse. Comparison of the spiral mode at low incidence with the spiral mode at high incidence

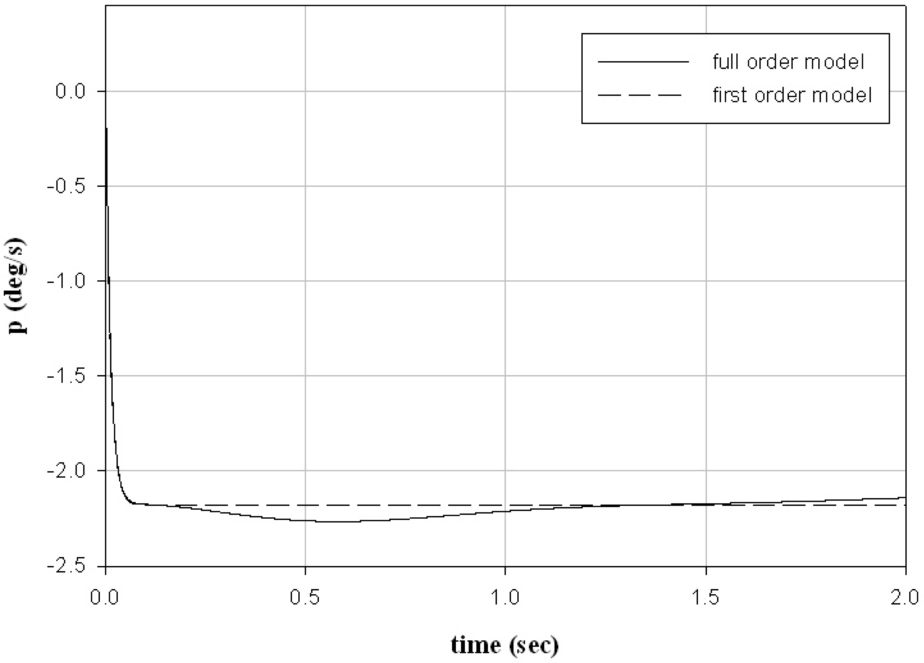

Fig. 4-14. Comparison between the first order and the complete state space model step aileron response (flight condition correspondent to the one in table 4-6)

4.12 Stability Characteristics

The stability characteristics of the classical modes of motion were assessed across the flight envelope and compared with applicable flying qualities requirements, as suggested by (Prosser and Wiler 1976). Prosser and Wiler (1976) seem to be the definitive reference on RPV flying qualities, although it does not have much in the way of unnamed aircraft flying qualities data. In fact any criteria that it does set forward are quoted from Military specification MIL-F-8785B. It suggested that these guidelines be followed in the absence of any unmanned flying qualities data.

It can be seen that the *Demon* is classed as a Class I aircraft and can be expected to operate in Flight Phase Category A, B and C.

Coupled with the simulation development an off-line linear stability analysis has been carried out with the aid of Mathcad in order to validate the model results. The full implementation is documented in appendix C. A computation of the aerodynamic derivatives required to build up the system matrices has been carried on (using hand-computation) following the definition given in full in Cook (2007). Two separate computational procedures of system matrices help to uncover modeling errors and to check correctness and accuracy of numerical linearization performed in the Simulink environment. Results of these computations are shown in Table 4-7 and Table 4-8. Comparison of the alternatives analyses shows very good agreement. Moreover the values compare vary favourably with the results obtained from the reduced order linear analysis conducted in Chapter 3. The trend of the stability mode is in agreement with the main observation derived from the reduced order analysis conducted in Chapter 3.

Table 4-7. Longitudinal dynamic stability modes approximations

Airspeed (m/s)	Computed				Analytical			
	Short period mode		Phugoid mode		Short period mode		Phugoid mode	
	ζ_s	ω_s (rad/s)	ζ_p	ω_p (rad/s)	ζ_s	ω_s (rad/s)	ζ_p	ω_p (rad/s)
30	0.474	4.32	0.060	0.416	0.433	4.685	0.072	0.414
40	0.420	6.18	0.097	0.318	0.428	6.253	0.091	0.310
50	0.475	6.91	0.148	0.275	0.426	7.817	0.132	0.248

Table 4-8. Lateral dynamic stability modes approximations

Airspeed (m/s)	Computed				Analytical			
	Spiral mode	Roll mode	Dutch roll mode		Spiral mode	Roll mode	Dutch roll mode	
	T_s (s)	T_r (s)	ζ_d	ω_d (rad/s)	T_s (s)	T_r (s)	ζ_d	ω_d (rad/s)
30	13.8	0.020	0.421	4.17	11.2	0.020	0.433	4.053
40	41.3	0.014	0.39	5.20	45.4	0.014	0.386	5.315
50	149.2	0.011	0.379	6.29	228.6	0.011	0.368	6.561

The Phugoid damping across the flight envelope is shown in Fig. 4-15 and the MIL-F8785C level 1 flying qualities requirements are superimposed. The Phugoid mode is adequately stable and the damping ratio meets the minimum requirements.

Note that the short period mode is stable for all the velocities. Its frequency increases with increasing velocity but the damping is essentially constant.

The variation in SPPO damping across the flight envelope is shown in Fig. 4-16 and superimposed are the relevant MIL-F8785C flying qualities. The damping ratio meets the minimum requirements.

The linearized lateral directional modes are all stable across the flight envelope. The Dutch roll mode damping across the flight envelope is shown in Fig. 4-17. The Dutch roll mode is very well damped. From Fig. 4-18 the variation of product of Dutch roll damping and frequency across the flight envelope can be seen. Superimposed on the same figure are the applicable MIL-F8785C flying qualities requirements.

The roll mode is stable across the flight envelope and meets the most stringent level 1 MIL-F8785C flying qualities requirements as it can be seen from Fig. 4-19. The roll mode time constant is extremely short.

The spiral model is plotted in Fig. 4-20. Note that this mode is very stable with a time constant unusually long.

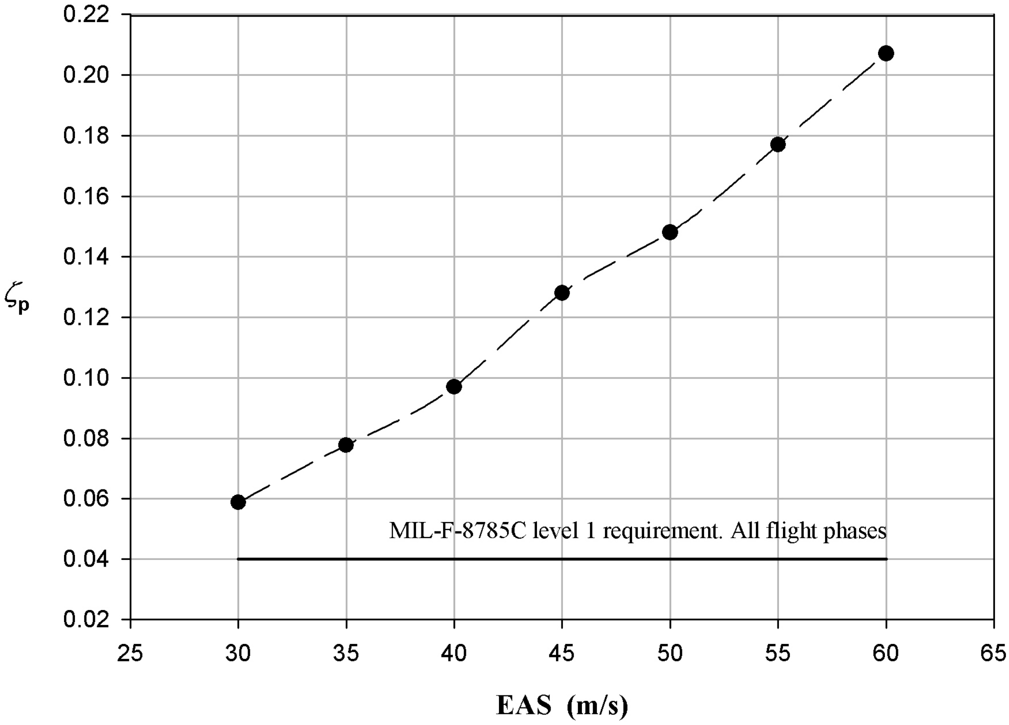

Fig. 4-15. Phugoid damping ratio of basic airframe plotted against equivalent airspeed

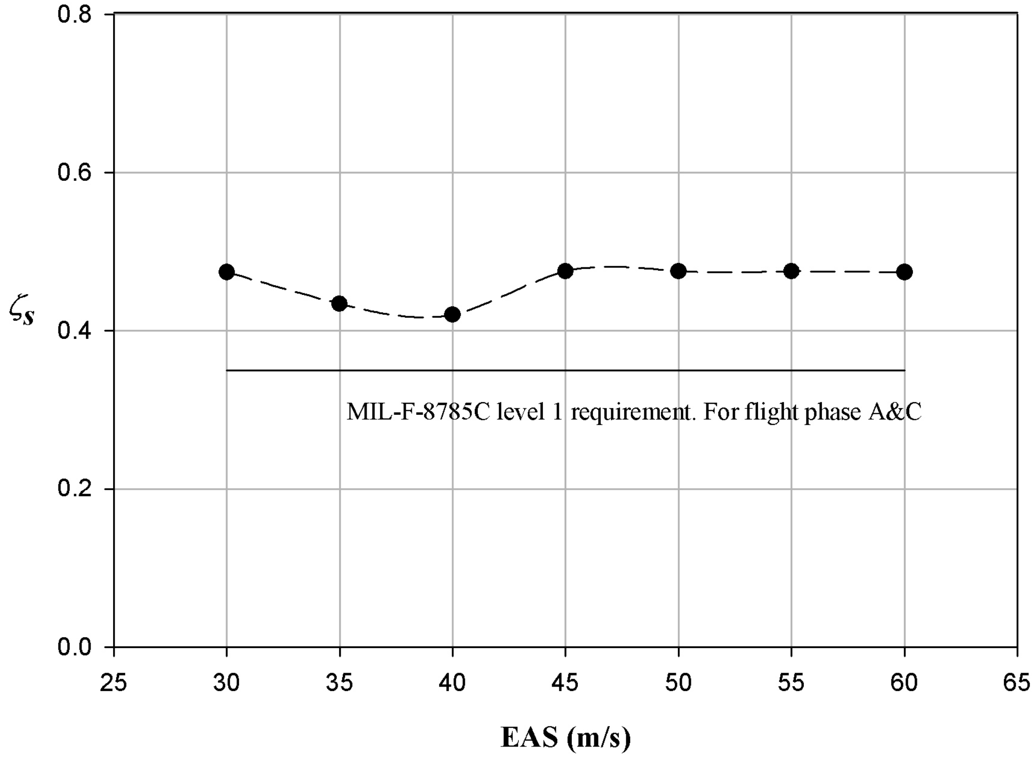

Fig. 4-16. Short period damping ratio of basic airframe plotted against equivalent airspeed

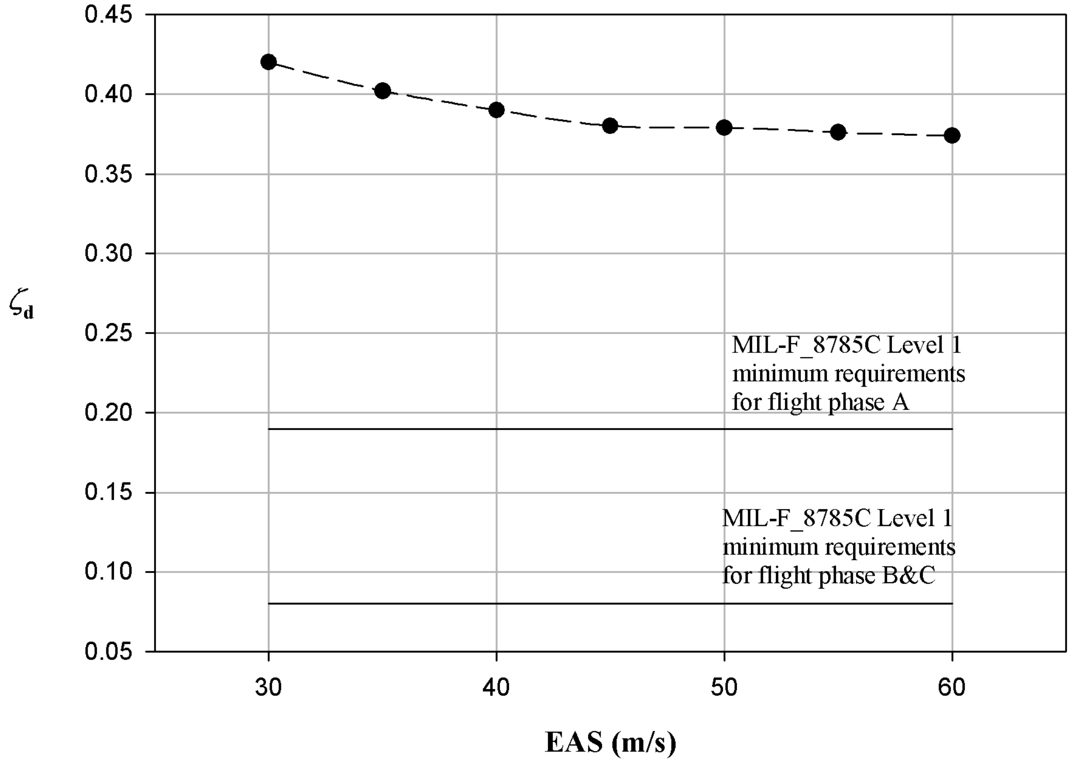

Fig. 4-17. Dutch roll damping ratio of basic airframe plotted against equivalent airspeed

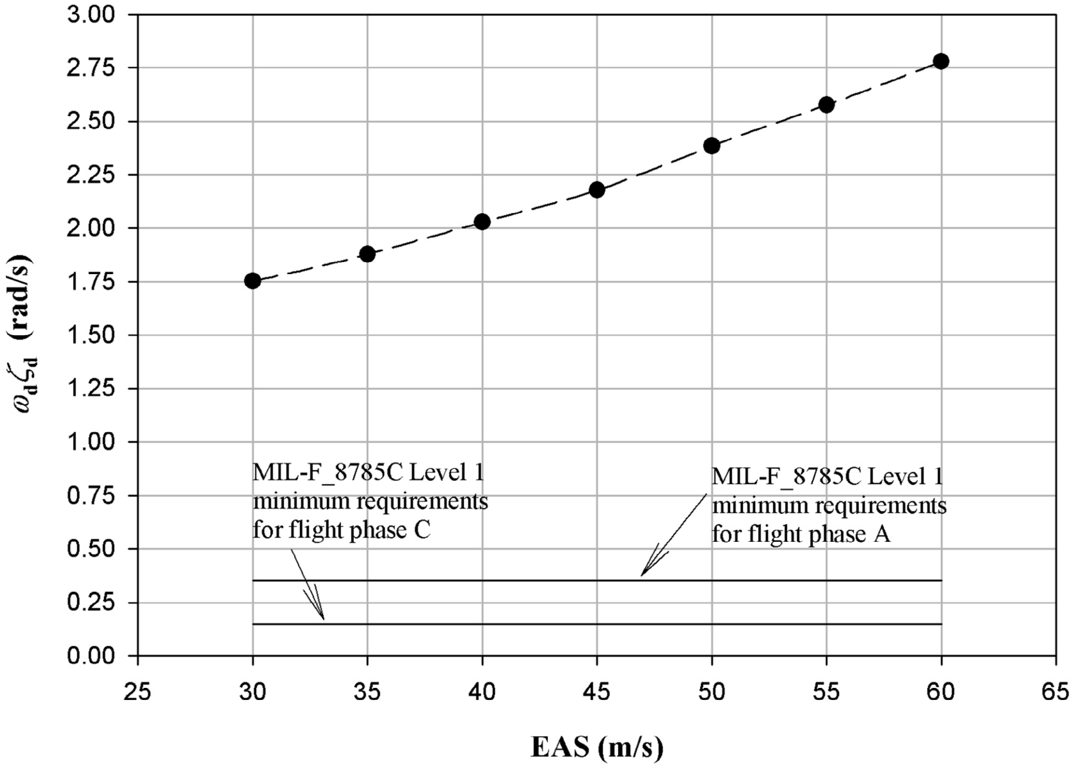

Fig. 4-18. Product of Dutch roll damping ratio and frequency of basic airframe plotted against equivalent airspeed

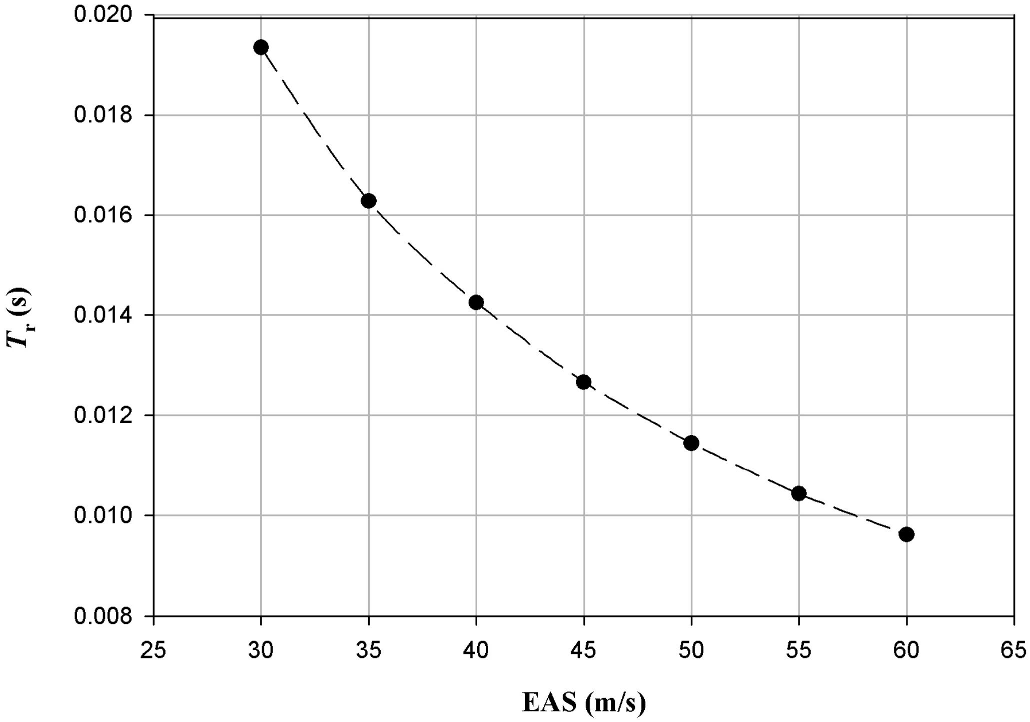

Fig. 4-19. Roll mode time constant of basic airframe plotted against equivalent airspeed- MIL-F-8785C level flying qualities maximum roll mode time constant requirement: $T_r < 1$

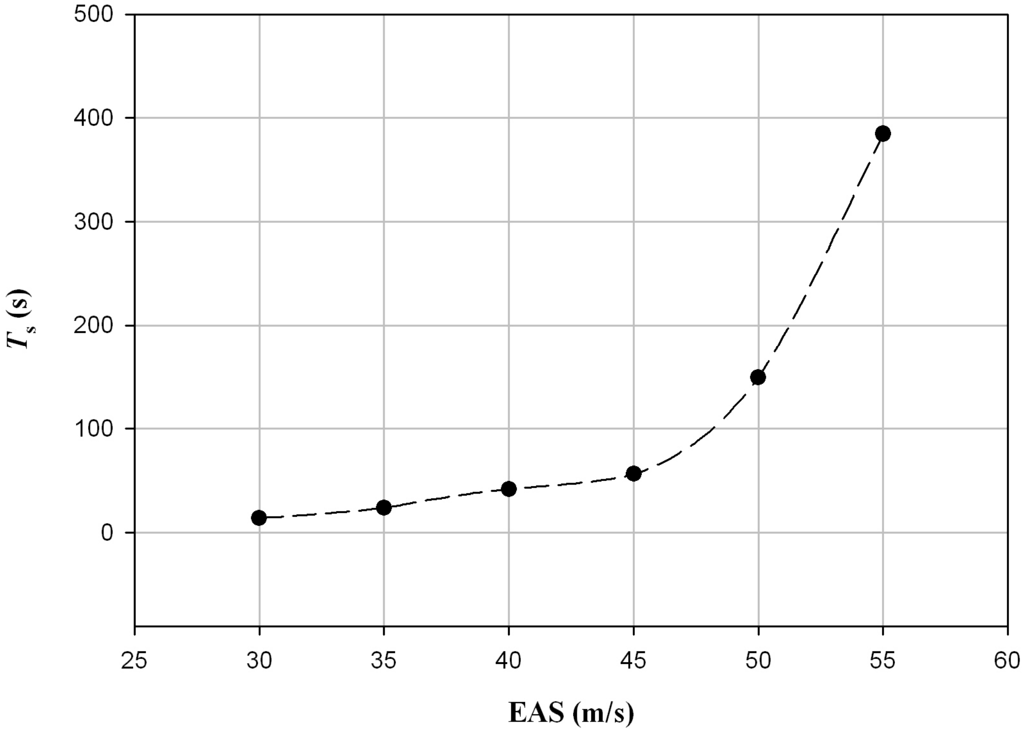

Fig. 4-20. Spiral mode time constant of basic airframe plotted against equivalent airspeed. Most stringent MIL-F-8785C level flying qualities minimum time constant

requirement: $T_s < 17.3$

5 DUAL SLOT ACTUATOR DEVELOPMENT

5.1 Introduction

The aerodynamic research undertaken by Manchester University (Frith & Wood, 2004) has established the operational principles for practical flapless control of air vehicles by flow control means utilising the Coanda effect. In particular, it has been demonstrated that a wing trailing edge incorporating a narrow span-wise slot through which high pressure air is blown over the Coanda surface can produce usable control forces and moments.

Modulation of the air supply to the slot by means of a control valve enables unidirectional force and moment generation for control of the vehicle. Replacing conventional ailerons with span-wise pairs of slots permits differential operation sufficient for lateral control. However, modulation of the resultant control force and moment generated by fixed trailing edge geometry, utilising internal air flow throttling, raises the engineering challenge of avoiding the worst effects of dynamic interaction between the air supply system components. Thus, smooth proportional control by means of an air supply control valve suggests a less amenable engineering solution to a practical mechanism for vehicle control. Potential engineering difficulties include increased mechanical complexity for bi-directional control, control lag associated with airflow throttling and, probably most significantly, the back pressure impact of intermittent bleed air demand on a small gas turbine engine compressor.

Those considerations led eventually to the bi-directional flow control actuator solution described in the following paragraphs.

5.2 Circulation control actuator concept

An alternative CC mechanisation developed at Cranfield comprises an actuator device capable of proportional bi-directional control; the general arrangement of the flow control actuator concept is shown in Fig. 5-1. The small wedge shaped plenum chamber comprising the body of the device is envisaged as an interchangeable replacement for a conventional flap surface as shown.

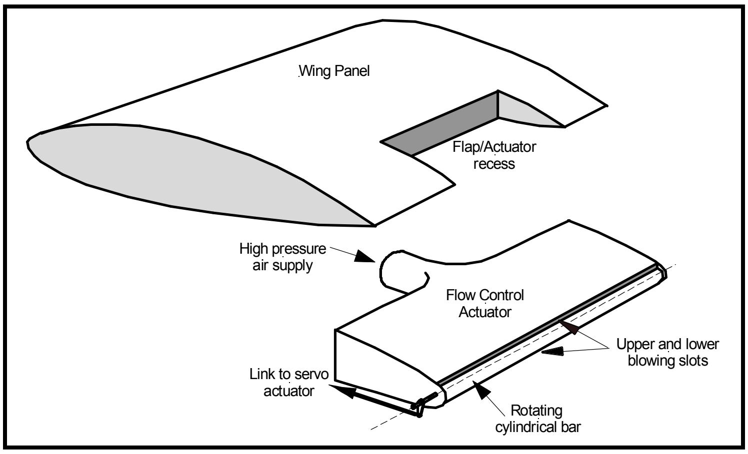

Fig. 5-1. General arrangement of a flow control actuator installation

The trailing edge of the actuator incorporates an upper and lower slot separated by a span-wise cylindrical bar which acts as the Coanda surface. A cross section of the trailing edge of the device is shown in Fig.5-2b. The cylindrical bar is free to rotate eccentrically about its longitudinal (span-wise) axis, which is offset from its symmetrical axis, such that the upper and lower slots can be adjusted from fully open to fully close in an asymmetric manner. Thus by rotating the bar proportional bi-directional modulation of the lift force can be effected.

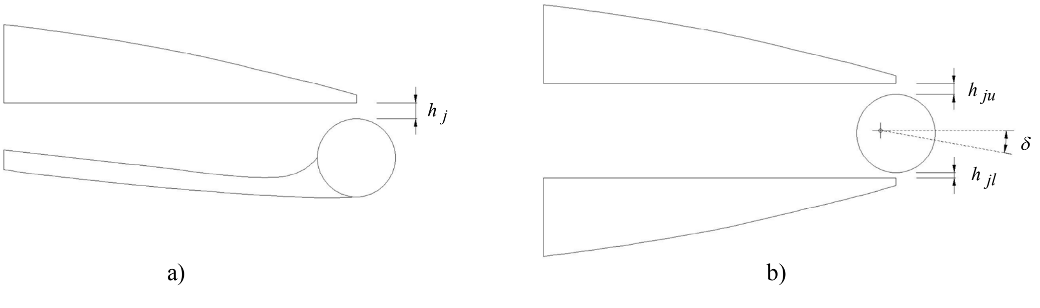

a) b)

Fig. 5-2. Section view of a wing trailing edge arrangement for a a) conventional fixed slot and b) bi-directional circulation control actuator

The flow control actuator avoids some of the problems of the fixed slot arrangement described above. In particular, a continuous uninterrupted air supply is required, and since the total slot area remains constant, there is no back pressure effect on the air supply source during normal operation. Since the device has only one moving part with minimal inertia a high operational bandwidth is possible, and since there is no air flow throttling control lag is insignificant. However, since the trailing edge slots and Coanda surface geometry are critical to the performance of the device, precision engineering accuracy is required if an appropriate level of control resolution is to be achieved.

5.3 Experimental setup and test techniques

In order to test the concept, a prototype flow control actuator was designed and manufactured at a scale compatible with the *Demon* air vehicle. To facilitate wind tunnel testing the device was inserted into the trailing edge of a rectangular wing panel in place of a conventional interchangeable flap surface. The test wing panel was manufactured with a symmetric RAE 104 aerofoil section, which is the same as that used for the section of the *Demon* wing. The key geometric parameters for the test wing, flow control actuator and interchangeable flap are given in Table 5-1.

		Test wing with flap	**Test wing with CC actuator**
Span (m)	b	0.6	0.6
Chord (m)	c	0.3	0.3
Thickness /chord ratio	t/c	0.15	0.15
Area (m^2)	S	0.180	0.177
TE thickness (mm)		1.0	5.0 (at actuator te)
Flap span (mm)		150	150
Flap chord (mm)		66	58

Table 5-1. Test wing and actuator geometry

An interchangeable conventional control surface with $0.25b$ and $0.22c$ was implemented to act as the baseline reference. It was interchangeable with a circulation control (CC) actuator of equal span-wise extent, but reduced chord length due to the inset circular trailing edge. The wing area was decreased by about 2% with the CC actuator installed. The flow control actuator consists of a simple wedge shaped plenum chamber, the upper and lower trailing edge surfaces of which have adjustable knife edges to set the slot heights above and below the cylindrical Coanda surface. High pressure air is supplied to the plenum chamber by means of an internal pipe connection, and the Coanda surface is actuated by means of a small model control servo driven from a standard PC. Dimensioned drawings may be found in appendix D.

Coanda surface radius (mm)	*r*	2.5
Nominal slot height range (mm)	*h*	0.2-0.5
-	*r/c*	0.8 %
-	*h/c*	0.07 - 0.17 %
-	*h/r*	8 - 20 %

Table 5-2. Trailing edge slot geometry

The trailing edge slot geometry was chosen as described by the parameters listed in Table 5-2.

Wind tunnel tests were performed in an open jet subsonic wind tunnel at Cranfield University and a three component floor balance was used to measure the aerodynamic forces acting upon the wing. The free stream velocity was set at 30 m/s, corresponding to a free-stream Reynolds number of approximately 6.7×10^5.

The experimental test rig comprising the wing mounted on the balance and placed in the working section is shown in Fig. 5-3a. The trailing edge of the flow control actuator is shown in Fig. 5-3b.

A summary of the tests performed is listed below:

i) Verification of wing performance and evaluation of conventional control surface performance.

ii) Jet height (*h/r*) optimization study of a single slot trailing edge circulation control actuator.

iii) Evaluation of the control forces generated by a dual slot CC actuator.

a) Rectangular wing installed on 3 component balance.

b) TE detail of bi-directional actuator.

Fig. 5-3. Photographs of the experimental setup

5.3.1 Blowing parameters and experimental methods

Aerodynamic performance of a circulation control device is characterized as a function of slot flow momentum coefficient, C_μ, which is the momentum flux exiting from the slot normalized by the free stream dynamic pressure and a reference area – usually the area of the wing with full span trailing edge slot. It is important to define the blowing momentum coefficient as,

$$C_\mu = \frac{\dot{m}_j V_j}{Q_{dyn} S} = 2 \frac{h_j}{c} \frac{b_j}{b} \frac{M^2{}_j}{M^2{}_\infty} \tag{5-1}$$

where the definition only holds for an isentropic duct and when the jet exit static temperature and density would be identical to the ambient values.

The local Mach number at the jet exit slot is calculated from the isentropic equation expanding the plenum stagnation pressure to free stream static pressure as,

$$M_j = \sqrt{\frac{2}{\gamma - 1}\left(\left(\frac{P_c}{P_\infty}\right)^{\frac{\gamma-1}{\gamma}} - 1\right)} \tag{5-2}$$

Where the subscript 'c' implies total conditions in the blowing plenum duct, the subscript '∞' refers to free-stream conditions.

The actual ambient pressure at the slot exit is not exactly free static pressure and it is difficult to assess accurately. Thus free stream static pressure is assumed as a matter of convenience and convention.

The pressure within the plenum was monitored using a pressure transducer and data were transferred to the computer via an A-to-D card. The blowing momentum coefficient was then obtained from Eqs. (5-1) and (5-2), using the nominal slot height set under no flow conditions. This is assumed as a matter of convenience, as the actual slot height (+/-0.05mm) may vary along the span under loaded conditions.

5.4 Experimental results and analysis

5.4.1 Characteristic of the baseline wing

The chosen aerofoil section is of a classical symmetrical profile. The lift increases linearly with angle of attack up to about α=12° and stall occurs beyond α=14° (Fig. 5-4). The lift curve slope was found to be $C_{L\alpha}$=2.23 rad^{-1} at the relatively low free stream Reynolds number of Re=6.7x10^{5} and aspect ratio of AR=2, which is quite in agreement to that predicted by Helmbold-Diederich formula for low aspect ratio wing and reported by Laiton, (1989). A direct comparison with the wing-CC actuator combination is made in Fig. 5-4. It shows that a negligible decrease of the overall wing lift curve slope is the result. This effect is attributed to the increased trailing edge thickness from 0.003c to 0.017c over a span wise extent of 0.25b. The resulting decrease in wing area has been taken into account for the evaluation of C_L. Experimental data for a RAE 104 profile at the same Re are compared in Table 5-3.

The clean wing drag is shown in Fig. 5-5. Boundary layer transition was artificially introduced at 0.02c using a roughness with an average grain size of about 0.1mm and chord wise extent of 0.07c (top and bottom) The un-blown drag coefficient C_{D_o} is 0.032 for the CC wing at zero lift, which is about 12 % more than that of the conventional wing with the usual sharp trailing edge. The issue of a blunt TE for typical CC configurations at cruise will be addressed in the following section, where the advantage of having a dual blowing capability will be evident.

	Airfoil	**Wing** (AR=2)		**CC Wing** (AR=2.025)
	Experimental (Spence & Beasley, 1958)	Measured	Estimated (Helmbold)	Measured
$C_{L\alpha}$ (rad^{-1})	5.883	2.23	2.43	2.22

Table 5-3. Baseline lift curve slope

5.4.2 Single slot CC actuator

The blowing coefficient C_μ is the most critical parameter controlling the effectiveness of a CC actuator, an increase in C_μ resulting in an increase in lift. For fixed external conditions, i.e. a constant denominator in Eq. (5-1), a large C_μ may be obtained by either a high mass flow and relatively low exit velocity or a high exit velocity with a relatively low mass flow. These traits may be explored by varying the jet exit area via the jet slot height, which herein is referenced to the Coanda surface radius, i.e. *h/r*.

Wood (1985) reported that smaller slot heights result in a larger return in lift at constant C_μ which implies that a high jet velocity/momentum ratio are required for an effective actuator. To confirm this, tests were performed at constant free-stream Mach number but varying slot height (*h/r*) and blowing coefficient (C_μ) at a fixed angle of attack. The results obtained at a fixed angle of attack (α=0^o) are presented in Fig. 5-6. For a fixed Coanda surface radius of *r/c*=1%, a *h/r* of 0.08% performed better than a *h/r* of 0.2 %. In the initial linear portion of the curve the lift augmentation (dC_L/dC_μ) for the smallest slot was 44 compared to the 25 augmentation for the larger slot. A small *h/r* gave rise to a non-linear relationship with a notable change in the lift augmentation. A dead-band at low C_μ was discovered particularly remarkable for the smallest slot heights.

Fig. 5-7 shows the same data as Fig. 5-6, but replaces C_μ with velocity ratio along the abscissa of the graph. It serves to emphasize that an equivalent C_μ is attainable with significantly different pressure ratios and therefore jet exit Mach numbers. The circulation control airfoil poses an optimization problem dependent on whether the blowing air supply is mass flow rate or pressure ratio limited.

A shift in the lift augmentation efficiency occurs at a velocity ratio of around 3 and corresponds to the transition from a linear to a square root like response in Fig. 5-6. This may be attributed to the transition from boundary layer control to super-circulation, as it has been previously observed by Englar, (2000). The super-circulation effect predominates when the momentum is large and the deflected extending jet acts in a manner similar to that of a jet flap. In fact the lift increment in the non linear region was found to be almost the same for different slot height and equal to,

$$\frac{\partial C_L}{\partial C_\mu} = \frac{1.2}{\sqrt{C_\mu}}$$

The measured value of C_D requires an additional correction term to develop a lift/drag ratio that can be compared to that of conventional airfoils. Some account should be taken of the power necessary to produce the kinetic energy of the jet. An incremental drag coefficient associated with the kinetic energy of the jet is (Wood, 1985):

$$\Delta C_D = \frac{1}{V_\infty} \frac{d(KE)}{dt} = C_\mu \frac{V_j}{2V_\infty} \tag{5-3}$$

With this correction the equivalent drag coefficient is:

$$C_{D_e} = C_D + C_\mu \frac{V_j}{2V_\infty} \tag{5-4}$$

It should be noted that the kinetic energy or power that is added to the equivalent drag, dominates the equation and leads to drag values that hide the thrust generated by a typical CC airfoil.

The efficiency can be represented by the lift to equivalent drag ratio, as shown in Fig. 5-8. Comparison of two slot configurations indicates a greater efficiency of the larger slot. This is a result of the drag benefits of the larger slot. The peak efficiency occurs in the vicinity of the transition region (refer to Fig. 5-7), as has been already observed in Jones (2005).

Another performance parameter of interest is the lift-increment-per-power ratio, shown in Fig. 5-9 . The total fluidic power has been introduced by Jones, (2005), and it can be expressed as the power required to supply the jet velocity head plus the power lost at the intake as the fluid power is drawn into the large reservoir,

$$P_f = \frac{1}{2}\rho V_j^{\,2}\frac{\dot{m}}{\rho} + \dot{m}V^2_{\infty} \tag{5-5}$$

And non –dimensionally,

$$C_{P_f} = \frac{P_f}{q_\infty V_\infty S} = C_\mu \frac{V_j}{2V_\infty} + C_\mu \frac{V_\infty}{2V_j} \tag{5-6}$$

The comparisons are made at ΔC_L=0.1 and ΔC_L=0.15 which is consistent with the two transition regions highlighted before. The smaller slot develops more lift for a given power setting but as the blowing is increasing into the super-circulation region, the influence of the slot height on lift-to-power augmentation decreases.

Table 5-4 provides a comparison of the CC tested with other CC airfoils. The RAE104 performs as CC un-cambered elliptical airfoil of 15% thickness. The GAAC effectiveness is notably higher due to the camber and the higher Coanda radius.

	Lift Augmentation	$\Delta C_L/C_{pf}$ (ΔC_L=0.5)
RAE104 *(h/r=0.08)*	44.5	27
GACC *(h/r=0.07)*(Jones,2005)	60.3	44.3
CC elliptical(Englar,1978)	30	26.3
Jet flap(Spence,1958)	7	7.48

Table 5-4. Comparison of powered system

5.4.3 Performance of a dual slot circulation

The dual slot flow control actuator was set up to operate at constant plenum pressure corresponding to a constant blowing coefficient. In analogy with conventional control surfaces, the Coanda cylinder deflection δ is defined as positive when it results in a positive lift increment. At the datum control angle $\delta=0^{o}$ the upper and lower slots are of equal height. The Coanda cylinder rotation is physically limited by the engineering design of the actuator, being a function of the eccentricity of the hinge and *h/r* ratio. At the largest angular deflection δ_{max}.the lower slot was closed and the upper slot was fully open with actual slot height *h/r*.

The proof of concept for the dual slot actuator is given in Fig. 5-10 for *h/r*=0.2 and C_μ= 0.02, i.e.V_j/V_∞ = 5. The lift coefficient is a linear function of the cylinder deflection with a lift increment for $\delta_{\max}$ = ±15° of ΔC_L=±0.15. The effectiveness of actuation, in terms of $dC_L/d\delta$ is almost constant with angle of attack.

To evaluate the control effectiveness of the flow control actuator, its performance was compared with that of an equivalent span flap. Clearly, the comparison is of limited value since the flap performance is a function of its chord ratio c_f/c and span size, whereas the actuator performance is a function of C_μ and *h/r*. However, since the input command to both controls is an angular displacement derived from a standard servo-actuator, it is interesting to compare the effectiveness of two similar sized installations. The comparison is also shown in Fig. 5-10 where the incremental lift is plotted as a function of flap deflection angle η and actuator control angle δ. In spite of the limited scope of the experiment it is clear that both characteristics are essentially linear and have similar levels of performance. The CC actuator was found to have a superior effectiveness for C_μ=0.02:

$$\left[\frac{dC_L}{d\delta}\right]_{C_\mu=0.02} = 0.57 rad^{-1} \qquad \frac{dC_L}{d\eta} = 0.3 rad^{-1}$$

The actuator effectiveness is a function of C_μ and *h/r*. Fig. 5-11 and Fig. 5-12 explore this dependency. Clearly for constant TE geometry a higher jet exit velocity gives rise to an increased effectiveness, whereas the smaller slot exhibits a larger effectiveness with a limited cylinder rotation of $\delta_{\max}$=±7° . An inherent limitation of the mechanical arrangement to position the slot knife edges caused small misalignments which were large enough to cause significant leakage through the closed slot and a loss in maximum lift increment in comparison with the single slot configuration where the lower slot was sealed to avoid leakage.

Pitching moment is affected by the lift and centre of pressure variations. By definition the aerodynamic centre is the chord-wise location about which the pitching moment is not influenced by changes in lift. The location of the pressure centre on the reference chord in terms of aerodynamic coefficients is given by Eq. (5-7).

$$h_{cp} \approx h_{c/4} - \frac{C_{M_{c/4}}}{C_L} \tag{5-7}$$

From a theoretical point of view circulation control is equivalent to a conventional wing having a vanishingly small flap at the trailing edge. In the case of a flap chord approaching zero length, the centre of lift due to flap deflection is for a short span wing of AR= 2 at 69%*c* (Campbell et al., 1956). The experimental pitching moment for the dual slot circulation control actuator as resolved around the quarter chord is presented in Fig. 5-13. The dual slot flow control actuator shows a more negative pitching moment than the mechanical flap which is assumed to be due to the extreme aft pressure peak due to the jet slot efflux. The aerodynamic centre (*ac)* for the lift due to blowing is at 70%*c* for the larger slot and at 63 %c for the smaller slot. The *ac* for lift due to flap deflection is at 45%*c*.

5.4.4 Drag with dual slot system

The dual slot CC wing can develop a range of lift coefficients at any given angle of attack. By deflecting the cylinder up and down the lift can be incremented or decremented from the unblown value, including passing though zero lift. Thus, there is a wide drag polar diagram for each angle of attack. In Fig. 5-14 the drag increment from the unblown value is plotted, corresponding to $\alpha=0^o$. At zero angle of attack the drag increment is the induced component associated with the development of lift due to dual blowing only. The drag increment due to flap deflection is plotted in the same graph.
The unblown drag due to flap deflection equals that with the same lift obtained by blowing. The drag data collapses to one single parabolic polar diagram. Therefore, the induced drag for lift developed by CC is essentially the same as that from the conventional flap.

The most reliable measurement technique for experimentally determining the drag of a blown airfoil is the momentum-loss method that employs a wake pressure rake. The profile drag can be determined by integrating the wake profile measured 1 chord downstream of the trailing edge (Pope, 1954). For blown airfoils, it is important to note that the measured profile drag from a wake rake must be corrected by subtracting the momentum that was added by the CC system. The total horizontal forces on a 2D model do indeed exceed that indicated by conventional wake rake calculations by the quantity $\dot{m}V_\infty$ (Wood & Nielsen, 1985). Considering a frictionless hypothetical case where the jet is exhausted at a total head equal to free stream total head easily confirms this principle. Here, the wake will indicate zero drag, but the model will experience a trust of $\dot{m}V_\infty$. The net forces are equal to:

$$C_D = C_{D\,RAKE} - C_\mu \frac{V_\infty}{V_j} \tag{5-8}$$

Where,

$$C_{D\,RAKE} = \frac{2}{c}\int\left(\sqrt{\frac{q}{q_\infty}} - \frac{q}{q_\infty}\right)dy \tag{5-9}$$

To address the issue of a blunt trailing edge for typical CC configurations at cruise, the dual blowing capability, i.e. upper and/or lower blowing on the Coanda surface enables the operator to adjust thrust for a given lift during cruise. Wake surveys were made to determine the ability of dual equal slot flow (no lift increment) to eliminate the wake momentum deficit that results from drag. Fig. 5-15 illustrates the wake filling result, for mid-span at a location of 1 chord length from the trailing edge. The wake profile has been favourably influenced by the momentum flux from the two slots. With blowing off a nice pressure distribution exists. As blowing is increased the pressure variation becomes smaller (C_μ=0.008) until it actually reverse and become a thrust (C_μ=0.02). A velocity ratio of 3 correspondent to C_μ=0.003 was sufficient to compensate for the excess drag due to a blunt trailing edge (see Fig. 5-16).

The wake profile shown in Fig. 5-17 corresponds to the fixed blowing of C_μ=0.02 and total slot height of h=0.5 mm. As the cylinder moves from the neutral position to a positive and negative deflection respectively the peak shifts down and up, indicating that the upper and lower jet mix efficiently.

5.5 Mathematical model

The upper surface exit slot geometry of the flow control actuator is shown in Fig. 5-18, the lower slot being geometrically similar is not shown. The control angle δ defines the Coanda surface movement about the centre of rotation and is positive as indicated – a positive control angle results in a positive lift increment. The upper and lower slot height is h_0 when the control angle is zero. The offset of the centre of rotation from the axis of the Coanda cylindrical surface is denoted λr, where r is surface radius. Thus, referring to the geometry in Fig. 5-18, it is easily shown that the upper and lower slot height varies as a function of control angle as follows, (derivation is reported in Appendix D). For the upper slot,

$$h_{j_u} = h_0 + r + r\left(\lambda \sin\delta - \sqrt{1-\lambda^2(1-\cos\delta)^2}\right) \tag{5-10}$$

And for the lower slot,

$$h_{j_l} = h_0 + r - r\left(\lambda \sin\delta + \sqrt{1-\lambda^2(1-\cos\delta)^2}\right) \tag{5-11}$$

Now the lift developed by blowing high pressure air through a slot is governed by the blowing momentum coefficient C_μ, which for a part span slot is given by,

$$C_\mu = \frac{\dot{m}_j V_j}{Q_\infty S} = \frac{\rho h_j b_j V_j^2}{\frac{1}{2}\rho V_\infty^2 S} = \frac{2h_j b_j}{cb}\left(\frac{V_j}{V_\infty}\right)^2 \tag{5-12}$$

Thus, the upper and lower slot blowing momentum coefficient variation with control angle is given by substituting Eqs (5-10) and (5-11) into Eq. (5-12),

$$\begin{aligned} C_{\mu_u} &= \frac{2rb_j}{\bar{\bar{c}}b}\left(\frac{V_j}{V_\infty}\right)^2\left(\frac{h_0}{r}+1+\left(\lambda \sin\delta - \sqrt{1-\lambda^2(1-\cos\delta)^2}\right)\right) \\ C_{\mu_l} &= \frac{2rb_j}{\bar{\bar{c}}b}\left(\frac{V_j}{V_\infty}\right)^2\left(\frac{h_0}{r}+1-\left(\lambda \sin\delta + \sqrt{1-\lambda^2(1-\cos\delta)^2}\right)\right) \end{aligned} \tag{5-13}$$

It follows directly that the upper and lower slot incremental blowing momentum coefficients due to control angle are given by,

$$\Delta C_{\mu_u} = \frac{2rb_j}{\bar{\bar{c}}b}\left(\frac{V_j}{V_\infty}\right)^2\left(\lambda\sin\delta - \sqrt{1-\lambda^2(1-\cos\delta)^2}\right)$$
$$\Delta C_{\mu_l} = -\frac{2rb_j}{\bar{\bar{c}}b}\left(\frac{V_j}{V_\infty}\right)^2\left(\lambda\sin\delta + \sqrt{1-\lambda^2(1-\cos\delta)^2}\right) \qquad (5\text{-}14)$$

Lift augmentation due to blowing for a velocity ratio $V_j/V_{oo} < 3$ was found to be a linear function of the blowing momentum coefficient for a given slot height and the effectiveness is defined,

$$K_\mu = \frac{\partial C_L}{\partial C_\mu} \qquad (5\text{-}15)$$

Now the lift increment due to upper slot blowing is positive and the lift increment due to lower slot blowing is negative, thus the total lift increment due to the combined effect of both slots is given by,

$$\Delta C_L = K_\mu\left(\Delta C_{\mu_u} - \Delta C_{\mu_l}\right) \qquad (5\text{-}16)$$

The lift increment due to control angle follows directly by substituting equations (5-14) into equation (5-16),

$$\Delta C_L = K_\mu \frac{4rb_j}{\bar{\bar{c}}b}\left(\frac{V_j}{V_\infty}\right)^2 \lambda\sin\delta \cong 4K_\mu\left(\frac{\lambda rb_j}{S}\right)\left(\frac{V_j}{V_\infty}\right)^2\delta \qquad (5\text{-}17)$$

since typically the control angle is small and $\delta<\pm20°$.

Experimental data from Fig. 5-11 have been fitted with the Eq. (5-17), where K_μ is taken as the lift augmentation of an equivalent single slot operating at the same conditions, and results are shown in Fig. 5-19. The curve fit,

$$\Delta C_L = 4\cdot25\left(\frac{1\cdot150}{90\cdot10^3}\right)\left(\frac{V_j}{V_\infty}\right)^2\delta \qquad (5\text{-}18)$$

is in excellent agreement with all the data.

Lift augmentation due to blowing for a velocity ratio $V_j/V_{oo} > 3$ was found to be proportional to $\sqrt{C_\mu}$. Expressing C_μ as in Eq. (5-12), it follows,

$$\Delta C_L = K_v\sqrt{C_\mu} = \sqrt{2}K_v \frac{h_j}{c}^{0.5}\sqrt{\frac{b_j}{b}\frac{V_j}{V_\infty}} \tag{5-19}$$

The experimental data can be fit with Eq. (5-19), as shown in Fig. 5-7.
Taking the first term of the Taylor expansion of Eq. (5-19) around
d the nominal slot height h_0/c, the lift augmentation in Eq. (5-19) becomes,

$$\Delta C_L\left(\frac{h_j}{c}\right) - \Delta C_L\left(\frac{h_0}{c}\right) \approx \frac{\sqrt{2}}{2}K_v\sqrt{\frac{b_j}{b}\frac{V_j}{V_\infty}}\left(\frac{h_{j0}}{c}\right)^{-0.5}\left(\frac{h_j}{c} - \frac{h_0}{c}\right) \tag{5-20}$$

It follows that the lift augmentation of the upper and lower slot respectively is given by,

$$\begin{aligned}
\Delta C_{Lu}\left(\frac{h_{ju}}{c}\right) - \Delta C_{Lu}\left(\frac{h_0}{c}\right) &\approx \frac{\sqrt{2}}{2}K_v\sqrt{\frac{b_j}{b}\frac{V_j}{V_\infty}}\left(\frac{h_{j0}}{c}\right)^{-0.5}\left(\frac{h_{ju}}{c} - \frac{h_0}{c}\right) \\
\Delta C_{Ll}\left(\frac{h_{jl}}{c}\right) - \Delta C_{Lu}\left(\frac{h_0}{c}\right) &\approx \frac{\sqrt{2}}{2}K_v\sqrt{\frac{b_j}{b}\frac{V_j}{V_\infty}}\left(\frac{h_{j0}}{c}\right)^{-0.5}\left(\frac{h_{jl}}{c} - \frac{h_0}{c}\right)
\end{aligned} \tag{5-21}$$

Thus the total lift increment due to the combined effect of both slots is given by,

$$\Delta C_L = \left(\Delta C_{L_u} - \Delta C_{L_l}\right) \tag{5-22}$$

The lift increment due to control angle follows directly by substituting Eqs. (5-21) into Eq. (5-22),

$$\Delta C_L \approx \frac{\sqrt{2}}{2}K_v\sqrt{\frac{b_j}{b}\frac{V_j}{V_\infty}}\left(\frac{h_0}{c}\right)^{-0.5}\left(\frac{h_{ju}}{c} - \frac{h_{jl}}{c}\right) \approx \frac{\sqrt{2}}{2}K_v\sqrt{\frac{b_j}{b}\frac{V_j}{V_\infty}}\left(\frac{h_0}{c}\right)^{-0.5}\frac{\lambda r}{c}\delta \tag{5-23}$$

since typically the control angle is small and $\delta < \pm 20°$.
Experimental data from Fig. 5-11 and Fig. 5-12 have been fitted with the Eq. (5-23), with K_v=1.2. Results are shown in Fig. 5-19.

5.6 Simulation of steady circulation control dual actuator

This section reports a comparison of experimental measurements and preliminary CFD predictions for the dual slot actuator. An initial 2D Computational Fluid Dynamics (CFD) study was performed at BAE Systems UK, on a wing section of the experimental configuration and preliminary results are presented in this section. The purpose of the study was to assist the experiments, ascertain the capability of CFD to predict the dual slot actuator behaviour and confirm the trends found experimentally. The definition of the TE Coanda geometry used in the CFD study is given in Table 5-5.

r (mm)	5.0
r/c	0.8 %
h (mm)	1

Table 5-5. Definition of Coanda geometry - CFD

Clearly, the comparison of experimental measurements and CFD predictions is of limited value for the following reasons:

1- CFD results are valid for a wing section, whereas experimental results refer to a low aspect ratio wing with a partial span CC blowing.

2- CFD study adopts the same Coanda surface geometry, being r/c ratio the same as the experimental one. However, the height of the slot adopted in the CFD study is double the experimental one.

However, once confirmed the validity of CFD predictions, it is interesting to carry out some qualitative evaluation from the CFD results (pressure distributions, velocity contours, etc.) which are not, otherwise, available from the wind tunnel experiments.

To facilitate comparison with experimental results, CFD results have been corrected using finite aspect ratio wing theory and partial span corrections detailed in appendix D.

Fig. 5-20 shows the 2D baseline lift coefficient of the airfoil. The simulated 2D lift curve slope compares well with the one obtained experimentally from Spence and Beasley, (1958). The lift curve slope obtained from 2D calculations has been used to calculate the 3D lift curve slope for a finite aspect ratio wing, using finite aspect ratio wing theory corrections, reported in appendix D. This corrected lift curve slope was used to predict the lift coefficient up to an angle of attack of 10^{o}. Experimental data showed that lift varies linearly in this region. It can be seen from Fig. 5-20 that the agreement between estimated and measured values of lift is fairly good.

Fig. 5-21 shows the CFD predicted variation of 2D augmented lift for single upper slot blowing, at a fixed angle of attack of zero degree. Data have been computed for two different values of pressure supply to the CC actuator plenum, respectively p_c=0.25psi and p_c=0.50psi.

The CFD lift increment due to TE blowing was corrected for partial span to take into account the limited span-wise extent of the TE device and facilitate comparison with experimental results. Clearly the computed lift augmentation is lower than the experimental one, due to a higher slot height adopted in the CFD study (as it was experimentally observed, a higher slot results in a lower return in lift for a constant blowing momentum).

Fig. 5-22 shows the computed change in lift with dual slot CC actuator corresponding to a constant pressure supply of 0.25psi, with cylinder deflection limited at $\delta = \pm 30^{\circ}$. The lift varies linearly with cylinder deflection angle as it was experimentally observed. It can be noticed, also, that the effectiveness is constant at all the angle of attack simulated and this result is in agreement with experimental evidence.

Drag obtained from the 2D computation was assumed to be skin friction drag only and therefore the induced drag was added:

$$C_D = C_{Di} + \left\lfloor C_{Df} \right\rfloor_{2D} \tag{5-24}$$

The lift distribution was not measured directly and the Oswald efficiency was calculated via:

$$e = \frac{1}{\left(\frac{dC_D}{dC_L^2}\right)\pi AR} = \frac{1}{K_1 \pi AR} \tag{5-25}$$

For a wing of low aspect ratio e is found to be close to 1, and this value was used in the computation.

The change in drag due to differential trailing edge blowing derived from CFD is superimposed on the experimental drag increment in Fig. 5-23. It can be seen that the agreement between estimated and measures values of lift is fairly good.

The computed speed contours of the jet are illustrated in Fig. 5-24 for a solution with 0.25psi total pressure jet, corresponding to a maximum velocity jet at the exit of 50m/s, with the configuration in 25m/s free stream flow. It can be seen that the Coanda effect is correctly predicted with the jet being deflected. The simulation predicts the separation on the lower surface of the cylinder.

The simulated static pressure distribution on the wing section is shown in Fig. 5-25 and Fig. 5-26. This gives some insight into the airfoil loading produced by blowing. The characteristic saddle back shape is typical of CC airfoils. It can be seen that the increase in circulation resulting from blowing produces an increased loading over the complete section. In particular, significant suction can be seen at both the leading and trailing edge. At positive incidence the leading peak is more pronounced, while at zero angle of attack the rear adverse gradient is further aft and of larger magnitude. The strong asymmetry in the pressure distribution results in the rearward movement in centre of pressure and explains the quite large negative pitching moment observed experimentally.

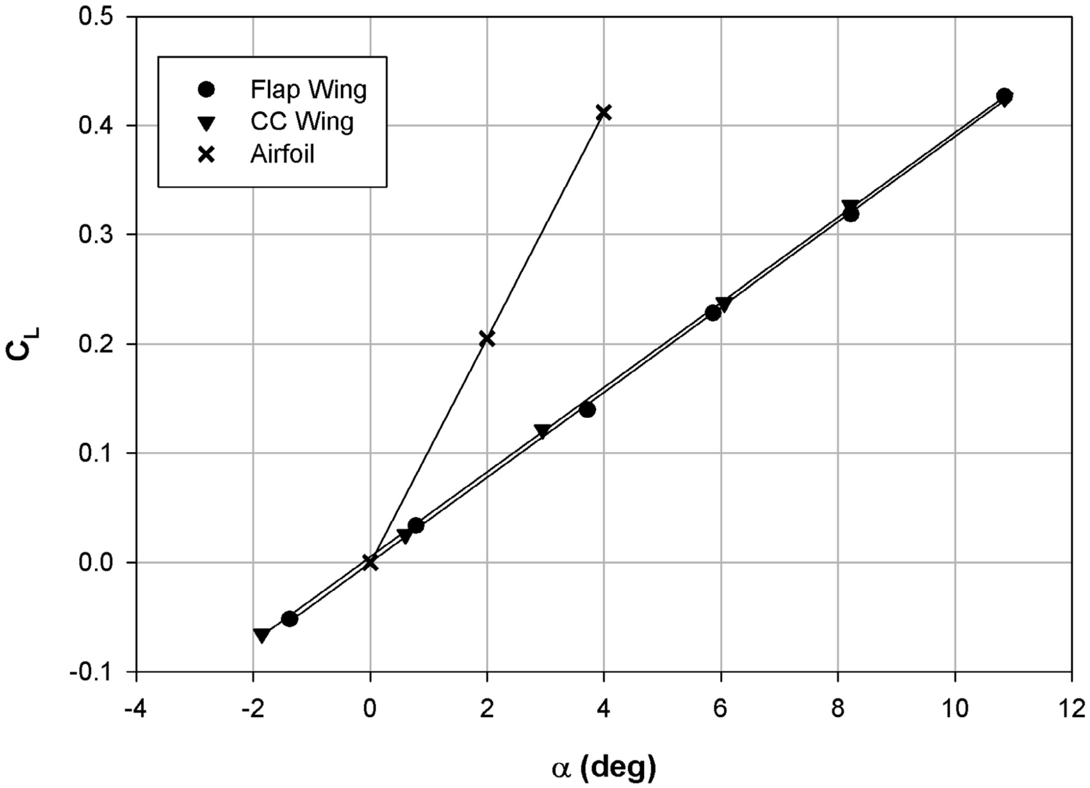

Fig. 5-4. Comparison of the baseline lift coefficient with no blowing

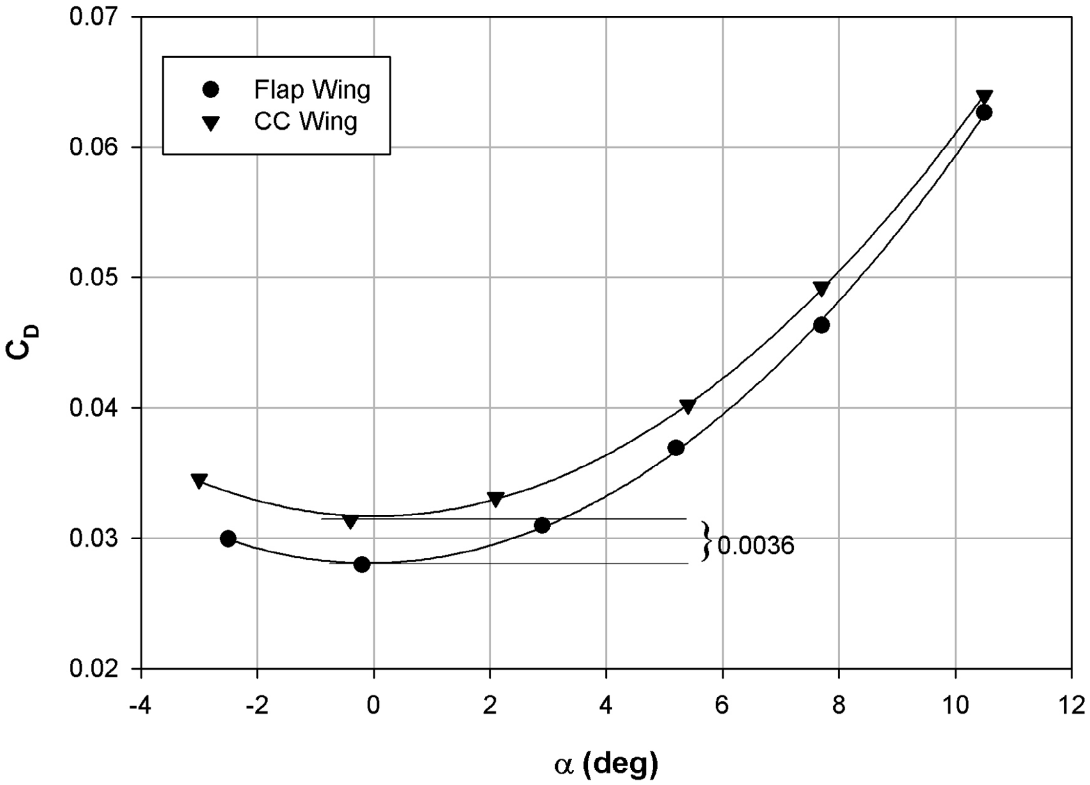

Fig. 5-5. Comparison of the baseline drag coefficient with no blowing

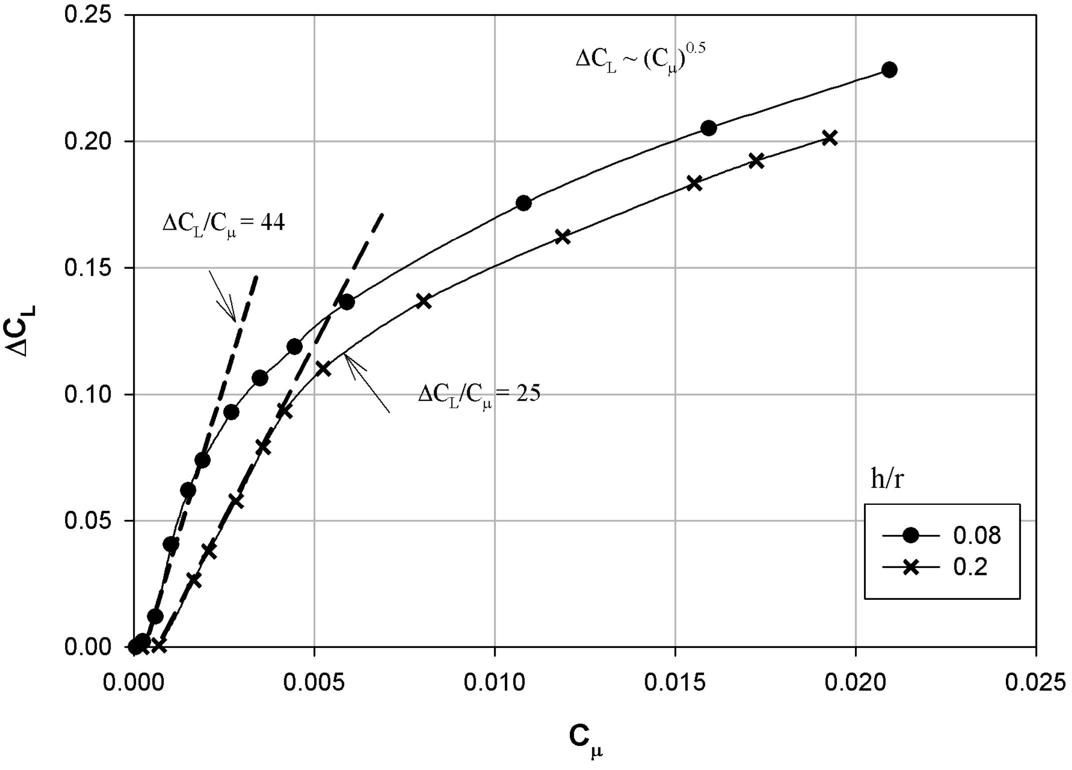

Fig. 5-6. Effect of slot height on lift generation – $\alpha = 0^{o}$

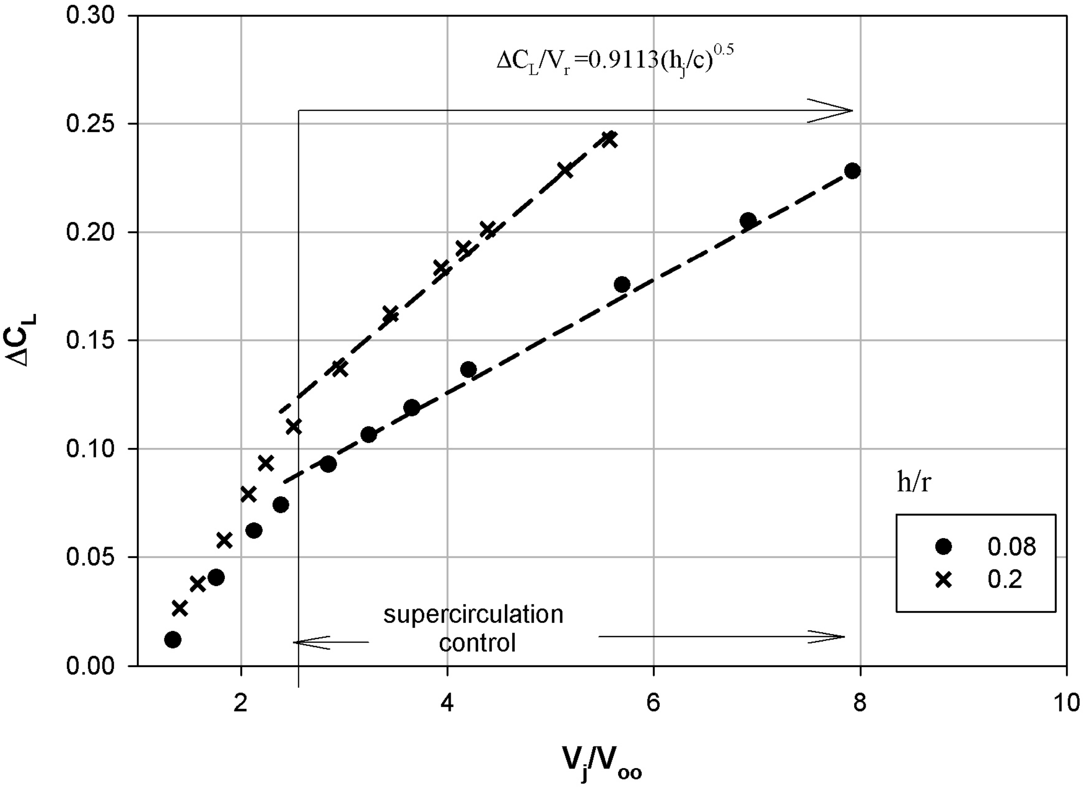

Fig. 5-7. Effect of jet velocity on lift generation – $\alpha = 0^{o}$

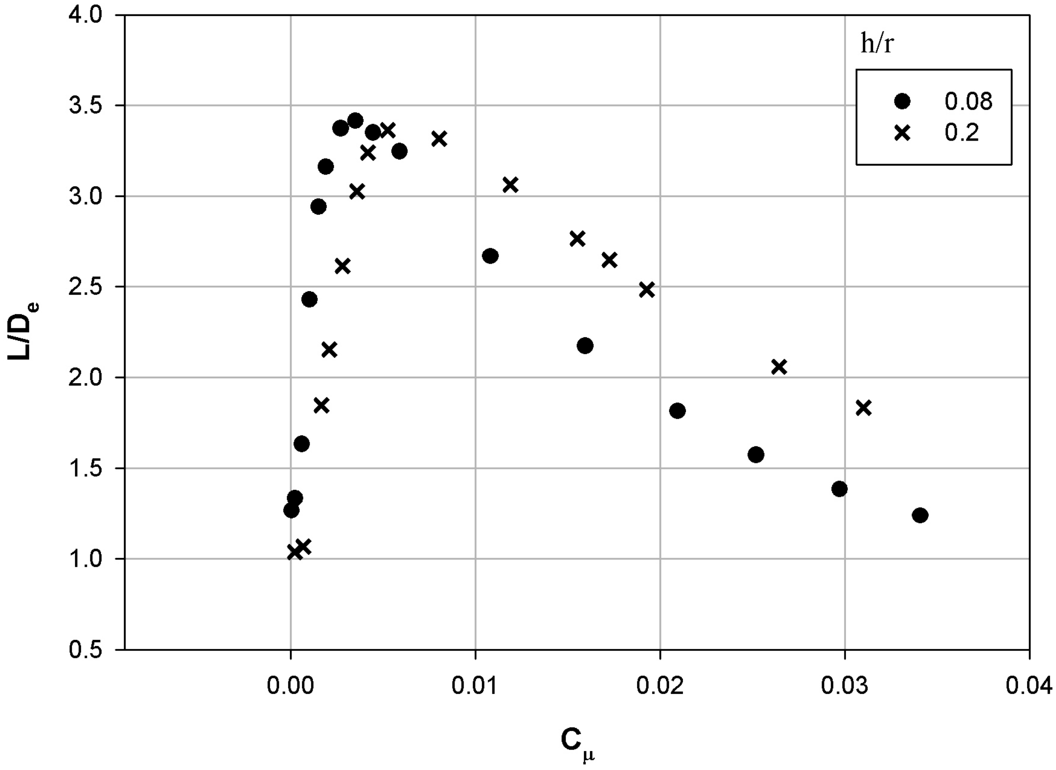

Fig. 5-8. Efficiency comparison of two different slot heights

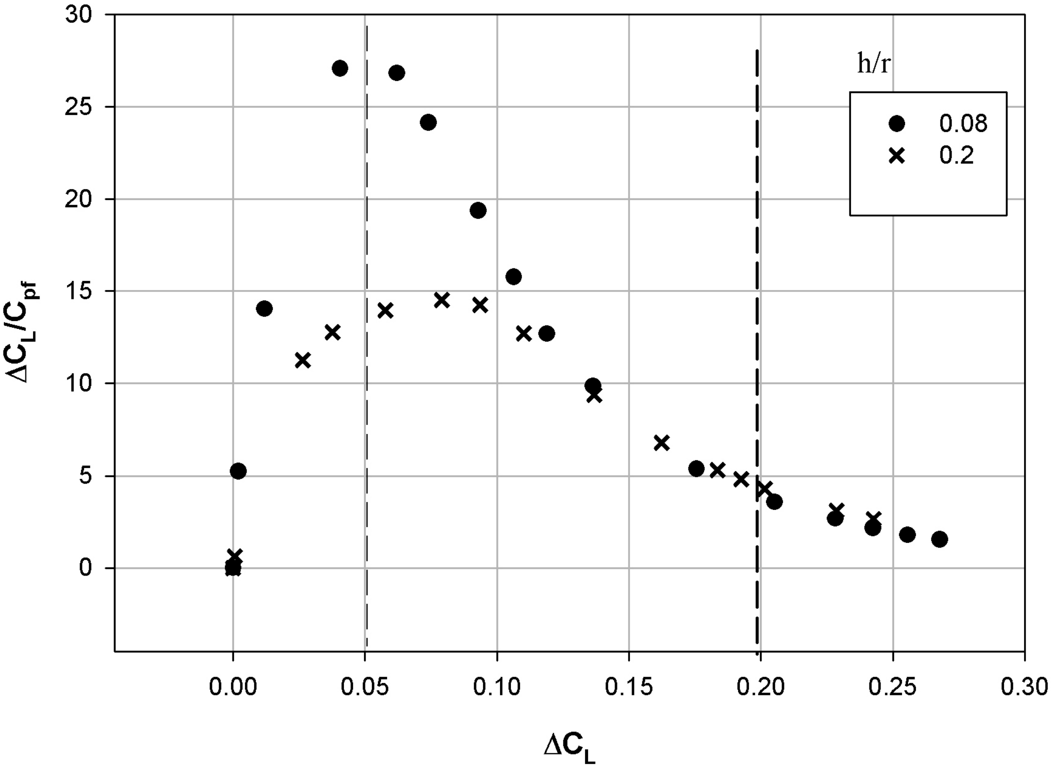

Fig. 5-9. Lift per fluidic power comparison for two different slot heights – $\alpha = 0^{\mathrm{o}}$

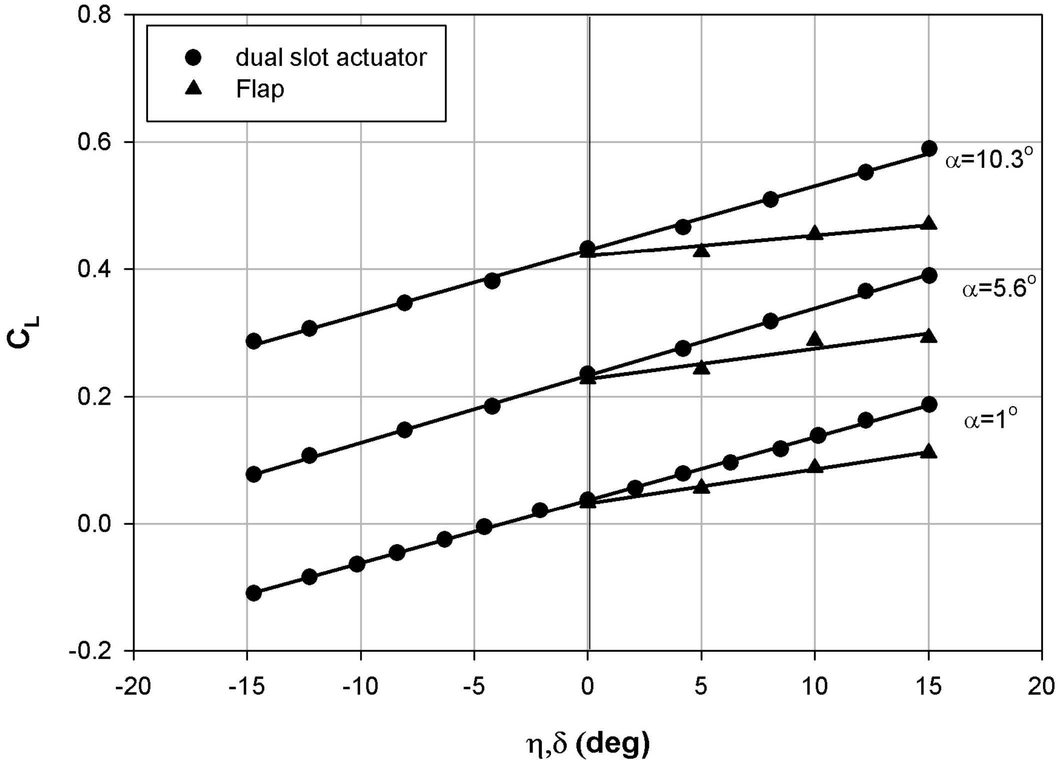

Fig. 5-10. Comparison of flap high lift characteristic with dual slot CC actuator – h/r=0.2, C_μ=0.02

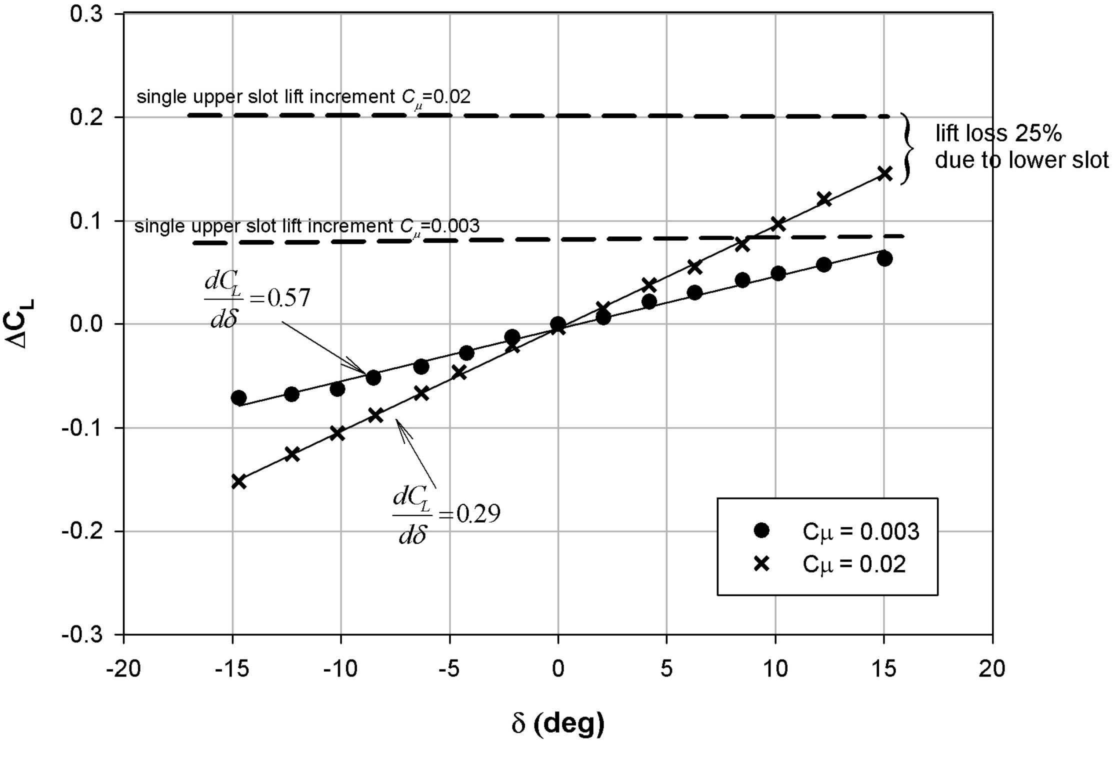

Fig. 5-11. Lift increment dual slot actuator– h/r=0.2, α=0°

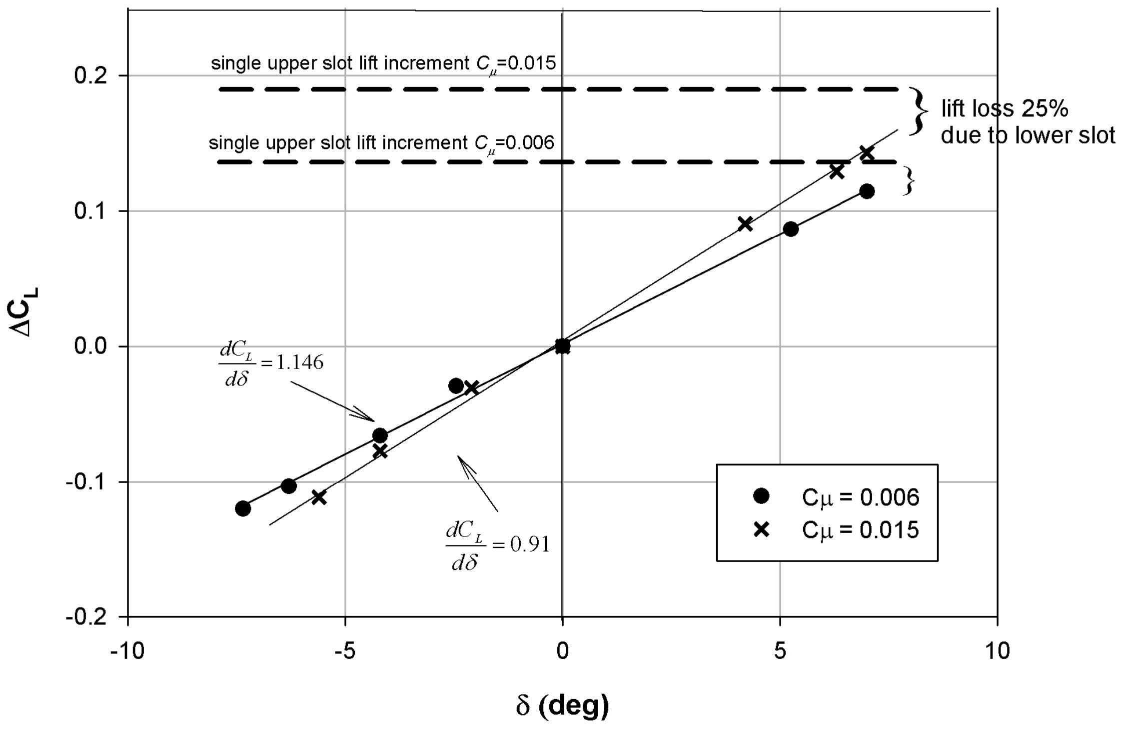

Fig. 5-12. Lift increment dual slot actuator– h/r=0.08, α=0°

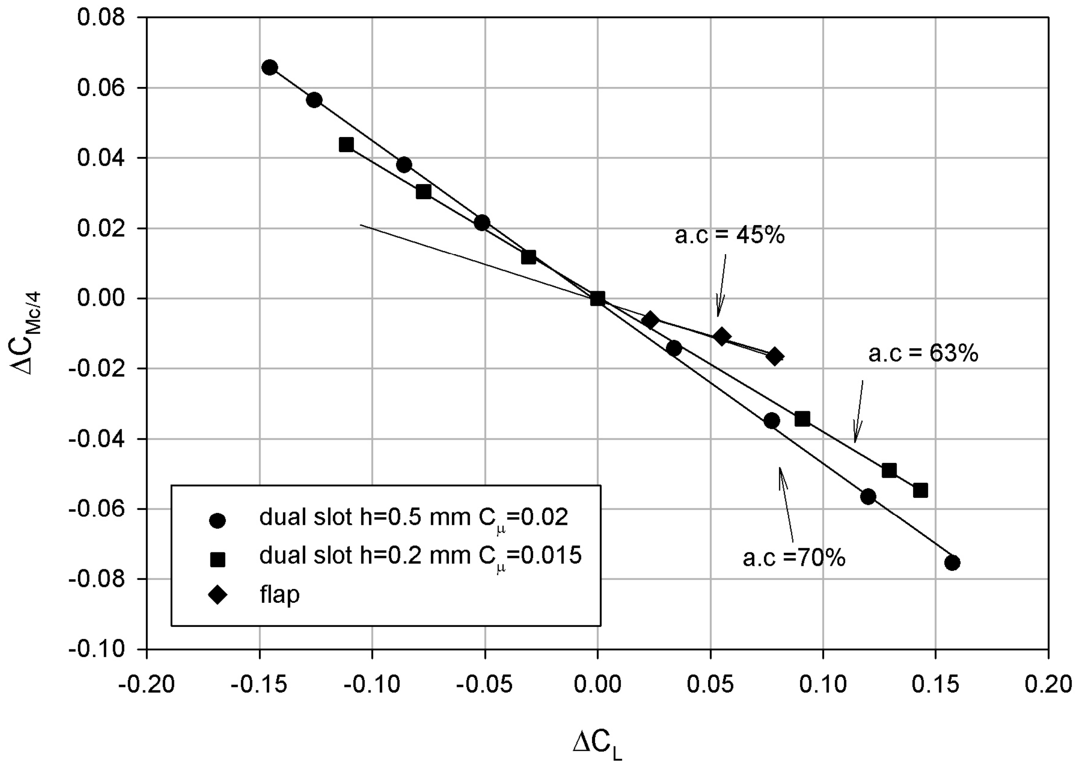

Fig. 5-13. Variation of pitching moment with control angle deflection – α=0°

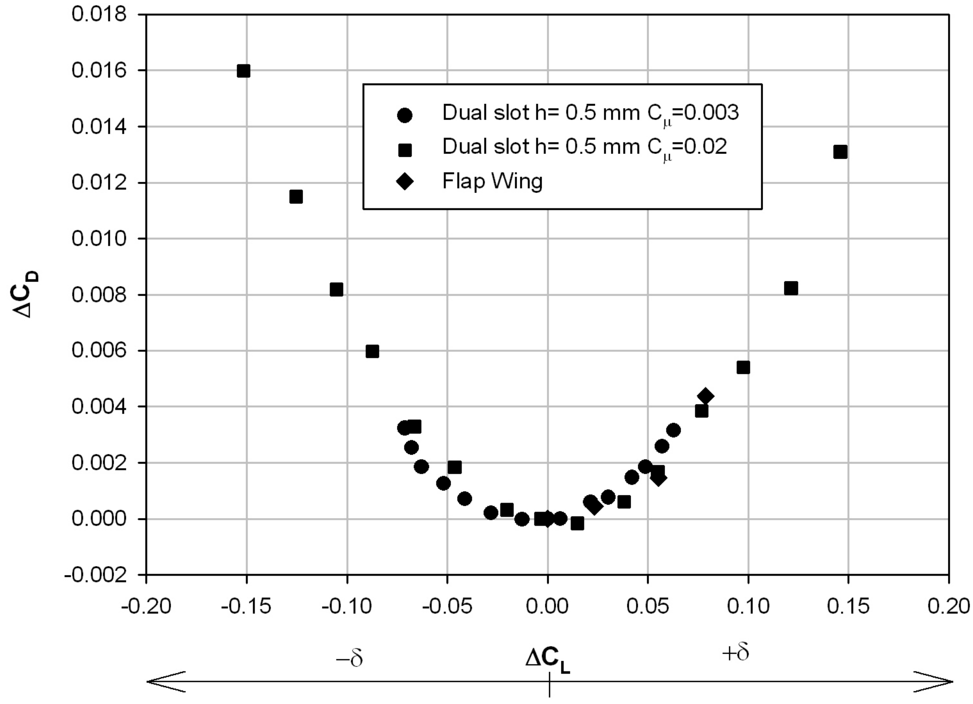

Fig. 5-14. Drag polar– α=0°

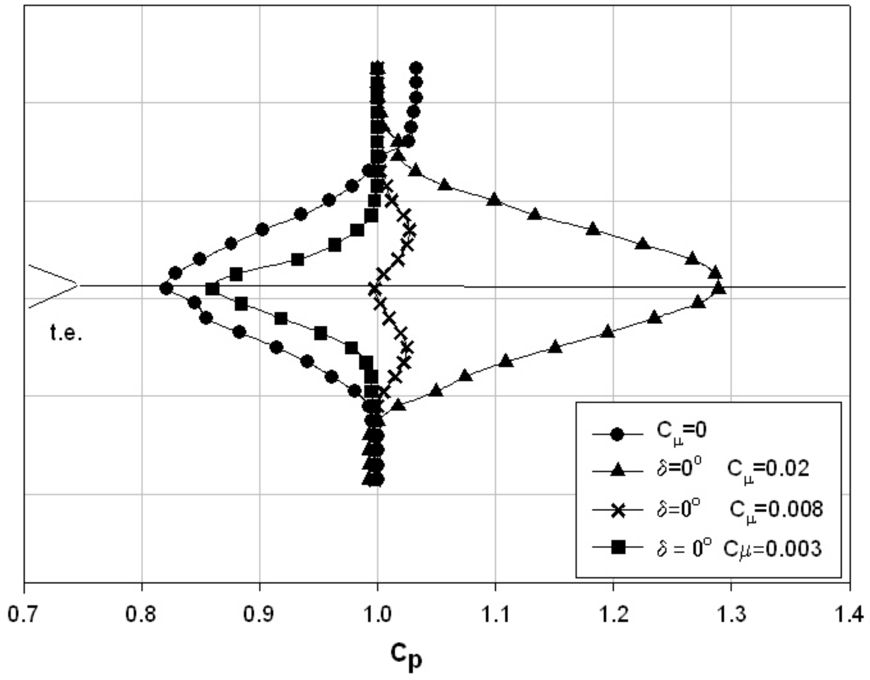

Fig. 5-15. Wake profile measurement 1 chord downstream, mid-span – h/r=0.2, δ=0°

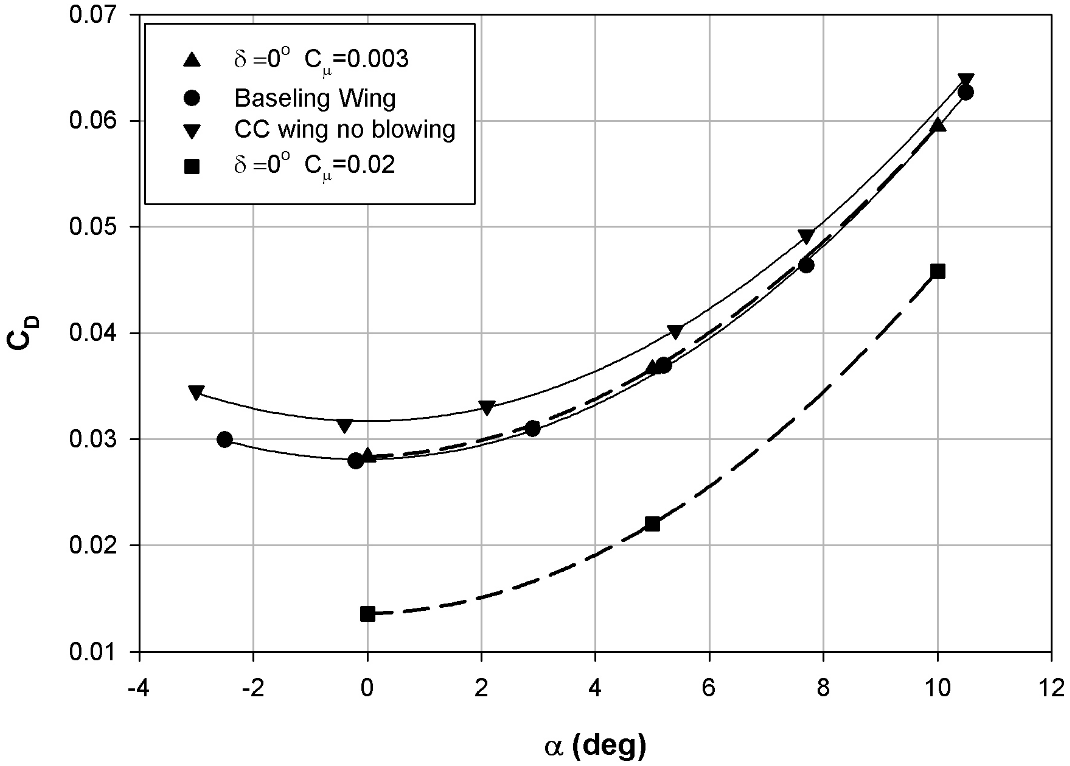

Fig. 5-16. Comparison of the drag polar of the baseline wing with the drag polar of the CC wing with and without blowing

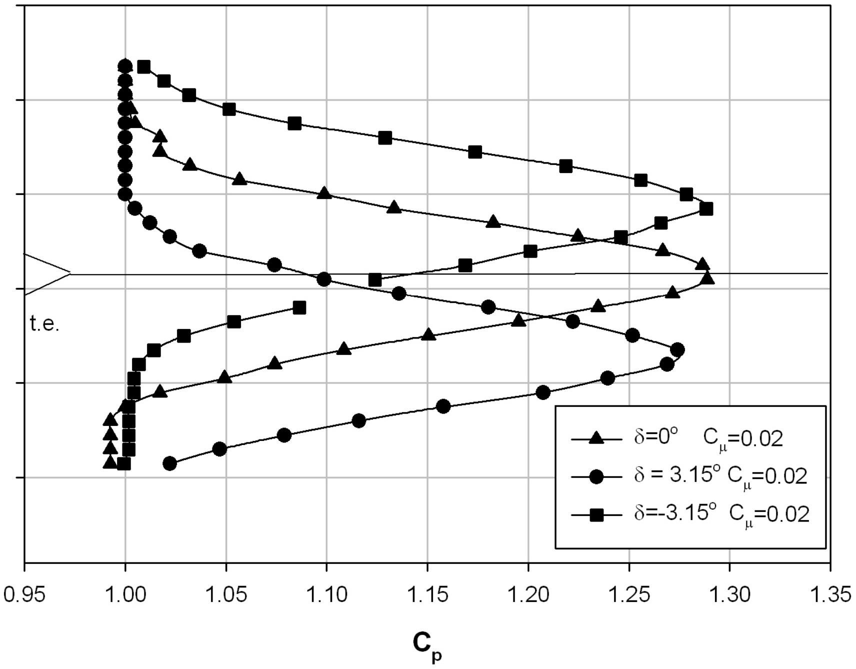

Fig. 5-17. Wake profile measurement 1 chord downstream, mid-span – *h/r*=0.5, wake deflection

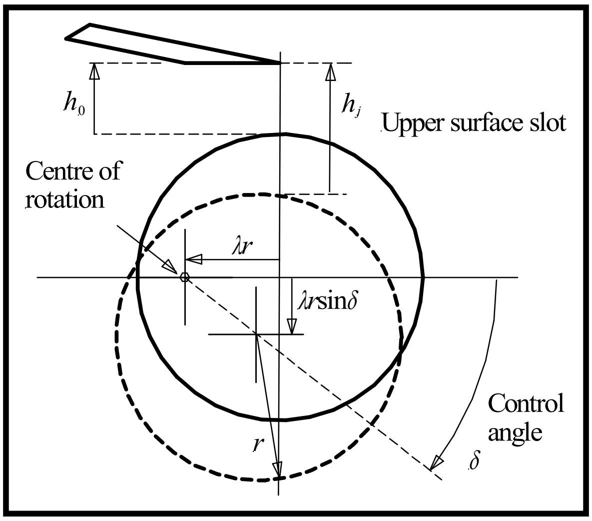

Fig. 5-18. Flow control actuator slot geometry

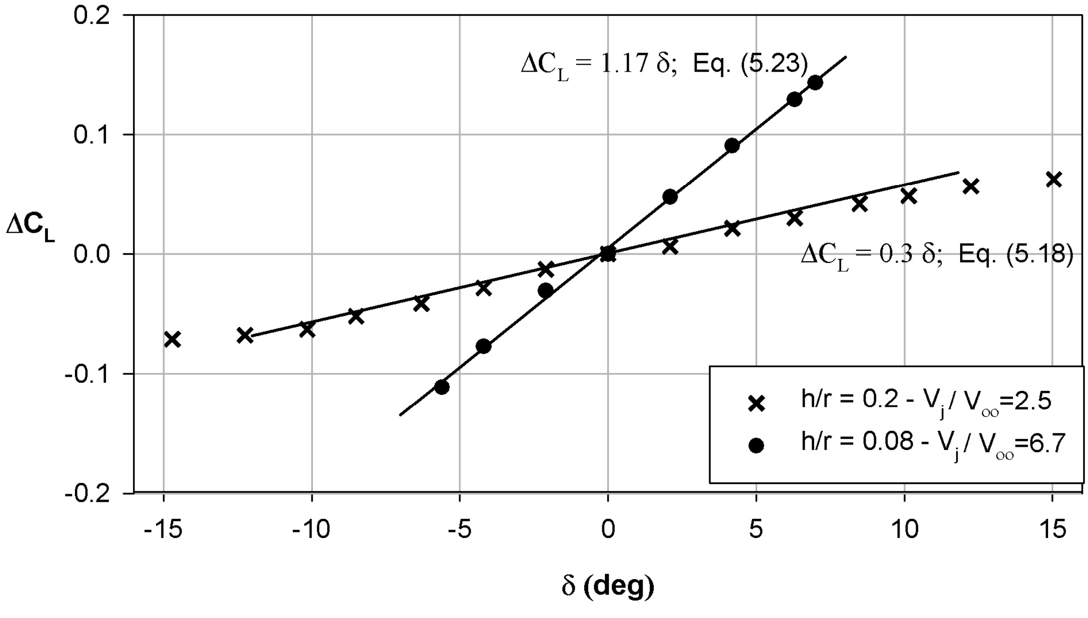

Fig. 5-19. Comparison of the mathematical model with the experimental data; (— curve fit)

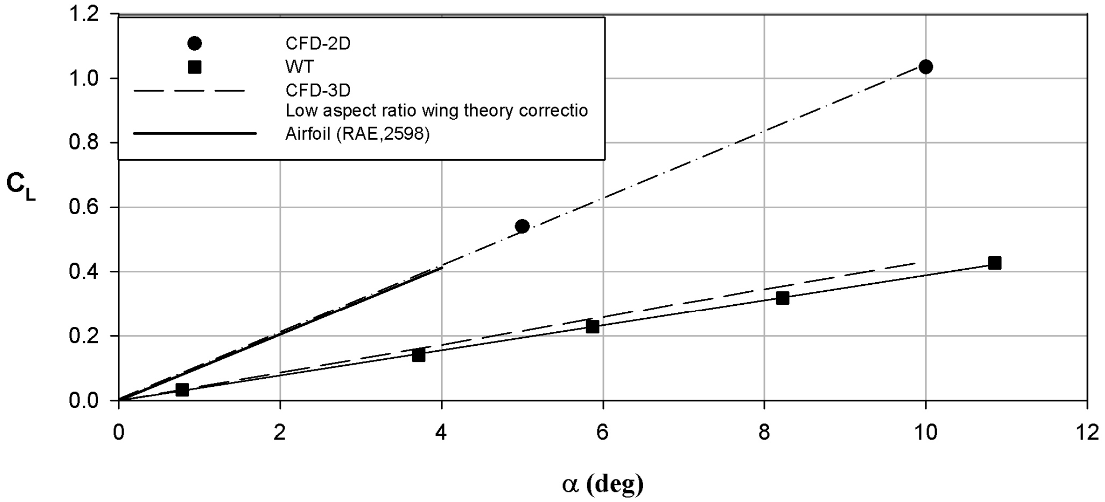

Fig. 5-20. Comparison of the computed baseline lift coefficient with wind tunnel results

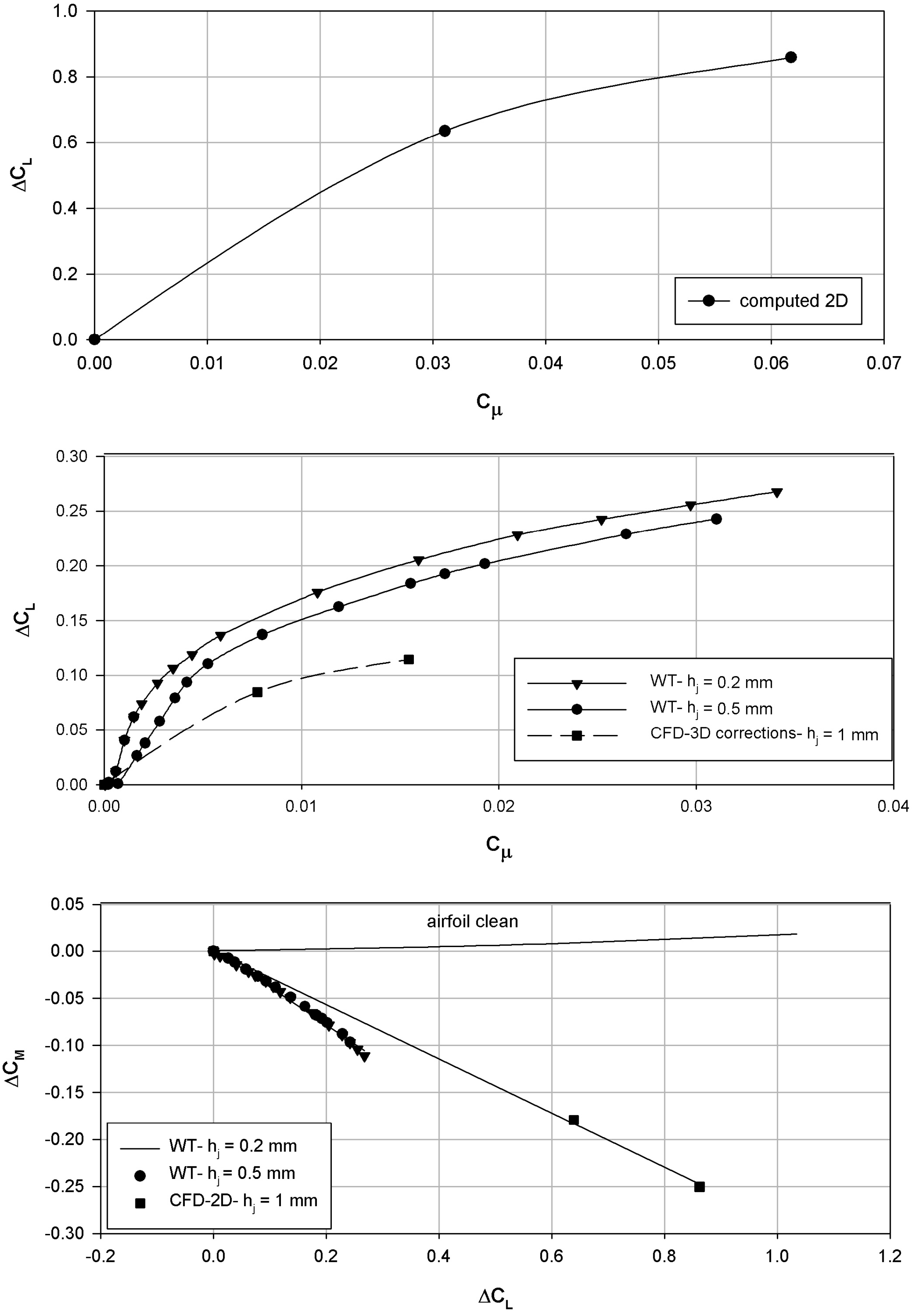

Fig. 5-21. Single slot trailing edge blowing. $\alpha = 0^o$

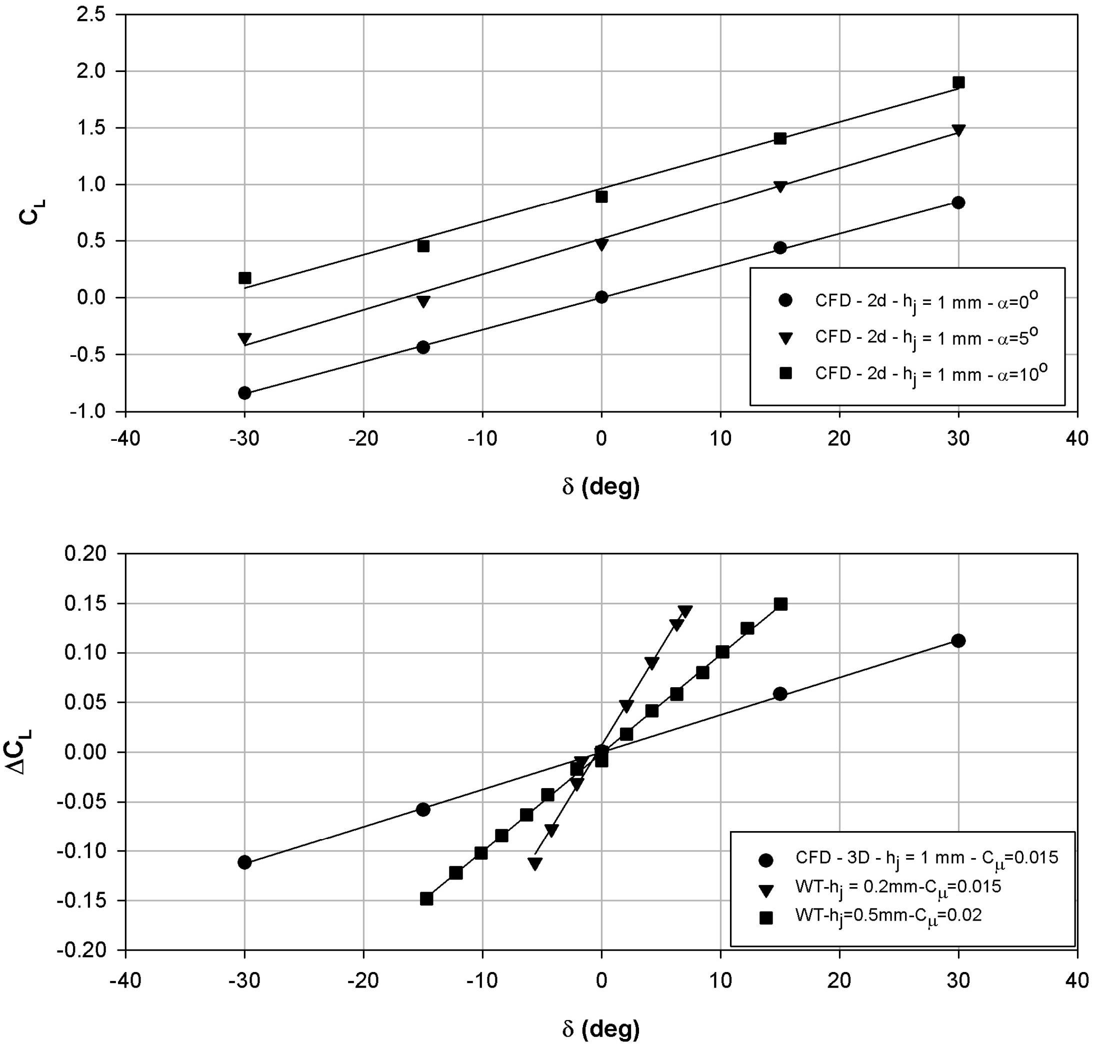

Fig. 5-22. Change in lift due to differential trailing edge blowing. $\alpha = 0^{\mathrm{o}}$

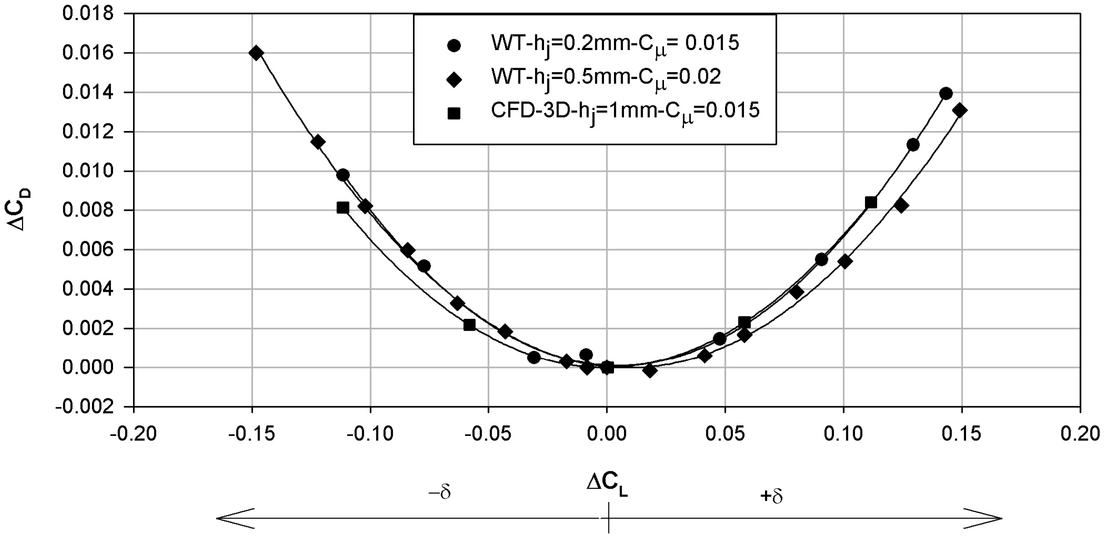

Fig. 5-23. Change in drag due to differential trailing edge blowing. $\alpha = 0^{\mathrm{o}}$

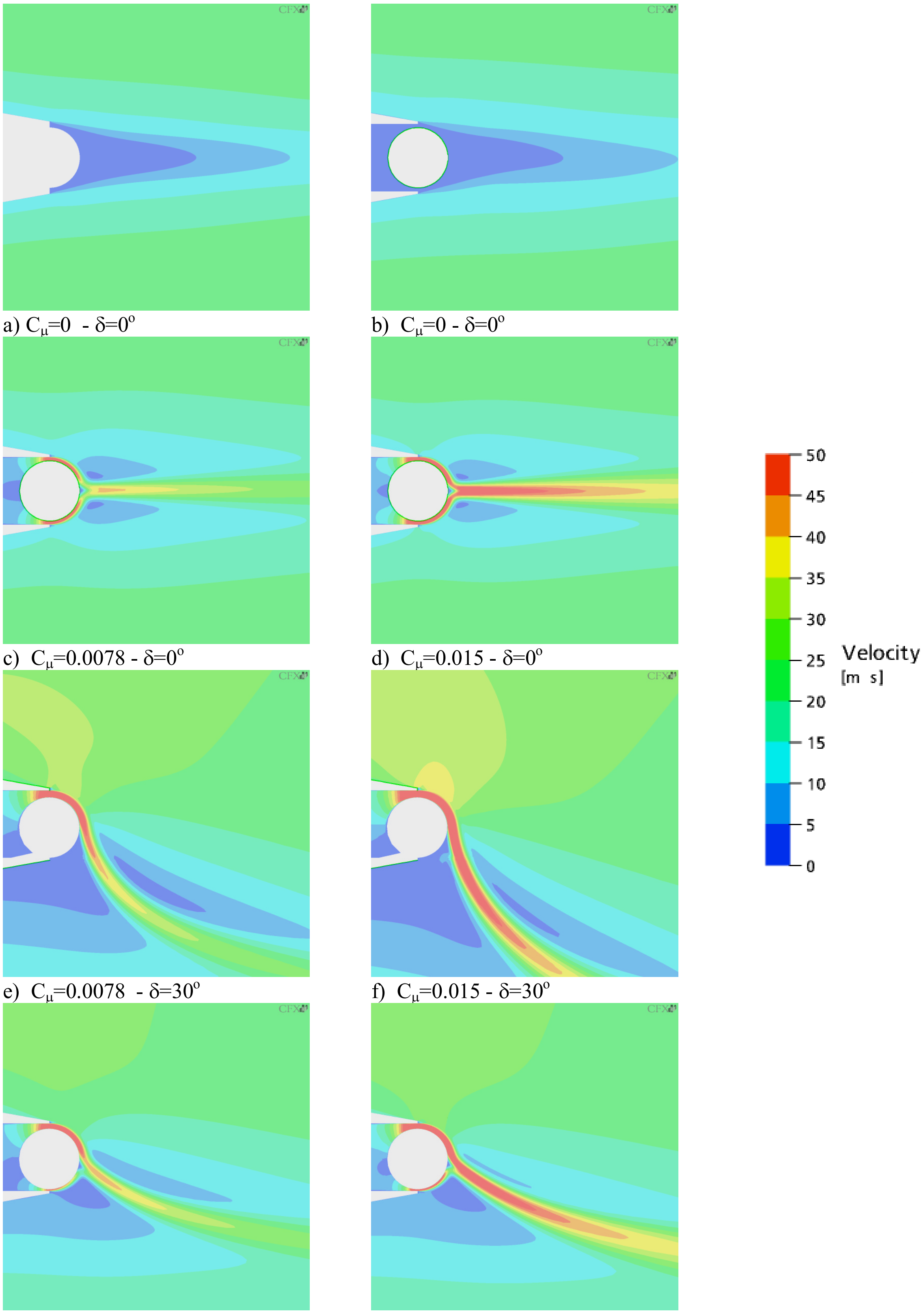

a) C_μ=0 - δ=0°

b) C_μ=0 - δ=0°

c) C_μ=0.0078 - δ=0°

d) C_μ=0.015 - δ=0°

e) C_μ=0.0078 - δ=30°

f) C_μ=0.015 - δ=30°

g) C_μ=0.0078 - δ=15°

h) C_μ=0.015 - δ=15°

Fig. 5-24. Speed contours

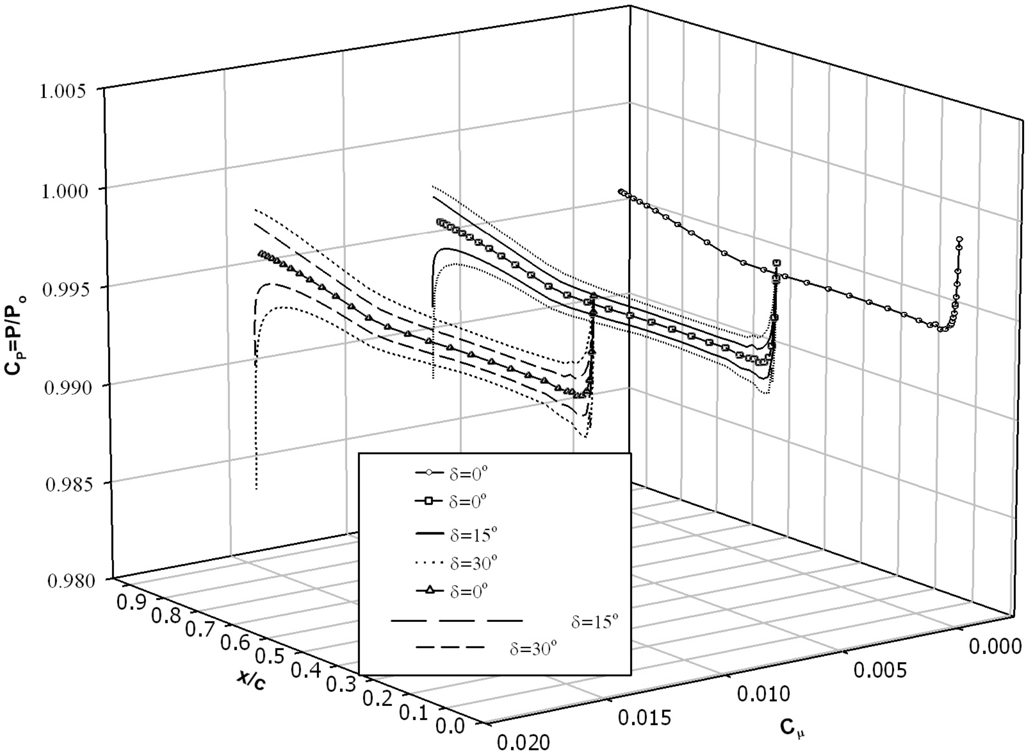

Fig. 5-25. Simulated static pressure distribution on the airfoil – α=0°

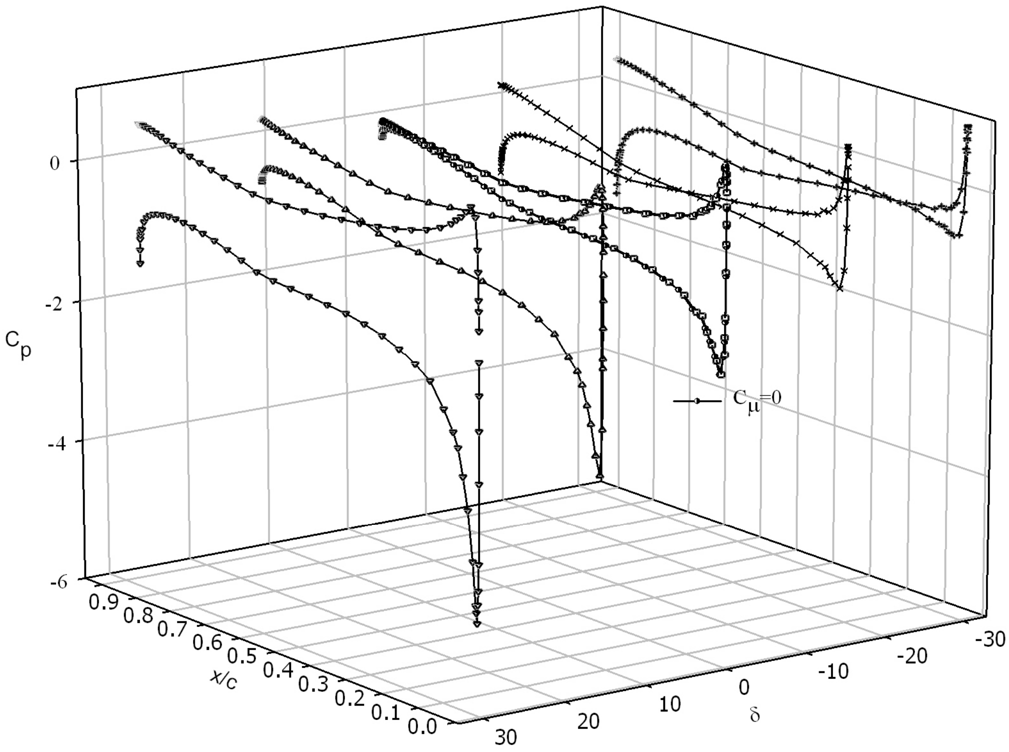

Fig. 5-26. Simulated static pressure distribution on the airfoil – α=5° and constant blowing

6 FLAPLESS FLIGHT CONTROL

6.1 Introduction

The following sections seek to identify the key differences between mechanical and fluid controls and hence define the role of control gain and control efficiency in control sizing. This section also considers the factors that determine the control effectiveness, i.e. control saturation limits or effort/power saturation due to the finite performance of the pneumatic power supply for the actuator.

Results of the wind tunnel test evaluations previously described (Chapter 5), were incorporated into the design of a fluidic manoeuvre effector to control the air vehicle in roll. This required prediction of the blown aircraft's roll authority, with available or postulated air sources powering the system, in order to assess, with a first order approximation, the performance at flight conditions representative of the *Demon* flight envelope.

Baseline *Demon* geometry and aerodynamic characteristics from ½-scale wind tunnel results have been described already in Chapter 3 and these data were used in the following analyses as a comparative sample case to investigate the key differences in control sizing and effectiveness.

Aerodynamic forces F are defined in terms of dimensionless coefficient C_F, the flight dynamic pressure Q_{dyn}, and a reference area S, as follow:

$$F = C_F Q_{dyn} S \tag{6-1}$$

Consider a conventional mechanical flap surface that produces a force output in response to a control surface deflection. From basic aerodynamic theory the change in local lift produced by the control input δ can be expressed in non dimensional form as:

$$C_F = C_{F\delta}\delta \tag{6-2}$$

where $C_{F\delta}$ is the effectiveness and it is usually a function of the size of the geometric surface (ratio of the control surface area over the lifting surface area).

Consider now a CC actuator that produces a reaction force output in response to a momentum input μ. As it has been shown in Chapter 5 the control force can be obtained from the product of a gain term and the momentum input or in dimensionless terms:

$$C_F = K_\mu C_\mu \tag{6-3}$$

Where K_μ is the CC effectiveness and it is a function of span-wise extent of blown trailing edge, the ratio of trailing edge radius to lifting section chord and the ratio of blowing slot height to trailing edge radius. For fluidic controls, Eq. (6-3), the control input is now a dimensionless coefficient as opposed to a angle. This means that the actual dimensional control input required to achieve a given control force coefficient is not independent of the reference momentum $Q_{dyn}S$. This implies that as the free stream speed increases, an increasing amount of input momentum is required to achieve a given force coefficient.

For mechanical controls, control saturation can arise from two different sources. Firstly, the control may reach the end of its geometric travel, i.e. reach δ_{max}, or, secondly, the maximum force available to move the control may be exceeded, i.e. an actuation effort/power limit. Also, at low speeds, an aircraft has reduced airflow over the wing and vertical stabilizer. This causes the control surfaces (ailerons, elevator and rudders) to be less effective. Similarly, for fluidic controls, two different saturation limits exist based on geometry and control/power constraints. In a similar manner to mechanical controls, geometric limits for fluidic controls manifest as a break point in the control response curve after which control gain is greatly reduced, i.e. where further increases in input momentum produce little change in the aerodynamic forces acting on a body. For CC system, a geometric limit exists due to the limited surface extent of the curved trailing edge: this will typically limit the attachment angle of the jet to less than 180^o. The control/power saturation limits for fluidic actuation arise due to the finite performance of the pneumatic power supply for the actuator. In this case the power can be expressed as the total fluidic power required for supplying the jet velocity head. In terms of control/power saturation, engineering constraints for engine bleed or dedicated Auxiliary Power Unit (APU) pneumatic power supplies lead to the systems being mass flow limited or pressure limited. There also exists a third type of saturation due to jet separation at high jet Mach numbers. Separation is brought on by high pressure ratio across the nozzle, large slot heights and small radii on the Coanda surfaces (Wood & Nielsen, 1985). Previous work has shown circulation control can be achieved with high supersonic jet, although such a jet loses a significant portion of its momentum to wall shear (Englar, 1975).

A principal feature of the *Demon* aircraft variant is that the hinged control surfaces shall be replaced with CC actuator sufficient to demonstrate total flapless control of the vehicle in roll. The performance specification reference that must be met for the CC system is defined by the roll maneuver performed using conventional ailerons.
An estimate of the roll control power can be obtained by a simple strip method of integrating the incremental change in roll due to a change in control deflection over the region containing the CC aileron:

$$C_{LL} = C_{LL_{C_\mu}} C_\mu = K_\mu \frac{\bar{y}}{b} C_\mu \tag{6-4}$$

where $C_{LL_{C\mu}}$ is the unit of roll moment per unit of momentum input.

Assuming the aircraft is constrained to rotate around its x-axis only and solving the equation of pure rolling motion, steady state roll rate can be obtained,

$$\frac{p_{ss} b}{V_\infty} \approx \frac{C_{LLC\mu}}{C_{LL\,p}} C_\mu \tag{6-5}$$

where $C_{LL\,p}$ is the roll damping derivatives.

From Eqs. (6-4) and (6-5) the mass flow rate required to perform a roll manoeuvre can be calculated as,

$$\dot{m} = \frac{\rho}{2} \sqrt{\frac{p_{ss} A_j S V_\infty C_{LL\,p}}{K_\mu \bar{y}}} \tag{6-6}$$

It shows that for a given control location on the aircraft, wing geometry and flight speed, the mass flow required is minimized by maximizing the CC gain, K_μ, and minimizing the CC slot area, A_j.

If air is bled from the compressor stage of a gas turbine engine, the pressure available is typically well in excess of the typical maximum delivery pressure ratio of around 2 (sonic exit conditions) needed for fluidic control applications. Because of this, the main power system constraint is mass flow rate availability. Therefore, it can be seen that for efficiency the slot design should be driven towards using a high jet velocity. The control gain is maximized by minimizing the dimensionless slot curvature *h/r* (experimental results in Chapter 5 suggest that good performance is obtained for a dimensionless slot curvature of around 0.08 or less).

6.2 Circulation Control actuator model

A model of the flow control device has been developed for incorporation into the *Demon* air vehicle simulation.

The system has been modelled as shown in Fig. 6-1 and Fig. 6-2. Air is supplied continuously to the plenum chamber and the jet momentum is directed through a moving trailing edge actuated by means of a small model control servo as shown in Fig. 6-3. The model derivation of each block in Fig. 6-2 is carried out in the following paragraphs.

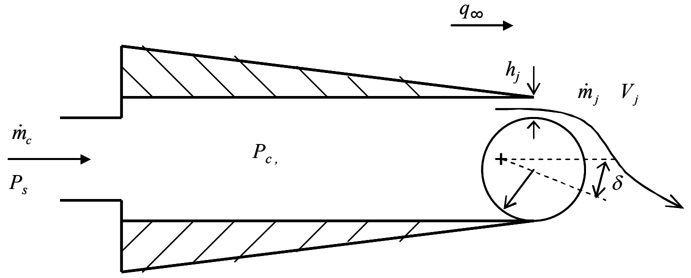

Fig. 6-1. Circulation control actuator system representation (a)

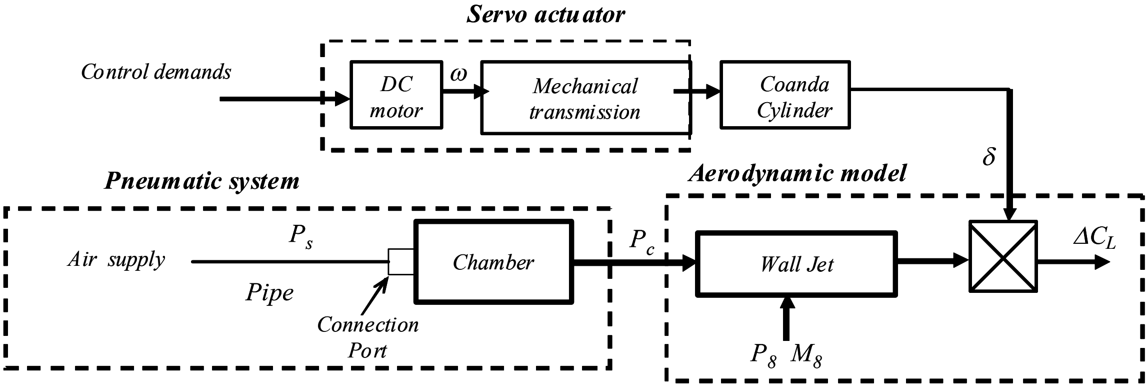

Fig. 6-2. Circulation control actuator system representation (b)

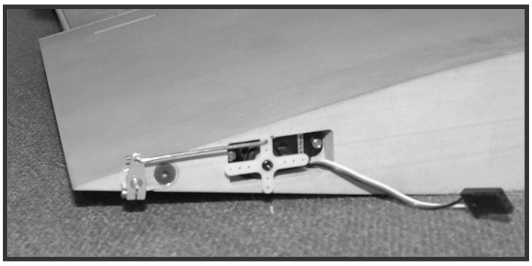

Fig. 6-3. Experimental servo actuator installation

6.2.1 Pneumatic system model

The model of the pneumatic system determines the plenum pressure P_c subject to the following simplifying assumptions:

(i) Gas is ideal.
(ii) Gas density is uniform in the chamber and in the pipe.
(iii) Gas flow through the pipe is an isentropic process.
(iv) Flow in the connection port is isentropic.
(v) Flow leakage is negligible.
(vi) A quasi stagnation condition exists inside the plenum chamber.
(vii) The ambient pressure at the slot exit is the free stream static pressure.

The transient of the gas in the chamber has been modelled as variable volume between two restrictions (Bigras, Wong & Botez, 2001), (Anderson, 1967). In accordance with assumptions (i), (ii), (iii) the dynamic model of the gas in the chamber is given by the following relations,

$$\dot{P}_c = \frac{\gamma R T_c}{V_c}(\dot{m}_c - \dot{m}_j) \tag{6-7}$$

Where P_c, V_c, T_c and $\dot{m}_c$ are respectively the pressure, volume, temperature and mass flow in the plenum chamber. *R* is the ideal-gas constant and *γ* is the ratio of specific heats of the gaseous medium. In accordance with assumption (iii), the temperature in the chamber is given by the following relations:

$$T_c = T_{c0}\left(\frac{P_c}{P_{c0}}\right)^{\frac{\gamma-1}{\gamma}} \tag{6-8}$$

Where P_{c0} and T_{c0} are the initial conditions. According to assumption (iv) and (v) the flow in the valve and in the connection port are then modelled as follow:

$$\dot{m}_c = \frac{C_c A_c P_s}{\sqrt{RT_s}} f_r\left(\frac{P_c}{P_s}\right) \qquad P_s \geq P_c \tag{6-9}$$

Where A_c is the orifice area of the connection port and P_s, T_s are the pressure and the temperature respectively of the air supply. C_c is the orifice discharge coefficient. The piecewise flow function f_r in Eq. (6-9) is defined as:

$$f_r = \begin{cases} \sqrt{\dfrac{2\gamma}{\gamma-1}}\sqrt{y^{\frac{2}{\gamma}} - y^{\frac{\gamma+1}{\gamma}}} & y \geq r_c \\ \sqrt{\gamma\left(\dfrac{2}{\gamma+1}\right)^{(\gamma+1)/\gamma-1)}} & y < r_c \end{cases} \tag{6-10}$$

Where r_c is the critical pressure ratio given by $r_c = (2/\gamma+1)^{\gamma/(\gamma-1)}$.

As a matter of convenience the plenum stagnation pressure is expanded to free stream static pressure. Thus, the jet mass flow rate $\dot{m}_j$ can be calculated isentropically using compressible flow equation,

$$\frac{\dot{m}_j\sqrt{RT_c}}{A_j P_c} = \sqrt{\frac{2}{\gamma-1}\left(\frac{P_\infty}{P_c}\right)^{\frac{2}{\gamma}}\left(1-\left(\frac{P_\infty}{P_c}\right)^{\frac{\gamma-1}{\gamma}}\right)} \tag{6-11}$$

The local Mach number at the jet exit slot is determined from the isentropic equation,

$$M_j = \sqrt{\frac{2}{\gamma - 1}\left(\left(\frac{P_c}{P_\infty}\right)^{\frac{\gamma-1}{\gamma}} - 1\right)} \tag{6-12}$$

6.2.2 Servo actuator model

The transient of the pneumatic system is governed by a first order model, Eq. (6-7), with a lag which is dependent on the volume of the line. Given that the volume of the chamber is small, the pressure transient is negligible and the open loop response of the system is governed mainly by the transient of the actuator, since this is the slowest component in the system. Measurements of the response of the experimental actuator enabled a second order model to be described as,

$$\frac{\delta}{\delta_d} = \frac{\omega^2}{s^2 + 2\omega\varsigma + \omega^2} \tag{6-13}$$

Where δ_d the commanded deflection angle and δ is the actual deflection angle, ω is the frequency of the system, estimated as 15rad/s, and ς is the damping ratio, estimated as 0.85.

6.2.3 Prediction of the Lateral Aerodynamic characteristics of the Demon/CC

In the absence of wind tunnel test evaluation of a 3-D *Demon*/CC model, semi-empirical methods were used to reduce data obtained from wind tunnel tests on the rectangular wing into 3-D finite wing data for the *Demon*, spanning the same portion of the wing as the existing inboard mechanical ailerons (surface No. 2).

Let S_{eff} be the fraction of wing area ahead of the part span trailing edge slot, then the full span lift increment due to the CC actuator can be expressed as,

$$\frac{dC_{L_F}}{d\delta} \approx \frac{dC_L}{d\delta}\frac{S}{S_{eff}} \tag{6-14}$$

The lift increment due to trailing edge blowing was derived by applying a part span correction (ESDU 74012) to take into account the limited span-wise extent of the TE device. Using the same notation as in ESDU:

$$\Delta C_{LF} = \Delta C_L / 0.32 \tag{6-15}$$

The lift increment per unit control deflection ΔC_L has been defined in Eqs. (5-17) and (5.22) in Chapter 5. The implementation of the method is given in appendix E.

Thus, an effective 2-D momentum coefficient can be defined based on CC actuator performance installed in a given wing plan-form. Let b_j be the trailing edge slot part span, then from the definition of flow momentum coefficient, it follows that,

$$C_{\mu 2-D} = C_{\mu 3-D} \frac{b}{b_j} \tag{6-16}$$

An estimate of the roll control power for an aileron can be obtained by a simple strip method integrating the incremental change in roll due to a change in control deflection over the region containing the aileron:

$$C_{LL_\delta} = \frac{\partial C_{LF}}{\partial \delta} \frac{1}{Sb} \int_{y_i}^{y_o} c(y) y dy \tag{6-17}$$

Where $\frac{\partial C_{LF}}{\partial \delta}$ is the section lift coefficient on the station containing the aileron which control effectiveness is thought dependant only on the *h/r* and *h/c*, *c* being the mean aerodynamic chord of the section ahead the CC actuator

A semi-empirical method (ESDU 88013) has been used to estimate the rolling moment derivative due to the operation of the CC actuator. The method is derived from the strip method described in Eq. (6-17) and it adjusts the data for sweep, aspect ratio and partial span flap effects. The implementation of the method is given in appendix E.

The design variables for the CC actuator are listed in Table 6-1. The plenum aspect ratio determines the chord-wise extent of a CC unit. In the present work, the goal has been to replace the mid-span hinged surfaces with CC actuator and the existing space for these surfaces has been replaced with a plenum without trying to reduce the chord-wise extent. If the plenum aspect ratio (height of the slot over its span-wise extent) is small then it is still possible to achieve good uniformity of total pressure at the slot. For a given plenum geometry, the total pressure uniformity at the slot exit also depends on the geometric tolerances of the slot itself.

Slot total pressure uniformity is maximized by maximizing the slot geometric uniformity, however, there is a design and manufacturing cost associated with decreasing slot tolerances and it becomes increasingly expensive to maintain a given slot geometric uniformity as the mean slot height decreases.

Parameter		**wing with flap**	**wing with CC actuator**
Flap span (% *b/2*)		~ 15%	~15%
Flap chord (% *c*)		~ 6.5%	-
Slot curvature	h/r	-	~ 6 %
Coanda surface radius/ fraction of the wing ahead the CC chord	r/c	-	< *1%*
Plenum AR	h/b_j	-	*0.2%*

Table 6-1. Mechanical flap and CC actuators geometries**.**

If the ailerons were substituted with the CC system, the parameter $dC_{LL}/d\delta$ would remain valid, representing the rolling moment increment per unit control angle deflection. This value would be a function of the blowing and, hence, the velocity ratio. Fig. 6-4a shows the variation of rolling moment per angle deflection of the cylinder with increasing blowing from the plenum. The rolling moment derivative for the inboard and outboard mechanical aileron is superimposed. Fig. 6-4b shows, also, the corresponding corrected mass flow rate, blowing momentum coefficients and jet velocity ratio, according to the model described in paragraph 6.2.

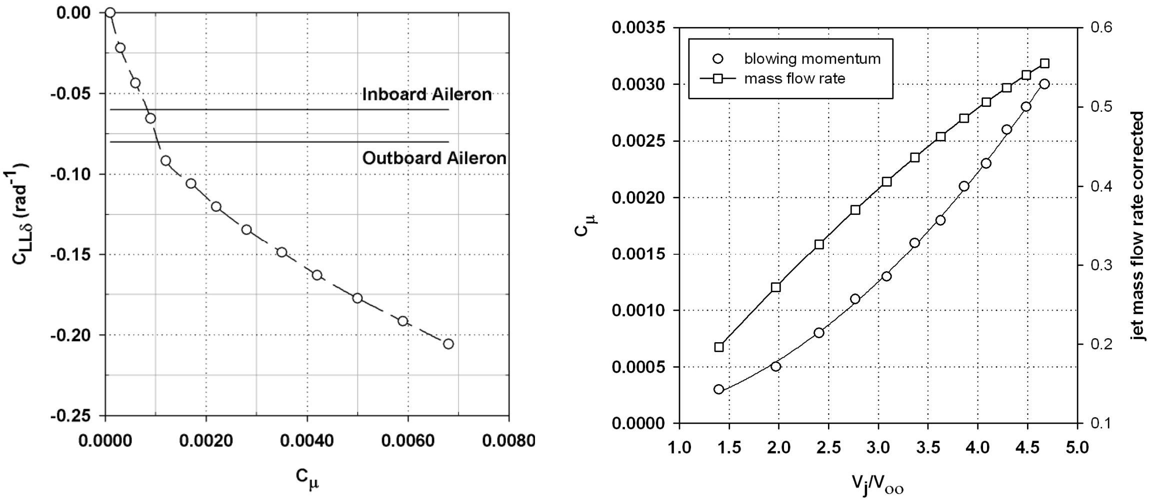

Fig. 6-4. a) Rolling moment derivatives evaluated for the CC actuator replacing the inboard aileron of the *Demon*. b) Air supply requirements

Clearly the main advantage of a dual slot actuator is the possibility of achieving differential control through actuation on the left and right wing. This would maintain symmetry in the control and would have the main advantage of cancel out the pitching moment created by the high lift effectors. This observation was discussed in the previous Chapter 5.

The rolling moment generated blowing differentially from the left and right CC actuators replacing ailerons is shown in Fig. 6-5a. The rolling moment due to differential deflection of the ailerons (ξ) is shown on the same graph over an actuator control angle of $\pm10^o$. The data indicates that a 10^o deflection of an aileron could be generated instead using a blowing coefficient of 0.001 at each plenum.

The blowing momentum coefficient is the most critical parameter controlling the effectiveness of the CC unit. For a fixed slot geometry and chamber pressure the blowing momentum coefficient is an inverse function of the dynamic pressure, i.e. the flight velocity. Therefore in order to maintain a constant effectiveness air supply pressure should increase with flight velocity. Fig. 6-5b shows the variation of pressure ratio in the chamber with flight speed within the flight envelope.

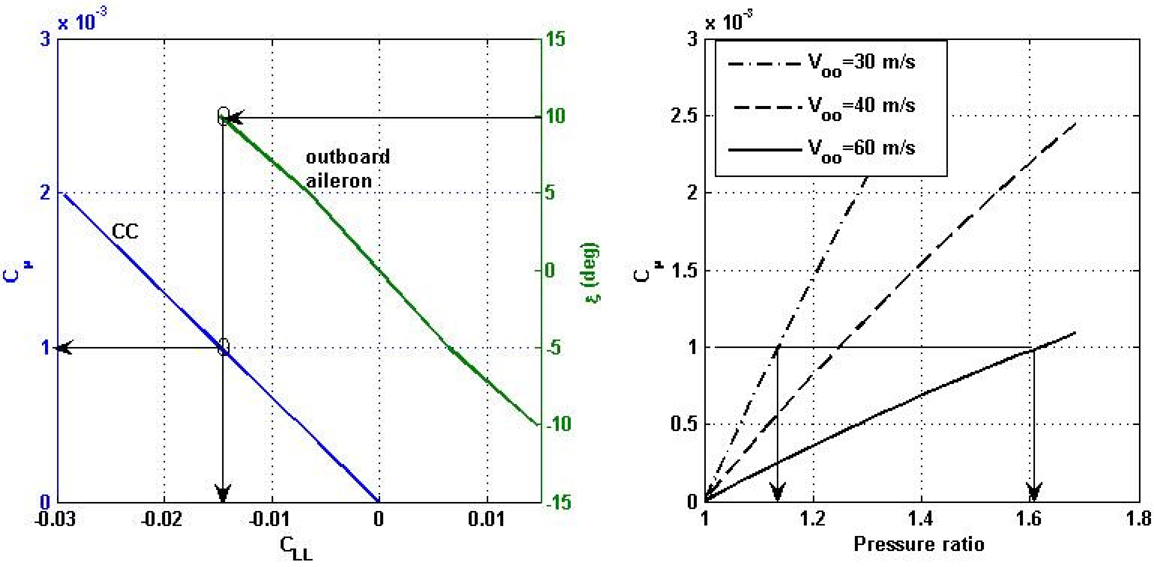

Fig. 6-5. a) Comparison of the differential rolling moment at different blowing setting with differential rolling moment achievable with mechanical aileron deflection. b) Chamber pressure variation with flight speed

6.3 Pneumatic power supply

Different options have been considered within the *Demon* system design to supply compressed air to the CC actuator.

The power can be extracted from the thrust engines resulting in an available thrust level reduction. A blowing air compressor driven from the propulsion unit through a shaft is the most thrust efficient method of engine power extraction. Moreover this solution allows the compressor to be sized in accordance to the needs at the blowing slot. However, the engineering complexity and cost penalty made this method not a viable option. Considering that the momentum required is less than 10% of the installed thrust, the engine compressor bleed can provide relatively cool high pressure air, with the advantage of high pressure ducting which requires much smaller duct and provides better span-wise distribution.

6.3.1 Engine with bleed

The reduced static thrust associated with bleed air can be computed from cycle analysis on T-S diagram of a jet engine. The magnitude of the turbine and compressor efficiencies (η_c, η_t) and the temperature ratio's (t_{3r}, t_{4r}) for the compressor and the turbine, determine the thrust loss associated with bleed air ($b = \dot{m}_b / \dot{m}$) and forward speed (V_e).

The ratio of the static thrust with the bleed to the thrust without can be expressed as (Loth, 1987),

$$\frac{T_b}{T} = \frac{\dot{m}(1-b)V_{eb}}{\dot{m}V_e} \quad where \quad \frac{V_{eb}}{V_e} = \sqrt{\frac{C_{1b}}{C_1}} \tag{6-18}$$

$$and \quad C_1 = f\left(t_{3r}, t_{4r}, \eta_c, \eta_t, b\right)$$

From Eq. (6-18) the reduced static thrust associated with bleed air can be computed as function of the bleed mass ratio (b),

$$\frac{T - T_b}{T} \approx k_b b \tag{6-19}$$

k_b is the percentage of thrust loss per bleed rate and it is dependant on the component efficiencies and the temperature ratio’s for the compressor and the turbine.

A pneumatic power supply system, based on the AMT micro jet turbine engine compressor bleed, has been designed, developed and tested at Manchester University (Wilde et al., 2007); The analysis and discussion which follows is based on data mainly from this source. The effect of engine bleed mass flow rate on thrust for a range of throttle setting is shown in Fig.6-6. Test data were corrected for standard atmospheric conditions and static uninstalled engine thrust is a function of power setting and bleed ratio. Bleed flow is a function of total engine airflow at a specific throttle setting. Bleed mass flow rate is presented non dimensionalized using the maximum mass flow rate extracted. The engine throttle regulates the fuel flow rate via the engine control unit (ECU). For a given throttle setting the fuel flow is constant. An exception to this rule is if the engine approaches the maximum or minimum shaft spool speed. In this case the engine will regulate the fuel flow in order to remain within the spool speed limits. At maximum throttle the engine will maintain the maximum spool speed, by regulating the fuel flow rate. The exhaust gas temperature increases with higher bleed. The maximum bleed mass flow taken from the engine is limited by the turbine inlet temperature, particularly at low throttle. In practise this was imposed by limiting the exhaust gas temperature to 1100K.

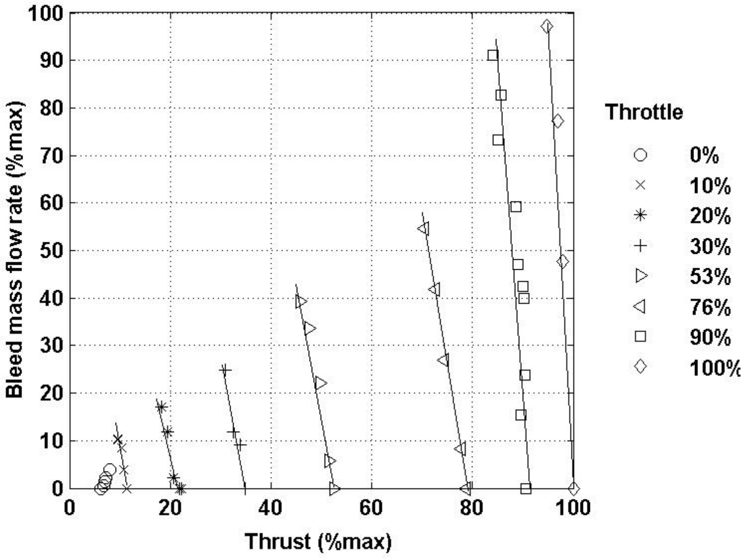

Fig.6-6. Static thrust performance of uninstalled AMT Olympus micro jet engine with bleeds @ STP

Thrust losses as a function of bleed rate at each throttle setting can be extracted from Fig.6-6 and are presented in Fig.6-7a. Hence k_b can be calculated from Eq. (6-19) and results are reported in Fig.6-7b.

Thrust loss due to bleed averaged about 0.3N of thrust per gram per second of bleed air. Bleed system can produce large amounts of mass flow at high throttle setting. Below a throttle setting of 30% a low mass flow rate is produce with a large impact on thrust loss.

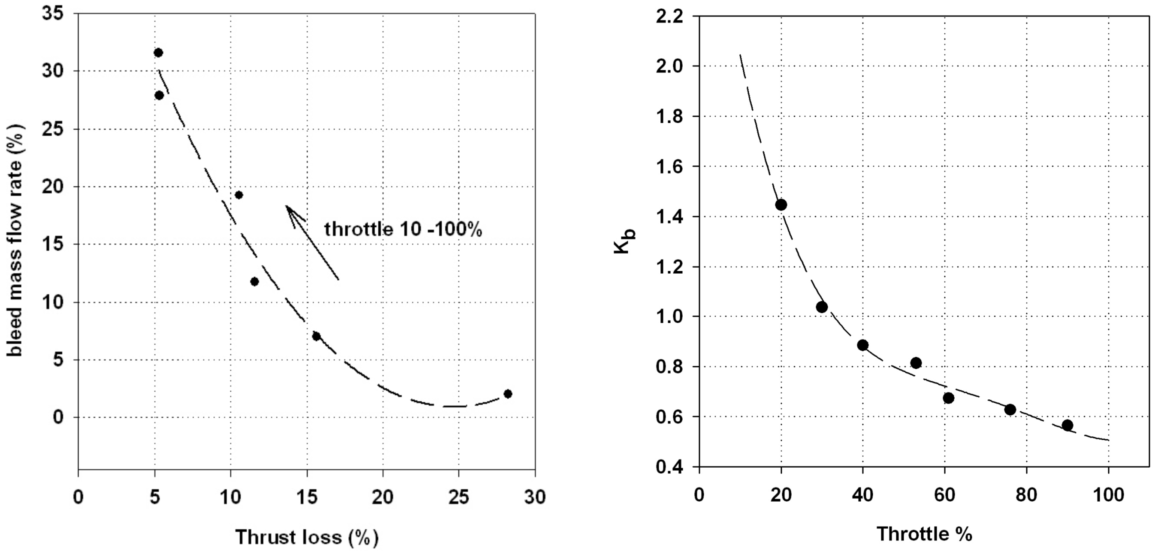

Fig.6-7. a) Thrust loss versus maximum bleed mass flow rate. b) Thrust loss per bleed rate at each throttle setting

For a blowing mass flow rate b.$\dot{m}$, the blowing jet thrust T_j is obtained from:

$$T_j = b\dot{m}V_j = bT(V_j / V_e) \tag{6-20}$$

The ratio between the exhaust velocity from the engine V_e and the jet velocity V_j for high pressure bleed due to pressure losses in the ducting and temperature drop can be estimated as approximately 0.8. So the bleeding requirement in the flight envelope at different throttle setting can be estimated using Eq. (6-20), for a required blowing momentum of 0.001, Fig.6-8. Clearly the CC can be fed from the engine under the condition the throttle setting to be higher than 30%.

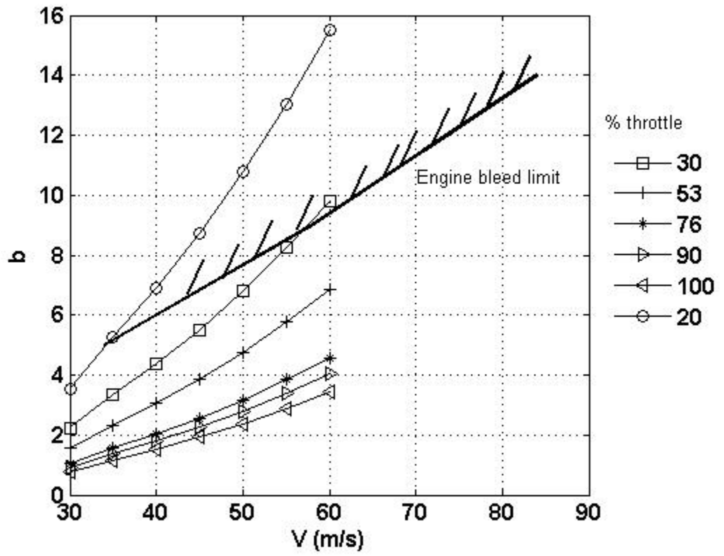

Fig.6-8. Bleeding requirements at different throttle setting and different speed within the flight envelope

During cruise the engine will be operating at 30-35 % throttle setting. The 10 % bleed mass flow requirement can be met with a thrust penalty of around 12 %.

The impact of thrust loss on the flight performance can be particularly significant regarding the overall flight envelope. It must be observed that the *Demon* flight speeds are relatively low and the amount of thrust spent during the different flight phases is small compared to the total installed one. The loss of thrust due to bleed for constant throttle settings is an issue due to the coupling between thrust and bleed mass flow rate. The throttle setting must be inferred depending on the thrust required and bleed mass flow rate. Considering steady level flight, Fig. 6-9 shows the changing in throttle setting required for any given velocity within the flight envelope when 10% mass flow rate is bled; for the design cruise speed V_C the throttle setting required is about 45% of the throttle setting. For the stall speed V_S the throttle setting required is about 42% of the throttle setting and for the design dive speed V_D it is 65%. Therefore in the whole level flight speed range the thrust loss due to engine compressor bleeding does not affect the aircraft ability to fly.

.

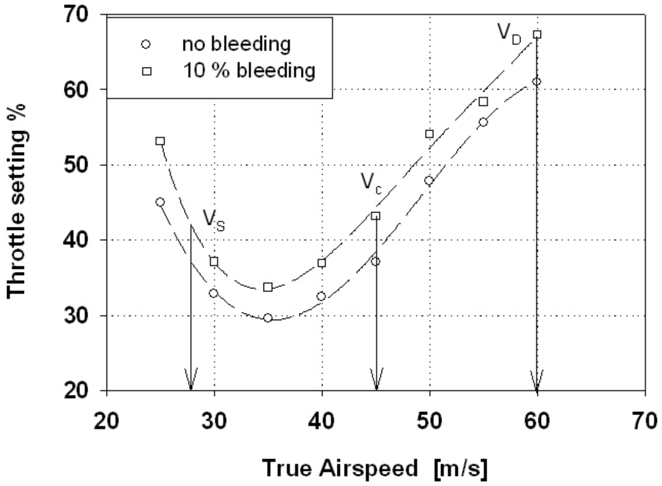

Fig. 6-9. Throttle setting required for steady level flight as a function of true airspeed @ 121m

If the aircraft is required to maneuver at higher load factors, the increase of induced drag must be considered in the analysis. The maximum steady bank angle in a coordinated turn is limited by the maximum thrust available, according to,

$$\phi_{\max} \propto W\sqrt{\frac{1}{(T-D_0)}} \tag{6-21}$$

The effect of the reduction in maximum thrust due to bleeding on maximum bank angle is illustrated in Fig. 6-10. The limits become more stringent if a bank angle in a steady climb turn is considered, due to the further reduction of the excess power caused by the component of weight that needs to be balanced.

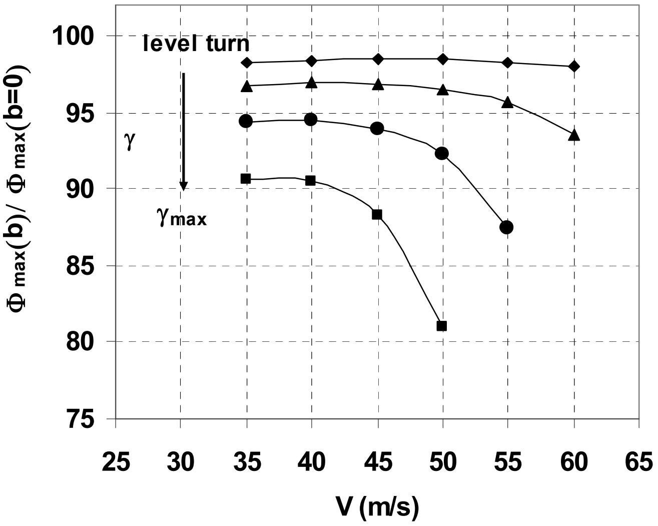

Fig. 6-10. Effect of bleeding on max turning bank angle

A significant limitation on using fluidic technology in combination with bleeding from the engine is represented by descending flight. Descending flight is a trade off between flying at a sufficient high velocity to guarantee a thrust setting high enough to bleed and not too high to compromise the efficiency of the CC actuator, as it has been observed before, the last is an inverse function of the flight speed. In order to slow down the aircraft, whilst keeping a high throttle setting, it is necessary to increase the parasite drag artificially, using for example spoilers.

During the approach the throttle setting is low (almost idle) and below the limit under which no air can be bled from the engine. One solution could be flying on the back side of the power curve at minimum level speed corresponding to maximum lift coefficient. The visibility during landing approach is not an issue for a UAV; therefore the aircraft could approach at very high angle attack. However, flying slow, on the backside of the power curve, is not recommended because no power is then left over to assist in stall recovery.

From these observations it was concluded that the CC air mass flow requirements may be provided by a relatively light weight Auxiliary Power Plant (APU) and this solution was chosen for the *Demon* UAV. The APU selected for the project is a micro turbo-shaft engine driving a compressor wheel delivering pressurised air and designed by Wren Turbine Ltd. Details of the APU can be found in Lawson (2008). This solution was envisaged as a risk reduction; besides not losing any thrust, the power can be controlled separately from the main engine thrust setting In this manner the blowing pressure is independent of the thrust level, thereby simplifying the operation with CC and the flight control system design. However, these advantages are counteracted by an increase in weight and cost. Fortunately, those implications are mitigated by the position of the APU in the *Demon* aircraft. The APU is envisaged to be mounted inside the nose fairing; this will help moving the *cg* forward to achieve the desired level of stability, actually reducing the amount of balance required.

7 FLIGHT CONTROL SYSTEM DESCRIPTION

7.1 Introduction

This chapter describes the proposed flight control system (FCS) installation for the *Demon* UAV developed under the umbrella of the EPSRC/BAE Systems FLAVIIR research programme.

The FCS has been tailored around the *Demon* UAV configuration for the first flight test campaign. This utilizes four trailing edge devices per wing, only three of which are of a conventional design (Surfaces No. 1, 3 and 4), where the fourth (Surface No. 2) is a novel technology implementation of a circulation control system (CC) device. In addition to the CC devices, a fluidic thrust vectoring system (FTV) is applied to the vehicle providing control over the exhaust jet direction within the engine nozzle. A conventional control surface is used for the fin and rudder assembly.

The pressurised air to power the circulation control system (CCS) is provided using an APU located in the nose bay, between the front bulkhead and nose-wheel attachment. The APU is a micro turbo-shaft engine driving a centrifugal compressor wheel delivering an absolute maximum pressure of 1.7bar at a maximum temperature of 300K. Figure 7-1 shows the *Demon* model with the main systems installed.

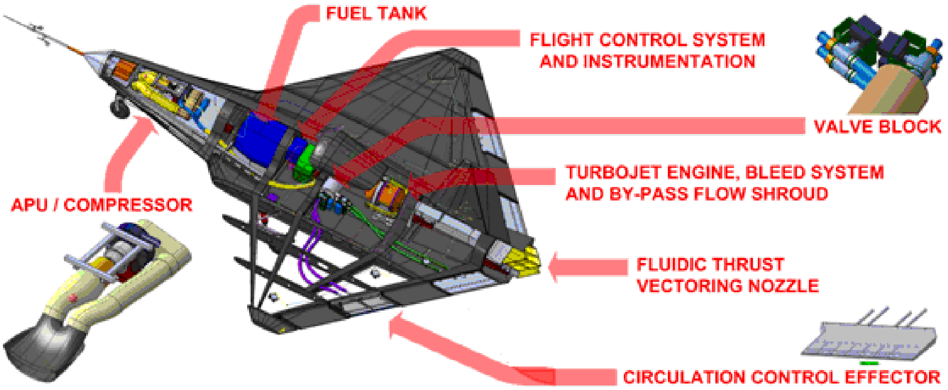

Fig 7-1. Demon global systems view

The *Demon* FCS is based on the FCS developed and flight proven by Cranfield Aerospace (CAe) on the *Observer* UAV system. An overview description of the CAe miniature digital system hardware can be found in Cook, (2007b). The original FCS architecture has been modified to meet the explicit functional requirements of *Demon.*
The FCS is separated into a primary system and an advanced guidance system. The semi-autonomous system philosophy provides for a safety pilot who can take over from the autonomous system at any time during a flight. In view of the relatively high risk associated with the flapless control features of *Demon,* the semi-autonomous control philosophy is proposed and that the primary control and trim functions will remain on-line at all times under the command of a safety pilot. Thus the safety pilot can engage and disengage the advanced guidance and control functions, and can intervene at any time to recover control of the vehicle, or to make small flight path adjustments whilst under auto-pilot control.
The development of the advanced guidance system is beyond the main purpose of the research reported in this thesis. The aim is to propose an architecture with provision for switching to alternative advanced primary control laws in flight and a level of flexibility to facilitate future experimental flight research.

The primary flight control system retains the same functionality as that designed by CAe but with modifications to allocate commands to the various flap and flapless motivators, to allow for conventional take-off and landing (rather than catapult launch and parachute recovery) and to provide a degree of safety in the event of failure of the flapless controls.

The assumed operating procedure for the proposed flight test demonstrations determines the primary flight control system architecture. The safety pilot will execute a conventional take-off, climb to safe altitude and establish *Demon* in level flight cruise at the specified trim condition. The pilot may then engage the primary flight control system and execute demonstration manoeuvres using flow control devices. The pilot may also engage the advanced guidance system which will execute a pre-programmed demonstration manoeuvre entirely automatically, provided he keeps his hands off the controls during the demonstration. On completion of the manoeuvre, the pilot will disengage the advanced guidance system and complete a manual recovery, approach and landing in the usual way. This is considered to be a safe procedure since the vehicle trim condition is not lost during the demonstration.

7.2 Primary flight control system architecture

The main features of the primary flight control system retain those of the CAe FCS with modifications to facilitate the flapless control devices interface and simplifications to ease the interface conditions for the advanced guidance and control algorithms. The longitudinal FCS architecture is shown on Fig.7-2 and the lateral-directional FCS architecture is shown on Fig.7-3 and both are self explanatory. A description of sensed and internal FCS variable is given in Table 7-1. The main functional features of the FCS are summarised as follows, and these should be considered in the context of the figures to which they relate.

- Manually set roll, pitch and yaw trim is held on the mechanical flying control surfaces such that in the event of loss of air supply to the flapless controls, or loss of the engine the trim condition is not lost. Also, by holding trim on the mechanical flap controls the problems associated with constant flow vector offset and constant trim air supply demand are avoided.
- Normal operating mode primary piloted flight control is made by means of a conventional roll/pitch stick spring loaded to centre such that in trim the command signal outputs are zero. The command characteristic is *attitude command* since that has been adopted by CAe and demonstrated to provide a sound strategy for remote control of a small UAV. In normal operation roll and pitch commands are routed via the flapless flow control devices. A proportional system with no integral feedback is used, so as to make mode switching easy in that the integrator initial conditions do not need to be remembered or set following an FCS mode change.
- A reversionary piloted flight control mode is incorporated for emergency recovery of the vehicle. This mode can be selected (switch S1) by the pilot at any time, or engaged automatically following engine or air supply failure. This mode provides a direct command from the roll/pitch stick to the

mechanical flying control surfaces in the manner of a radio controlled model aircraft. Consequently, when engaged this mode provides a *rate command* characteristic.

- Engine thrust is not commanded directly. Instead, it is incorporated into a speed command loop which is tailored to avoid rapid changes in thrust demand and includes a minimum thrust protection limit (F1). Airspeed demand (trim) is selected manually by the pilot. Again this is a proportional feedback with no integral feedback. By demanding airspeed rather than thrust, the control loop will automatically compensate for thrust droop in the presence of variable compressor air bleed for the fluidic thrust vectoring control systems.
- Provision is made for simple three axis rate stabilisation and the loops are closed around the mechanical flying control surfaces only. This avoids additional demands on the flapless controls and ensures that stabilisation remains effective, along with trim, following emergency reversion to rate command. The p,q and r feedback are limited so that a gyro failure would not result in a hard-over of the control surfaces.
- Control input mixing is avoided to simplify the system and to enable the advanced guidance and control algorithms to drive directly on to the primary control motivators, with the exception of engine thrust. Engine thrust is controlled indirectly via the speed demand loop.
- Turn coordination functions are included in the attitude command system to assist pilot manoeuvring. These functions are not available in the emergency rate command mode.
- The advanced guidance and control algorithms may be engaged/disengaged (switch S2) by the safety pilot at any time during flight. Once engaged, additional switching may be required to activate the various navigation modes.

Variable	Description	Sense
V_{da}	Airspeed demand from advanced controller	+ve increase
V_d	Trim airspeed demand (pilot)	+ve increase
δ_{pitch}	Pitch stick position (pilot)	+ve stick pull
δ_{roll}	Roll stick position (pilot)	+ve stick to starboard
ϕ_d	Roll attitude demand	+ve starboard wing down
η	Elevator angle	+ve trailing edge down
η_d	Elevator angle demand	+ve trailing edge down
η_{da}	Elevator angle demand from advanced controller	+ve trailing edge down
η_τ	Equivalent fluidic elevator angle	+ve trailing edge down
$\eta_{\tau d}$	Equivalent fluidic elevator angle demand	+ve trailing edge down
$\eta_{\tau da}$	Equivalent fluidic elevator angle demand from advanced controller	+ve trailing edge down
η_{trim}	Elevator angle to trim	+ve trailing edge down
θ_d	Pitch attitude demand	+ve nose up
θ_{trim}	Pitch attitude to trim (pilot)	+ve nose up
τ	Thrust	+ve forward
τ_d	Thrust demand	+ve forward
ξ	Aileron angle	+ve starboard TE down
ξ_{cc}	Equivalent circulation control aileron angle	+ve starboard TE down
ξ_{ccd}	Equivalent circulation control aileron angle demand	+ve starboard TE down
ξ_{ccda}	Equivalent circulation control aileron angle demand from advanced controller	+ve starboard TE down
ξ_d	Aileron angle demand	+ve starboard TE down
ξ_{da}	Aileron angle demand from advanced controller	+ve starboard TE down
ξ_{trim}	Aileron angle to trim (pilot)	+ve starboard TE down
ζ	Rudder angle	+ve TE to port
ζ_d	Rudder angle demand	+ve TE to port
ζ_{da}	Rudder angle demand from advanced controller	+ve TE to port
ζ_{trim}	Rudder angle to trim (pilot)	+ve TE to port

Table 7-1. Flight control system variables

7.3 FCS hardware description

The FCS system hardware comprises the Blue Bear Systems Research Ltd (BBSR) generic FCS module: SNAP; SNAP is a single board computer which runs a Linux based operating system with a unique application called *snapharness.* An overview of the system is given in Smith, (2008). SNAP includes a number of Micro Electrical Mechanical Sensors (MEMS); these provide basic rate, acceleration and pressure readings to the control law. *Snapharness* uses this data to provide body attitudes. SNAP uses a standard onboard SD card for logging all flight data and therefore providing expandable memory capacity.

It is intended that the *Demon* FCS will utilise the same hardware installation with the minimum number of modifications tailored to meet the needs of the application. Proposed modifications include increase the number of PWM servo drive outputs from the current 8 to match the number of independent controlled elements in *Demon*.

Furthermore, due to SNAP's open architecture, the FCS software code implemented in SIMULINK will be exported to SNAP using the Real Time Workshop (RTW).

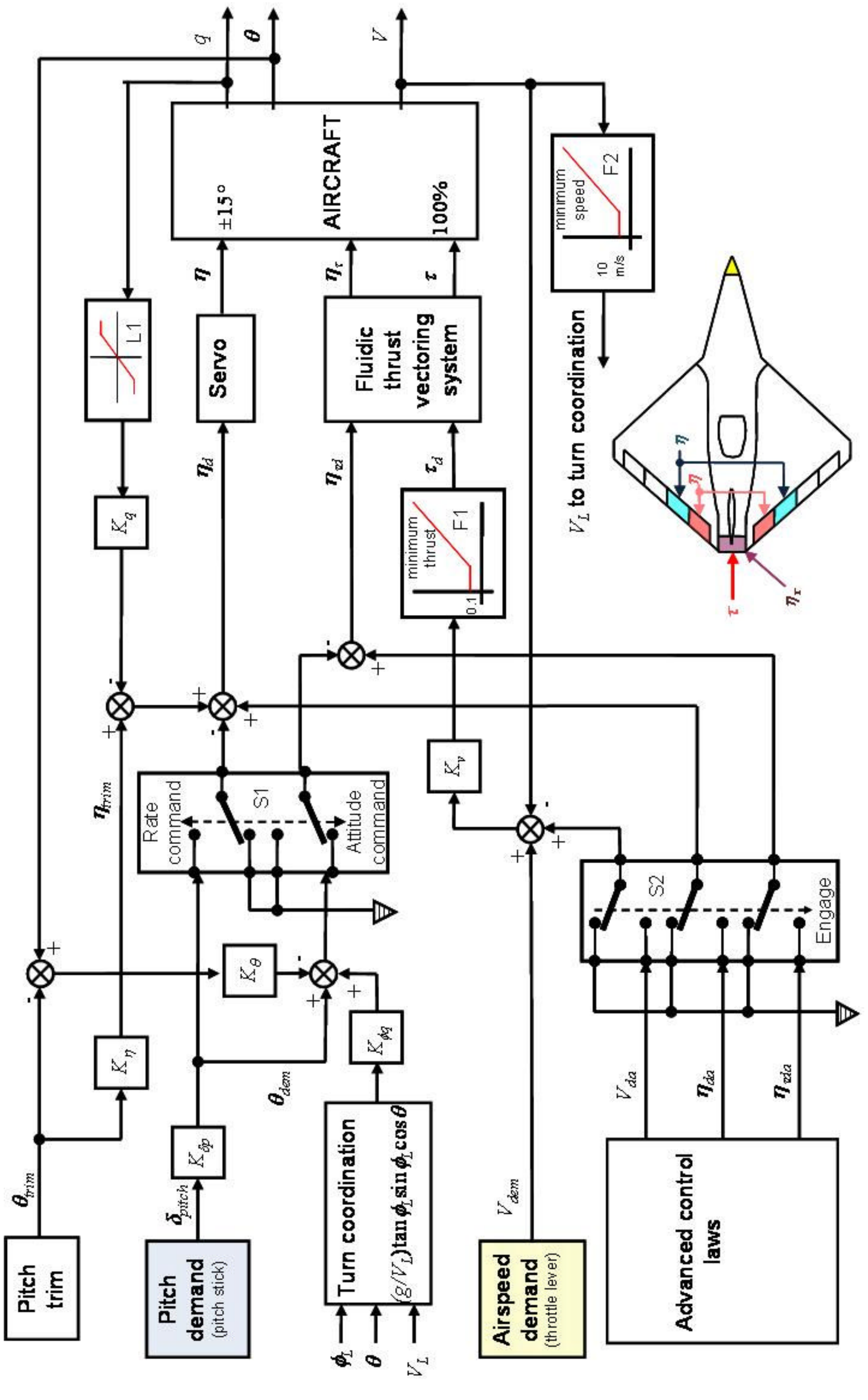

Fig 7-2. Longitudinal Primary Flight Control System

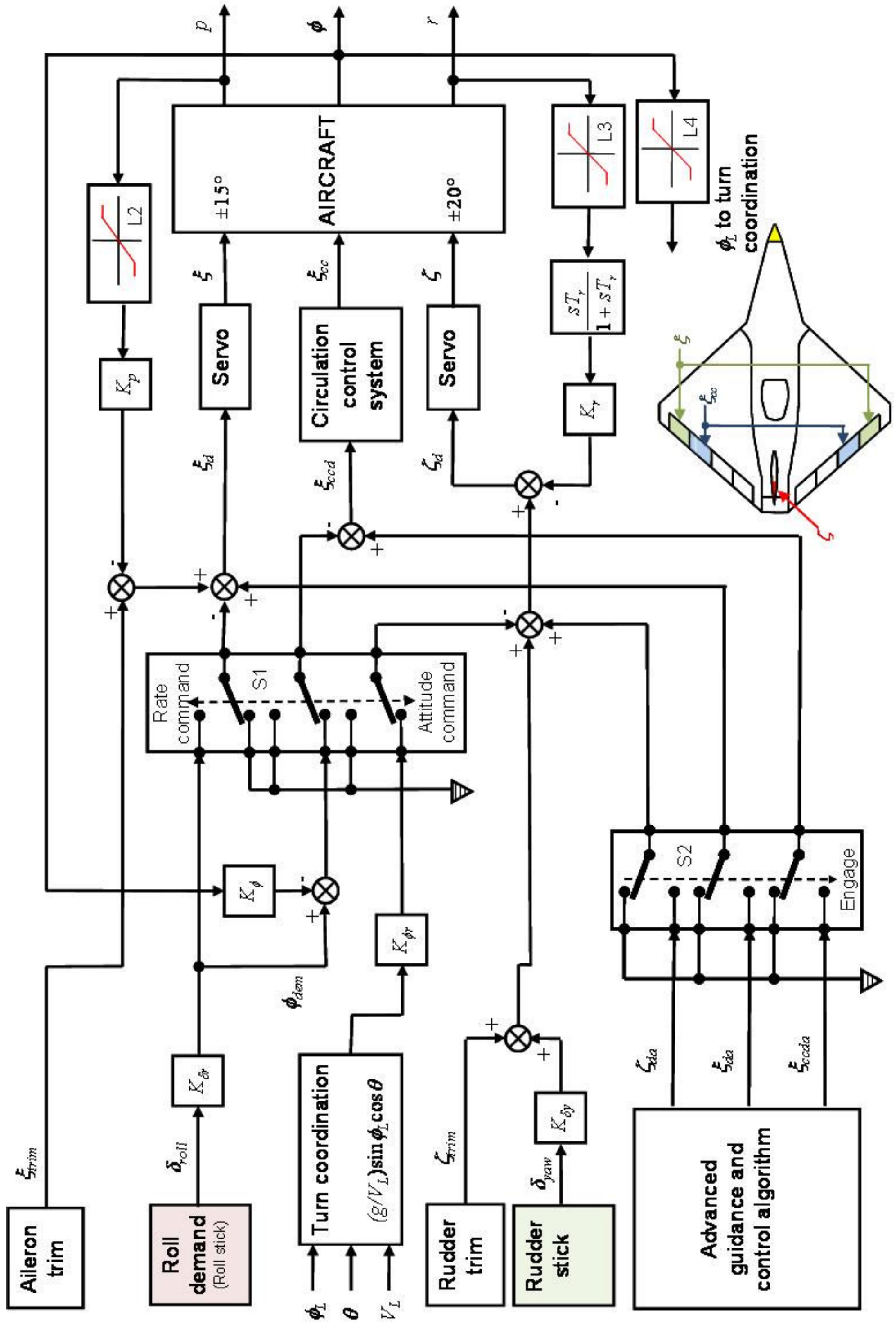

Fig 7-3. Lateral – Directional Primary Flight Control System

8 FLIGHT CONTROL SYSTEM DESIGN

8.1 Longitudinal primary flight control system

The following sections describe the design of the longitudinal primary Flight Control Systems (FCS). The final design of the longitudinal architecture is of the form presented in Fig. 8-1. The main functional features of the longitudinal Flight Control System are summarised as follows:

- Manually set pitch trim is held on the mechanical flaps (surfaces No.3 and No. 4) such that in the event of loss of air supply to the flapless controls, or loss of the engine the trim condition is not lost. Also, by holding trim on the mechanical flap controls the problems associated with constant flow vector offset and constant trim air supply demand are avoided.
- The command characteristic is *attitude command.* Although provision has been made such that in normal operation pitch commands are routed via the flapless flow control devices, the design of flapless flight control system for the longitudinal axis is beyond the purpose of this study. In the design, described here, pitch command is routed via the mechanical flaps.
- Engine thrust is not commanded directly. Instead, it is incorporated into a speed command loop which is tailored to avoid rapid changes in thrust demand. Airspeed demand (trim) is selected manually by the pilot.
- Provision is made for longitudinal axes rate stabilisation and the loop is closed around the mechanical flying controls (surfaces No.3 and No. 4) only.
- Turn coordination functions are included in the attitude command system to assist pilot manoeuvring.

8.2 Longitudinal Stability Augmentation System design

In the absence of flying qualities requirements for UAV's, piloted aircraft flying qualities have been applied as suggested by (Prosser & Wiler, 1976) and those have been shown in Chapter 4.

Gains have been chosen to meet the design objectives of the longitudinal Stability Augmentation System (SAS), which were:

- Increase Short Period Pitching Oscillation (SPPO) damping ratio to 0.7 across the flight envelope. This value allows for any degradation to stability that may occur when the other loops are closed subsequently.
- To augment the response characteristics so that the steady state is reached with appropriate rise time.
- To endow the aircraft with good long term holding characteristics.

The design process is described for one specific flight condition. Initially the design was carried out in the linear environment using the linearized model extracted from the non-linear simulation. The performance of this design was then verified in the non- linear environment.

The design process assumes, in the first instance, that the dynamics of the gyro sensors are not intrusive and may be ignored. However, the effect of the actuator and engine lag has been assessed during the design process.

The systems consist of a pitch rate feedback to elevator with a gain in the feedback path, plus pitch attitude feedback to elevator with a gain in the feedback path. The auto-throttle consists of a proportional feedback of the speed error to the throttle. Elevator trimming requirements are provided by means of a look up table, which is to contain the required elevator to trim scheduled with flight speed velocity, as shown in Fig. 8-2.

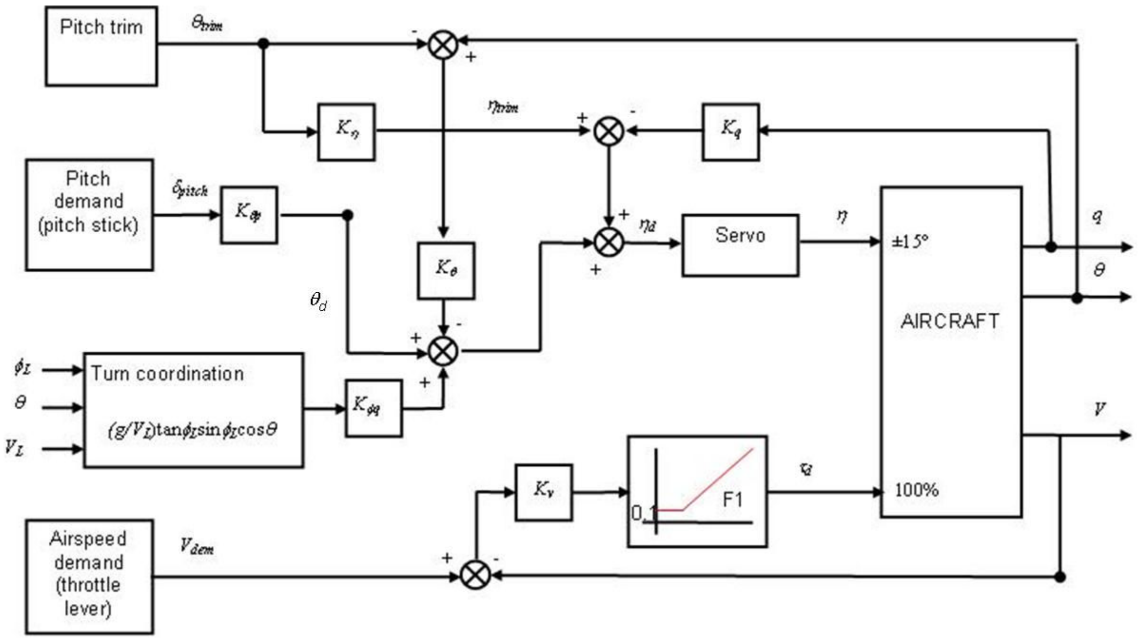

Fig. 8-1. Longitudinal flight control system architecture

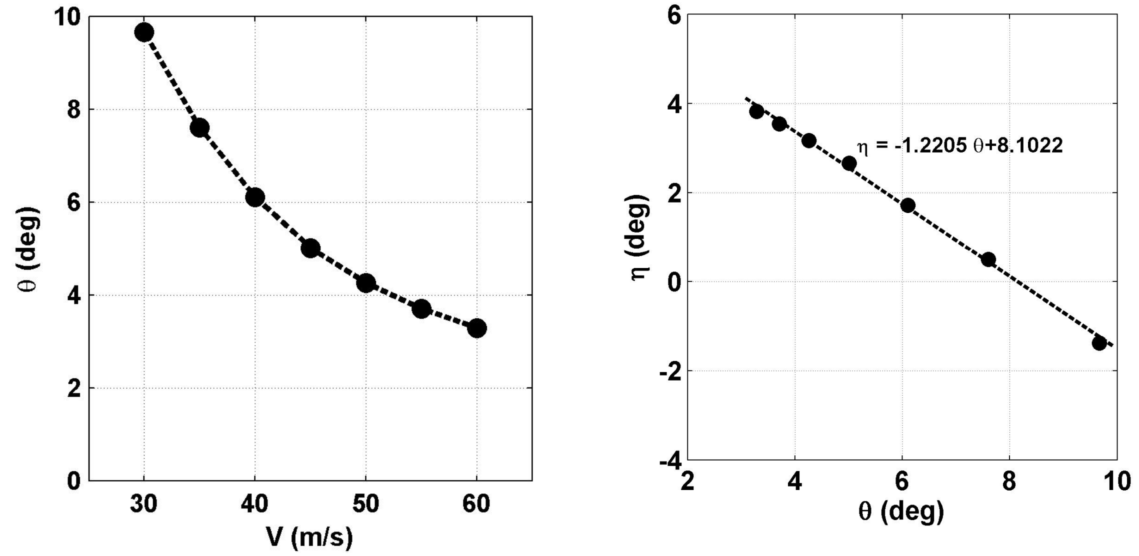

Fig. 8-2. Pitch trim design

Assuming the aircraft in trimmed straight and level flight, the control law relating attitude demand to elevator is given by Eq. (8-1):

$$\eta_d = \theta_d - K_\theta(\theta - \theta_{trim}) - K_q q + \eta_{trim} \tag{8-1}$$

Note that Eq. (8-1) omits turn coordination feeback.

The control law relating engine speed to speed demand is given by Eq. (8-2):

$$\tau_d = K_v(V_d - V) \tag{8-2}$$

8.2.1 Longitudinal stability augmentation system closed loop analysis

The dynamics of the aircraft model in a level flight cruise condition at 130m altitude and 40m/s true airspeed, are given by the state description,

$$\dot{\mathbf{x}} = \mathbf{A}\mathbf{x} + \mathbf{B}\mathbf{u}$$

$$\begin{bmatrix} \dot{u} \\ \dot{w} \\ \dot{q} \\ \dot{\theta} \end{bmatrix} = \begin{bmatrix} -0.0578 & 0.32 & -4.133 & -9.754 \\ -0.1682 & -3.009 & 38.59 & -1.045 \\ 0.0785 & -0.7328 & -2.189 & 0 \\ 0 & 0 & 1 & 0 \end{bmatrix} \begin{bmatrix} u \\ w \\ q \\ \theta \end{bmatrix} + \begin{bmatrix} -0.0004 \\ -0.2647 \\ -0.6621 \\ 0 \end{bmatrix} \eta \tag{8-3}$$

The basic aircraft state equation was then augmented with the actuator dynamics. The reader is referred to Chapter 4 for a description of the actuator model. The actuator state equation can be realised in controllable companion form,

$$\begin{bmatrix} \dot{\eta} \\ \dot{v}_\eta \end{bmatrix} = \begin{bmatrix} 0 & 1 \\ -625 & -30 \end{bmatrix} \begin{bmatrix} \eta \\ v_\eta \end{bmatrix} + \begin{bmatrix} 0 \\ 625 \end{bmatrix} \eta_d \tag{8-4}$$

When the coefficient matrices (8-3) are augmented by the addition of Eq. (8-4) to introduce the actuator dynamics, the result is:

$$\dot{x} = \begin{bmatrix} & & & & & 0 \\ & \mathbf{A} & & \mathbf{B} & & 0 \\ & & & & & 0 \\ & & & & & 0 \\ 0 & 0 & 0 & 0 & 0 & 1 \\ 0 & 0 & 0 & 0 & -625 & -30 \end{bmatrix} \begin{bmatrix} u \\ w \\ q \\ \theta \\ \eta \\ v_\eta \end{bmatrix} + \begin{bmatrix} 0 \\ 0 \\ 0 \\ 0 \\ 0 \\ 625 \end{bmatrix} \eta_d \tag{8-5}$$

The purpose of the pitch SAS is to provide satisfactory damping for the short period mode. The feedback of pitch rate to elevator control will modify the damping and the phugoid mode will be largely unaffected by this feedback.

The open loop state Eq. (8-5) can now be used to obtain the transfer functions needed for root locus design, at the design flight condition. The transfer function from η_d to q is found to be:

$$\frac{q}{\eta_d} = \frac{-23709.7182\,s\,(s+0.09084)\,(s+2.979)}{(s^2+0.06074s+0.0993)\,(s^2+5.195s+35.13)\,(s^2+30s+625)}\,\frac{\mathrm{deg}}{\mathrm{deg}\cdot s} \qquad (8\text{-}6)$$

The stability modes of the open loop aircraft (actuator modes are not shown) are:

$$\begin{aligned} \text{Phugoid damping ratio} \quad & \zeta_p = 0.096 \\ \text{Phugoid undamped natural frequency} \quad & \omega_p = 0.315\ \text{rad/s} \\ \text{Short period damping ratio} \quad & \zeta_s = 0.438 \\ \text{Short period undamped natural frequency} \quad & \omega_s = 5.93\ \text{rad/s} \end{aligned}$$

Fig. 8-3 shows the root-locus plot for negative values of K_q. As the pitch rate feedback is increased the short period damping is rapidly increased and the poles become real for relatively low values of K_q. A practical value of gain is K_q=-0.1rad/rad/s which increases the short period damping to 0.7, simultaneously increasing the natural frequency of the mode to 7.54rad/s. At this value of feedback gain the change in phugoid characteristics are almost insignificant.

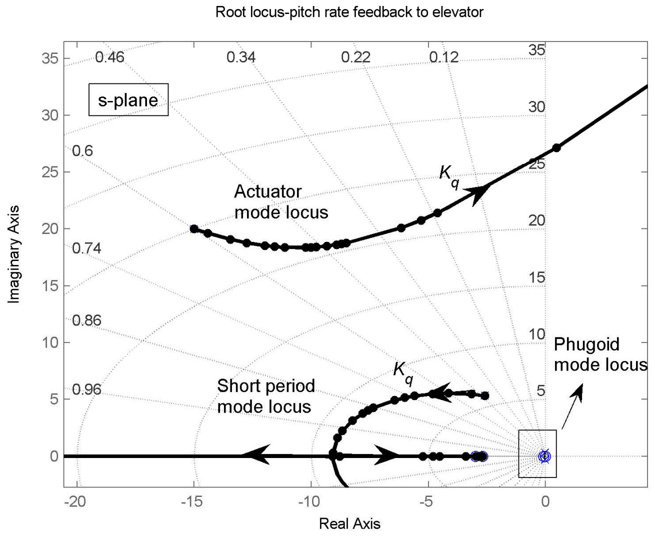

Fig. 8-3. Root locus plot —pitch rate feedback to elevator

8.2.2 Attitude command loop design

The design process for the pitch attitude command loop uses the inner loop from the previous paragraph and linearizes the complete dynamics (aircraft plus inner loop) with pitch attitude angle as an output, under the same flight condition.

The transfer function from the pitch rate command to the pitch attitude angle is given by:

$$\frac{\theta}{q_d} = \frac{-23709.7182\, s\,(s+0.09084)\,(s+2.979)}{(s^2+0.06242s+0.07678)\,(s^2+10.56s+56.92)\,(s^2+24.63s+498.9)}\,\frac{\text{deg}}{\text{deg/s}} \quad (8\text{-}7)$$

K_θ is designed primarily to give good command characteristic without upsetting closed loop stability. The effect of pitch attitude feedback on transfer function (8-7) can be deduced from the root locus in Fig. 8-4. The root locus plot, pitch attitude feedback to elevator for negative values of K_θ, when K_q=-0.1rad/rad/s, shows that the phugoid poles move to the real axis and eventually they terminate on the two remaining zeros. When the effect of actuator is taken into account the short period poles must move toward the right half plane. Thus the short period becomes less damped and the phugoid damping increases. A pitch attitude feedback gain of K_θ= -0.3 rad/rad was chosen which would result in a good level of closed loop phugoid stability without reducing the short period mode stability too much.

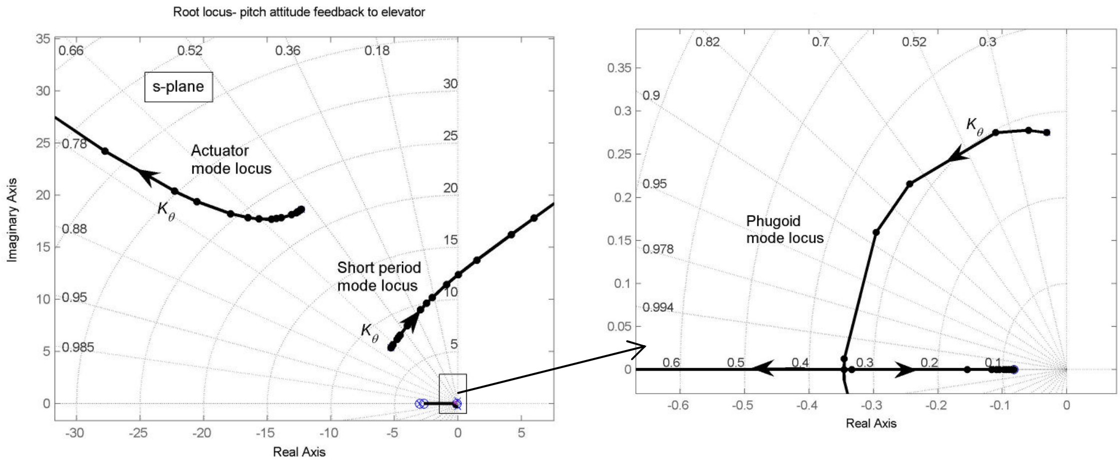

Fig. 8-4. Root locus plot—pitch attitude feedback to elevator

Thus the longitudinal stability modes have been augmented to:

$$\begin{aligned} \text{Phugoid damping ratio} \quad & \zeta_p = 0.97 \\ \text{Phugoid undamped natural frequency} \quad & \omega_p = 0.34 \text{ rad/s} \\ \text{Short period damping ratio} \quad & \zeta_s = 0.6 \\ \text{Short period undamped natural frequency} \quad & \omega_s = 7.9 \text{ rad/s} \end{aligned}$$

8.3 Auto-throttle design

The auto-throttle loop consists of a speed error feedback to throttle through a proportional controller. The throttle servo and engine response has been modelled by a single 3s lag. The stability characteristic of the SPPO will remain almost the same, while the phugoid will be replaced by two non oscillatory modes: the surge mode and the heave mode. The design of the auto-throttle loop was carried out in the non-linear environment, where adjustments of the gain were made.

8.4 Longitudinal Stability Augmentation System gains selection

Initially, using the root locus technique, values of the controller gains were determined for each of the flight conditions under consideration in the linear environment. An assessment of these gains was made and it was determined that the gains need not be scheduled. It was found that single values of the two controller gains $K_{q,}$ K_θ could be found that gave a satisfactory performance throughout the flight envelope. This is due to the fact that the longitudinal modes characteristics do not vary significantly in the flight envelope considered, as it was observed in Chapter 4; the short period damping ratio is almost constant in the range of velocity considered.

Having used the root locus technique to determine values of the controller gains that gave the required stability characteristics, the gains were adjusted accordingly so as to augment the response shape, while maintaining the nominal stability characteristics. The values of the controller gains were then assessed in the non-linear environment, where small tuning adjustments were made.

As per the auto-throttle loop, the values of proportional gains were checked in the non linear environment and they were assessed so as to maintain the indicated airspeed within 2% of the reference speed, while maintaining the stability of the closed loop. The values of the controller gains that were assessed as being suitable to achieve the design objective are presented in Table 8-2.

Controller gain	Value
K_q (rad/rad/s)	-0.1
K_θ (rad/rad)	-0.3
K_v (%/m/s)	35

Table 8-2. Longitudinal controller gains

As classical control method has been used, any uncertainties in the aerodynamic data are implicitly allowed for in the design process. The safety allowance will still be adequately satisfactory. The augmented air-vehicle is not sensitive to control gain accuracy, because gains have chosen to give enough stability margin for normal operation.

8.5 Lateral primary flight control system

The following sections describe the design of the lateral primary Flight Control Systems (FCS). The final design of the lateral architecture is of the form shown in Fig. 8-5.

The main functional features of the lateral control system are summarised as follows:

- Manually set roll and yaw trim is held on the mechanical flying control surfaces (Surface No. 1 and rudder) such that in the event of loss of air supply to the flapless controls the trim condition is not lost.
- The lateral command characteristic is *roll attitude command*. In normal operation roll commands are routed via the CC devices.
- The power required for blowing with circulation control is to be provided by an APU. Air is supplied continuously to the plenum chamber at a constant total pressure at a value sufficient to endow the aircraft with acceptable lateral control in the flight envelope. The internal airflow is not modulated and therefore the actuation of the main trailing edge bar is the only input to the system.

- Provision is made for a lateral axes rate stabilisation and the loops are closed around the mechanical flying control surfaces only (surfaces No.4 and rudder).
- Turn coordination functions are included in the attitude command system to assist pilot manoeuvring.

8.6 Lateral Stability Augmentation System design

In the absence of flying qualities requirements for UAV's, piloted aircraft flying qualities have been applied as suggested by Prosser and Wiler (1976) and those were shown in Chapter 4.

From the analysis of the stability properties (Chapter 3-4) the objectives of the lateral SAS were defined. These are:

- To improve stability of the spiral mode across the flight envelope.
- Increase dutch roll mode damping ratio to 0.5 across the flight envelope.

The design process is described for one specific flight condition. Initially the design was carried out in the linear environment using the linearized model extracted from the non-linear simulation. The performance of this design was then verified in the non- linear environment.

The design process assumes, in the first instance, that the dynamics of the gyro sensors are not intrusive and may be ignored. However, the effect of the actuators has been assessed during the design process.

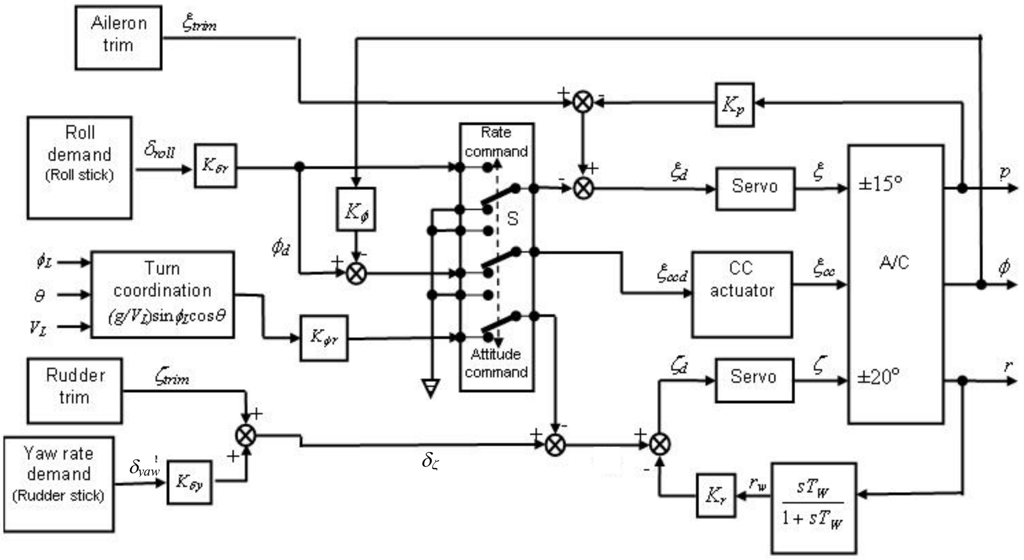

Fig. 8-5. Lateral flight control system

8.6.1 Lateral Stability Augmentation System architecture

The system consists of roll rate feedback to aileron, with a gain in the feedback path, plus roll attitude feedback to CC actuator with a gain in the feedback path. Yaw rate is fedback to the rudder to augment the damping ratio of the dutch roll mode. A wash-out filter has been added to the yaw rate feedback loop to prevent yaw rate feedback opposing the turn during steady turning flight.

It can be seen that the control law relating roll attitude demand to CC actuator is given by Eq. (8-8):

$$\xi_{ccd} = \Phi_d - K_\Phi \Phi \tag{8-8}$$

Inner loop stability augmentation is held on the conventional mechanical aileron (normally, ξ_{trim}= 0):

$$\xi_d = -K_p p \tag{8-9}$$

For the directional control axis, the control law is given by Eq. (8-10):

$$\zeta_d = \delta_\zeta - K_r\left(\frac{sT_w}{1+sT_w}\right)r \qquad (8\text{-}10)$$

Note that Eq. (8-10) omits turn coordination feeback.

8.6.2 Lateral stability augmentation system closed loop analysis

The dynamics of the aircraft model in a level flight cruise condition at 130m altitude and 40m/s true airspeed, are given by the state description,

$$\begin{bmatrix} v \\ p \\ q \\ r \end{bmatrix} = \begin{bmatrix} -0.3177 & 4.6258 & -39.7333 & 9.7542 \\ -3.2417 & -70.3965 & 3.1240 & 0 \\ 0.7001 & 1.5980 & -3.5877 & 0 \\ 0 & 1.0000 & 0.0107 & 0 \end{bmatrix} \begin{bmatrix} v \\ p \\ q \\ r \end{bmatrix} + \begin{bmatrix} 0.0136 & 0.0136 & 0.1010 \\ -2.4734 & -5.2749 & 0.6181 \\ 0.0105 & 0.0482 & -0.3694 \\ 0 & 0 & 0 \end{bmatrix} \begin{bmatrix} \xi \\ \xi_{cc} \\ \zeta \end{bmatrix} \qquad (8\text{-}11)$$

The state equations have been augmented with the actuator models (rudder, aileron and CC servo respectively) and a washout filter. The washout filter time constant T_w is normally of the order of 1s and $T_w = 1$ s is used here, since it was found to be quite satisfactory.

The solution of Eq. (8-11) leads to the open loop transfer functions needed for root locus design, at the design flight condition. The transfer functions of primary interest are:

$$\frac{r_W}{\varsigma} = \frac{-13229.1375\, s\,(s+67.57)\,(s^2+0.2772s+0.2988)}{(s+70.22)\,(s+0.02425)\,(s^2+4.06s+27.03)\,(s^2+30s+625)(s+1)}\,\frac{\text{deg}}{\text{deg}\,s} \qquad (8\text{-}12)$$

$$\frac{r_W}{\xi} = \frac{376.0312\, s\,(s-307.4)\,(s^2+2.58s+5.13)}{(s+70.22)\,(s+0.02425)\,(s^2+4.06s+27.03)\,(s^2+30s+625)(s+1)}\,\frac{\text{deg}}{\text{deg}\,s} \qquad (8\text{-}13)$$

$$\frac{r_W}{\xi_{cc}} = \frac{689.748\, s\,(s-107.5)\,(s^2+3.425s+6.66)}{(s+70.22)\,(s+0.02425)\,(s^2+4.06s+27.03)\,(s^2+25.5s+225)(s+1)}\,\frac{\text{deg}}{\text{deg}}. \qquad (8\text{-}14)$$

$$\frac{p}{\varsigma_c} = \frac{22135.7063\,(s-0.02579)\,(s-6.354)\,(s+7.888)}{(s+70.22)\,(s+0.02425)\,(s^2+4.06s+27.03)\,(s^2+30s+625)}\,\frac{\text{deg}}{\text{deg}\,s} \qquad (8\text{-}15)$$

$$\frac{p}{\xi}=\frac{-88578.6375\,(s-0.02511)\,(s^2+3.935s+28.56)}{(s+70.22)\,(s+0.02425)\,(s^2+4.06s+27.03)\,(s^2+30s+625)}\frac{\deg}{\deg s} \tag{8-16}$$

$$\frac{p}{\xi_{cc}}=\frac{-75571.0252\,(s-0.02511)\,(s^2+3.91s+27.89)}{(s+70.22)\,(s+0.02425)\,(s^2+4.06s+27.03)\,(s^2+25.5s+225)}\frac{\deg}{\deg s} \tag{8-17}$$

The dutch roll poles are almost cancelled out of the *p/ξ* and *p/ξ_{cc}* transfer function by the complex zeros. Therefore weak coupling exists between the rolling and yawing motions. At higher angle of attack the dutch roll poles will typically not be cancelled out and the dutch roll mode will involve greater yaw – roll couplings.

The lateral – directional stability mode characteristics are as follows (actuator mode and wash out time constant not reported):

Dutch roll damping ratio	$\zeta_d = 0.390$
Dutch roll undamped natural frequency	$\omega_d = 5.20$ rad/s
Spiral mode time constant	$T_s = 41.3s$
Roll mode time constant	$T_r = 0.015s$

Roll time constant variation with flight conditions was illustrated in Chapter 4, showing that this time constant was acceptably fast even at high angles of attack corresponding to a landing approach condition, when a good roll response may be needed. Therefore closed loop control of roll rate is not necessary to reduce the variation in aircraft roll performances with flight conditions as the roll-subsidence mode has already a very short time constant.

The required improvement in yaw damping is achieved by the closure of a simple negative feedback loop from a yaw rate gyro sensor to the rudder actuator.

The transfer function relating yaw rate response r_w to the rudder input ζ is Eq. (8-12).

A root locus plot for closing the yaw rate loop through the feedback gain K_r is shown in Fig. 8-6. The role pole is almost exactly cancelled out by a numerator zero in Eq. (8-12). The roll mode is therefore insensitive to this feedback option.

The actuator poles move to the right. As the magnitude of K_r is increased, the spiral mode moves slightly closer to the washout zero at the origin and the washout pole moves toward the complex zero. The dutch roll poles move approximately around an arc of constant natural frequency and increasing damping ratio. For values of feedback gain $K_r < -0.02$rad/rad/sec the dutch roll mode becomes critically damped.

The value of feedback gain chosen for this flight condition is K_r=-0.06rad/rad/sec, which is entirely adequate as it gives a dutch roll damping ratio of ζ_{dr}=0.5. The change into the roll and spiral modes are indiscernible.

The lateral – directional stability mode characteristics are as follow (actuator mode and wash out time constant not reported):

Dutch roll damping ratio	$\zeta_d = 0.534$
Dutch roll undamped natural frequency	$\omega_d = 5.24$ rad/s
Spiral mode time constant	$T_s = 42s$
Roll mode time constant	$T_r = 0.014s$

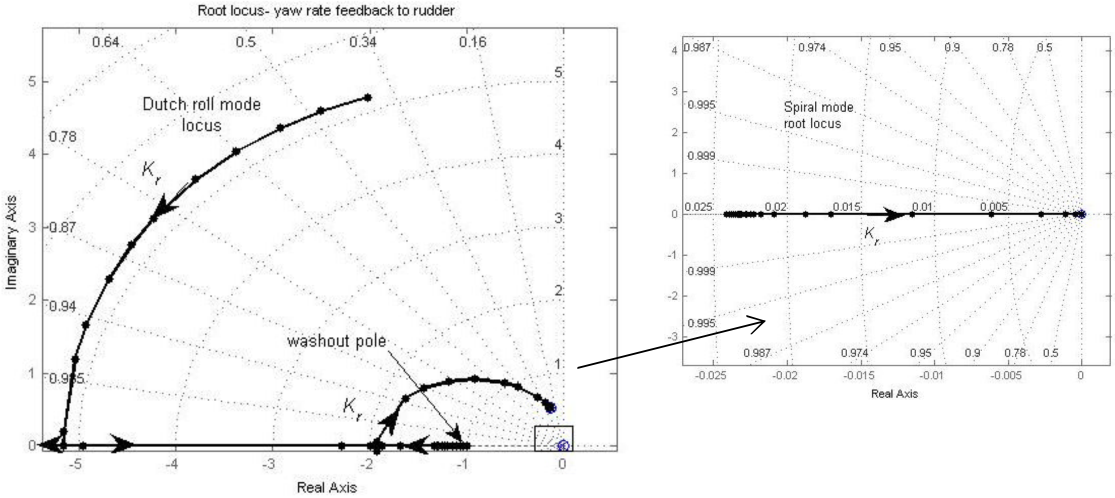

Fig. 8-6. Root locus plot — yaw rate feedback to rudder

A roll attitude command controller has been designed in order to control the bank attitude of the aircraft. K_Φ is designed primarily to give good command characteristic without upsetting closed loop stability. The bank attitude feedback gives the aircraft positive stiffness and stabilizes the spiral mode.

The closed-loop transfer function from the roll rate command to the bank angle is found to be,

$$\frac{\phi}{p_c}=\frac{-75467.1532(s+1)(s^2+3.99s+28.18)}{(s+70.19)(s+1.058)(s+0.02265)(s^2+4.284s+28.51)(s^2+25.5s+216)} \qquad (8\text{-}18)$$

Or, approximately:

$$\frac{\phi}{p_c}=\frac{-75467.1532}{(s+70.19)(s+0.02265)(s^2+25.5s+216)}\frac{\deg}{\deg} \qquad (8\text{-}19)$$

When the bank angle feedback loop is closed around Eq. (8-19) the root locus plot shows that the spiral mode moves to the left the complex poles to the right and the roll rate stability slightly decreases.

At a bank angle feedback gain of K_Φ=0.1 rad/rad the stable spiral mode time constant was T_s~2s. With this value of gain the bank angle control loop is satisfactorily fast. Thus the lateral –directional stability modes have been augmented as per Table 8-3.

Mode	Open loop	Closed loop
Dutch roll damping ratio	0.396	0.533
Dutch roll undamped natural frequency	5.20	5.23 rad/s
Spiral mode time constant	41.3 s	2.87 s
Roll mode time constant	0.015 s	0.015 s
Washout filter time constant	1 s	1.07 s
Rudder actuator frequency	25	24.2
Rudder actuator damping	0.6	0.586
CC actuator frequency	15	~15
CC actuator damping	0.85	~0.85

Table 8-3. Lateral modes of the un-augmented and augmented aircraft

8.6.3 Lateral stability augmentation system gain selection

Initially, using the root locus technique, values of the controller gains were determined for each of the flight conditions under consideration in the linear environment. An assessment of these gains was made and it was determined that there was a significant difference in the magnitude of the gains with increasing speed. As a result it was decided that the values of the controller gains would be scheduled with flight speed.

Having used the root locus technique to determine values of the controller gains that gave the required stability characteristics, the gains were adjusted accordingly so as to augment the response shape, while maintaining the required stability characteristics.

These values of the controller gains were assessed in the non linear environment, where small adjustments were made. The values of the controller gains that were assessed as being suitable to achieve the design objective are presented in Fig. 8-7 and Fig. 8-8.

It is interesting to compare the gain schedules when the roll command is routed via the CC actuator with the case when the roll command is routed via the mechanical aileron (Fig. 8-8 and Fig. 8-9). The aileron effectiveness, as it was described in Chapter 3, varies with angle of attack, becoming smaller at high angle of attack, hence causing undesirable variations in aircraft roll performance. On the other hand the CC actuator effectiveness is not affected by change in incidence but is proportional to the ratio of the jet and free-stream velocity. Therefore it is less effective at high speed for a given jet momentum, although this effect will be partially compensated by the fact the magnitude of the rolling moment is by definition proportional to square of the free stream velocity. These considerations are reflected in the gains scheduling.

The roll response has been assessed with the simulation. In order to capture the modified spiral time constant a step attitude demand has been input. The time response was obtained with the yaw rate and roll rate loops closed with the feedback gains shown above. The input amplitude was adjusted so that response was of similar amplitude for different velocities. Fig. 8-10 exhibits a significant improvement in the bank angle speed of the response at all the velocities tested.

As classical control method has been used, any uncertainties in the aerodynamic data are implicitly allowed for in the design process. The safety allowance will still be adequately satisfactory. The augmented air-vehicle is not sensitive to control gain accuracy, because gains have chosen to give enough stability margin for normal operation.

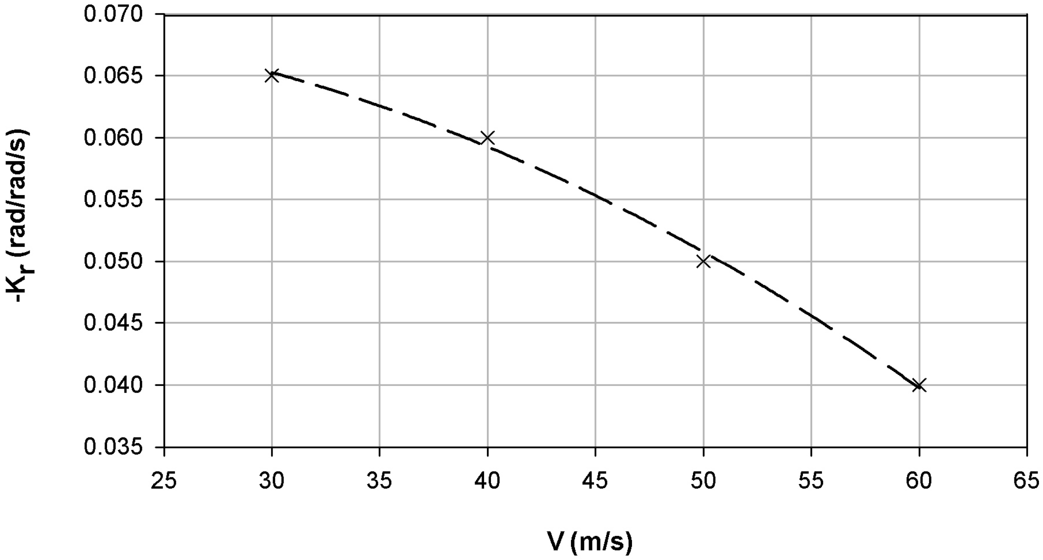

Fig. 8-7. Yaw rate feedback gain to rudder

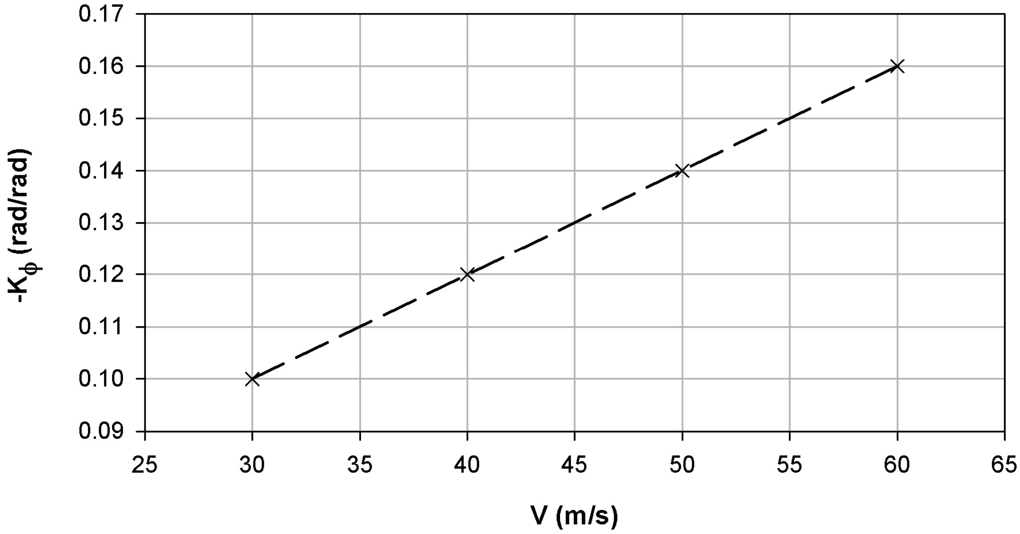

Fig. 8-8. Bank attitude feedback gain to cc actuator

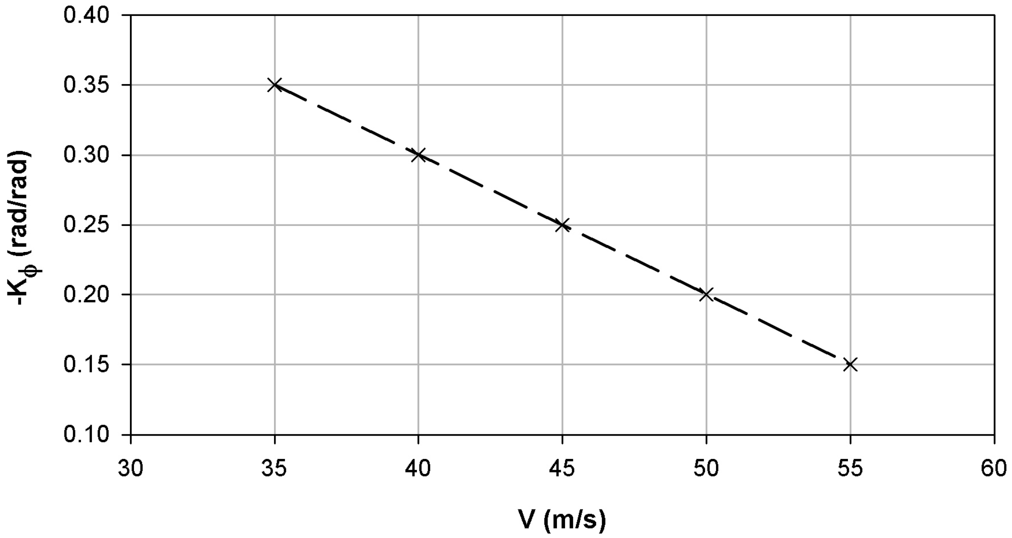

Fig. 8-9. Bank attitude feedback gain to aileron

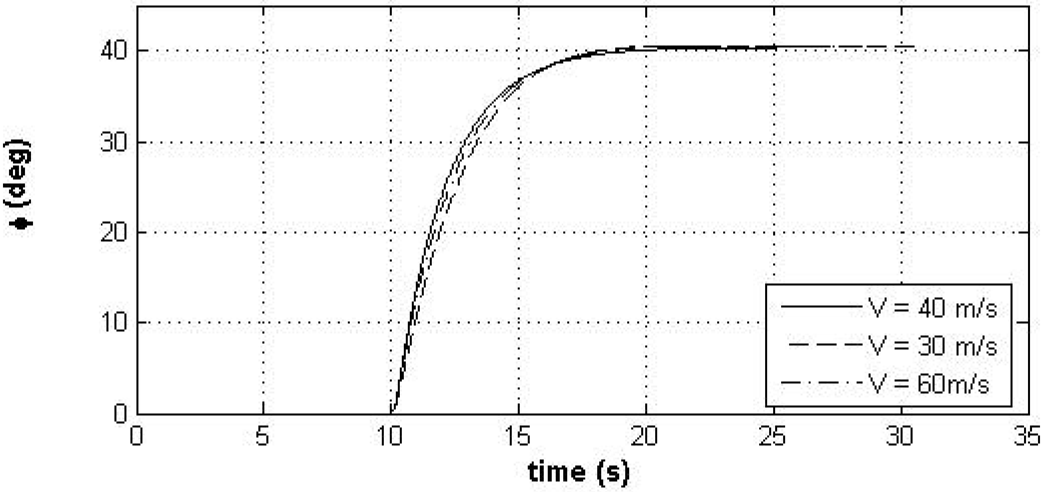

Fig. 8-10. Bank attitude time response

8.7 Turn coordination and turn compensation

If the aircraft is held at some other attitude rather than wings level, additional control systems must be used to control sideslip and pitch rate, so that a coordinated turning motion is produced. In a coordinated turn both the lateral acceleration and the sideslip are zero. The result is that the aerodynamic lift force is normal to the y-axis. This is the most efficient turn since the sideslip is zero, and drag usually increases rapidly with sideslip.

There is additional requirement for turning motion, and this is non zero pitch rate.

The turn can be specified by the Euler angle rate $\dot{\psi}$. Then, given values of the attitude angle ϕ and θ, both the pitch rate and the yaw rate required for a constant altitude turn can be calculated from the kinematic equation as:

$$\begin{bmatrix} q \\ r \end{bmatrix} = \begin{bmatrix} \sin\phi\cos\theta \\ \cos\phi\cos\theta \end{bmatrix} \dot{\psi} = \begin{bmatrix} g/V\tan\phi\sin\phi\cos\theta \\ g/V\sin\phi\cos\theta \end{bmatrix} \tag{8-20}$$

The pitch rate and the yaw rate can be calculated using signals from the gyro sensor and fed back to the pitch rate control system and rudder respectively as a command. This is an open loop control and provides turn compensation that allows the aircraft to be manoeuvred by applying commands to the bank angle control system.

The control law relating attitude demand to elevator, augmented with the turn compensation, is given by Eq. (8-21):

$$\eta_d = \theta_d - K_\vartheta(\theta - \theta_{trim}) - K_q q + K_{\phi q}\left(g/V\tan\phi\sin\phi\cos\theta\right) + \eta_{trim} \tag{8-21}$$

For the directional control axis, the control law augmented with the turn compensation is given by Eq. (8-22):

$$\zeta_d = \delta_\zeta - K_{\phi r}\left(g/V\sin\phi\cos\theta\right) - K_r\left(\frac{sT_w}{1+sT_w}\right)r \tag{8-22}$$

The values of the controller gains were assessed in the non linear environment and they are shown in Table 8-4.

Controller gain	Value
K_{Φ_q}	-0.38
K_{Φ_r}	$-0.004V + 0.38$

Table 8-4. Turn coordination gains

8.8 Stability Augmentation System analysis

8.8.1 Longitudinal dynamics

The simulation has been initialized at a condition of straight and level flight at a velocity of 40m/s and an altitude of 130m. The aircraft response to a pitch demand step input is shown in Fig. 8-11. It is evident that the aircraft response is well damped, the short period being almost indistinct. The pitch response, θ, is smooth and eventually settles down within 5 s. From the elevator angle, η, time history it can be seen that the actuator dynamic is fast compared to the aircraft's response.

The pitch attitude hold characteristic returns the vehicle to a trim attitude at the time manual control manoeuvre inputs are removed, as shown in Fig. 8-12. The vehicle returns to the reference attitude without overshooting.

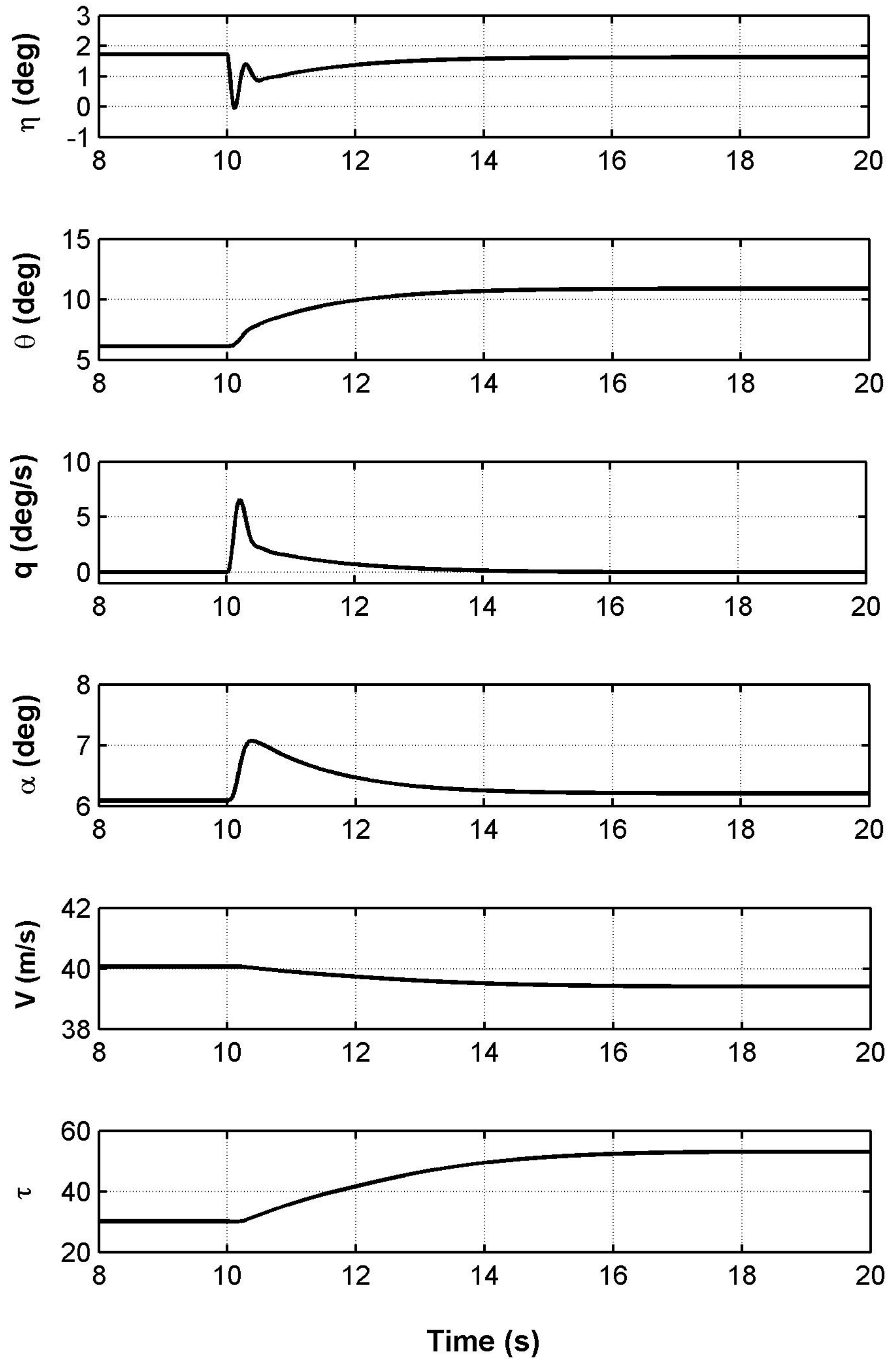

Fig. 8-11.Pitch demand step input-time response

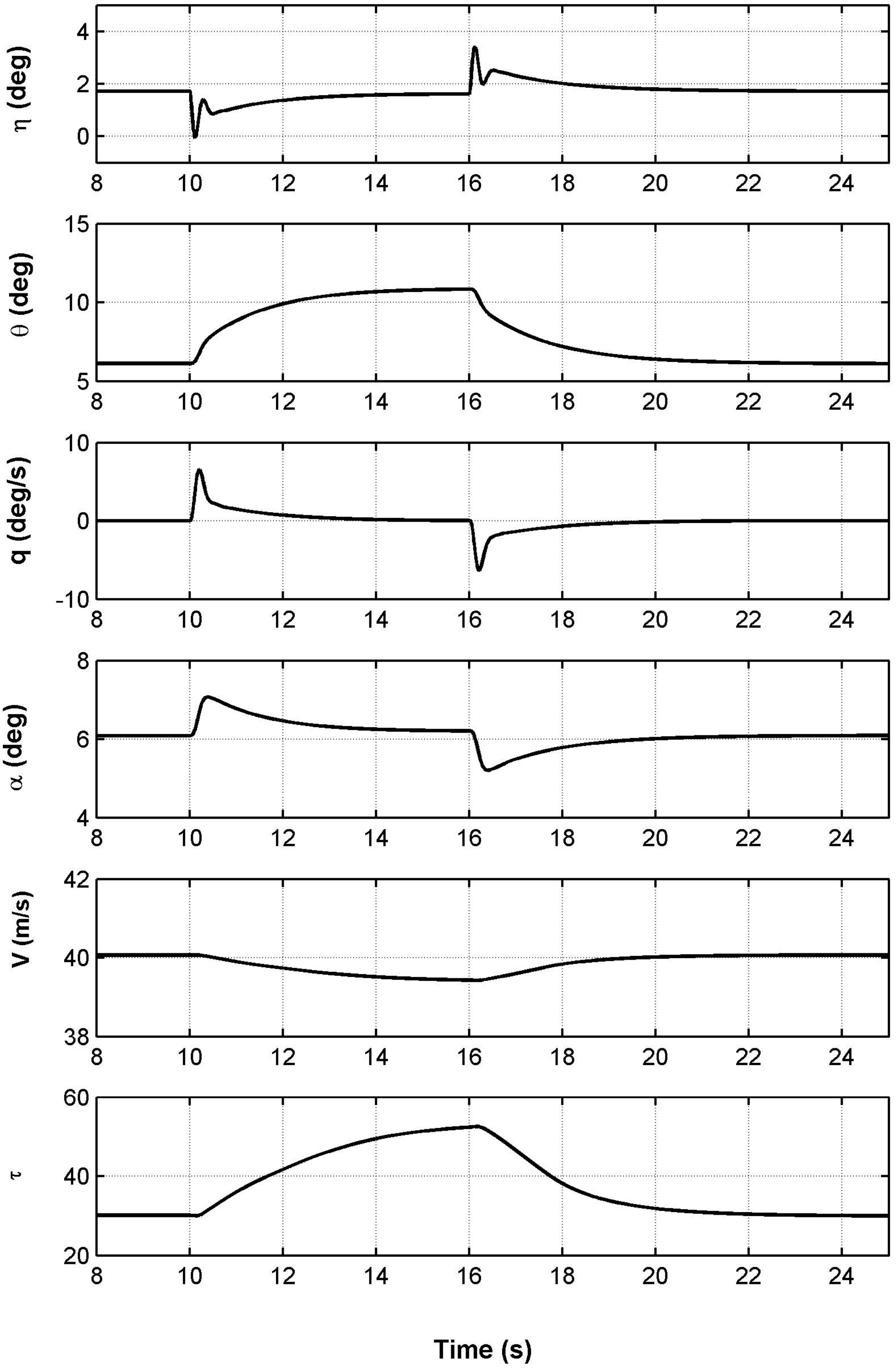

Fig. 8-12.Pitch demand step input-time response

8.8.2 Lateral dynamics

The simulation has been initialized at a condition of straight and level flight at a velocity of 40m/s and an altitude of 121m. A bank angle $\Phi_d = 40^o$ is demanded after 10s. The aircraft enters a coordinated turn of radius R = 200m. Fig. 8-13 shows the longitudinal variables time response during simulation. The speed did not decrease during the 30-s simulation, thanks to the closed loop turn compensation. The altitude is maintained within the accuracies specified in MIL-F-8785C (±60ft for a bank angle between 30-60 deg). Fig. 8-14 shows respectively the lateral variables time response during simulation. The bank angle settled down within 5 s and the response is well damped. The sideslip is kept almost zero through rudder deflection. The control deflections are within limits and sufficiently small to indicate an appropriate gain selection.

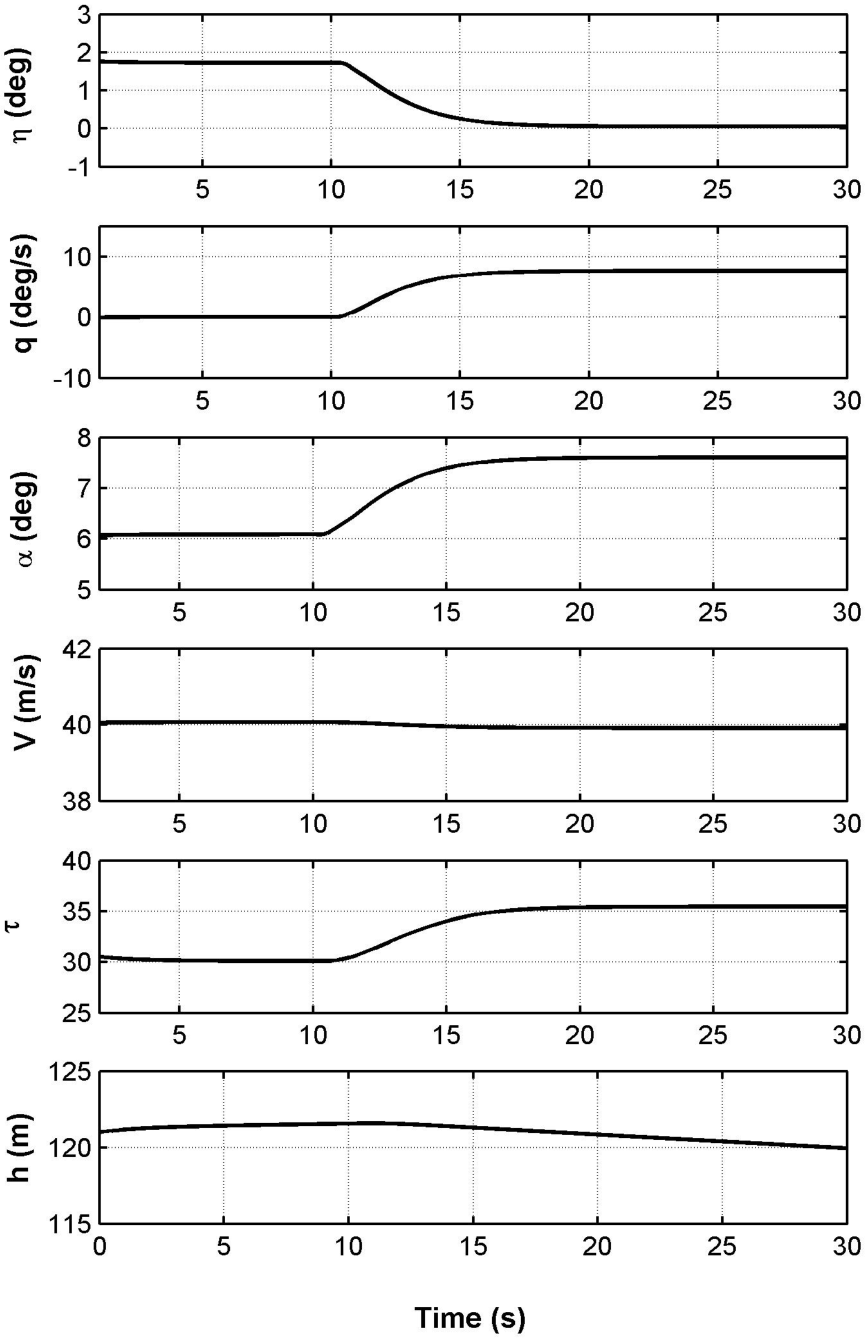

Fig. 8-13.Longitudinal variables time response during simulation of a coordinated turn

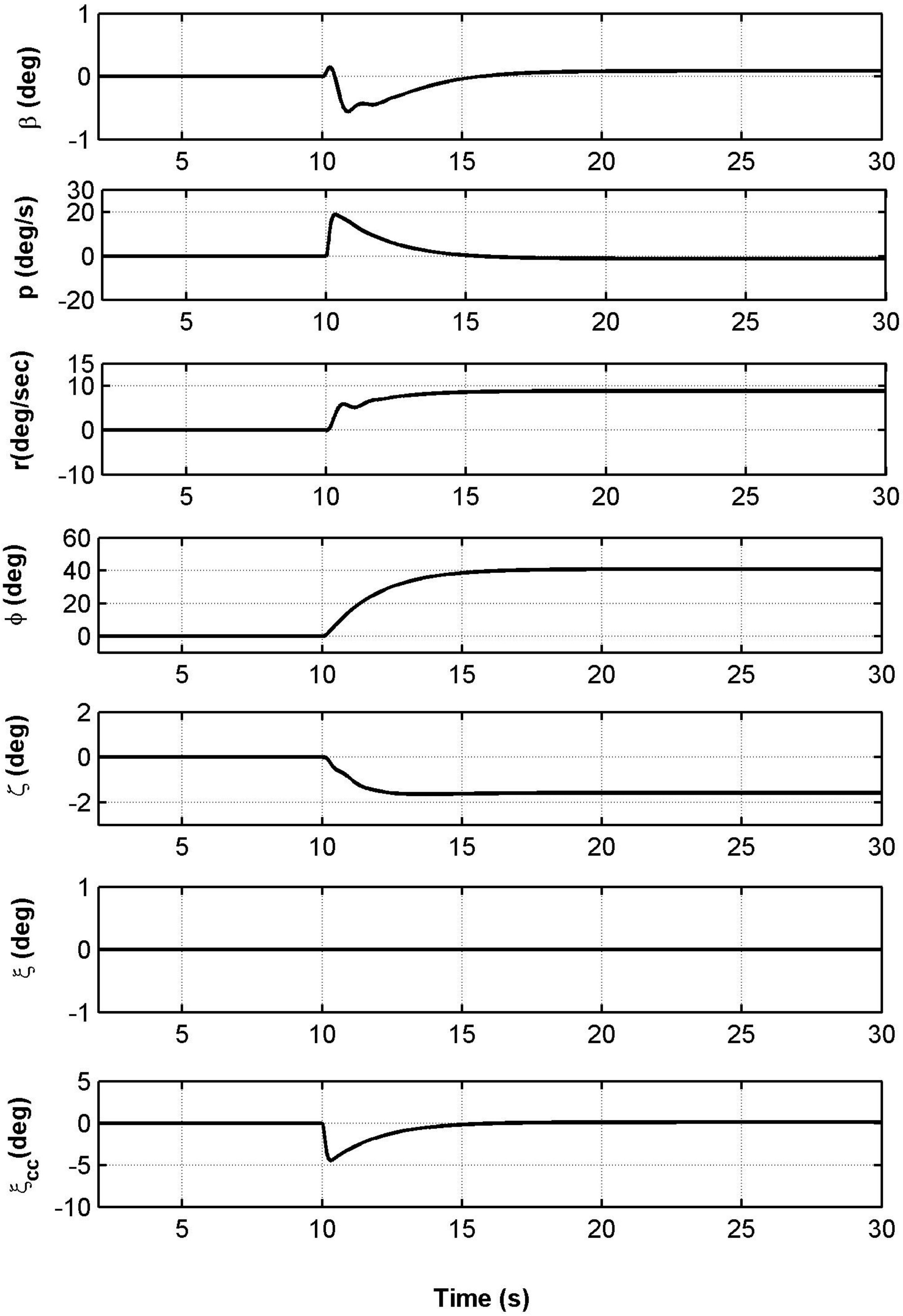

Fig. 8-14.Lateral variables time response during simulation of a coordinated turn

8.8.3 Directional dynamics

The simulation has been initialized at a condition of straight and level flight at a velocity of 40m/s and an altitude of 130m. Fig. 8-15 shows the ground track of the aircraft in response to a bank angle steering command. The altitude and the speed did not decrease during the 35-s simulation, thanks to the closed loop turn compensation. Fig. 8-16 shows respectively the bank angle response, the angle of attack, the sideslip angle, the cc-actuator cylinder deflection and the rudder deflection. The bank angle settled down within 5 s and the response is well damped. The control deflections are within limits.

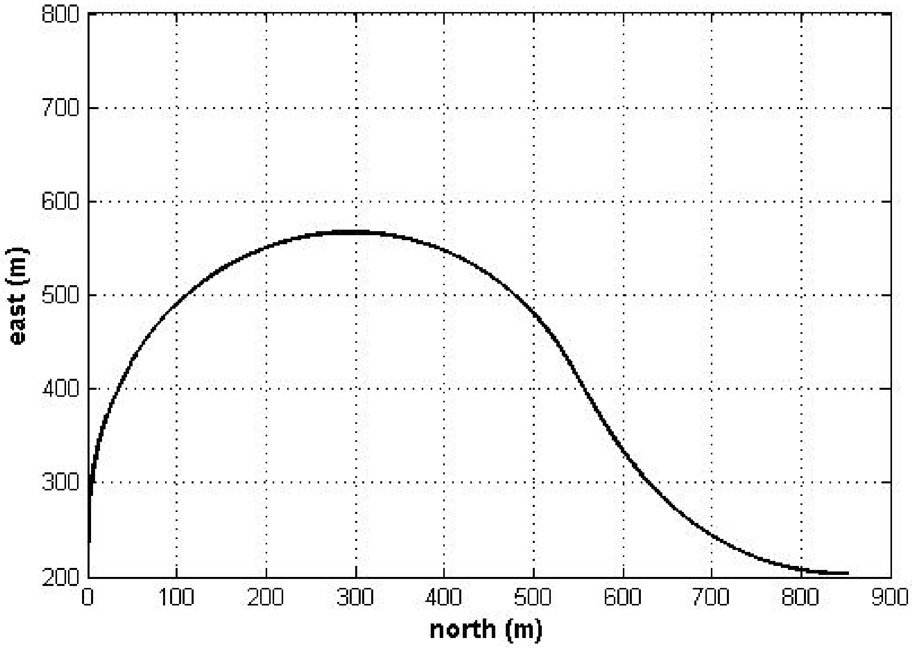

Fig. 8-15.Ground track during bank-angle steering

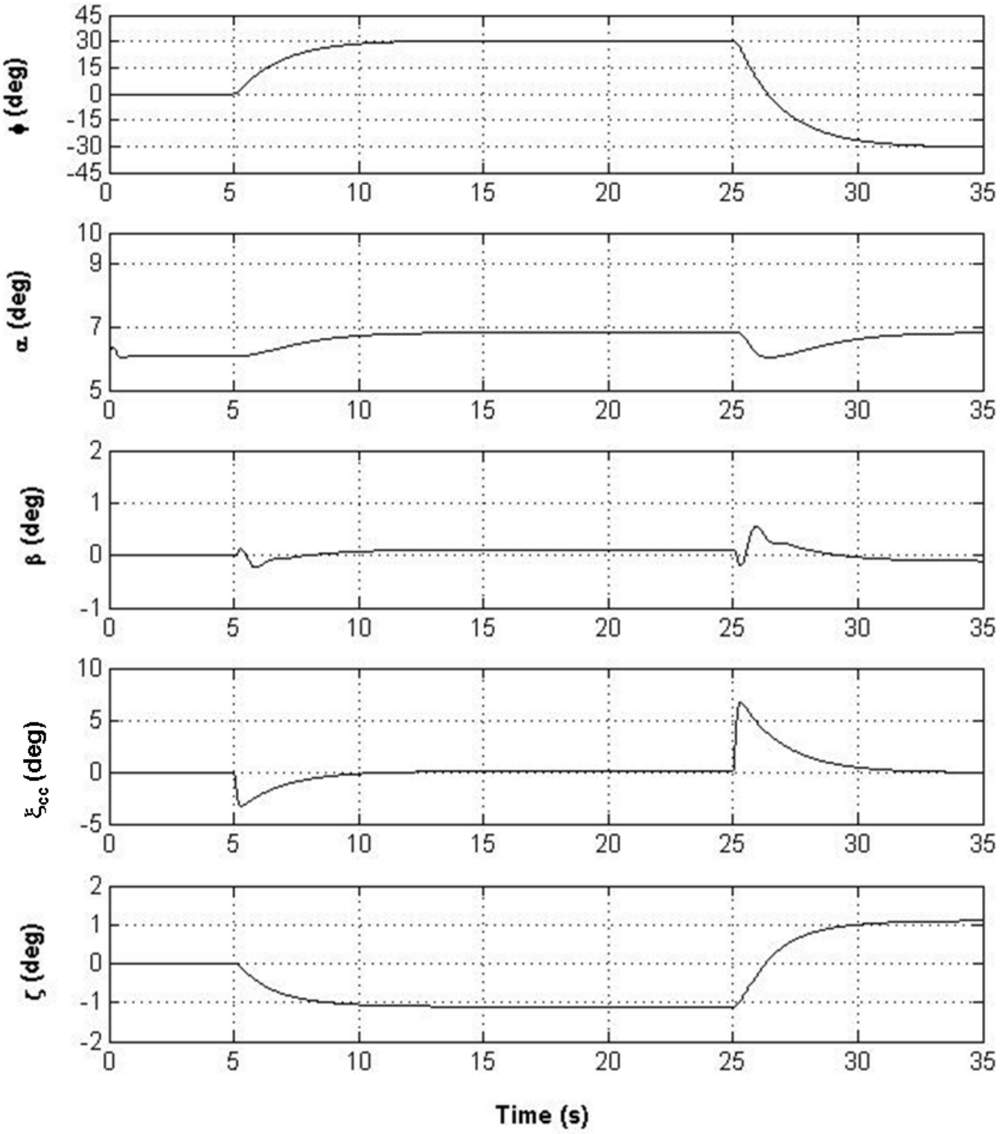

Fig. 8-16.Variables variation during simulation of bank steering

8.8.4 Control authority limit

Control systems limiting can be investigated with abrupt large amplitude commands. This highlights the importance of modelling control surface rate and deflection limits so that the simulation results are not unrealistic.

The simulation has been initialized at a condition of straight and level flight at a velocity of 40m/s and an altitude of 130m. Fig. 8-17 shows the ground track of the aircraft in response to a large bank angle steering command, which causes the CC actuator to saturate, as it is shown in the CC actuator deflection (ξ_{cc}) time history in Fig. 8-18. The directional controls are still able to control sideslip and the elevator is not saturated so that there is still longitudinal control available, sufficient to avoid pitch departure.

Due to the geometrical constraints the mechanical limits of the CC actuator are such that saturation could be reached if an excessive bank angle is demanded. In the described FCS the maximum step bank angle change allowed without saturating the CC is 50deg. This is, in fact, a manifestation of the control/power saturation limit due to finite performance of pneumatic power supply. As a matter of fact, geometrical constraints can be overcome if a greater air pressure supply is supplied, being the effectiveness of CC control a function, for a fixed geometry installation, of the velocity ratio of the jet and free stream.

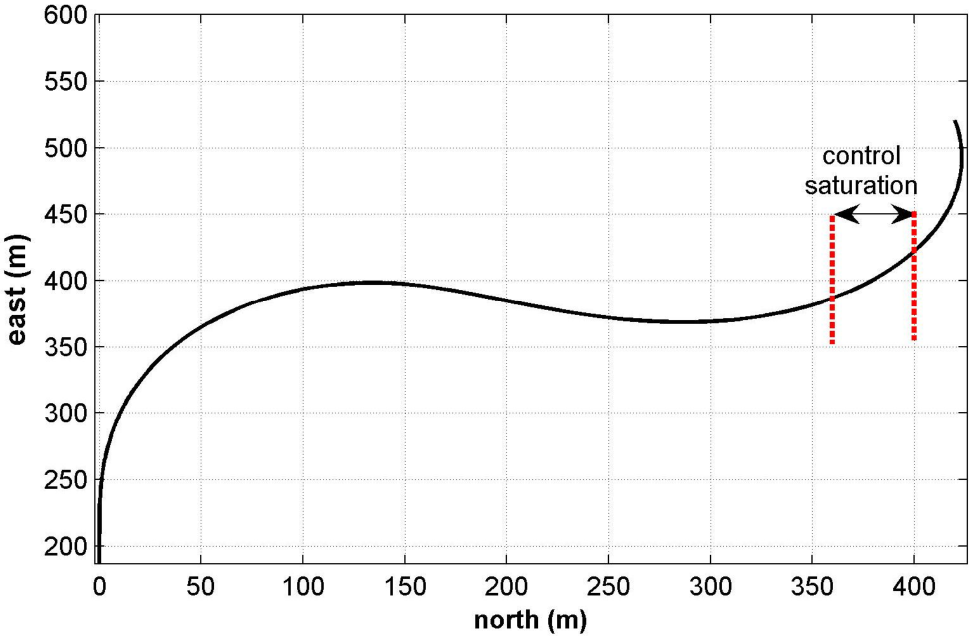

Fig 8-17.Ground track during bank-angle steering with control saturation

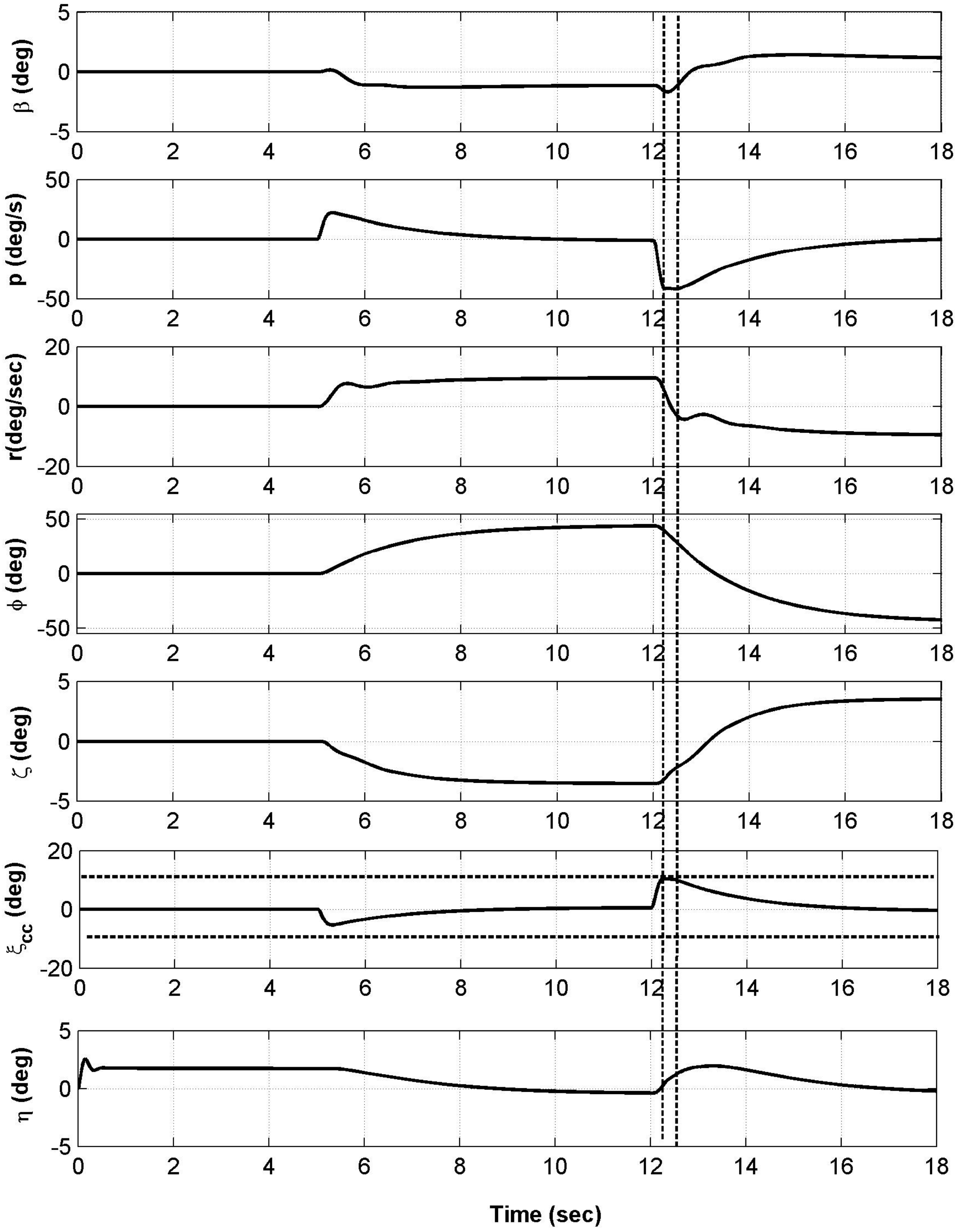

Fig 8-18.Variables variation during simulation of bank steering with control saturation

9 CONCLUSIONS AND RECOMMENDATIONS

9.1 Introduction

The preceding research described the supporting Flight Dynamics contribution to the design of a low observable UAV demonstrator (*Demon*) as part of a national research programme (FLAVIIR). In particular, the study demonstrated an integrated flight control and fluidic control system which employs a CC actuator to enhance or replace the traditional roll control motivator.

Wind tunnel tests of a full-span 50% scale *Demon* model were successfully carried out and delivered a representative aerodynamic model of the vehicle. A high fidelity 6DoF simulation model for the airplane was developed based on wind tunnel experiments and was used to assess vehicle trim, and stability and control properties. Simulations proved the vehicle to have acceptable stability properties and good controllability over the design operating range.

A novel alternative to a conventional single slot trailing edge circulation control actuator that enables proportional bi-directional control has been developed. The circulation control actuator has been manufactured and tested and experimental evaluation has shown the flow control actuator concept to be a practical solution to the problem of direct flow control at subsonic velocities and, hence, to have significant potential to act as a direct replacement for a mechanical control surface. The potential of the device has been recognized by BAE Systems who have filed a patent application (P.A.N. 0617428.8).

A mathematical model of the flow control actuator, for interfacing the fluidic device with the flight control system, has been derived and incorporated in the dynamic model of the air vehicle. The model has established the factors that determine the effectiveness of the CC effectors, in a similar manner to conventional trailing edge devices. The model has been used to predict flapless performance controllability of the aircraft and it has resulted, also, in a valuable asset for interpreting the requirements for a secondary air supply system and for establishing a practical source of the volume of air flow required. In particular, specific saturation limits and their impact on different flight operation phases have been assessed.

The dynamic simulation model of the flapless and flap configuration proved to be a usable tool for proper flight dynamic representation and design of the Flight Control System.

A semi-autonomous Flight Control System to assist control by a remote pilot throughout the flight has been developed. A configurable control architecture that shares control moment demand with conventional and fluidic motivators was proven to provide a sufficient degree of safety and flexibility to facilitate experimental flight research. Simulation results showed that the CC actuator, in conjunction with the elevator and rudder, can effectively control the *Demon* attitude.

9.2 Conclusions

9.2.1 Air Vehicle modeling

The stability and control analysis of the *Demon* indicates that a satisfactory vehicle behavior is expected over the design operating range. In particular:

- The position of the *cg* results in a positive static margin and positive longitudinal stability. As the angle of attack increases there is a significant rearward shift of the aerodynamic centre which results in a higher static margin. Nevertheless, there is sufficient control power to trim, over the design operating range, leaving enough margin for maneuvering.
- All the dynamic modes are stable across the flight envelope.
- Positive lateral and directional stability is maintained over an increased angle of attack range. In particular, the sweepback of the wing has inherent lateral stability that increases with increasing lift coefficient, resulting in a high level of lateral stability at low speed and a low level of lateral stability at high speed. This

is reflected in the spiral mode time constant; at high speed the spiral mode is close to neutrally stable and manifests itself as a very slow exponential convergence.

- Due to a relatively large wing area the damping terms attain significant values with respect to more conventional configurations. In particular this is reflected in the high roll damping which results in a very short mode time constant.

9.2.2 Circulation Control Actuator

The flow control actuator alleviates the problems associated with a fixed slot arrangement:

- The total slot area remains constant and continuous air supply is required. Consequently, control bandwidth limitations associated with internal air flow throttling, to modulate the resultant control force and moment, are avoided. Additionally, there is no back pressure effect on the air supply source; this could be especially critical when air demand is bled from a small gas turbine engine compressor.
- The flow control actuator can be integrated with conventional flap controls, relying on minimal change, since the input command is an angular displacement.

Experimental evaluation has demonstrated:

- A remarkably linear lift response to rotation of the trailing edge Coanda surface, through an equivalent control angle, within the operational envelope reported.
- Bi-directional incremental lift generation comparable to a mechanical flap of similar trailing edge span and at a relatively modest blowing momentum coefficient. The experiments have also shown that the bi-directional nature of control remains fully functional up to the limit of the bandwidth of the model aircraft servo (approximately 20 rad/s) used to actuate the Coanda surface. Thus, since the bandwidth of the servo is much greater than that of the *Demon*, the dynamic performance of the flow control actuator is entirely compatible with the control requirements of subsonic UAVs.
- A significant drag reduction was shown for dual steady blowing (upper and lower slot blowing simultaneously) compared with the un-blown configuration. The

dual blowing capability addresses the issue of a blunt trailing edge for typical CC configurations at cruise. This result indicates, also, that slot thrust can be adjusted for a given lift to reach an optimum cruise configuration.

- A more negative pitching moment, compared with a mechanical flap of similar trailing edge span, was observed. Aerodynamic centre of lift due to blowing was found to be located at about 66% of the chord. This finding suggests that, if CC acts as a replacement for aileron to provide roll control, differential blowing on each side of the aircraft is necessary to cancel out the pitch down moment. Hence, the bi-directional nature of the CC actuator addresses this problem.

9.2.3 Flapless Flight Control

From the analysis and discussions the following conclusion can be made:

- The fluidic devices can be modelled as momentum amplifiers specified by a gain term and saturation limits.
- Unlike conventional mechanical controls, for fluidic controls, the dimensionless control input required to achieve a given control force coefficient is not independent of the reference momentum, hence, as the free-stream speed increases, an increasing amount of input momentum is required to achieve a given force coefficient.
- The saturation of fluidic controls is similar to geometric controls. Two saturation limits exist based on geometry and effort/power constraints. For CC systems, geometric saturation typically limits the attachment angle of the jet to less than 180° due to the extent of the curved trailing edge. The control/power saturation is mass/pressure flow limited due to engineering constraints for engine bleed or dedicated auxiliary power unit.
- Roll control power equivalent to that of conventional ailerons can be achieved at practical slot blowing conditions. Results indicate that the effect of a 10^{o} deflection of aileron could be generated instead using a blowing coefficient of 0.001 at each plenum.
- CC provides the ability to control the *Demon* flying demonstrator in roll using high pressure air supplied by the engine compressors during moderate-high periods of engine operation. If the engine blowing power take off is constant then

the excess jet momentum should be dumped or throttled as desired. However, thrust losses associated with engine bleeding limit the manoeuvre flight with respect to the same configuration using a mechanical control device. The most critical condition is represented by a steady climb turn, where up to a maximum of 10% loss in performance was observed compared with no bleeding case.

- Descending flight is the most critical flying condition when fluidic controls are powered by air bled from the main engine. Engine needs to be throttled back to slow down the aircraft, as the *Demon* lacks air-brakes.
- From these observations it was concluded that the CC air mass flow requirements may be provided by a relatively light weight auxiliary turbo-compressor. In this manner the blowing pressure is independent of the main thrust level, thereby simplifying the operation with CC and the flight control system design.

9.2.4 Flight Control System

A semi-autonomous primary flight control system has been designed and the following conclusions can be made:

- The FCS provides a safe stable platform with dynamics compatible with expected manouevre envelope of the *Demon*. The control characteristics are consistent with carefree remote handling of a Demon-class UAV.
- The configurable control architecture enables allocation of commands to conventional flap control, circulation control and thrust vectoring separately and in combination.
- CC actuator can be integrated in the flight control system and provides auxiliary lateral stability augmentation, within the saturation constraints.
- A flight control strategy, where longitudinal and lateral directional controls share multiple aerodynamic control effectors (mechanical and fluidic motivators), has been demonstrated to be successful in alleviating the demand on a single fluidic effector. This may be particularly useful for future tailless aircraft, especially considering the atmospheric disturbance conditions and resulting increased demand for pitch and lateral control, coupled with the inherently directional unstable platform of a tailless aircraft.
- The system flexibility was designed to facilitate future flight research.

9.3 Recommendations for future work

It has been recently anticipated that the *Demon* will be scaled by 15% when compared to the original *Eclipse* UAV. The vehicle wing span will be increased to 2.53 m with fuselage length of 2.88 m, giving an estimated flight weight of about 70kg. The vehicle will be powered by a *Titan* AMT engine, with a maximum thrust of 360N. The 6DoF simulation model will be modified and re-issued to reflect the current design status, and to integrate new external data coming from other projects partners. In particular, the simulation should be updated to include a model of the fluidic thrust vectoring system developed by Manchester University.

Refinements of the flight control system are required prior to first flight. Extensive simulation should be used to establish value of maximum climb and dive pitch angle and maximum bank angle so as to provide carefree handling. In light of the results, authority limits need to be modified so as to give the best margin for safe behavior.
The simulation model will be used to assist a series of simulated flight trials in the UAV flight simulation suite at BAE Systems, Warton. The results will determine the limits of the achievable flight envelope and drive the test plan for the first flights.
Due to the level of uncertainty around the fluidic control gain that will be achieved on the final vehicle, the initial flight control systems have to be robust to this uncertainty. It is believed that the robust LPV design methodology, undertaken at Leicester University within the FLAVIIR project (Chen, Gu, Postlethwaite, and Natesan, 2008), could provide a promising starting point for such an endeavor. More pragmatically, it would make sense to do some very basic system identification on the fluid controls as part of the initial flight tests.

The performance of the prototype actuator was limited by some features of its engineering design. However, with improved design it should be possible to develop the capability of the actuator to improve its range, resolution, weight and compressed air consumption to provide a compact, robust and modular alternative to a conventional flap for use in small scale air vehicles.
The following features of the actuator could be improved by design, with a resultant improvement in performance:

1) Improved plenum design to avoid span-wise asymmetry in the exit flow.

2) Higher mechanical accuracy of the trailing edge gap setting resulting in a more uniform slot height with span.

Further electro-mechanical developments of the flow control actuator should be investigated. In particular it is proposed to seek an alternative means for actuating the cylindrical trailing edge bar within the device enclosure. It is envisaged that a successful flow control actuator design will be self contained with a pipe connection for air delivery and an electrical connection for actuation.

While the possibility of replacing a conventional roll control motivator with a CC actuator has been demonstrated, further work could assess the full potential of fluidic control as a primary lateral and pitch control effector.

Further experimental work using the full-span model may be undertaken to investigate the application of the CC actuator control to yaw control and pitch trim. An investigation of the aerodynamic characteristics of the *Demon* without the vertical tail should be carried out to obtain aerodynamic data for the vertical-tail-less configuration using CC as suitable alternative yaw effectors to the rudder. This investigation could eventually lead to fully flapless flight. As fluidic systems are considerably less complex mechanically than other high lift devices, this may be significantly beneficial when contemplating maintenance, production costs and reliability.

The *Demon* presents a redundancy in control motivators which could call for effective control allocation or re-allocation (in case of actuator failures) to distribute the required control moment over available effectors. The objective of control allocation could be to choose a configuration of the control effectors (actuators) to meet a specified objective, subject to saturation constraints. In the case of actuator failures, it is desirable to “reconfigure” the control allocation scheme (re-allocation) in order to make best use of the remaining healthy actuators

REFERENCES

[1] Anon. Engineering Science Data Unit (ESDU) data item 88013: *Rolling Moment Derivatives,* L_ξ, *for Plain Aileron at Subsonic Speeds*.

[2] Anon. Engineering Science Data Unit (ESDU) data item 74012: *Conversion of Lift Coefficient Increment due to Flaps from Full Span to Part Span*.

[3] Anon. *Standard Atmosphere-Tables and Data for altitudes to 65,000 Feet*. NACA Report 1235. International Civil Aeronautical Organisation, Montreal, Canada, December 1952 & NACA Langley Aeronautical Laboratory, Langley Field, Va., U.S.A., February 1954.

[4] Anon. Military *Specifications-Flying qualities of piloted airplanes*. MIL-F-8785C. Department of Defence, USA, 1980.

[5] Alexander, M., Anders, S.G. and Johnson, S.K. A. Wind Tunnel Experiment for Trailing Edge Circulation Control on a 6% 2-D Airfoil up to Transonic Mach Numbers. *Proceedings of the 2004 NASA/ONR Circulation Control Workshop*, Hampton, VA, June 2004, pp. 407-435.

[6] Allegri, G. Flight Dynamics of the Eclipse-Based Unmanned Platforms. Flaviir project internal report InR151206, Cranfield University, 2006.

[7] Anderson, B. W. *The Analysis and Design of Pneumatic Systems*. Wiley, New York, 1967.

[8] Barlow, J.B., Rae, W.H. and Pope, A. *Low Speed Wind Tunnel Testing*. John Wiley, New York, 1999.

[9] Bigras, P., Wong, T. and Botez, R. Pressure Tracking Control of a Double Restriction Pneumatic System. *International Conference on Control and Applications*, June 2001, pp.273-278.

[10] Bradbrook, K. *Contribution to the Aerodynamic design for the Eclipse*. College of Aeronautics MSc Thesis, University of Cranfield, 1999.

[11] Cagle, C.M. and Jones, G.S. A Wind Tunnel Model to Explore Unsteady Circulation Control for General Aviation Applications. AIAA Paper 2002-3240, June 2002.

[12] Campbell, I. J., et al. Aerodynamic Characteristics of a Rectangular Wing of Small Aspect Ratio. ARC, RM No3142, 1956.

[13] Chen, J., Gu, D., Postlethwaite, I. and Natesan, K. Robust LPV Control of UAV with Parameter Dependent Performance. *17th IFAC World Congress*. Seoul, Korea, July 6-11, 2008, pp. 15070-15075.

[14] Cook, M.V. *Flight Dynamics Principles*. 8th ed. Edward Arnold, 2007.

[15] Cook, M.V. Demon Flight Control System Description. Flaviir project internal report AeR020307, Issue 1, Cranfield University, 2007.

[16] Duncan, W.J. *The principles of the Control and Stability of Aircraft*. Cambridge University Press, 1959, pp 137-142.

[17] Dunham, J. A Theory of Circulation Control by Slot Blowing Applied to a Circular Cylinder. *Journal of Fluid Mechanics*, Vol. 33, No. 3, pp. 495-514, 1968.

[18] Englar, R.J. Circulation Control for High Lift and Drag Generation on a STOL Aircraft. *Journal of Aircraft*, Vol. 12, No. 5, pp. 457-463, March 1975.

[19] Englar, R.J. and Hemmerly, R.A. Design of the Circulation Control Wing STOL Demonstrator Aircraft. *Journal of Aircraft,* Vol. 18, No. 1, pp. 51 -58, 1981.

[20] Englar, R.J. and Huson, G.G. Development of Adavanced Circulation Wing High Lift Airfoils. *Journal of Aircraft*, Vol. 21, No. 7, pp. 476-483, 1983.

[21] Englar, R.J. and Applegate, C.A. Circulation Control - A Bibliography of DTNRSDC Research and Selected Outside Reference (January 1969 through Decmber 1983). DTNSRDC – 84/052, 1984.

[22] Englar, R.J. and Al. Development of Circulation Control Technology for Powered -Lift STOL Aircraft. *Proceedings of The Circulation Control Workshop* 1986, NASA Ames Research Center, NASA CP-2432, February 19-21 1986, pp.491-513.

[23] Englar, R.J. Application of Circulation Control Technology to Advanced Subsonic Transport Aircraft. *Journal of Aircraft*, Vol. 31, No. 5, pp. 1160-1168, 1994.

[24] Englar, R.J., Niebur, C.S. and Gregory, S.D. Pneumatic Lift and Control Surface Technology Applied to a High Speed Civil Transport Configurations. AIAA paper 97-0036, January 1997.

[25] Englar, R.J. Circulation Control Pneumatic Aerodynamics: Blown Force and Moment Augmentation and Modification; Past, Present & Future. AIAA Paper 2000-2541, *Fluids 2000*, Denver, Colorado, 2000.

[26] Etkin B. *Dynamics of Atmospheric Flight*. John Wiley and Sons, Inc., 1972.

[27] Frith, S. P. and Wood, N.J. Circulation Control High Lift Applications on a Delta Wing. *CEAS Aerospace Aerodynamics Research Conference*, Cambridge, June 2002.

[28] Frith, S. P. and Wood, N.J. Effect of Trailing Edge Geometry on a Circulation Control Delta Wing. AIAA Paper 2003-3797, *21st applied Aerodynamics Conference*, Orlando, Florida, 2003.

[29] Frith, S. P. and Wood, N.J. Investigation of Dual Circulation Control Surfaces for Flight Control. AIAA Paper 2004-2211, *2nd AIAA Flow Control Conference*, Portland, Oregon, July 2004.

[30] Gledhill, A.R. *Flight control system and simulation development for the unmanned air vehicle-Eclipse.* College of Aeronautics MSc Thesis, Cranfield University, 1999.

[31] Harrison R.E. *The Design and Manufacture of the Eclipse Unmanned Turbojet Powered Air Vechicle – Programme Management, Mass, CG, Cost and Wind Tunnel Reporting*. College of Aeronautics MSc Thesis, Cranfield College of Aeronautics, November 1999.

[32] Huff, L. *Contribution to the Group Design Project for the Eclipse aircraft including Parametric Performance analysis, Computational Fluid Dynamic derivative analysis using the Euler code FLITE3D, Aerodynamic derivative analysis, Undercarriage simulation model for ACSL, Lateral control system design and Structural testing*. College of Aeronautics MSc Thesis, University of Cranfield, 1999.

[33] Imber, R. Exploratory Investigations of Circulation Control Technology: Overview for Period 1987–2003 NSWCCD. *Proceedings of the 2004 NASA/ONR Circulation Control Workshop,* NASA Ames Research Center, Jun. 2005, pp. 553-557, NASA CP-2432.

[34] Jones, G.S. Pneumatic flap performance for 2D Circulation Control Airfoil, Steady & Pulsed. *Proceedings of the 2004 NASA/ONR Circulation Control Workshop,* No.27, pp. 845-888, Jun. 2005. NASA/CP-2005-213509/PT2.

[35] Jones, G.S., Viken, S.A., Washburn, A.E., Jenkins, L. N. and Cagle, C.M. An Active Flow Circulation Controlled Flap Concept for General Aviation Aircraft Applications. AIAA Paper 2002-3157, *21st Applied Aerodynamics Conference*, Orlando, Florida, 2002,.

[36] Kind R. J. An Experimental Investigation of a Low Speed Circulation Control Airfoil. *The Aeronautical Quarterly*, Vol. XIX, pp.170-182, 1968.

[37] Kuipers, J.B. *Quaternion and Rotation Sequences: a Primer with Application to Orbits, Aerospace and Virtuality Reality*. Princeton University Press, October, 2002.

[38] Laiton, E.V. Lift-Curve slope for Finite Aspect Ratio Wings. *Journal of Aircraft*, Vol.26, No. 8, pp. 789-790, 1989.

[39] Lawson, G. Demon pneumatic power system. Flaviir internal report D100243, Issue1, Cranfield University, 2008.

[40] Liu, Y. *Numerical Simulations of the Aerodynamic Characteristics of Circulation Control Wing Sections*. PhD thesis, George Institute of Technology, 2003.

[41] Loth J. L. Flight performance of a Circulation Controlled STOL. *Journal of Aircraft,* Vol. 13, No. 3, pp. 169 -172, 1976.

[42] Loth, J.L. and Boasson, M. Circulation Controlled STOL Wing Optimisation. *Journal of Aircraft*, Vol.21, No. 2, pp. 128-134, 1984.

[43] Loth, J. L. Why Have Only Two Circulation-Controlled STOL Aircraft Been Built And Flown In Years 1974 - 2004. *Proceedings of the 2004 NASA/ONR Circulation Control Workshop*, Jun. 2005, pp. 603-640.

[44] Mcgowan, G., Gopalarathnam, A., and Jones, G.S. Analytical and Computational Study of Adaptive Circulation Control Airfoils. AIAA Paper 2004-4721, *22nd Applied Aerodynamics Conference and Exhibit*, Providence, Rhode Island, Orlando, 19 August 2004.

[45] Nielsen, J.N. and Biggers, J.C. Recent Progress in Circulation Control Aerodynamics. AIAA paper 87-0001, *AIAA 25th Aerospace Sciences Meeting*, Reno, Nevada, 1987.

[46] Prosser, C. F. and Wiler, C. D. RPV flying qualities criteria. TR AFFDL-TR-76-125, NASA, December 1976.

[47] Pugliese, A.J. Flight Testing the Circulation Control Wing. AIAA paper 79-1791, *AIAA Aircraft Systems and Technology Meeting,* New York, August 1979.

[48] Pope, A. *Wind Tunnel Testing*. 2nd edition, John Wiley&Sons, 1954.

[49] Rogers, E.O. and Donelly, M.J. Characteristics of a Dual Slotted Circulation Control Wing of Low Aspect Ratio Intended for Naval Hydrodynamic Applications. AIAA paper 2004-1244, *42nd Aerospace Sciences Meeting and Exhibit*, Reno, Nevada, 2004.

[50] Sellars, N.D., Wood, N.J. and Kennaugh, A. Delta wing Circulation Control Using the Coanda Effect. AIAA paper 2002-3269, *AIAA 1st Flow Control Conference*, St. Louis, June 2002.

[51] Smith, P. SNAP Flight Control System User Guide. Flaviir project internal report BBSR/SNAP/User_Guide/0.1, Blue Bear System Research, 2008.

[52] Spence, D.A. The Lift on a Thin Airfoil with a Jet Augmented Flap. *Aero. Quart*, Vol. 9, pp. 287-299, 1958.

[53] Spence, D.A and Beasley, J.A. The Calculation of Lift Slopes, Allowing for Boundary Layer, with Application to the RAE 101 and 104 Aerofoil. Report RAE/AERO 2598, 1958.

[54] Stevens B.L. and Lewis F.L. *Aircraft Control and Simulation*. John Wiley and Sons, Inc., 1992.

[55] Thomasson, P. G. A Method for the Analysis and Simulation of Discontinuous Systems. *European simulation conference*, Delft University, October 1993.

[56] Wilde, P.I.A., Gill K., Michie S.N. and Crowther W.J. Integrated Design of a Model-Scale Gas Turbine Powered Flapless Demonstrator Aircraft: A Case Study. AIAA paper 2007-7727, *7th AIAA Aviation Technology, Integration and Operations Conference (ATIO)*, Reston, VA, 2007.

[57] Wood, N.J. and Nielsen, J. Circulation Control Airfoils: Past Present, Future. AIAA paper 85-0204, *AIAA 23rd Aerospace Sciences Meeting,* Reno, Nevada, 1985.

[58] Wood, N.J. and Roberts L. The control of vertical lift on Delta Wings by tangential Leading Edge Blowing. AIAA paper 87-0158, *AIAA 25th Aerospace Sciences Meeting*, Reno, Nevada, 1987.

[59] Yarf-Abbasi, A. and Allegri, G. The Flying Demonstrator UAV configuration control document. Flaviir project internal report InR151204, Cranfield University, 2004.

[60] Flow Control Actuators, September 2006, Patent application number 0617428.8, The Patent Office, Newport, South Wales.

PUBLICATIONS

PEER REVIEWED JOURNAL PAPERS

[1] Cook, M.V., Buonanno, A. and Erbsloeh, S. D. A Circulation Control Actuator for Flapless Flight Control. *The Aeronautical Journal*, Vol. 112, No. 1134, pp.483-489, August 2008.

[2] Buonanno, A., Cook, M.V. and Erbsloeh, S. D. Experimental Determination of the Aerodynamic Performance of a Dual Slot Circulation Control Actuator. *Journal of Aircraft*. (Corrections under review).

CONFERENCE PAPERS

[1] Wilde, P., Buonanno, A., Crowther, B. and Savvaris, A. Aircraft Control Using Fluidic Maneuver Effectors. AIAA 2008-6406, *26th AIAA Applied Aerodynamics Conference*, Honolulu, Hawaii, Aug. 18-21, 2008.

[2] Buonanno, A., Cook, M.V. and Erbsloeh, S. D. Development of a Bi-Directional Circulation Control Actuator. *2nd European Conference for Aerospace Sciences*, Brussels, July 2007.

[3] Buonanno, A., Cook, M.V. and Erbsloeh, S. D. Differential Circulation Control for a Flapless Flight Control UAV. *22nd Bristol UAV Systems Conference*, Bristol, April 2007.

[4] Buonanno, A., M.V. Cook, S. D. Erbsloeh. Flight Dynamic Simulation of a Flapless Flight Control UAV. *25th International Congress of the Aeronautical Sciences*, Hamburg, November 2006.

APPENDIX A

½ SCALE DEMON MODEL WIND TUNNEL TEST

A.1 Wind tunnel test corrections

Following acquisition of the force and moment data from each test case, corrections were made to the data, noting:

- No tare corrections are necessary as an internal six-component balance was used to take the measurements.
- Wake blockage (a reduction in wake pressure from the lateral constraint on flow due to the tunnel wall) was negligible.
- Solid blockage, dynamic pressure and incidence corrections were deemed necessary.

Notation in this section is consistent with the one presented in Barlow, Rae and Pope (1999).

A.1.1 Solid Blockage

Solid blockage arises simply due to the presence of the tunnel walls which confine the free air, and speed up the flow around the model. In this case it is used to correct the dynamic pressure measurements, and can also be directly applied as a tunnel flow velocity correction. The measurement is based on the model volume and tunnel cross-section. According to Barlow, Rae and Pope (1999), this can be taken into account through separate consideration of the wing and body, or by combining these and considering the whole model. A more ‘approximate’ solid blockage can also be calculated using an alternative correction factor, although this is usually applied to unusual shapes, and should be limited to a model/test section area ratio of 7.5%. The solid blockage correction based on total model volume was applied to the data, Eq. (A-1). The solid blockage ε_{sb} as a function of the whole model volume, V_{MODEL}, is given by,

$$\varepsilon_{sb} = \frac{KV_{MODEL}}{C^{3/2}} \tag{A-1}$$

where K is 0.9 and C is tunnel cross-sectional area. The solid blockage correction was found to be small, ε_{sb}=002.

A.1.2 Dynamic Pressure (q) Correction

The solid blockage correction is applied to the dynamic pressure, q_A, to produce a corrected value of q_C (Barlow, Rae and Pope, 1999).

$$q_c = q_A(1+\varepsilon_{sb})^2 \tag{A-2}$$

The corrected dynamic pressure values were used in the calculation of all the aerodynamic coefficients.

A.1.3 Incidence correction

The measured values of angle of attack must also be subject to wall corrections which account for the effects of the tunnel wall on the vortex wake shed from the vehicle. The corrected angle of attack (α_c) is related to the geometric angle of attack (same as measured angle of attack (α_g) by the addition of a correction factor, $\Delta\alpha_w$ (Barlow, Rae and Pope, 1999).

$$\alpha_c = \alpha_g + \Delta\alpha_w \tag{A-3}$$

where, in degrees,

$$\Delta\alpha_w = \frac{\delta S C_{Lw}}{C} * 57.3 = 0.879 C_{Lw} \tag{A-4}$$

δ is a dimensionless wall correction factor, S is the model wing area, C is the tunnel cross sectional area, and C_{LW} is the model wing lift coefficient of each particular run (at α_g). δ is obtained graphically from the reference text Barlow, Rae and Pope (1999). Additional wall corrections could also be made to lift and drag coefficients, but these were deemed negligible.

A.2 Data quality and repeatability

Table A-1 states the flow uniformity throughout the working section of the 8x6 low speed wind tunnel.

Turbulence	u' = 0.1%
Uniformity	±0.7% over 93% horizontal ±1.1% over 91% vertical
Angularity	0.25° yaw 0.75° pitch

Table A-1. Flow uniformity of the 8x6 wind tunnel (MacManus, 2005)

The 6-component balance accuracy is summarized in table A-2.

	Lift	**Pitching Moment**	**Drag**	**Side Force**	**Yawing moment**	**Rolling moment**
Max Load	140 kgf	15 kgf	25 kgf	40 kgf	12 kgf	5 kgf
Std %	0.03	0.03	0.07	0.05	0.03	0.06

Table A-2. 6-Component balance accuracy (95% confidence level)

Repeatability was monitored and assessed within the same wind on run and within the same test series. Each of the tests started with complete resetting of the model.

Figure A-1 shows results of repeatability for the lift, pitching moment and drag coefficient respectively. The configuration used for the tests was the clean configuration, with the control surfaces of the model fixed at zero degree deflection.

Figure A-2 shows results of repeatability for the yawing moment, rolling moment and side force coefficient respectively. Two series of test are reported: clean configuration, with the control surfaces of the model fixed at zero degree deflection and 8 deg sideslip measurements. In order to explore the trend and increase the level of confident in the region between 5 and 10 degrees angle of attack, 1 degree of angle-of-attack step increase was selected.

It has been demonstrated that the level of repeatability, reported in table A-3 can be achieved.

	Within a test series
ΔC_L	± 0.001
ΔC_M	± 0.001
ΔC_D	± 0.0005
ΔC_{LL}	± 0.0015
ΔC_N	± 0.00015
ΔC_Y	± 0.0005

Table A-3. Data repeatability for the Demon half scale model

From the result of the repeatability test, it can be said that the acquired data guarantees a full level of confidence.

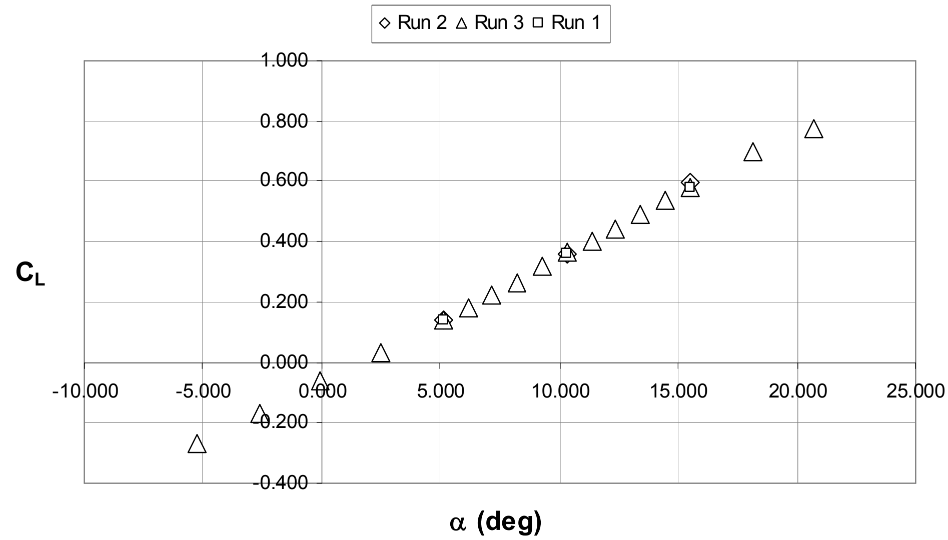

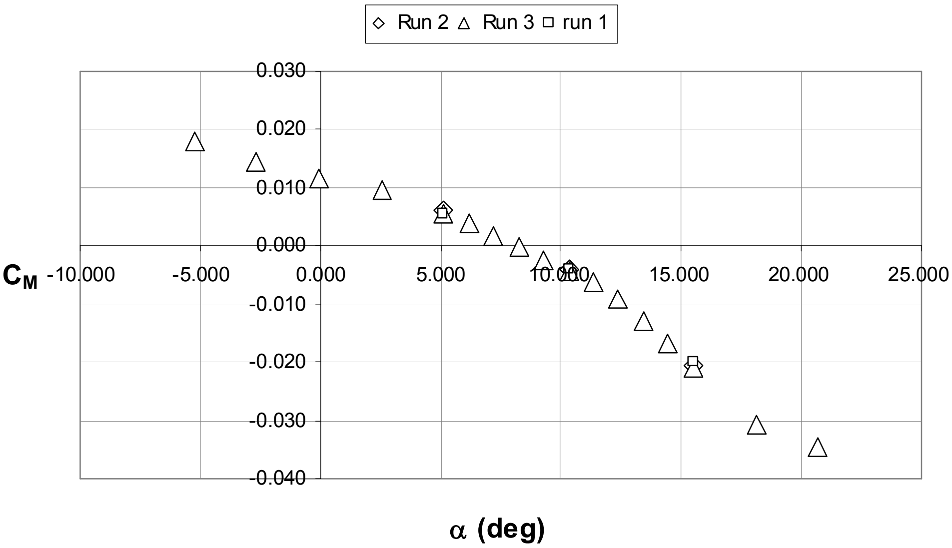

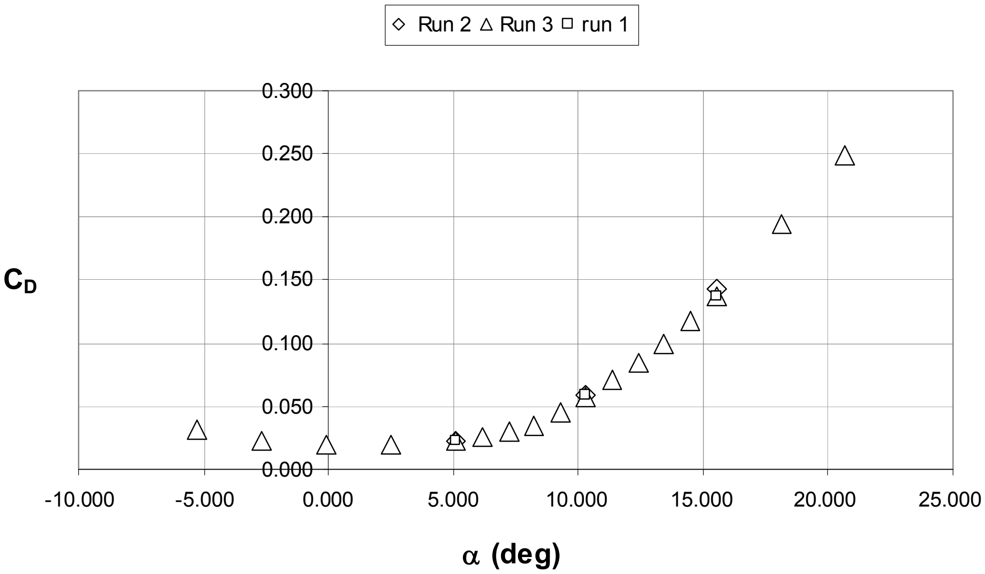

Fig. A-1. Longitudinal data repeatability

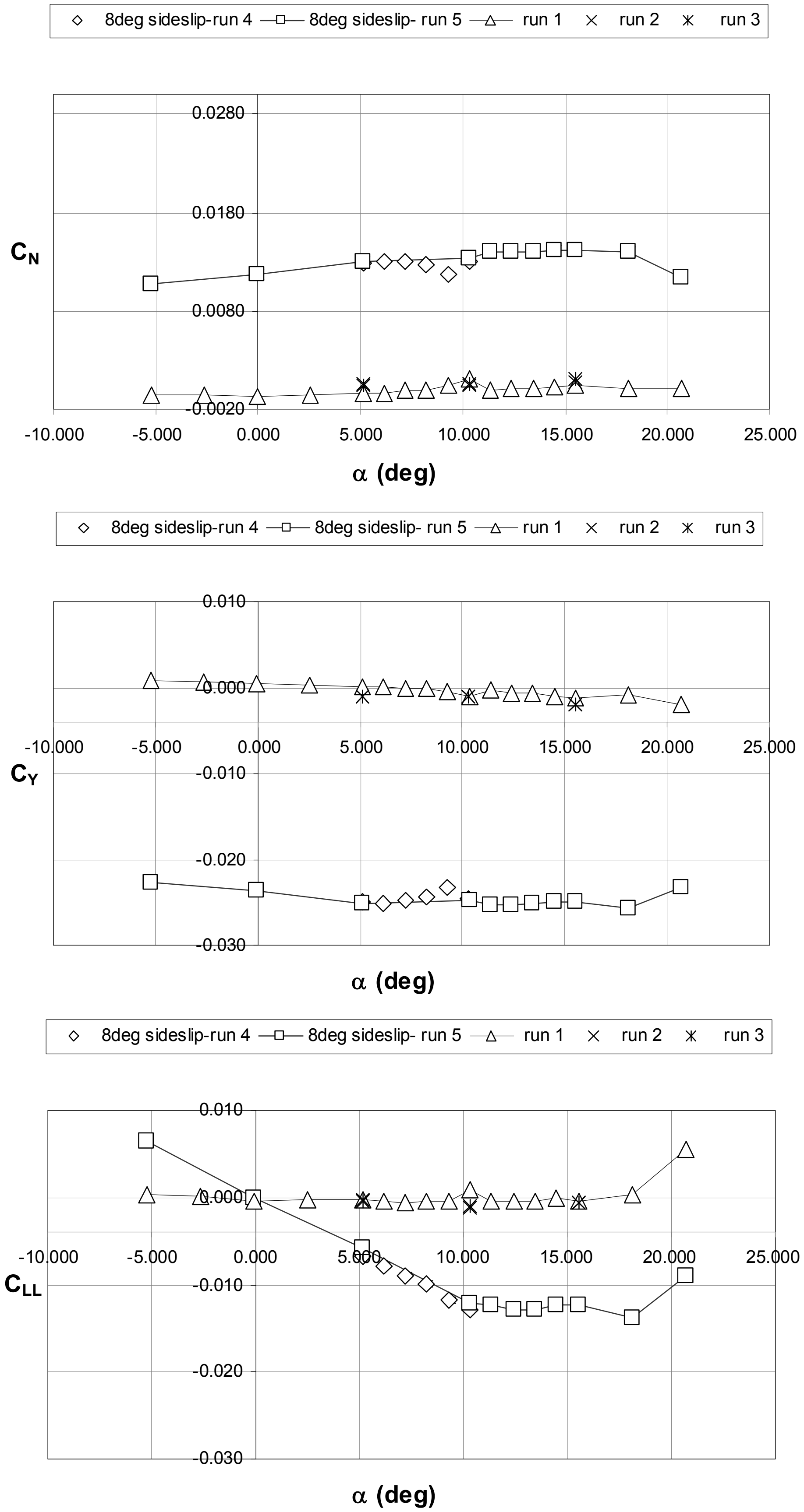

Fig. A-2. Lateral data repeatability

APPENDIX B

SIMULATION MODEL DEVELOPMENT

B.1 Dynamics module

B.1.1 The generalized force and moment equations

The derivation of the equations of motion of a rigid symmetric aircraft is based on that presented by Cook (2007).

The force equation of a rigid body, which described the motion of the *cg* about an orthogonal axis system co-located with the *cg* in the body are given by:

$$\begin{bmatrix} X \\ Y \\ Z \end{bmatrix} = m\begin{bmatrix} \dot{U} & -rV & qW \\ \dot{V} & -pW & rU \\ \dot{W} & -qU & pV \end{bmatrix} \qquad \text{(B-1)}$$

where m is the total mass of the body.

Equation (B-1) after rearranging and with the addition of the gravitational term, Eq. (4-15), becomes,

$$\begin{aligned} \dot{U} &= rV - qW + g\sin\theta + \frac{X}{m} \\ \dot{V} &= pW - rU + g\sin\Phi\cos\theta + \frac{Y}{m} \\ \dot{W} &= qU - pV + g\cos\Phi\cos\theta + \frac{Z}{m} \end{aligned} \qquad \text{(B-2)}$$

The moment equations of a rigid body which describe the rotational motion about the orthogonal axes through the vehicle's *cg*, since the origin of the axis is co-located with the *cg* in the body, are given by:

$$\begin{aligned} L &= I_x\dot{p} + qr(I_z - I_y) - I_{xz}(\dot{r} + pq) \\ M &= I_y\dot{q} + pr(I_x - I_z) + I_{xz}(p^2 - r^2) \\ N &= I_z\dot{r} + pq(I_y - I_x) - I_{xz}(\dot{p} - qr) \end{aligned} \qquad \text{(B-3)}$$

Note that Eq. (B-3) is based on the assumption of the lateral symmetry of the aircraft. Equation (B-3) can be rearranged to provide the angular accelerations:

$$\begin{aligned} \dot{p} &= (c_1 r + c2p)q + c_3 L + c_4 N \\ \dot{q} &= c_5 pr - c_6(p^2 - r^2) + c_7 M \\ r &= (c_8 p - c_2 r)q + c_4 L + c_9 N \end{aligned} \qquad \text{(B-4)}$$

where the inertial coefficients can be defined as:

$$\begin{array}{ccc} \Gamma c_1 = (I_y - I_z)I_z - I^2{}_{xz} & \Gamma c_2 = (I_x - I_y + I_z)I_{xz} & \Gamma c_3 = I_z \\ \Gamma c_4 = I_{xz} & c_6 = \dfrac{I_z - I_x}{I_y} & c_6 = \dfrac{I_{xz}}{I_y} \\ c_6 = \dfrac{1}{I_y} & \Gamma c_8 = (I_x - I_y)I_x + I^2{}_{xz} & \Gamma c_9 = I_x \\ & \Gamma = I_x I_z - I^2{}_{xz} & \end{array} \qquad \text{(B-5)}$$

B.1.2 Kinematics equations

$$\begin{aligned} \dot{\Phi} &= p + q\sin\Phi\tan\theta + r\cos\Phi\tan\theta \\ \dot{\theta} &= q\cos\Phi - r\sin\Phi \\ \dot{\Psi} &= q\sin\Phi\sec\theta + r\cos\Phi\sec\theta \end{aligned} \qquad \text{(B-6)}$$

B.1.3 Rotation in space

Transformation from body axes to earth axes, and vice versa, is done through the transformation matrix known as the direction cosine matrix (*DCM*). *DCM* can be defined as presented in Eq. (B-7) and in terms of Euler angle as in Eq. (B-8)

$$\begin{bmatrix} x \\ y \\ z \end{bmatrix}_b = \begin{bmatrix} l_1 & l_2 & l_3 \\ m_1 & m_2 & m_3 \\ n_1 & n_2 & n_3 \end{bmatrix} \begin{bmatrix} x_0 \\ y_0 \\ z_0 \end{bmatrix}_e \qquad \text{(B-7)}$$

Where

$$
\begin{aligned}
l_1 &= \cos\theta\cos\Psi \\
l_2 &= \cos\theta\sin\Psi \\
l_3 &= -\sin\theta \\
m_1 &= \sin\Phi\sin\theta\cos\Psi - \cos\Phi\sin\Psi \\
m_2 &= \sin\Phi\sin\theta\sin\Psi + \cos\Phi\cos\Psi \\
m_3 &= \sin\Phi\cos\theta \\
n_1 &= \cos\Phi\sin\theta\cos\Psi + \sin\Phi\sin\Psi \\
n_2 &= \cos\Phi\sin\theta\sin\Psi - \sin\Phi\cos\Psi \\
n_3 &= \cos\Phi\cos\theta
\end{aligned}
\tag{B-8}
$$

B.1.3.1 Quaternion

The Euler technique in defining the orientation in space is simple but its weakness is the singularity, when the pitch approaches 90^{o}, as it could be infer by Eq. (B-6).

Alternatively to the use of Euler angle for defining the orientation of the aircraft is the use of the quaternion method (Kuipers, 2002). The *DCM* in terms of the quaternion can be defined as in Eq. (B-9):

$$
DCM = \begin{bmatrix} e_0^2 + e_1^2 - e_2^2 - e_3^2 & 2(e_1e_2 - e_0e_3) & 2(e_0e_2 + e_1e_3) \\ 2(e_0e_3 + e_2e_1) & e_0^2 - e_1^2 + e_2^2 - e_3^2 & 2(e_3e_2 - e_1e_0) \\ 2(e_1e_3 - e_0e_2) & 2(e_1e_0 + e_3e_2) & e_0^2 - e_1^2 - e_2^2 + e_3^2 \end{bmatrix} \tag{B-9}
$$

The rate of change of the Euler parameter $e_0\ e_1\ e_2\ e_3$ with respect to the rotational rates $p\ q\ r$ is presented in Eq. (B-10).

$$
\begin{bmatrix} \dot{e}_0 \\ \dot{e}_1 \\ \dot{e}_2 \\ \dot{e}_3 \end{bmatrix} \begin{bmatrix} 0 & -p & -q & -r \\ p & 0 & r & -q \\ q & -r & 0 & p \\ r & q & -p & 0 \end{bmatrix} \begin{bmatrix} e_0 \\ e_1 \\ e_2 \\ e_3 \end{bmatrix} \tag{B-10}
$$

The initial values of the four quaternion parameters can be derived from the Euler angles by Eq. (B-11). Therefore Euler angles need to be calculated at the start of the simulation for initialization of the quaternions.

$$\begin{aligned}
e_0 &= \cos\frac{\Psi_0}{2}\cos\frac{\theta_0}{2}\cos\frac{\Phi_0}{2}+\sin\frac{\Psi_0}{2}\sin\frac{\theta_0}{2}\sin\frac{\Phi_0}{2}\\
e_1 &= \cos\frac{\Psi_0}{2}\cos\frac{\theta_0}{2}\sin\frac{\Phi_0}{2}-\sin\frac{\Psi_0}{2}\sin\frac{\theta_0}{2}\cos\frac{\Phi_0}{2}\\
e_2 &= \cos\frac{\Psi_0}{2}\sin\frac{\theta_0}{2}\cos\frac{\Phi_0}{2}+\sin\frac{\Psi_0}{2}\cos\frac{\theta_0}{2}\sin\frac{\Phi_0}{2}\\
e_3 &= \sin\frac{\Psi_0}{2}\cos\frac{\theta_0}{2}\cos\frac{\Phi_0}{2}-\cos\frac{\Psi_0}{2}\sin\frac{\theta_0}{2}\sin\frac{\Phi_0}{2}
\end{aligned} \qquad \text{(B-11)}$$

The Euler angle, ϕ, θ, and ψ, which describes the angular orientation of the body axes system relative to the earth axes system can eventually be derived as functions of quaternion parameters as in Eq. (B-12): .

$$\begin{aligned}
\Phi &= \tan^{-1}\left(\frac{2*(e_0e_1+e_2e_3)}{e_0^2-e_1^2-e_2^2+e_3^2}\right)\\
\theta &= \sin^{-1}\left(-2*(e_1e_3-e_0e_3)\right)\\
\Psi &= \tan^{-1}\left(\frac{2*(e_0e_3+e_2e_1)}{e_0^2+e_1^2-e_2^2-e_3^2}\right)
\end{aligned} \qquad \text{(B-12)}$$

The quaternion technique has been implemented in the non linear simulation. However, in order to trim the model and obtain the linear state space model out of the non linear simulation model the quaternion block-set have been replaced by the Euler one through Eqs. (B-6) and (B-7). This allows reducing number of states and, hence, improving states interpretation.

B.1.4 Navigation equations

The 3 navigation equations are simply the body axis velocities transformed using the *DCM* into the earth axis component.

$$\begin{bmatrix} V_N \\ V_E \\ V_D \end{bmatrix}_E = [DCM]^T \begin{bmatrix} U \\ V \\ W \end{bmatrix}_B \qquad \text{(B-13)}$$

B.1.5 Auxiliary equations

Incidence, α, sideslip, β and the true airspeed, V_T, can be derived from body axes velocities, using the following expressions:

$$\begin{aligned}
&\tan\alpha = \frac{W}{U} \\
&\sin\beta = \frac{V}{V_T} \\
&\textit{where } V_T = \sqrt{(U^2 + W^2 + V^2)}
\end{aligned} \qquad \text{(B-14)}$$

B.1.6 Inclusion of wind

Assuming that the local wind has north, east and down components V_{WN}, V_{WE} and V_{WD} respectively and that it is locally constant over a region considerably larger than the size of the aircraft, wind shearing effect and torques on the aircraft can be ignored. Therefore, the velocity *cg* with respect of air is governed by:

$$\begin{bmatrix} U \\ V \\ W \end{bmatrix}_r = \begin{bmatrix} U \\ V \\ W \end{bmatrix}_B - [DCM] \begin{bmatrix} V_{WN} \\ V_{WE} \\ V_{WD} \end{bmatrix} \qquad \text{(B-15)}$$

Where the subscript ‘r’ refers to the resultant body axes velocities which must be used in the calculation of the aerodynamic forces and moments, since those are created by the motion of the aircraft relative to the surrounding air.

APPENDIX C

AERODYNAMIC MODEL FOR THE DEMON AIRCRAFT (Mathcad Code)

Coupled with the 6DoF simulation model, an aerodynamic model for the *Demon* air-vehicle was developed in Mathcad. In particular, the programme calculates an estimate of the symmetric trim state of the aircraft for the selected *Demon* airspeed range; the programme computes the stability aerodynamic derivatives, following the definitions given in Cook (2007), required for the longitudinal and lateral state space model description. The program printout is reported.

1. Aircraft condition

Mass [kg] $m := 44.2$

$W := m \cdot 9.81$

Moment of inertia (kgm^2)
(Referred to body axis)

$I_{xB} := 1.38$

$I_y := 11.11$

$I_{zB} := 12.28$

$I_{xy} := 0$

$I_{xzB} := -0.25$

c.g. location (m)
(w.r.t. the nose and
the flat base of the aircraft)

$X_{cg} := 1.203$

$Y_{cg} := 0$

$Z_{cg} := 0.33$

2. Atmosphere condition

Altitude [m] $\text{height} := 121.92$

$\text{densitySL} := 1.225$

Temperature ratio $\text{Tratio} := 1 - 0.0065 \dfrac{\text{height}}{1000}$

Air density (kg/m^3) $\rho := \text{Tratio}^{4.2558844359} \cdot \text{densitySL}$

Speed of sound $a := \sqrt{1.4 \cdot 287 \cdot \text{Tratio} \cdot 288}$

3.Set up velocity range for computations

Counter $i := 0..7$

Velocity Range (m/s) $V_i := 30 + i \cdot 5$

Mach number $M_i := \dfrac{V_i}{a}$

4. Aircraft Geometry - constant

Wing area (m^2) $S := 2.365$

Wing mean chord (m) $\mathrm{mac} := 1.34$

Span (m) $b := 1.1$

c.g. position (%c) $h_{cg} := \frac{X_{cg}}{\mathrm{mac}}$

5.Wing- Body Aerodynamics

Wing body CL-α (rad-1) $CL_{\alpha} := 2.3667$

Zero angle of attack lift $CL_0 := -0.0669$

Lift damping derivative $CL_q := 1.37$

Lift coefficient due to Elevator (rad^1) $\alpha\_\mathrm{int} := (-0.051245171\ \ 5.129958143\ \ 10.32109832\ \ 15.51467673)^T$

$CL\eta := (0.262\ \ 0.256\ \ 0.289\ \ 0.325)^T$

Lift coefficient $CL(\mathrm{alfa},\mathrm{eta}) := CL_{\alpha}\cdot(\mathrm{alfa})\cdot\frac{3.14}{180} + CL_0 + \mathrm{linterp}(\alpha\_\mathrm{int}, CL\eta, \mathrm{alfa})\cdot \mathrm{eta}\cdot\frac{3.14}{180}$

Pitching moment at CG clean

$$CM_{cg}(\mathrm{alfa}) := \mathrm{if}[\mathrm{alfa} \le 2.8, -0.0004\mathrm{alfa} + 0.0110, \mathrm{if}[(\mathrm{alfa} > 2.8)\cdot(\mathrm{alfa} \le 11.8), -0.002\mathrm{alfa} + 0.0160, -0.0038\mathrm{alfa} + 0.386]]$$

Wing - body CM-α [rad-1] $CM_{\alpha}(\mathrm{alfa}) := \mathrm{if}[\mathrm{alfa} \le 2.8, -0.0222, \mathrm{if}[(\mathrm{alfa} > 2.8)\cdot(\mathrm{alfa} \le 11.8), -0.1123, -0.2203]]$

Pitch. coefficient due to Elevator deflection [rad^1] $CM_{\eta} := (-0.1307\ \ -0.1295\ \ -0.1467\ \ -0.1673)^T$

Pitching moment at CG $CM_{cg}(\mathrm{alfa},\mathrm{eta}) := CM_{cg}(\mathrm{alfa}) + \mathrm{linterp}(\alpha\_\mathrm{int}, CM_{\eta}, \mathrm{alfa})\cdot\left(\mathrm{eta}\cdot\frac{3.14}{180}\right)$

Pitch damping derivatives $CM_q := -0.473$

Drag calculation

Parasite drag $CD_0 := 0.0184$

Drag polar clean config. $CD(\mathrm{alfa}) := \mathrm{if}\left(\mathrm{alfa} \le 8.2, 0.2331 \cdot CL(\mathrm{alfa}, 0)^2 + 0.0184, 0.3853 CL(\mathrm{alfa}, 0)^2 + 0.0076\right)$

Lift induced drag coeff. $K(\mathrm{alfa}) := \mathrm{if}(\mathrm{alfa} \le 8.2, 0.2331, 0.3853)$

Drag de to flap (rad-1) $CD_\eta := (0.00349681\ 0.021916727\ 0.049920157\ 0.086716899)^T$

Drag coefficient $C_D(\mathrm{alfa}, \mathrm{eta}) := CD(\mathrm{alfa}) + \mathrm{linterp}\left(\alpha\_\mathrm{int}, CD_\eta, \mathrm{alfa}\right) \cdot \left(\mathrm{eta} \cdot \frac{3.14}{180}\right)$

6.Wing body Aero Centre calculation

$$h_{ac}(\mathrm{alfa}) := h_{cg} - \left[\frac{1}{\left(CL_\alpha + C_D(\mathrm{alfa}, 0)\right) \cdot \cos\left(\mathrm{alfa} \cdot \frac{3.14}{180}\right) + \left(CL_\alpha \cdot 2 \cdot CL(\mathrm{alfa}, 0)\, K(\mathrm{alfa}) - CL(\mathrm{alfa}, 0)\right) \cdot \sin\left(\mathrm{alfa} \cdot \frac{3.14}{180}\right)}\right] \cdot \left(CM_\alpha(\mathrm{alfa})\right)$$

7.Static margin calculatio *n*

$$h_n(\mathrm{alfa}) := h_{cg} - \frac{CM_\alpha(\mathrm{alfa})}{CL_\alpha}$$

8.Thrust model

$Z_t := 0$

Thrust as a function of
Mach and height

Olympus 190

$$RPM := \begin{pmatrix} 0 \\ 10 \\ 20 \\ 30 \\ 40 \\ 50 \\ 60 \\ 70 \\ 80 \\ 90 \\ 100 \end{pmatrix} \qquad TH := \begin{pmatrix} 2.5636 \\ 22.3818 \\ 38.7091 \\ 60.6727 \\ 87.9273 \\ 110.9091 \\ 131.1091 \\ 141.6727 \\ 155.2364 \\ 164.8727 \\ 172.5818 \end{pmatrix}$$

Thrust interpolation $T_X(\tau) := \mathrm{linterp}(RPM, TH, \tau)$

Forces in body axes

$$CN(\alpha,\eta) := CL(\alpha,\eta)\cdot\cos\left(\frac{\alpha}{57.3}\right) + C_D(\alpha,\eta)\cdot\sin\left(\frac{\alpha}{57.3}\right)$$

$$CX(\alpha,\eta) := -CL(\alpha,\eta)\cdot\sin\left(\frac{\alpha}{57.3}\right) + C_D(\alpha,\eta)\cdot\cos\left(\frac{\alpha}{57.3}\right)$$

<u>9.Trim flight condition: steady state level fligh *t*</u>

set trim flight condition

Flight path angle $\gamma := 0$

Dynamic pressure $Qdyn(Vtot) := 0.5\cdot\rho\cdot(Vtot)^2$

Set start value for solving the equations:

angle of attack $\alpha := 0$

elevator angle $\eta := -2$

throttle angle $\tau := 0.1$

Given

$$CN(\alpha,\eta) - \frac{W}{(Qdyn(Vtot)\cdot S)}\cdot\cos\left[\frac{(\gamma+\alpha)}{57.3}\right] = 0$$

$$CM_{cg}(\alpha,\eta) - \frac{T_X(\tau)\cdot\frac{Z_t}{mac}}{Qdyn(Vtot)\cdot S} = 0$$

$$\frac{T_X(\tau)}{Qdyn(Vtot)\cdot S} - CX(\alpha,\eta) - \frac{W}{(Qdyn(Vtot)\cdot S)}\cdot\sin\left[\frac{(\gamma+\alpha)}{57.3}\right] = 0$$

$trim(Vtot) := Find(\alpha,\eta,\tau)$ $\quad trim(45) = \begin{pmatrix} 4.864 \\ 2.775 \\ 33.139 \end{pmatrix}$

SUMMARY RESULTS OF TRIM CALCULATIONS

$V_i =$

30
35
40
45
50
55
60
65

$$\alpha\text{trim} = \begin{pmatrix} 9.66 \\ 7.401 \\ 5.9 \\ 4.864 \\ 4.119 \\ 3.567 \\ 3.147 \\ 2.819 \end{pmatrix} \qquad \eta\text{trim} = \begin{pmatrix} -1.317 \\ 0.501 \\ 1.823 \\ 2.775 \\ 3.429 \\ 3.913 \\ 4.282 \\ 4.568 \end{pmatrix} \qquad \text{trhottletrim} = \begin{pmatrix} 31.427 \\ 28.339 \\ 30.322 \\ 33.139 \\ 36.918 \\ 41.767 \\ 48.025 \\ 55.749 \end{pmatrix}$$

10.LONGITUDINAL DYNAMIC STABILITY

Fixed the flight condition for the linearization $k := i$

10.1 Calculation of centain derivatives

Lift coefficiency dependency on mach number $dCLdM := 0$

Drag coefficiency dependency on mach number $dCDdM := 0$

Drag coefficient dependency on angle of attack

$\alpha trimr := sort(\alpha trim)$ Reverse column order of data so that interpolation will work

$CDtrimr := sort(CDtrim)$

$a2_k := linterp(\alpha trimr, CDtrimr, \alpha trim_k + 0.2)$ $a1_k := linterp(\alpha trimr, CDtrimr, \alpha trim_k - 0.2)$

$dCDd\alpha r_k := \frac{(a2_k - a1_k) \cdot 57.3}{0.4}$ rad $^{-1}$ $dCDd\alpha := reverse(sort(dCDd\alpha r))$ rad $^{-1}$

Pitch damping $Cm_q := -0.473$

$Cm_{\alpha dot} := 0$

$CL_{\alpha dot} := -0$

$CL_q := 1.37$

Thrust derivative with respect to velocity

$dTdV_k := 0$

10.2 Dimensional Longitudinal aerodynamic Stability derivatives estimates referred to wind axe

$$X_{u_k} := -2\cdot\frac{Qdyn\left(V_k\right)\cdot S}{V_k}\cdot CDtrim_k + dTdV_k$$

$$X_{w_k} := \left(CLtrim_k - dCDd\alpha_k\right)\cdot\frac{Qdyn\left(V_k\right)\cdot S}{V_k}$$

$$X_{q_k} := 0$$

$$X_{wd_k} := 0$$

$$Z_{u_k} := -2\cdot\frac{Qdyn\left(V_k\right)\cdot S\cdot CLtrim_k}{V_k}$$

$$Z_{w_k} := -\left(CL_\alpha + CDtrim_k\right)\cdot\frac{S\cdot Qdyn\left(V_k\right)}{\left(V_k\right)}$$

$$Z_{q_k} := CL_q\cdot Qdyn\left(V_k\right)\cdot S\cdot\frac{mac}{2\cdot V_k}$$

$$Z_{wd_k} := -CL_{\alpha dot}\cdot\frac{Qdyn\left(V_k\right)\cdot S\cdot mac}{2\cdot\left(V_k\right)^2}$$

$$M_{u_k} := 0$$

$$M_{w_k} := CM_\alpha\left(\alpha trim_k\right)\cdot\frac{Qdyn\left(V_k\right)\cdot mac\cdot S}{V_k}$$

$$M_{q_k} := Cm_q\cdot Qdyn\left(V_k\right)\cdot S\cdot\frac{mac^2}{2\cdot V_k}$$

$$M_{wd_k} := Cm_{\alpha dot}\cdot Qdyn\left(V_k\right)\cdot S\cdot\frac{mac^2}{2\cdot\left(V_k\right)^2}$$

10.3 Dimensional Longitudinal aerodynamic control   derivatives estimates referred to wind axes

$$X_{\eta_k} := -Qdyn\left(V_k\right)\cdot S\cdot 2\cdot K\cdot\left(C_{L\eta}\right)^2\cdot\left(\eta trim_k\right)$$

$$Z_{\eta_k} := -Qdyn\left(V_k\right)\cdot S\cdot\left(C_{L\eta}\right)$$

$$M_{\eta_k} := -Qdyn\left(V_k\right)\cdot S\cdot mac\cdot\left(CM_\eta\right)$$

State equation format **dx/dt = Ax+Bu**

10.4 Elements of the A matrix : coincise derivative in terms of dimensional derivatives in wind axes

$$x_{u_k} := \frac{X_{u_k}}{m} + X_{wd_k}\cdot\frac{Z_{u_k}}{m\cdot\left(m - Z_{wd_k}\right)} \qquad x_{w_k} := X_{wd_k}\cdot\frac{Z_{w_k}}{m\cdot\left(m - Z_{wd_k}\right)} + \frac{X_{w_k}}{m}$$

$$z_{u_k} := \frac{Z_{u_k}}{m - Z_{wd_k}} \qquad z_{w_k} := \frac{Z_{w_k}}{m - Z_{wd_k}}$$

$$m_{u_k} := \frac{\left(M_{wd_k}\cdot Z_{u_k}\right)}{I_y\cdot\left(m - Z_{wd_k}\right)} + \frac{M_{u_k}}{I_y} \qquad m_{w_k} := \left(\frac{M_{w_k}}{I_y}\right) + Z_{w_k}\cdot\frac{M_{wd_k}}{I_y\cdot\left(m - Z_{wd_k}\right)}$$

$$x_q := 0 \qquad x_\theta := -9.81$$

$$z_{q_k} := \frac{\left[m\cdot V_k + \left(Z_{q_k}\right)\right]}{m - Z_{wd_k}} \qquad z_\theta := 0$$

$$m_{q_k} := \left(\frac{M_{q_k}}{I_y}\right) + \frac{\left[\left(V_k\cdot m + Z_{q_k}\right)\cdot M_{wd_k}\right]}{I_y\cdot\left(m - Z_{wd_k}\right)} \qquad m_\theta := 0$$

10.5 Elements of the B matrix in wind axis:coincise longitudinal control derivatives

$$x_{\eta_k} := X_{wd_k}\cdot\frac{Z_{\eta_k}}{m\cdot\left(m - Z_{wd_k}\right)} + \frac{X_{\eta_k}}{m} \qquad z_{\eta_k} := \frac{Z_{\eta_k}}{m - Z_{wd_k}} \qquad m_{\eta_k} := Z_{\eta_k}\cdot\frac{M_{wd_k}}{I_y\cdot\left(m - Z_{wd_k}\right)} + \frac{M_{\eta_k}}{I_y}$$

$$AI_k := \begin{pmatrix} x_{u_k} & x_{w_k} & x_q & x_\theta \\ z_{u_k} & z_{w_k} & z_{q_k} & z_\theta \\ m_{u_k} & m_{w_k} & m_{q_k} & m_\theta \\ 0 & 0 & 1 & 0 \end{pmatrix} \qquad B_k := \begin{pmatrix} x_{\eta_k} \\ z_{\eta_k} \\ m_{\eta_k} \\ 0 \end{pmatrix}$$

11.LATERAL DIRECTIONAL AERODYNAMIC STABILITY

11.1 Moment and product of inertia transformations from body axes to wind axis reference

$$I_{x_k} := I_{xB}\cdot\left(\cos\left(\alpha trim_k\cdot\frac{3.14}{180}\right)\right)^2 + I_{zB}\cdot\left(\sin\left(\alpha trim_k\cdot\frac{3.14}{180}\right)\right)^2 - 2\cdot I_{xzB}\cdot\sin\left(\alpha trim_k\cdot\frac{3.14}{180}\right)\cdot\cos\left(\alpha trim_k\cdot\frac{3.14}{180}\right)$$

$$I_{z_k} := I_{zB}\cdot\left(\cos\left(\alpha trim_k\cdot\frac{3.14}{180}\right)\right)^2 + I_{xB}\cdot\left(\sin\left(\alpha trim_k\cdot\frac{3.14}{180}\right)\right)^2 + 2\cdot I_{xzB}\cdot\sin\left(\alpha trim_k\cdot\frac{3.14}{180}\right)\cdot\cos\left(\alpha trim_k\cdot\frac{3.14}{180}\right)$$

$$I_{xz_k} := I_{xzB}\cdot\left[\left(\cos\left(\alpha trim_k\cdot\frac{3.14}{180}\right)\right)^2 - \left(\sin\left(\alpha trim_k\cdot\frac{3.14}{180}\right)\right)^2\right] + \left(I_{xB} - I_{zB}\right)\cdot\left(\sin\left(\alpha trim_k\cdot\frac{3.14}{180}\right)\cdot\cos\left(\alpha trim_k\cdot\frac{3.14}{180}\right)\right)$$

11.2 Derivative calculations - Wind axes reference

alpha for interpolation

$\alpha i := (-10\ \ -5\ \ 0\ \ 2.5\ \ 5\ \ 7.5\ \ 10\ \ 12.5\ \ 15\ \ 17.5\ \ 20\ \ 22.5\ \ 25\ \ 30\ \ 35\ \ 40)^T$

$\alpha := (-0.051245171\ 5.129958143\ 10.32109832\ 15.51467673)^T$

Wing-body contributions

$C_{y\beta} := (-0.2374\ \ -0.2448\ \ -0.2297\ \ -0.2273)^T$

$C_{LL\beta} := (-0.0041\ \ -0.0584\ \ -0.1208\ \ -0.1145)^T$

$C_{n\beta} := (0.1193\ \ 0.1282\ \ 0.1227\ \ 0.1319)^T$

$C_{yr} := 0$

$$C_{nr} := (-2.81\cdot 10^{-1}\ \ -2.72\cdot 10^{-1}\ \ -2.80\cdot 10^{-1}\ \ -2.90\cdot 10^{-1}\ \ -3.04\cdot 10^{-1}\ \ -3.22\cdot 10^{-1}\ \ -3.44\cdot 10^{-1}\ \ -3.69\cdot 10^{-1} \ldots$$

$$C_{LLp} := (-7.31\cdot 10^{-1}\ \ -7.03\cdot 10^{-1}\ \ -6.82\cdot 10^{-1}\ \ -6.83\cdot 10^{-1}\ \ -6.91\cdot 10^{-1}\ \ -6.92\cdot 10^{-1}\ \ -6.80\cdot 10^{-1}\ \ -6.24\cdot 10^{-1} \ldots$$

$$C_{np} := (2.26\cdot 10^{-2}\ \ 1.35\cdot 10^{-2}\ \ 1.35\cdot 10^{-2}\ \ -7.51\cdot 10^{-3}\ \ -1.49\cdot 10^{-2}\ \ -2.35\cdot 10^{-2}\ \ -3.64\cdot 10^{-2}\ \ -6.37\cdot 10^{-2}\ \ -1. \ldots$$

$$C_{yp} := (-2.09\cdot 10^{-1}\ \ -1.04\cdot 10^{-1}\ \ -1.04\cdot 10^{-1}\ \ 5.19\cdot 10^{-2}\ \ 1.05\cdot 10^{-1}\ \ 1.59\cdot 10^{-1}\ \ 2.17\cdot 10^{-1}\ \ 2.89\cdot 10^{-1}\ \ 3.72\cdot 1 \ldots$$

Aileron_

$C_{y\xi} := (0.0124\ \ 0.0147\ \ 0.0193\ \ 0.0108)$

$C_{LL\xi} := (-0.0807\ \ -0.0823\ \ -0.0937\ \ -0.0736)^{T}$

$C_{n\xi} := (-0.006\ \ -0.008\ \ -0.014\ \ -0.005)$

rudder

$C_{y\zeta} := 0.11$

$C_{LL\zeta} := (0.0173\ \ 0.0181\ \ 0.0101\ \ 0.0157)^{T}$

$C_{n\zeta} := -0.09$

11.3 Lateral direction stability derivatives (dimensionless) in wind axes

$CY\beta_k := \mathrm{linterp}(\alpha, C_{y\beta}, \alpha trim_k)$

$CLL\beta_k := \mathrm{linterp}(\alpha, C_{LL\beta}, \alpha trim_k)$

$CYp_k := \mathrm{linterp}(\alpha i, C_{yp}, \alpha trim_k)$

$CLLp_k := \mathrm{linterp}(\alpha i, C_{LLp}, \alpha trim_k)$

$CYr_k := C_{yr}$

$CLLr_k := \mathrm{linterp}(\alpha i, C_{LLr}, \alpha trim_k)$

$CN\beta_k := \mathrm{linterp}(\alpha, C_{n\beta}, \alpha trim_k)$

$CNp_k := \mathrm{linterp}(\alpha i, C_{np}, \alpha trim_k)$

$CNr_k := \mathrm{linterp}(\alpha i, C_{nr}, \alpha trim_k)$

11.4 Lateral direction stability derivatives (dimensional) in wind axes

$$Y\beta_k := CY\beta_k \cdot \frac{Qdyn(V_k) \cdot S}{V_k}$$

$$L\beta_k := CLL\beta_k \cdot \frac{Qdyn(V_k) \cdot S \cdot b}{V_k}$$

$$Yp_k := CYp_k \cdot \frac{2\,Qdyn(V_k) \cdot S \cdot b}{V_k}$$

$$Lp_k := CLLp_k \cdot \frac{2\,Qdyn(V_k) \cdot S \cdot b^2}{(V)_k}$$

$$Yr_k := CYr_k \cdot \frac{2\,Qdyn(V_k) \cdot S \cdot b}{V_k}$$

$$Lr_k := CLLr_k \cdot \frac{2\,Qdyn(V_k) \cdot S \cdot b^2}{V_k}$$

$$N\beta_k := CN\beta_k \cdot \frac{Qdyn(V_k) \cdot S \cdot b}{V_k}$$

$$Np_k := CNp_k \cdot \frac{2\,Qdyn(V_k) \cdot S \cdot b^2}{V_k}$$

$$Nr_k := CNr_k \cdot \frac{2\,Qdyn(V_k) \cdot S \cdot b^2}{V_k}$$

11.5 Lateral direction control derivatives (dimensional) in wind axes

$$Y\xi_k := C_{y\xi} \cdot Qdyn\left(V_k\right) \cdot S \qquad L\xi_k := C_{LL\xi} \cdot Qdyn\left(V_k\right) \cdot S \cdot b$$

$$Y\zeta_k := C_{y\zeta} \cdot Qdyn\left(V_k\right) \cdot S \qquad L\zeta_k := C_{LL\zeta} \cdot Qdyn\left(V_k\right) \cdot S \cdot b$$

$$N\xi_k := C_{n\xi\_on\_CL} \cdot CLtrim_k \cdot Qdyn\left(V_k\right) \cdot S \cdot b$$

$$N\zeta_k := C_{n\zeta} \cdot Qdyn\left(V_k\right) \cdot S \cdot b$$

11.6 Elements of the B matrix : coincise derivative in terms of dimensional derivatives in wind axes

$$y\xi_k := \frac{Y\xi_k}{m} \qquad y\zeta_k := \frac{Y\zeta_k}{m}$$

$$l\xi_k := \frac{\left(Iz_k \cdot L\xi_k + Ixz_k \cdot N\xi_k\right)}{Ix_k \cdot Iz_k - \left(Ixz_k\right)^2} \qquad l\zeta_k := \frac{\left(Iz_k \cdot L\zeta_k + Ixz_k \cdot N\zeta_k\right)}{Ix_k \cdot Iz_k - \left(Ixz_k\right)^2}$$

$$n\xi_k := \frac{\left(Iz_k \cdot N\xi_k + Ixz_k \cdot L\xi_k\right)}{Ix_k \cdot Iz_k - \left(Ixz_k\right)^2} \qquad n\xi_k := \frac{\left(Iz_k \cdot N\zeta_k + Ixz_k \cdot L\zeta_k\right)}{Ix_k \cdot Iz_k - \left(Ixz_k\right)^2}$$

$$Al_k := \begin{pmatrix} y\,v_k & y\,p_k & y\,r_k & y\,\phi \\ l\,v_k & l\,p_k & l\,r_k & l\,\phi \\ n\,v_k & n\,p_k & n\,r_k & n\,\phi \\ 0 & 1 & 0 & 0 \end{pmatrix} \qquad Bl_k := \begin{pmatrix} y\xi_k & y\zeta_k \\ l\xi_k & l\zeta_k \\ n\xi_k & n\xi_k \\ 0 & 0 \end{pmatrix}$$

APPENDIX D

CC ACTUATOR WIND TUNNEL TEST

D.1 Drawings of the Circulation Control actuator wind tunnel test model

Top view:

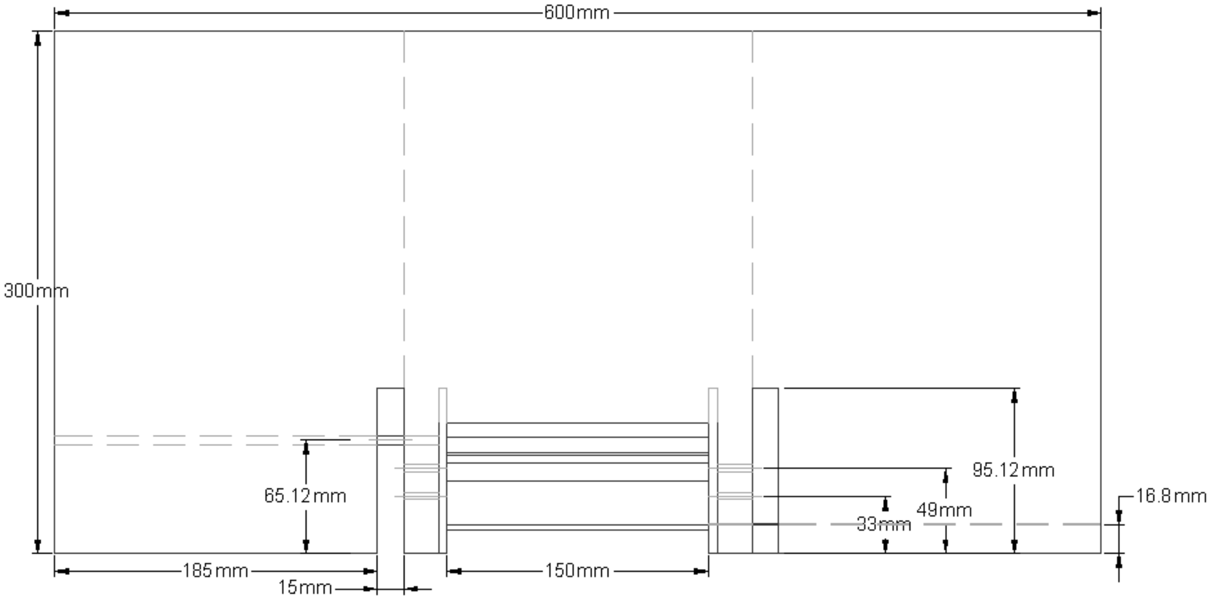

Side view:

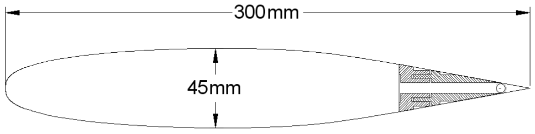

Detailed trailing edge geometry (slot height 0.05-0.2mm, centre of rotation of cylinder offset by 1mm):

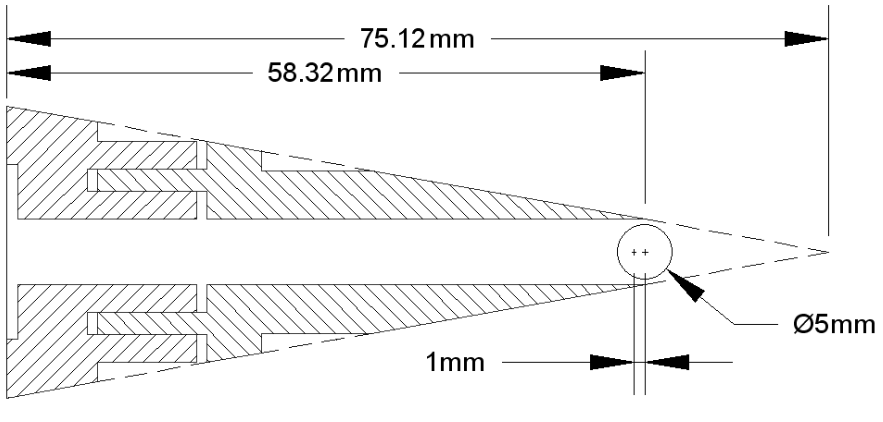

D.2 Corrections to wind tunnel data and CFD results

D.2.1 CC actuator wind tunnel test corrections

Following acquisition of the force and moment data from each test case, corrections were made to the data, noting:

- Solid or wake blocking effect are negligible for open test sections.
- Incidence corrections were deemed necessary.

Notation in this section is consistent with the one presented in Pope (1954).

The corrected angle of attack (α_c) is related to the geometric angle of attack (same as measured angle of attack (α_u) by the addition of a correction factor, $\Delta\alpha_t$ (Barlow, Rae and Pope, 1999).

$$\Delta\alpha_t = \Delta\alpha_{sc} + \Delta\alpha \tag{D-1}$$

The corrections for streamline curvature (boundary induce upwash along the chord) is as follows,

$$\Delta\alpha_{sc} = \tau_2 \delta \frac{S}{c} C_{L_w} = (-0.00256) C_{L_w} \tag{D-2}$$

General downwash correction is as follow:

$$\Delta\alpha = \delta \frac{S}{c} C_{L_w} = (-0.0256) C_{L_w} \tag{D-3}$$

τ_2 is the streamline curvature effect on angle, δ is a dimensionless wall correction factor, S is the model wing area, C is the tunnel cross sectional area, and C_{Lw} is the model wing lift coefficient of each particular run (at α_u). τ_2 and δ are obtained graphically from the reference text Pope (1954).

Hence, the corrected angle of attack is:

$$\alpha_c = \Delta\alpha_t + \alpha_u = \alpha_u + (-0.0282)C_{Lw} \tag{D-4}$$

Additional wall corrections could also be made to lift and pitching moment coefficients, but these were deemed negligible.

The induce drag increment due to the boundaries is:

$$\Delta C_D = \Delta\alpha {C_{Lw}}^2 = (-0.0256){C_{Lw}}^2 \tag{D-5}$$

A cylindrical section formed part of the support structure which was immersed in the free stream. Its added drag and reduction in wing moment have been taken into account.

Tare drag measurements have been made in isolation without the presence of the wing and these were deducted from the measured total drag.

Wing tips have been kept blunt and it is recognised that this results in an increased maximum lift coefficient being a function of the thickness to chord ratio. For *t/c*=0.15 an equivalent wing with rounded tips can be expected to have a reduction in maximum lift coefficient of about 0.05.

D.2.2 3D corrections of CFD data:

The lift curve slope a_0 obtained from CFD simulation has been used to calculate the 3D lift curve slope for a finite aspect ratio wing, using approximation derived by Helmbold and reported in Laiton, (1989),

$$\begin{aligned} a &= \frac{a_0 AR}{2 + (4 + AR^2)^{1/2}} = 2.4753 rad^{-1} \\ a_0 &= 5.976 rad^{-1}\text{ ; } AR = 2\text{ ;} \end{aligned} \tag{D-6}$$

The lift increment due to TE blowing was derived applying a part span correction (ESDU 74012) to take into account the limited span-wise extent of the TE device. Using the same notation as in ESDU:

$$\Delta C_L = 0.32 \Delta C_{LF} \tag{D-7}$$

Drag obtained from the 2D computation was assumed to be due to skin friction drag only and therefore the induced drag was added:

$$C_D = C_{Di} + \left\lfloor C_{Df} \right\rfloor_{2D} \tag{D-8}$$

The lift distribution was not measured directly and the Oswald efficiency was calculated via:

$$e = \frac{1}{\left(\dfrac{dC_D}{dC_L^2}\right)\pi A} = \frac{1}{K_1 \pi A} \tag{D-9}$$

where K_1 was derived from WT data.

No corrections were applied to the pitching moment coefficient.

D.3 Data quality and repeatability

The 3-component floor balance accuracy is summarized in table D-1.

	Lift	**Pitching Moment**	**Drag**
Max Load	20 kgf	0.4 kgf	4 kgf
Std %	0.03	0.06	0.04

Table D-4. 3 – Component floor balance accuracy

Repeatability was monitored and assessed within the same wind on run and within the same test series. Each of the tests started with complete resetting of the model. Figures D-1 and D-2 show results of repeatability for the lift, pitching moment and drag coefficient respectively. The results are obtained for α=0 and two different slot height, h/r= 0.16 and h/r=0.2 respectively.

Being the data scatters linked directly to errors associated with the blowing momentum measurement, some considerations regarding the errors associated with the slot set-up and, hence, the measurement of the non dimensional momentum coefficient should be taken into account in analysing the repeatability of the wind tunnel test measurements.

The measurement of the non dimensional momentum coefficient can be obtained from the measured pressure ratio inside the plenum and knowledge of the slot height. The slot height was set with a height gage under no flow conditions and locked into place with push and pull screws located approximately one inch from the slot exit inside the settling region of the jet plenum. However, span-wise jet velocities variations were observed at the slot exit. Most of these variations are associated with the wake of the internal push and pull screws used for setting the slot height. It was also discovered that the extreme inboard and outboard slot velocity was lower than the core region of the span. This is attributed to the internal flow separation. This does effectively reduce the blowing sections of the jet, and this correction has been taken into account in the evaluation of the blowing momentum.

The distance between the upper and lower slot slightly increased under load, variations being larger at higher pressure ratios. The maximum measurable variations were +-0.025. However, as there was no direct measurement of either the velocity profile or the mass flow rate, no exact determination of the slot height accuracy was possible.

All these errors contribute to the errors which ultimately affects the measurement of the non dimensional blowing momentum coefficient.

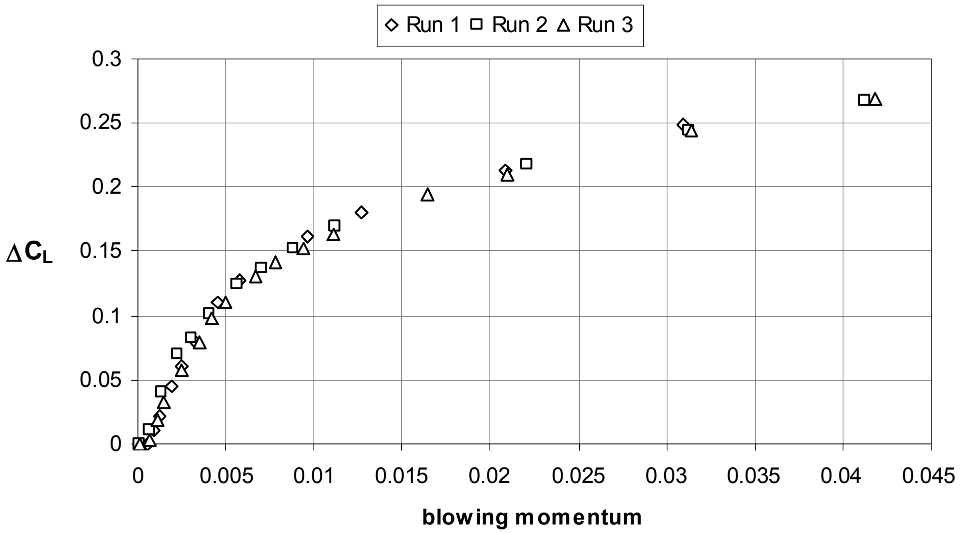

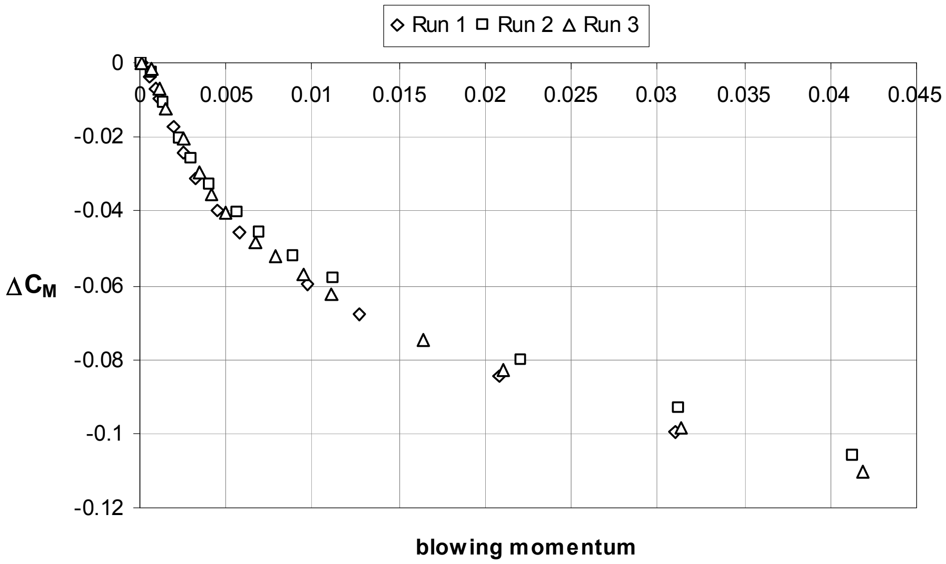

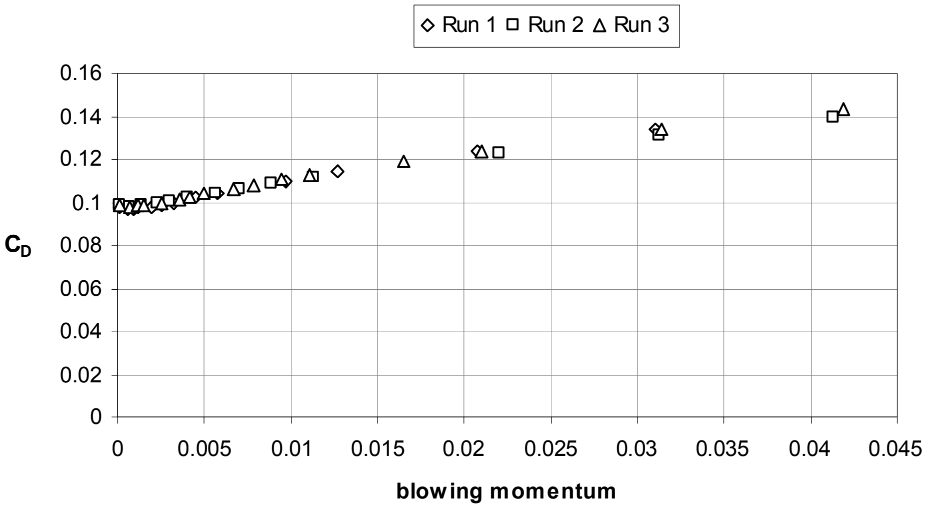

Fig. D-1. Data measurements repeatability - α=0, h/r =0.16

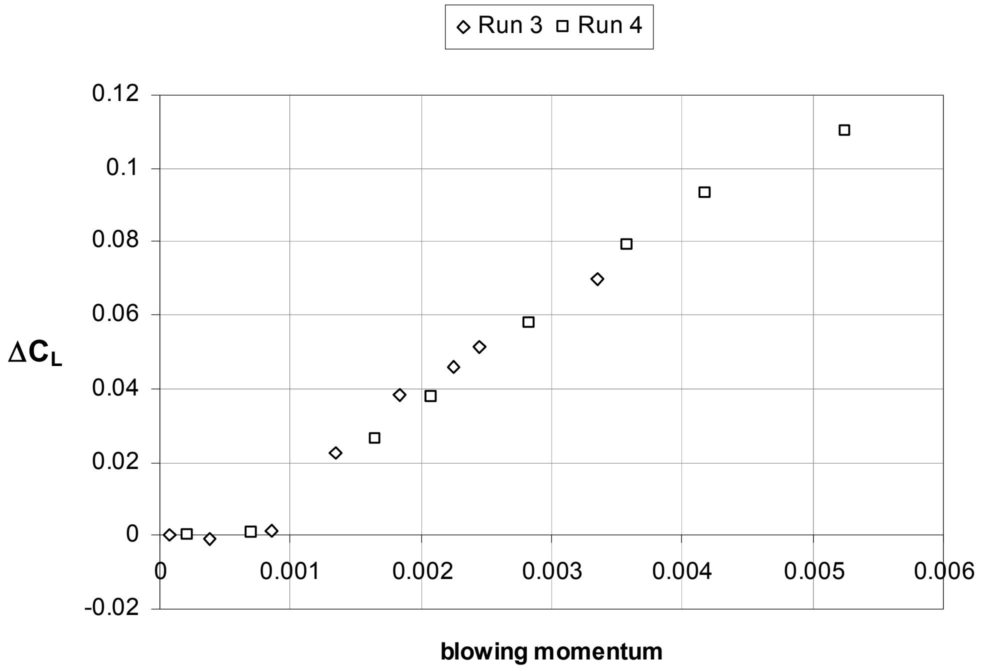

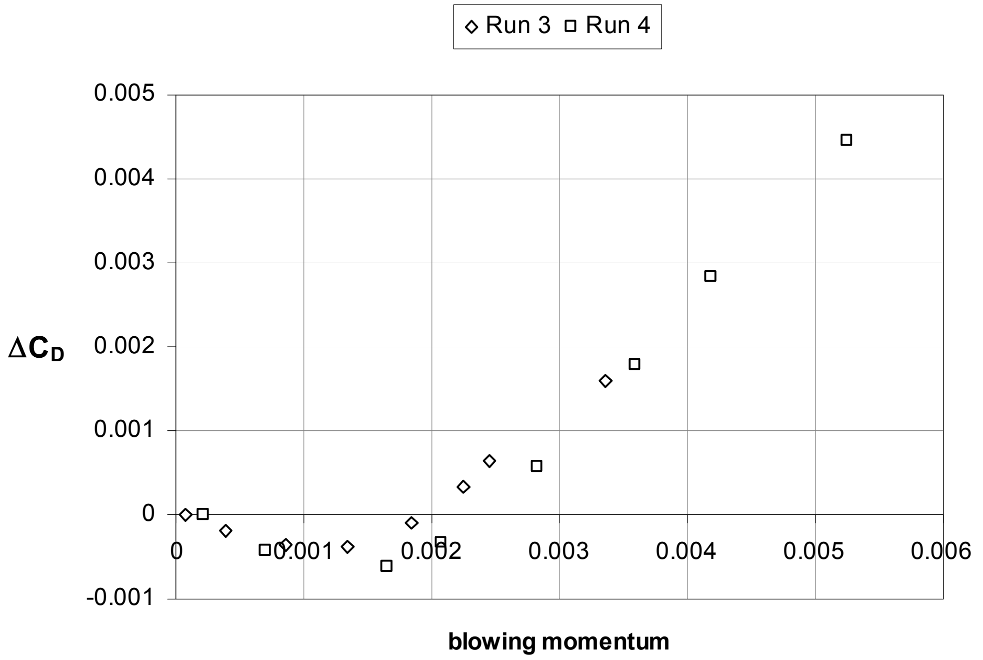

Fig. D-2. Data measurements repeatability - α=0, *h/r* =0.16

D.4 Mathematical derivation of the actuator geometry

Equation (5-10) and (5-11) have been derived as follow. Notation in this section is consistent with Fig. 5-18.

Considering the pivot as the origin of axes, the cylinder perimeter can be defined by the equation of a circle, which centre is offset of x_c and y_c respectively along the x and y axes:

$$(x-x_c)^2+(y-y_c)^2=r_c^{\,2} \qquad \text{(D-10)}$$

Thus, referring to the geometry in Fig. 5-18, it is easily shown that:

$$x_c=\lambda rCos\delta \quad y_c=\lambda rSin\delta \qquad \text{(D-11)}$$

The height of the slot is given by,

$$h_j=(r+h_0)-y_t \qquad \text{(D-12)}$$

Where y_t is the intersect of the circle with the vertical $x=\lambda r$, and it is equal to:

$$y_t=\pm r_c\sqrt{1-\lambda(1-\cos\delta)^2}+\lambda r_c\sin\delta \qquad \text{(D-13)}$$

Thus, substituting Eq. (D-13) into Eq. (D-12), the height of the upper slot is found to be:

$$h_{ju}=(r+h_0)-r_c\left(\sqrt{1-\lambda(1-\cos\delta)^2}-\lambda\sin\delta\right) \qquad \text{(D-14)}$$

The equation for the lower slot follows directly.

APPENDIX E

PREDICTION OF THE AERODYNAMIC CHARACTERISTICS OF THE DEMON/CC

E.1 Part span correction

The lift increment due to trailing edge blowing obtained from wind tunnel test on the rectangular wing was part-span corrected to take into account the limited span-wise extent of the TE device.

The corresponding full span lift coefficient increment is obtained from the part-span lift coefficient increment applying a part span correction method presented in ESDU 74012. Using the same notation as in ESDU,

$$\Delta C_{LF} = \Delta C_L / \left(\frac{\Delta C_{Lo}}{\Delta C_{LF}} - \frac{\Delta C_{Li}}{\Delta C_{LF}} \right) = \frac{\Delta C_L}{\Phi_o - \Phi_i} \qquad \text{(E-1)}$$

Factor Φ is a function of plan-form parameters and outboard and inboard limit of the flap (η) expressed as a percentage of the span. The values evaluated graphically for the test rectangular wing are presented in table E-1.

	η	Φ
Inboard	0.375	0.423
Outboard	0.625	0.71

Table E-1. Part span correction factor for the CC actuator installed in the rectangular wing

E.2 Rolling moment coefficient

A semi-empirical method (ESDU 88013) has been used for predicting the rolling moment derivative due to the operation of the CC actuator in the *Demon* plan-form replacing Surface No. 2.

The derivative for antisymmetric deflection of the actuators is given by Eq. (E-2),

$$C_{LL_\delta} = -1/2\bar{\eta}\frac{\partial C_{LF}}{\partial \delta}\left(\Phi_{\xi i} - \Phi_{\xi o}\right) \tag{E-2}$$

The derivative $\frac{\partial C_{LF}}{\partial \delta}$ is the rate of change of lift coefficient due to deflection of the CC actuator cylinder for full span trailing edge slot, as predicted in paragraph E.1.

In Eq. (E-2) $\bar{\eta}$ is taken as the mean of the control surface inboard and outboard limit measured at the hinge line and expressed as a fraction of the semi-span, in the form of,

$$\bar{\eta} = 1/2(\eta_o + \eta_i) \tag{E-3}$$

The function ϕ, evaluated at $\eta = \eta_i$ and $\eta = \eta_o$ respectively, is expressed as,

$$\Phi = K_1 - K_2 \tag{E-4}$$

where K_1 and K_2 are function of η and plan-form geometry and can be graphically evaluated. Values of the corrections factors obtained for the *Demon* plan-form are presented in table E-2.

	η	*K1*	*K2*
Inboard	0.635	0.85	0.055
Outboard	0.7899	0.15	0.0465

Table E-2. Rolling moment coefficient correction factors from Eq. (E-4)

APPENDIX F

DRAWINGS OF CC ACTUATOR INTEGRATION WITHIN THE FLYING DEMONSTRATOR

Initial CATIA drawings of the integration of the CC actuator within the 15% scale *Demon*, Fig. F-1 and Fig. F-2, have been produced in collaboration with the Cranfield Integration Group. The goal is to replace the hinged inboard aileron with a plenum, without reducing the chord-wise extent. Initial engineering drawings are reported.

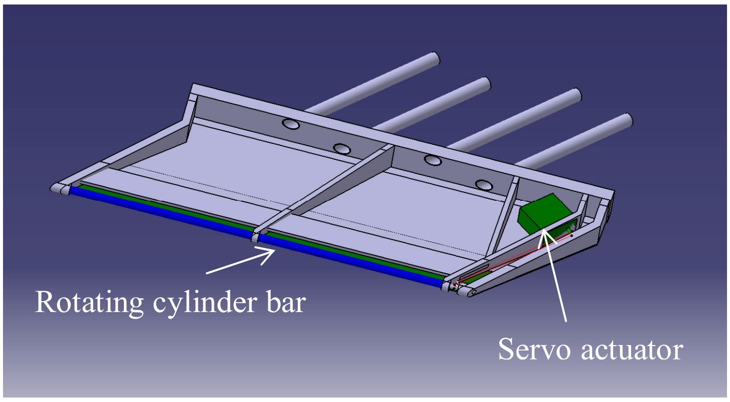

Fig. F-1. CATIA model illustrating the chamber internal arrangement

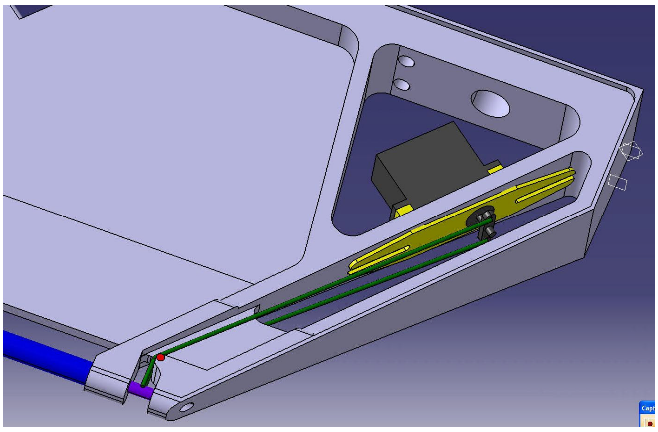

Fig. F-2. Detail of the servo actuator arrangement